APPLIED COMPUTATIONAL ELECTROMAGNETICS SOCIETY JOURNAL

June 2020
Vol. 35 No. 6
ISSN 1054-4887

The ACES Journal is abstracted in INSPEC, in Engineering Index, DTIC, Science Citation Index Expanded, the Research Alert, and to Current Contents/Engineering, Computing & Technology.

The illustrations on the front cover have been obtained from the research groups at the Department of Electrical Engineering, The University of Mississippi.

JUNE 2020 REVIEWERS: REGULAR PAPERS

Ercument Arvas
Ahmed Attiya
Adalbert Beyer
Toni Björninen
Robert Burkholder
Ali Çetin
Nunzia Fontana
Aleksandr Gafarov
Bernhard Hoenders
Guan-Long Huang
Taha Imeci
Tianqi Jiao
Ashutosh Kedar
Bin Li
Gaosheng Li
Yingsong Li
Mario Miscuglio
Adam Mock
Zia Ur Mohammad
Antonio Orlandi
Lionel Pichon
Dudla Prabhakar
Cheng Qian
Daniel Rodriguez Prado
Vince Rodriguez
Sayan Roy
Ting-Yen Shih
Yogesh Thakare
Sathiyapriya Thangavel
Ozgur Tuncer
Ioannis Vardiambasis
Marsellas Waller
Joshua Wilson
Qi Wu
John Young
Luyu Zhao

THE APPLIED COMPUTATIONAL ELECTROMAGNETICS SOCIETY JOURNAL

Vol. 35 No. 6 June 2020

TABLE OF CONTENTS – REGULAR PAPERS

Parallel Implementation and Branch Optimization of EBE-FEM Based on CUDA Platform

Yan Zhang, Xiuke Yan, Xudong Ren, Sheng Wang, Dongyang Wu, and Baodong Bai

School of Electrical Engineering
Shenyang University of Technology, Shenyang, 110870, China
yanxke@126.com

Abstract ─ The finite element analysis of large complex structures makes higher demand on memory capacity and computation speed, which leads to the inefficiency of traditional serial finite element method (FEM) for such large-scale problems. In this paper, the element-by-element finite element method (EBE-FEM) has been implemented parallelly on CUDA (Compute Unified Device Architecture) platform, and been programmed using C++ language. The thread branches that exist in parallel reduction program have been researched and optimized to improve parallel efficiency. The correctness of algorithms and programs are verified by the analysis of an open slot of motor. The optimized parallel program is applied to analyze the main magnetic field of a single-phase transformer. The results show that the EBE-FEM implemented on CUDA platform is more effective than serial EBE-FEM, and branch optimization can improve the speedup further.

Index Terms ─ Branch optimization, CUDA, EBE-FEM, parallel computation.

I. INTRODUCTION

When FEM is used to analyze the electromagnetic field of large electrical equipment, huge amounts of meshes are needed to get more accurate results, which leads to a large scale of computation. Using traditional serial FEM to calculate large-scale numerical problems, there will be problems such as too long calculation time and large calculation error, sometimes even unable to calculate. Therefore, more and more parallel FEM (PFEM) are developed and applied to numerical calculation and EBE-FEM is one of them [1]. EBE-FEM avoids the formation and storage of the global coefficient matrix, and has no requirement or restriction on the geometric shape and element number of the structure in the region [2,3]. The parallel computing of EBE-FEM can be implemented on the elements level, it has high parallelism. Combining EBE-FEM with advanced computing platform can solve the bottleneck problem of large-scale numerical computation.

GPUs represent one of the newest types of parallel processors. For its many-core nature, it is widely used in parallel calculation [4,5]. CUDA is a CPU+GPU heterogeneous parallel computing platform [6,7], which provides a reliable programming environment for GPU to perform data parallel processing. The EBE-FEM can be thought as a method which transforms a highly memory dependent problem to a massively computational dependent one, the latter can be parallelized efficiently. CUDA platform can make full use of the advantages of high parallelism of EBE-FEM [8,9]. GPUs are very good at computing, but weaker in logical judgments. For high-parallel and intensive computing, whether it is a small problem or a large problem, running on GPU in parallel is better than it on CPU in serial. Recent years, some CUDA function libraries, such as cuBLAS, cuBLAS-XT, etc. have been developed to implement computation on GPUs. However, they sometimes show poor speedup performance due to their non-optimized operating process. Thread branch may appear in the process of EBE-FEM parallel implementing on CUDA platform. It is one of the main factors to reduce the parallel efficiency. This problem can be solved by thread-data remapping method [10].

In this paper, EBE-FEM combined with Jacobi preconditioned conjugate gradient (J-PCG) method has been researched to realize parallel computation on CUDA platform. The thread branches in reduction operation has been investigated and thread-data remapping method on instruction-level is proposed to optimize addressing process of reduction operation. All the corresponding programs have been developed in C++. The correctness of the proposed algorithms and programs are verified by the analysis of an open slot of motor. The algorithms and programs have been applied to calculate the magnetic field in a single phase power transformer, the results have been analyzed and discussed.

II. METHOD DESCRIPTION

A. EBE technique

Using FEM, the Maxwell electromagnetic field equations can be discretized as linear equations:

Submitted On: December 17, 2019
Accepted On: April 12, 2020

$$\mathbf{Ax} = \mathbf{b}, \tag{1}$$

where $\mathbf{A}$ is the whole stiffness matrix, $\mathbf{x}$ the vector of unknown variables and $\mathbf{b}$ the system vector.

According to EBE-FEM, (1) can be expressed as:

$$\left(\sum_{e=1}^{E}\left(\mathbf{Q}^{(e)}\right)^{T}\mathbf{A}^{(e)}\mathbf{Q}^{(e)}\right)\left(\sum_{e=1}^{E}\left(\mathbf{Q}^{(e)}\right)^{T}\mathbf{x}^{(e)}\right)=\left(\sum_{e=1}^{E}\left(\mathbf{Q}^{(e)}\right)^{T}\mathbf{b}^{(e)}\right), \tag{2}$$

where $\mathbf{A}^{(e)}$ is element stiffness matrix, $\mathbf{b}^{(e)}$ the element vector and matrix $\mathbf{Q}^{(e)}$ represents transition between local and global numbering of the unknown variables for the element.

The main operation of CG method is the inner product of vectors, which is appropriate to realize parallel computation. Therefore, CG method has been used to solve the equations of EBE-FEM. The iteration of CG method can be expressed by:

$$\mathbf{x}_0 = (0, 0, ...0)^T, \ \mathbf{r}_0 = \mathbf{P}_0 = \mathbf{b}, \tag{3}$$

$$\alpha_k = \frac{(\mathbf{P}_k, \mathbf{b})}{(\mathbf{P}_k, \mathbf{AP}_k)}, \tag{4}$$

$$\mathbf{x}_{k+1} = \mathbf{x}_k + \alpha_k \mathbf{P}_k, \tag{5}$$

$$\mathbf{r}_{k+1} = \mathbf{b} - \mathbf{Ax}_{k+1}, \tag{6}$$

if $\mathbf{r}_k < \varepsilon$, stop iteration, $\mathbf{x} = \mathbf{x}_k$; else, update β_k and $\mathbf{P}_k$:

$$\beta_k = \frac{(\mathbf{r}_{k+1}, \mathbf{AP}_k)}{(\mathbf{P}_k, \mathbf{AP}_k)}, \tag{7}$$

$$\mathbf{P}_{k+1} = \mathbf{r}_{k+1} + \beta_k \mathbf{P}_k, \tag{8}$$

return to the equation (4), and continue iteration process.

In EBE method, the inner product $(\mathbf{r}, \mathbf{r})$ and $(\mathbf{P}, \mathbf{AP})$ can be calculated on each element as follow:

$$(\mathbf{r}, \mathbf{r}) = \mathbf{r}^T\mathbf{r} = (\mathbf{Q}^T\mathbf{r}^e)^T\mathbf{Q}^T\mathbf{r}^e = \sum_{e=1}^{E}(\mathbf{r}^e)^T\mathbf{s}^{(e)}, \tag{9}$$

$$\mathbf{s}^{(e)} = \mathbf{r}^e \oplus \sum_{j=adj(e)} \mathbf{r}^j, \tag{10}$$

$$(\mathbf{P}, \mathbf{AP}) = (\mathbf{QP})^T \mathbf{A}^e\mathbf{QP} = \sum_{e=1}^{E}\left(\mathbf{P}^{(e)}\right)^T \mathbf{A}^e\mathbf{P}^{(e)}, \tag{11}$$

$$\mathbf{Q} = \left(\mathbf{Q}^{(1)T}, \mathbf{Q}^{(2)T}, ..., \mathbf{Q}^{(E)T}\right)^T, \tag{12}$$

where $\mathbf{r}$ is the global residual vector, $\mathbf{r}^e$ is the local element residual vector, $\oplus$ refers to accumulation of the contribution made by all elements to the nodes of the element and adj(e) represents the adjacent element which share the common node with element e.

In order to improve its convergence further, the Jacobi preconditioned (JP) technology is applied to EBE-CG. The mathematic model of EBE-J-PCG was presented in [9]. The multi-core nature of GPU can exploit the parallelism of EBE-CG method considerably on CUDA platform.

B. Parallel realization on CUDA platform

CUDA is CPU+GPU heterogeneous computing platform, the programming model ensures that the GPU and CPU complement each other, which executes the complex logic control tasks on CPU and data-parallel computation-intensive tasks on GPU. Implementing EBE-FEM on CUDA, the CPU+GPU collaborative computing model is shown in Fig. 1.

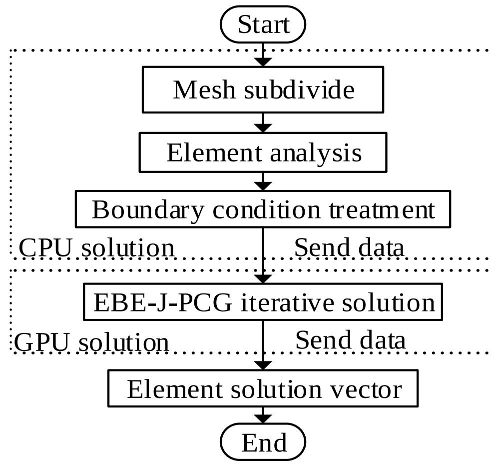

Fig. 1. Flow of CPU+GPU heterogeneous computing model of EBE-FEM.

In GPU solution, the EBE-J-PCG iterating solution for all elements can be operated at the same time. The calculations are performed by kernels with different function on GPU. The parallel computation on CUDA platform is realized by executing the kernel functions in parallel through thousands of threads. The inner product of vectors is executed parallelly for all elements by two kernels are shown as Fig. 2.

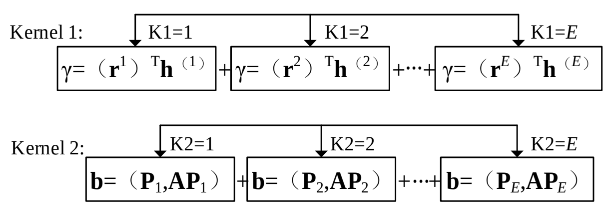

Fig. 2. Kernel functions with reduction operations.

The iterative process of EBE-J-PCG method can be given as:

(1) Initialization

(a) Set initial value,

$$\mathbf{x}_0^{(e)} = 0, \mathbf{r}^{(e)} = \mathbf{b}^e - \mathbf{A}^e\mathbf{x}_0^{(e)}. \tag{13}$$

(b) Jacobi precondition,

$$\mathbf{m}^e = diag\left(\mathbf{A}^e\right), \tag{14}$$

$$\mathbf{m}^{(e)} = \mathbf{m}^{e} \oplus \sum_{j=adj(e)} \mathbf{m}^{j}. \tag{15}$$

(c) Solve equations,

$$\mathbf{m}^{(e)}\mathbf{h}^{e} = \mathbf{r}^{e}. \tag{16}$$

(d) Calculate $\gamma_0 = (\mathbf{r}, \mathbf{h})$.

For e∈(1,2,...,E), use kernel 1 shown as Fig. 2.

(e) Calculate $\mathbf{p}^{(e)}$,

$$\mathbf{p}^{(e)} = \mathbf{h}^{(e)}. \tag{17}$$

(2) Calculate α.

For e∈(1,2,...,E), use kernel 1 and kernel 2 shown as Fig. 2,

$$\alpha = \frac{\left(\mathbf{P}_{k-1}, \mathbf{h}_{k-1}\right)}{\left(\mathbf{P}_{k}, \mathbf{AP}_{k}\right)}. \tag{18}$$

(3) Update $\mathbf{x}^{(e)}$ and $\mathbf{r}^{e}$,

$$\mathbf{x}^{(e)} = \mathbf{x}^{(e)} + \alpha\mathbf{p}^{(e)}, \tag{19}$$

$$\mathbf{r}^{e} = \mathbf{r}^{e} - \alpha\mathbf{A}^{e}\mathbf{p}^{(e)}. \tag{20}$$

(4) Solve equations,

$$\mathbf{m}^{(e)}\mathbf{h}^{e} = \mathbf{r}^{e}. \tag{21}$$

(5) Calculate $\gamma_{new} = (\mathbf{r}, \mathbf{h})$.

For e∈(1,2,...,E), use kernel 1 shown as Fig. 2.

(6) Judge convergence.

If $\gamma_{new} < \delta\gamma_0$, the calculation stops, else,

update $\mathbf{p}^{(e)}$,

$$\mathbf{p}^{(e)} = \mathbf{h}^{(e)} + (\gamma_{new} / \gamma_0)\mathbf{p}^{(e)}, \gamma_0 = \gamma_{new}. \tag{22}$$

Then, return to (2), where he is the element preprocessing vector, me is the vector of the main diagonal elements of each element.

Both of two kernels shown in Fig. 2 involve reduction operation. In EBE-J-PCG method, lots of reduction operations generate a large number of thread branches, which eventually lead to a deterioration in parallel efficiency. Although thousands of threads execute the same kernel functions, their operations and processed data may be different, which is due to the different allocation methods of threads.

C. Branch optimization method of thread-data remapping

Generally, threads are executed in parallel, however, if different threads contain different control conditions, threads that execute different condition paths can only be executed serially. This is called thread branch, which is one of the main factors affecting GPU parallel efficiency.

Path vector is introduced to express thread branches in a piece of code. **V** represents all possible thread path sets, take a warp containing 4 threads as an example:

$$\mathbf{V}[\text{tid}] = \left\{\text{p}_m[\text{tid}], \text{p}_n[\text{tid}], \text{p}_k[\text{tid}], \text{p}_l[\text{tid}]\right\}, \tag{23}$$

where p[tid] is the execution path, tid is the address of the current thread, and *m*, *n*, *k*, *l* represent four possible different paths respectively. When there is only one element in **V**, such as $\mathbf{V}[\text{tid}] = \left\{\text{p}_m[\text{tid}]\right\}$, thread branches do not occur in a warp.

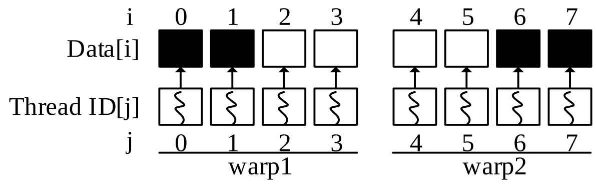

Fig. 3. Original thread-data mapping.

Suppose there are four threads in a warp shown as Fig. 3, squares in two different colors represent the data to be processed differently. The mapping relationship in warp1 is:

$$\text{Thread ID}[\text{j}](\text{j}=0,1) \rightarrow \text{Data1}[\text{i}](\text{i}=0,1), \tag{24}$$

$$\text{Thread ID}[\text{j}](\text{j}=2,3) \rightarrow \text{Data2}[\text{i}](\text{i}=2,3). \tag{25}$$

The mapping relationship in warp2 is:

$$\text{Thread ID}[\text{j}](\text{j}=4,5) \rightarrow \text{Data2}[\text{i}](\text{i}=4,5), \tag{26}$$

$$\text{Thread ID}[\text{j}](\text{j}=6,7) \rightarrow \text{Data1}[\text{i}](\text{i}=6,7). \tag{27}$$

A mapping relationship represents an execution path. The path vector is $\mathbf{V}[\text{tid}] = \left\{\text{p}_1[\text{tid}], \text{p}_2[\text{tid}]\right\}$ for both warp1 and warp2. Two execution paths exist in both warp1 and warp2, which results in thread branches.

To eliminate the threads branch, the mapping between thread and data can be reset, switch threads that execute the same code in different warp to the same warp so that all threads in a warp will take the same path.

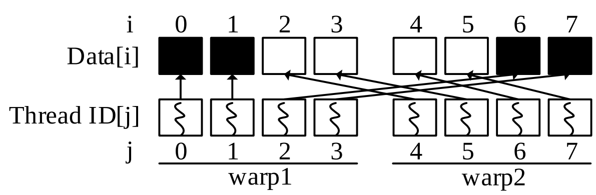

Fig. 4. Redirected thread-data mapping.

As shown in Fig. 4, change the direction of thread mapping, remap the threads in warp1 and warp2 so that the same type of data will be processed in the same warp. After remapping, the mapping relationship in warp1 is:

$$\text{Thread ID}[\text{j}](\text{j}=0,1,2,3) \rightarrow \text{Data1}[\text{i}](\text{i}=0,1,6,7). \tag{28}$$

The mapping relationship in warp2 is:

$$\text{Thread ID}[\text{j}](\text{j}=4,5,6,7) \rightarrow \text{Data2}[\text{i}](\text{i}=2,3,4,5), \tag{29}$$

therefore, path vector has been converted to $\mathbf{V}[\text{tid}] = \left\{\text{p}_1[\text{tid}]\right\}$ for warp1 and $\mathbf{V}[\text{tid}] = \left\{\text{p}_2[\text{tid}]\right\}$ for warp2, no thread branches exists in them.

D. Branch optimization of reduction operation in EBE-FEM

Generally, reduction operation adopts adjacent addressing mode, but this mode will generate many thread branches when EBE-FEM is executed on CUDA platform.

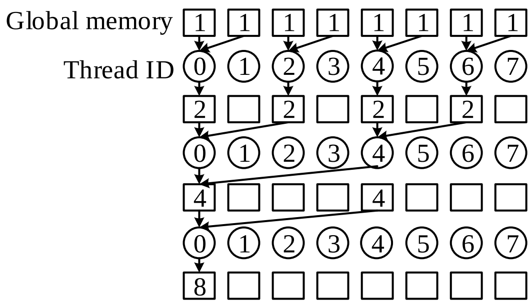

Fig. 5. Adjacent addressing mode.

Figure 5 shows the thread-data mapping of reduction program using adjacent addressing (Assume the reduction operation generates the sum of eight input data). Threads with even address execute addition operation for two adjacent data, threads with odd address do nothing except the parity checking of thread address. Even if only one thread involved in reduction operation, it needs to wait for the other seven threads to perform parity.

All threads in the warp need to be determined the parity, which will generate lots of thread branches. Thread-data remapping method is applied to addressing process to obtain better allocation of threads. Figure 6 shows the optimized addressing mode.

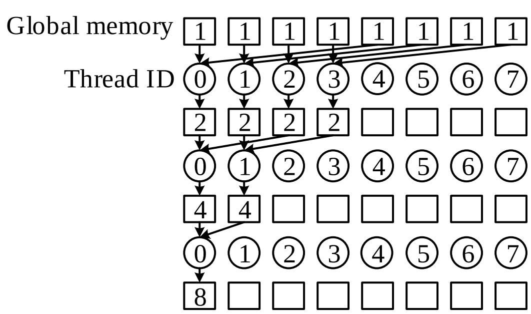

Fig. 6. Optimized addressing mode.

Change the thread data mapping relationship of adjacent addressing, the data involved in reduction operation are divided into two groups on average. The threads that execute addition operation are mapped sequentially to two data from the first group and the second group respectively. The threads in the second group are not involved in any operation, so they can be stopped by hardware, which will reduce useless operations and waiting. After thread-data remapping, the judgments for parity have been eliminated, thread branches have been reduced, which would improve the computational efficiency.

Branch optimization is an optimization method to GPU parallel technology, which improves parallel efficiency by reducing the number of logical judgments. In a multi-GPU environment, the degree of parallelism is higher and branch optimization is more critical, which can improve parallel efficiency more effectively.

III. APPLICATION AND ANALYSIS

The proposed method has been applied to analyze the magnetic field in an opening slot of motor and the field produced by a single-phase power transformer. All the programs have been developed in C++. The computations have been carried out on the Intel Xeon E5-2650 v2, 2.6GHz server with dual GPU (Nvidia Quadro K2000) and 256GB memory.

The main computation in this paper is the inner product of vectors, which is not complicated, and a single GPU can meet the computing requirements. In the subsequent research of multiphysics coupling problems, if the kernel function involves intensive complex parallel calculations, the multi-GPU method will be considered.

A. Magnetic field in an opening slot of motor

The opening slot of motor is shown as Fig. 7, it is an example to illustrate the traditional FEM in a book [11]. Due to its very simple model, few meshes and very regular mesh shapes, the magnetic potential on each node can be determined accurately by traditional FEM, and the results are given by the book.

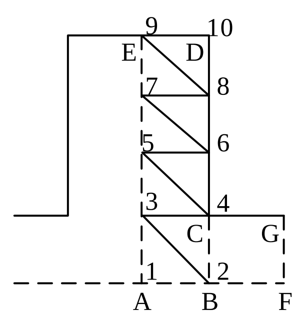

Fig. 7. Model and mesh of opening slot of motor.

In the model, AE and FG are the center lines of stator slot and tooth respectively, and AF is the center line of the air gap. Assuming BC is a magnetic line, rectangular ABDE can be taken as the solving region. Taking scalar magnetic potential φ_m as variable, the first boundary condition exists on AB and CDE. Setting $\varphi_m = 0$ on CDE, and $\varphi_m = 700$ A on AB, the magnetic potential on each node can be obtained.

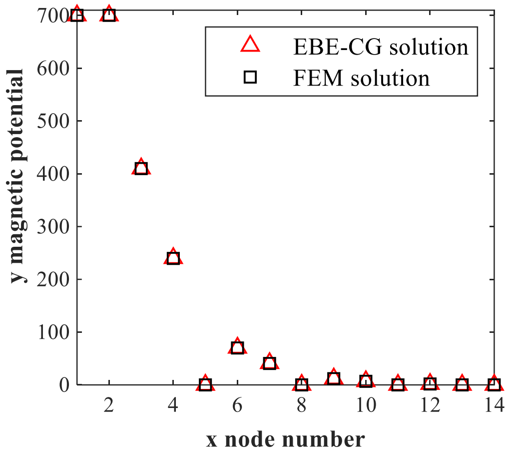

Fig. 8. Comparison of calculation results.

Figure 8 shows the comparison of the results calculated by parallel program of EBE-J-PCG method and traditional FEM. The maximum local error is 0.83%, which verifies the correctness of the EBE-J-PCG method and program.

B. Magnetic field analysis of a single-phase transformer

This method is applied to calculate the 2D quasi-static magnetic field distribution of single-phase DSP-241000kVA/500kV transformer which the secondary side is opened and the primary side is excited by rated current. Figure 9 shows the model and meshes of the transformer. The distribution of the magnetic lines and the magnetic flux density are shown in Figs. 10 and 11.

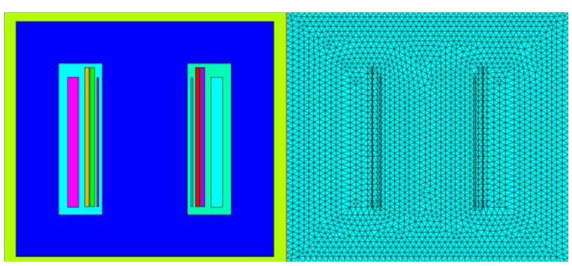

Fig. 9. The model and mesh of the transformer.

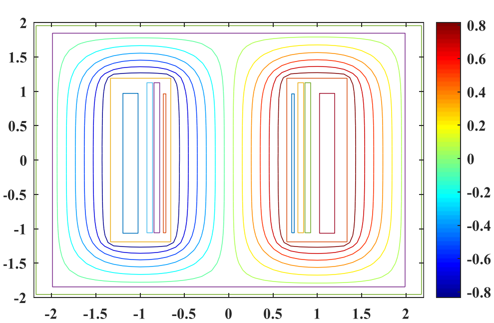

Fig. 10. Distribution of magnetic lines in transformer.

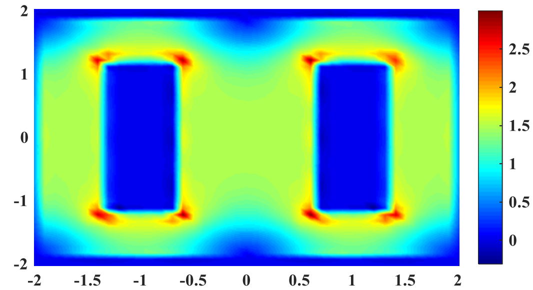

Fig. 11. Distribution of magnetic flux-density in transformer.

To investigate the effect of branch optimization, the transformer model has been divided into different mesh size. Furthermore, the magnetic field in the transformer is calculated by serial EBE-J-PCG, unoptimized parallel EBE-J-PCG and optimized parallel EBE-J-PCG respectively for comparison. The serial EBE-J-PCG program runs on CPU only, while the two parallel programs run on CUDA platform. The computation accuracy of the three methods are the same under the same mesh. Table 1 shows the calculation time of serial EBE-J-PCG program and speedups of parallel EBE-J-PCG program in different mesh size. Speedup is obtained by dividing serial time by parallel time (All the time in the table is in minutes).

Table 1: Calculation results of transformer model

Elements	Serial Time	Parallel without Optimization		Parallel with Optimization	
		Time	Speedup	Time	Speedup
8732	1.5	0.7	2.1	0.4	3.8
11443	2.6	1.2	2.2	0.6	4.3
40816	45.2	18.5	2.4	10.2	4.4
171338	1541.3	593.7	2.6	174.5	8.8

It can be seen from Table 1, compared with serial EBE-J-PCG method running on CPU only, parallel implementation on CUDA platform can improve the computation efficiency. However, thread branches in parallel computing can degrade computational efficiency, which can be seen from the similarity of speedup ratios obtained by non-optimized programs in computing different number of mesh. The proposed thread-data remapping method can solve this problem, the speedup ratios of parallel computation are improved obviously after optimization. Moreover, the larger scale computation is involved, the better acceleration can be obtained.

VI. CONCLUSION

In this paper, the EBE-J-PCG method has been implemented in parallel on CUDA platform, and thread branche in GPU kernel has been researched. The proposed thread-data remapping method can solve the problem of deterioration in parallel efficiency caused by thread branches, and this optimization method can improve the speedup ratio more obviously. Except the reduction operations, any branching parts of parallel programs based on CUDA platform can adopt the branch optimization method to improve parallel efficiency.

ACKNOWLEDGMENT

This work is supported in part by the National Natural Science Foundation under Grant 51577122 and in part by the Natural Science Foundation of Liaoning Province under Grant 20180550860.

REFERENCES

[1] D. M. Fernandez, M. M. Dehnavi, W. J. Gross, and D. Giannacopoulos, "Alternate parallel processing approach for FEM," *IEEE Trans. Magn.*, vol. 48, no. 2, pp. 399-402, Feb. 2012.

[2] E. Barragy, G. Raham, and F. Carey, "Parallel element-by-element solution scheme," *Int. J. Numer. Methods Eng.*, vol. 26, no. 11, pp. 2367-2382, 1988.

[3] X. Yan, X. Han, D. Wu, D. Xie, B. Bai, and Z. Ren, "Research on preconditioned conjugate gradient method based on EBE-FEM and the application in electromagnetic field analysis," *IEEE Trans. Magn.*, vol. 53, no. 6, pp. 1-4, June 2017.

[4] A. Capozzoli, O. Kilic, C. Curcio, and A. Liseno, "The success of GPU computing in applied electromagnetics," *Applied Comp. Electromag. Soc. Journal*, vol. 33, no. 2, pp. 148-151, Feb. 2018.

[5] J. C. K. Wake and S. Watanabe, "Scalable GPU-parallelized FDTD method for analysis of large-scale electromagnetic dosimetry problems," *Applied Comp. Electromag. Soc. Journal*, vol. 31, no. 6, pp. 661-668, June 2016.

[6] D. Wu, X. Yan, R. Tang, and D. Xie, "Parallel realization of element by element analysis of eddy current field based on graphic processing unit," *Applied Comp. Electromag. Soc. Journal*, vol. 33, no. 2, pp. 168-171, Feb. 2018.

[7] J. Nickolls, "GPU parallel computing architecture and CUDA programming model," *IEEE Hot Chips Symp., HCS*, pp. 1-12, May 2007.

[8] I. Kiss, S. Gyimothy, Z. Badics and J. Pavo, "Parallel realization of the element-by-element FEM technique by CUDA," *IEEE Trans. Magn.*, vol. 48, no. 2, pp. 507-510, Feb. 2012.

[9] S. Wang, X. Yan, Y. Zhang, and D. Wu, "Research on EBE-FEM realized by CUDA applying to electromagnetic field analysis," *IEEE Stud. Conf. Electric Mach. Syst., SCEMS*, 2018.

[10] E. Zhang, Y. Jiang, and Z. Guo, "Streamlining GPU applications on the fly: Thread branch elimination through runtime thread-data remapping," *Proc. Int. Conf. Supercomputing*, pp. 115-125, 2010.

[11] Z. Hu, *Analysis and Calculation of Motor Electromagnetic Fields*. Beijing: China Machine Press, 1989.

Yan Zhang He received his B.S. degree in Electrical Engineering and Automation from Langfang Normal University in 2017. He is currently working towards M.S degree in Shenyang University of Technology. His research interests include numerical analysis and parallel calculation of electromagnetic fields on CUDA platform.

Xiuke Yan received her B.S. degree, M.S. degree and Ph.D. degree in Electrical Engineering from Shenyang University of Technology, China, in 1996, 1999 and 2005, respectively. She is currently a Professor in Shenyang University of Technology. Her research interests include numerical analysis of coupled field and optimization design of electrical equipment, parallel algorithm research of finite element method.

High-Order Small Perturbation Method of Arbitrary Order for Conducting Rough Surface Scattering under TE Incidence

Qing Wang [1], Chen Lin [2], Zhen-Ya Lei [1], Jianq-Qiang Hou [1], and Lei Li [1]

[1] School of Electronic Engineering
Xidian University, Xi'an, Shaanxi 710071, China
wangqing@mail.xidian.edu.cn, zylei@xidian.edu.cn, jqhou@mail.xidian.edu.cn, leili@mail.xidian.edu.cn

[2] Second Research Department
Yangzhou Marine Electronic Institute, Yangzhou, Jiangsu 225001, China
xidianlc@163.com

Abstract ─ A novel closed-form high-order small perturbation method (HOSPM) for the analysis of scattering from 1-D conducting random rough surfaces under TE incidence is developed. The main theoretical contributions of the HOSPM are as follows: (1) our method yields a general high-order SPM form for scattered fields of arbitrary orders, (2) Faà di Bruno's formula is introduced into computational electromagnetics (CEM) for the first time to expand a tapered incident wave and its partial derivatives in power series form, and (3) the form is simple and easy to program and does not require any mathematical pretreatment. Comparisons are made between the method of moments (MOM) and different-order HOSPMs in terms of several aspects, including accuracy and time efficiency. The order convergence of the HOSPM is discussed, the regions of validity with regard to correlation lengths and root mean square (RMS) heights are demonstrated for the 2nd-order HOSPM, and the robustness of the 2nd-order HOSPM is proven over a broad range of frequencies.

Index Terms ─ Bistatic scattering coefficients, high-order small perturbation method, rough surface scattering, tapered wave, TE incidence.

I. INTRODUCTION

The scattering of EM waves from a random rough surface has been an important subject of research in recent decades because of its important applications in many diverse fields, including electromagnetic scattering [1-3], remote sensing [4], oceanography [5], communications [6], materials science [7-8], medical imaging [9] and applied optics [10-11]. Methods of studying rough surface scattering can be categorized into three groups: (1) approximation and analytical methods, (2) numerical methods and (3) semi-analytical methods. Approximation methods are based on physical approximations and are aimed at providing closed-form formulae for the scattered fields. The basic idea of numerical methods is to discretize the continuous variable and continuous functions, convert the differential equations into the difference equations, convert the integral equations to the form of finite sum, establish the convergent algebraic equations, and use the computer technology to solve the problem. Semi-analytical methods are a combination of numerical methods and analytical methods. The main principle of the semi-analytical methods is to reduce the dimension of multidimensional problems by using the family of low-dimensional solutions so as to simplify the calculation.

The small perturbation method (SPM) is a classic approximation method for rough surface with small-scale roughness [12-14]. The SPM produces a series expansion in the surface heights for a scattered field. There are two classic approaches to the SPM. The first one is based on the extended boundary condition (EBC) method. The surface currents on the rough surface are first calculated by applying the extinction theorem. The scattered fields can then be calculated from the diffraction integrals of the surface fields. The second approach makes use of the Rayleigh hypothesis to express the reflected and transmitted fields as upward- and downward-going waves, respectively. The field amplitudes are then determined from the boundary conditions [15]. Both perturbation methods yield the same expansion for the scattered fields.

There have been many quantitative studies aimed at analysis and applications of different-order SPMs. The first-order SPM has been used to predict scattering from multilayer stacks, especially light scattering from multilayer optical coatings [16-17]. The Born-approximation first-order SPM is frequently applied to high-frequency scattering from marine sediments [18]. In the original paper [19], scattered fields of up to second order in surface height were considered for scattering

Submitted On: December 30, 2019
Accepted On: May 4, 2020

from 2-D random rough surfaces. In [20], scattered fields were derived to third order in the surface height, and expressions for the scattered and transmitted powers were developed for deterministic and stochastic surfaces as well as periodic and nonperiodic surfaces. The fourth-order SPM was investigated with regard to scattering from two rough surfaces in a layered geometry in [21].

Most SPM studies can only supply solutions in the form of limited series. Usually, as series order increases, the integral dimensionality increases. The necessary calculations are complicated to code when they involve multiple integrals. Because high-order mathematical forms are always complex and difficult to program, there is no general form for an SPM of arbitrary orders. In order to solve these problems, this paper presents a semi-analytical version of the SPM for arbitrary orders, such that the highest order of the method can even be infinite. Therefore, the proposed method is called the high-order SPM (HOSPM). In this method, a tapered incident wave is used to avoid “edge diffraction”. Because the incident wave should also be expended in series form, another new consideration in the HOSPM is the introduction of Faà di Bruno's formula to expand a tapered incident wave and its partial derivatives in power series form. This is the first time that Faà di Bruno's formula has been used in CEM.

There are several differences between the classic SPM and our method. (1) The classic SPM makes use of the Rayleigh hypothesis. Our method is based on the Ewald-Oseen extinction theorem [22]. (2) Although both methods use Taylor series to expand the scattered and incident fields, the spectral amplitude inside the Fourier transform is expanded in series form in the classic SPM, whereas the total field is expanded into a Taylor series in our method. (3) In the classic SPM, the scattered fields are classified as either coherent or incoherent waves. In our method, this classification is not needed, and the scattered fields are calculated from the diffraction integrals of the total surface fields. (4) In the classic SPM, the Fourier coefficients are determined via multi-integrals, and the integral dimensionality increases as the order of the terms increases. Our method involves only 1-D integrals regardless of the order and thus is simpler to express in mathematical form and much easier to code. (5) Edge diffraction is not considered in the classic SPM, whereas our method considers tapered waves to eliminate edge diffraction.

The HOSPM is based on the assumption that the boundary conditions are perturbed around those of a smooth surface. To verify the validity of the HOSPM, its solution should be compared with a solution obtained without imposing any restriction on the rough-surface properties. Numerical methods are most suitable for this purpose. One of the most widely used numerical methods is the method of moments (MOM). Therefore, the MOM is chosen as the comparison method in this study to enable a more conclusive analysis. Simulations performed on 1-D one-layer conducting random rough surfaces with a Gaussian height distribution are reported. Such surfaces are the simplest to describe statistically and can be fully characterized by the surface correlation function. The Thorsos tapered wave [23] is chosen here for its accuracy and broad applications in the truncation of rough surfaces.

The paper is organized as follows. Section II gives the preliminaries. Section III presents all functions involved in the derivation of the HOSPM. In Section IV, many aspects of the HOSPM are analyzed, including accuracy, convergence, time efficiency, memory consumption, the influences of different correlation lengths and root mean square (RMS) heights, and frequency robustness. The conclusion is presented in Section V.

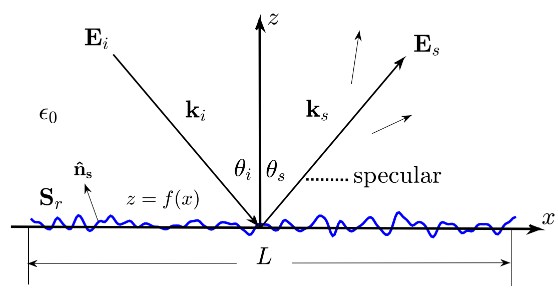

Fig. 1. Geometry for wave scattering by a conducting random rough surface.

II. PRELIMINARIES

The model under investigation is the 1-D conducting random rough surface shown in Fig. 1, and a two-dimensional scattering problem is considered. The analysis is conducted in the frequency domain, with the time-dependence factor $e^{-i\omega t}$ omitted throughout. The case of interest is the TE case, so the electric field has the form:

$$\mathbf{E} = \mathbf{y}\psi, \tag{1}$$

where ψ is the quantity of the electric field. Throughout the remainder of the paper, the scalar wave equation ψ is studied instead of $\mathbf{E}$ for simplicity.

Because the wave equation ψ is scalar, the scalar Green's Theorem is used, which has the form:

$$\begin{aligned}&\iint_V dv[\psi(\mathbf{r})\nabla^2 g(\mathbf{r},\mathbf{r}') - g(\mathbf{r},\mathbf{r}')\nabla^2\psi(\mathbf{r})]\\ &= \oint_S d\mathbf{S}\cdot[\psi(\mathbf{r})\nabla g(\mathbf{r},\mathbf{r}') - g(\mathbf{r},\mathbf{r}')\nabla\psi(\mathbf{r})],\end{aligned} \tag{2}$$

where $g(\mathbf{r},\mathbf{r}')$ is the Green's function; $\mathbf{S}$ is the closed surface composed of the rough surface $\mathbf{S}_r$ (shown in Fig. 1) and the half-circle $\mathbf{S}_i$, with a radius extending to infinity; $\mathbf{r}'$ is above the surface $\mathbf{S}_r$; and $\mathbf{r}$ is on the surface $\mathbf{S}_r$.

Upon the application of the extinction theorem [24], supposing that the surface is perfectly conducting and employing the Dirichlet boundary condition $\psi(\mathbf{r})=0$ for $\mathbf{r}$ on $\mathbf{S}_r$, the expression for the scattered field should be:

$$\begin{aligned}\psi_s(\mathbf{r}') &= \int_{S_r} ds\mathbf{n}_s\cdot[-g(\mathbf{r},\mathbf{r}')]\nabla\psi(\mathbf{r})\\ &= -\int_{S_r} dsg(\mathbf{r},\mathbf{r}')[\mathbf{n}_s\cdot\nabla\psi(\mathbf{r})]\\ &= -\int_{-L/2}^{L/2} dxg(\mathbf{r},\mathbf{r}')\sqrt{1+\left(\frac{df}{dx}\right)^2}\frac{\partial\psi(\mathbf{r})}{\partial n_s},\end{aligned}\tag{3}$$

where $\mathbf{r}'$ is located in the upper space; $z=f(x)$ is the surface height profile of the rough surface, with the spectral density function $W(k)$; and $\mathbf{n}_s$ is the unit normal vector of the rough surface pointing toward the upper space.

To prevent current discontinuity at the end points [24], we can use either a tapered incident wave or periodic boundary conditions [25-27]. Because the rough interface modeled in the simulation is of finite size, a tapered incident wave is used. The Thorsos tapered wave has been extensively applied for this purpose because of its low computational expense. The form of the tapered incident wave is as follows:

$$\psi_i(\mathbf{r}) = e^{ik(x\sin\theta_i - z\cos\theta_i)[1+w(\mathbf{r})]-\frac{(x+z\tan\theta_i)^2}{g^2}},\tag{4}$$

with

$$w(\mathbf{r}) = \frac{2(x+z\tan\theta_i)^2/g^2-1}{(kg\cos\theta_i)^2},\tag{5}$$

where k is the wave number of free space, θ_i is the incidence angle, and g is the tapering parameter.

III. FORMULATION

A. Solutions for the total and scattered fields

Because its variable has the form $\mathbf{r}=x\mathbf{x}+f(x)\hat{\mathbf{z}}$, the field $\psi(\mathbf{r})$ on the random rough surface is related to the profile of the scattering surface $f(x)$. In the case of a slightly rough surface, the RMS height h of the surface is far smaller than both the incident wavelength λ and the absolute value of $f(x)$. According to the power series expansion theory, which is valid when the variable (in our case, the absolute value of the height profile, $|f(x)|$) is small, the field on the rough surface can be expanded as a Taylor series about the field on the mean surface ($z=f(x)=0$):

$$\begin{aligned}\psi(\mathbf{r}) &= \sum_{m=0}^{n}\frac{f^m}{m!}\frac{\partial^m\psi}{\partial z^m}\bigg|_{z=0}\\ &= \psi|_{z=0} + f\frac{\partial\psi}{\partial z}\bigg|_{z=0} + \frac{f^2}{2!}\frac{\partial^2\psi}{\partial z^2}\bigg|_{z=0} + \frac{f^3}{3!}\frac{\partial^3\psi}{\partial z^3}\bigg|_{z=0}\\ &+ \frac{f^n}{n!}\frac{\partial^n\psi}{\partial z^n}\bigg|_{z=0},\end{aligned}\tag{6}$$

where ψ and f on the right are used in place of $\psi(\mathbf{r})$ and $f(x)$ for brevity. In this equation, n can theoretically approach infinity. $\psi(\mathbf{r})$ is composed of an incident field and a scattered field. The certain part of $\psi(\mathbf{r})$ is the incident field, and the uncertain part is determined by the scattered field. The scattered field on the rough space as well as the total field can be expressed as the sum of the zeroth-order field component, the first-order field component, and all other components up through the nth-order field component, as follows:

$$\psi_s(\mathbf{r}) = \sum_{m=0}^{n}\psi_m^s(\mathbf{r}).\tag{7}$$

Based on equations (6) and (7), the different-order series expressions for the total field on the surface should be as follows:

$$\psi_0(\mathbf{r}) = \psi_i|_{z=0} + \psi_0^s|_{z=0},\tag{8.0}$$

$$\begin{aligned}&\psi_1(\mathbf{r})\\ &= \psi_i|_{z=0} + \psi_0^s|_{z=0} + \psi_1^s|_{z=0} + f\frac{\partial}{\partial z}(\psi_i+\psi_0^s)\bigg|_{z=0},\end{aligned}\tag{8.1}$$

$$\begin{aligned}\psi_2(\mathbf{r}) &= \psi_i|_{z=0} + \psi_0^s|_{z=0} + \psi_1^s|_{z=0} + \psi_2^s|_{z=0}\\ &+ f\frac{\partial}{\partial z}(\psi_i+\psi_0^s+\psi_1^s)\bigg|_{z=0} + \frac{f^2}{2}\frac{\partial^2}{\partial z^2}(\psi_i+\psi_0^s)\bigg|_{z=0},\end{aligned}\tag{8.2}$$

$$\vdots$$

$$\psi_n(\mathbf{r}) = \sum_{m=0}^{n}\frac{f^m}{m!}\cdot\frac{\partial^m}{\partial z^m}\left(\psi_i + \sum_{l=0}^{n-m}\psi_l^s\right)\bigg|_{z=0},\tag{8.n}$$

where ψ_i, ψ_0^s, ψ_1^s, ... and ψ_n^s are used as abbreviations for $\psi_i(\mathbf{r})$, $\psi_0^s(\mathbf{r})$, $\psi_1^s(\mathbf{r})$, ... and $\psi_n^s(\mathbf{r})$, respectively. Based on equation (8.n), the partial derivatives of $\psi_n(\mathbf{r})$ with respect to x and z should be:

$$\frac{\partial\psi_n(\mathbf{r})}{\partial x} = \sum_{m=1}^{n+1}\frac{f^{m-1}}{(m-1)!}\cdot\frac{\partial^{m-1}}{\partial z^{m-1}}\left(\frac{\partial\psi_i}{\partial x} + \sum_{l=0}^{n-m+1}\frac{\partial\psi_l^s}{\partial x}\right)\bigg|_{z=0},\tag{9}$$

$$\frac{\partial\psi_n(\mathbf{r})}{\partial z} = \sum_{m=1}^{n}\frac{f^{m-1}}{(m-1)!}\cdot\frac{\partial^m}{\partial z^m}\left(\psi_i + \sum_{l=0}^{n-m}\psi_l^s\right)\bigg|_{z=0}.\tag{10}$$

Because equations (8.0) to (8.n) represent total field expressions of different orders, each of them should obey the same boundary condition at the interface. By simultaneously applying the Dirichlet boundary condition to equations (8.0) ~ (8.*n*), the 0th-order through *n*th-order expressions for the scattered field on the mean surface *z*=0 can be obtained as follows:

$$\psi_0^s(\mathbf{r})\Big|_{z=0} = -\psi_i\big|_{z=0}, \tag{11.0}$$

$$\psi_1^s(\mathbf{r})\Big|_{z=0} = -f\left.\frac{\partial\left(\psi_i+\psi_0^s\right)}{\partial z}\right|_{z=0}, \tag{11.1}$$

$$\psi_2^s(\mathbf{r})\Big|_{z=0} = -f\left.\frac{\partial \psi_1^s}{\partial z}\right|_{z=0} - \frac{f^2}{2!}\left.\frac{\partial^2\left(\psi_0^s+\psi_i\right)}{\partial z^2}\right|_{z=0}, \tag{11.2}$$

$$\vdots$$

$$\psi_n^s(\mathbf{r})\Big|_{z=0} = -\frac{f^n}{n!}\left.\frac{\partial^n \psi_i}{\partial z^n}\right|_{z=0} - \sum_{m=1}^{n}\frac{f^m}{m!}\left.\frac{\partial^m \psi_{n-m}^s}{\partial z^m}\right|_{z=0}. \tag{11.n}$$

To obtain the *n*th-order partial derivatives of the scattered field on the rough surface $\psi_n^s(\mathbf{r})$, the spectral domain integral is used as follows:

$$\psi_n^s(\mathbf{r}) = \int_{-\infty}^{\infty} dk_x A_n(k_x) e^{i[k_x x + k_z f(x)]}, \tag{12}$$

where $k_z = \sqrt{k^2 - k_x^2}$. In this way, the scattered field is expressed in the space domain as an accumulated spectrum of waves with different propagation directions and different amplitudes. $A_n(k_x)$ is the amplitude of each wave in the spectrum. The following relationships are obtained on the mean surface:

$$\psi_n^s(\mathbf{r})\Big|_{z=0} = \int_{-\infty}^{\infty} dk_x A_n(k_x) e^{ik_x x}, \tag{13}$$

$$A_n(k_x) = \frac{1}{2\pi}\int_{-\infty}^{\infty} dx\left[\psi_n^s(\mathbf{r})\Big|_{z=0}\right] e^{-ik_x x}, \tag{14}$$

$$\left.\frac{\partial^m \psi_n^s(\mathbf{r})}{\partial z^m}\right|_{z=0} = i^m \int_{-\infty}^{\infty} dk_x k_z^m A_n(k_x) e^{ik_x x}, \tag{15}$$

$$\left.\frac{\partial \psi_n^s(\mathbf{r})}{\partial x}\right|_{z=0} = i\int_{-\infty}^{\infty} dk_x k_x A_n(k_x) e^{ik_x x}, \tag{16}$$

$$\left.\frac{\partial^m}{\partial z^m}\left(\frac{\partial \psi_n^s(\mathbf{r})}{\partial x}\right)\right|_{z=0} = i^{m+1}\int_{-\infty}^{\infty} dk_x k_x k_z^m A_n(k_x) e^{ik_x x}. \tag{17}$$

By calculating the Fourier transform of equation (14), $A_n(k_x)$ is determined. The amplitude is substituted into equations (15), (16) and (17), and the inverse Fourier transforms are applied subsequently. Accordingly, the partial derivative terms $\left[\partial^m \psi_n^s(\mathbf{r})/\partial z^m\right]\Big|_{z=0}$, $\left[\partial \psi_n^s(\mathbf{r})/\partial x\right]\Big|_{z=0}$ and $\{\partial^m/\partial z^m\left[\partial \psi_n^s(\mathbf{r})/\partial x\right]\}\Big|_{z=0}$ can be determined. These partial derivative terms are needed in the calculation of equations (8.0) ~ (8.*n*), (9) and (10). The partial derivatives of the tapered incident field are derived in Appendix.

B. Bistatic scattering coefficients

As expressed in equation (3), the scattered field in the upper space can be obtained by integrating the Green's function with the directional derivative of the total field at the interface $\mathbf{S}_r$. The two-dimensional Green's function in equation (3) is:

$$g(\mathbf{r},\mathbf{r}') = \frac{i}{4}H_0^{(1)}\left(k\,|\,\mathbf{r}-\mathbf{r}'\,|\right). \tag{18}$$

When this Green's function is expanded at infinity, the Hankel function $H_0^{(1)}\left(k|\mathbf{r}-\mathbf{r}'|\right)$ can be approximated as follows when $\mathbf{r}'$ is located at an infinitely far distance and the observation is in the direction of $\mathbf{k}_s = \sin\theta_s\mathbf{x} + \cos\theta_s\mathbf{z}$:

$$H_0^{(1)}\left(k|\mathbf{r}-\mathbf{r}'|\right) \approx \sqrt{\frac{2}{\pi k|\mathbf{r}-\mathbf{r}'|}}e^{i\left(k|\mathbf{r}-\mathbf{r}'|-\frac{\pi}{4}\right)} \approx \sqrt{\frac{2}{\pi k r'}}e^{ikr'}e^{-i\frac{\pi}{4}}e^{-ik\left[x\sin\theta_s + f(x)\cos\theta_s\right]}. \tag{19}$$

Upon substituting equations (18) and (19) into equation (3) and setting the total field to be of *n*th-order, the scattered fields can be written as:

$$\psi_s(\mathbf{r}') = -\frac{i}{4}\sqrt{\frac{2}{\pi k r'}}e^{-i\frac{\pi}{4}}e^{ikr'}\psi_n^{N_s}(\theta_s), \tag{20}$$

with

$$\psi_n^{N_s}(\theta_s) = \int_{-L/2}^{L/2} dx e^{-ik\left[x\sin\theta_s + f(x)\cos\theta_s\right]}\sqrt{1+\left(\frac{df}{dx}\right)^2}\frac{\partial \psi_n(\mathbf{r})}{\partial n_s}, \tag{21}$$

where

$$\frac{\partial \psi_n(\mathbf{r})}{\partial n_s} = \nabla\psi_n(\mathbf{r})\cdot\mathbf{n_s}, \tag{22}$$

and

$$\mathbf{n_s} = \frac{-\frac{df}{dx}\hat{x}+\hat{z}}{\sqrt{1+\left(\frac{df}{dx}\right)^2}}. \tag{23}$$

Consequently,

$$\psi_n^{N_s}(\theta_s) = \int_{-L/2}^{L/2} dx e^{-ik\left[x\sin\theta_s + f(x)\cos\theta_s\right]}\left[-\frac{df}{dx}\frac{\partial \psi_n(\mathbf{r})}{\partial x} + \frac{\partial \psi_n(\mathbf{r})}{\partial z}\right], \tag{24}$$

where $\partial\psi_n(\mathbf{r})/\partial x$ and $\partial\psi_n(\mathbf{r})/\partial z$ can be obtained from equations (9) and (10).

The expression for the normalized far-field bistatic scattering coefficients (BSCs) is [24]:

$$\sigma_n(\theta_i,\theta_s) = \frac{r' S_s(\mathbf{r}')}{-\int_{-\infty}^{\infty} dx \left(S_{inc}\cdot\hat{\mathbf{z}}\right)_{z=0}} = \frac{-\frac{1}{2\eta k}\operatorname{Im}\left[\psi_n^s(\mathbf{r}')\nabla\psi_n^s{}^*(\mathbf{r}')\right]}{P_{inc}}. \quad (25)$$

For a plane wave, $\mathbf{S}_{inc}\cdot\hat{\mathbf{z}} = -\cos\theta_i/(2\eta)$, and η is the intrinsic impedance of free space. Accordingly, the power P_{inc} received by the rough surface should be:

$$P_{inc} = -\int_{-\infty}^{\infty} dx \left(\mathbf{S}_{incp}\cdot\hat{\mathbf{z}}\right)\Big|_{z=0} = -\int_{-\infty}^{\infty} dx \frac{1}{2\eta}\cos\theta_i. \quad (26)$$

The value of the quantity expressed in equation (26) approaches infinity. This makes the calculation of $\sigma_n(\theta_i,\theta_s)$ impossible. However, this dilemma can be resolved by using the Thorsos tapered wave as the incident wave[23]. In this case,

$$\sigma_{n(\text{tapered wave})}(\theta_i,\theta_s) = \frac{\frac{1}{2\eta}\frac{1}{8\pi k}\left|\psi_n^{N_s}(\theta_s)\right|^2}{P_{inc(\text{tapered wave})}} = \frac{\left|\psi_n^{N_s}(\theta_s)\right|^2}{8\pi k g\sqrt{\frac{\pi}{2}}\cos\theta_i\left[1-\frac{1+2\tan^2\theta_i}{2k^2g^2\cos^2\theta_i}\right]}, \quad (27)$$

where

$$P_{\text{inc(tapered wave)}} = \frac{\cos\theta_i}{2\eta} g\sqrt{\frac{\pi}{2}}\left(1-\frac{1+2\tan^2\theta_i}{2k^2g^2\cos\theta_i}\right). \quad (28)$$

The BSCs can then be determined using equation (27) and the related equations above.

C. Monte Carlo simulation

To obtain the statistical averages of the BSCs for random rough surfaces, Monte Carlo simulations are used. In the simulation process, independent samples of rough surfaces are first generated, and the BSCs for each sample are individually computed. Then, the statistical averages of the BSCs for m independent computations are determined as follows:

$$\bar{\sigma}^m = \left[\sigma^m + \bar{\sigma}^{m-1}\cdot(m-1)\right]/m, \quad (29)$$

where m $(1 \le m \le M)$ is the index representing the number of computations, M is the total number of surface realizations, $\bar{\sigma}^m$ is the statistical average, and σ^m is the value from the mth simulation.

IV. VALIDATION

In this section, several numerical examples are presented to evaluate the HOSPM in terms of many aspects, including accuracy, convergency, time efficiency, the influences of correlation lengths and RMS heights, and frequency robustness. Because of its wide range of accuracy [28], the MOM is employed as the method for comparison. The general formulation of the MOM is described in [24], and all code for implementing the MOM is based on Dr. Tsang Leung's Electromagnetic Wave MATLAB Library. Because this paper considers a 1-D problem under TE incidence, all simulations default to HH polarization. To fully exploit the computational efficiency of FFT operations, the number of points on the rough surface is set to be a power of two.

A. Accuracy and convergency

A table and a figure are presented in this subsection. Because subsection D addresses the influences of frequency, a fixed wavelength of $\lambda = 1\text{m}$ is considered in subsection A, B and C. All of the parameters used to generated the results shown in Fig. 2 are listed in the figure, including the rough surface length L, the RMS height h, the correlation length l, the tapering parameter g, the incidence angle θ_i, the number of points N on the surface and the number of iterations (samples) M; these are also the parameters used for the simulations reported in Table 1.

Table 1: The accuracy of HOSPM on backscattering and forward scattering direction and relative errors between different orders

n	**Δ_b(dB)**	**Δ_s(dB)**	**Σ_n**
1	0.59	0.40	/
2	0.23	0.41	0.027
3	0.24	0.39	0.049
4	0.24	0.39	1.90×10^{-7}
5	0.24	0.39	1.28×10^{-5}
6	0.24	0.39	1.13×10^{-7}
7	0.24	0.39	1.15×10^{-8}
8	0.24	0.39	1.75×10^{-11}

n: order of HOSPM.
Δ_b: $|\sigma_{n(\text{MOM})}-\sigma_{n(\text{HOSPM})}|$ in the backscattering angle.
Δ_s: $|\sigma_{n(\text{MOM})}-\sigma_{n(\text{HOSPM})}|$ in the forward scattering angle.
Σ_n: relative error for the nth-order HOSPM.

Figure 2 shows the BSCs for 1-D perfectly electrically conducting (PEC) Gaussian random rough surfaces obtained using different-order HOSPMs and the MOM. In the figure, the curves obtained using the 1st-, 2nd-, 4th- and 8th-order HOSPMs do not show significant differences. The curve of MOM and the curves from HOSPMs match well to the left of the specular scattering point. The value of BSCs generally coincide between the HOSPMs and the MOM over a wide range of scattering angles from precisely -89˚to 41˚. As can be seen from Fig. 2 in the manuscript, the BSCs generally coincide between the HOSPMs and the MOM over a wide range of scattering angles from approximately -89˚ to 41˚, with good matching for many angles.

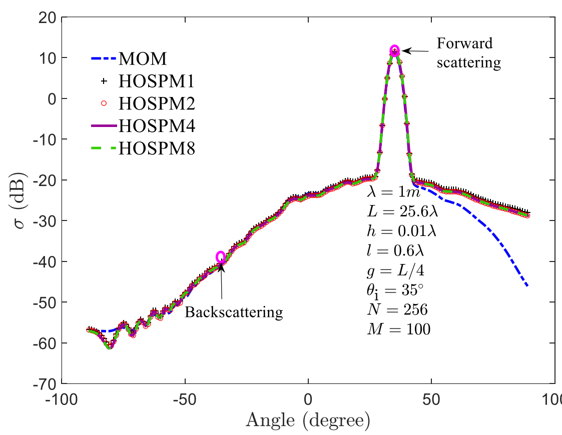

Fig. 2. Comparisons of the BSCs by 1st-order, 2nd-order, 4th-order and 8th-order HOSPM and MOM.

The biggest difference between the two methods lies in how to get the value of the term $\left[-\frac{df}{dx}\frac{\partial\psi_n(\mathbf{r})}{\partial x}+\frac{\partial\psi_n(\mathbf{r})}{\partial z}\right]$ in the integrand in Eq. (21). MOM uses a numerical method which is solving the matrix, and HOSPM uses the method which is a series of formulas related to the series expansion. Therefore, the final values obtained by the two methods are difficult to be exactly the same, which is the main reason why the matching between HOSPM and MOM is not good for angle larger than 41˚.

For more specific investigations, two representative angles, the backscattering angle and the forward scattering angle, are selected as objects of study. These two angles are also of the greatest interest compared with other angles.

Table 1 presents the results for the precision of the different-order HOSPMs in the backscattering and forward scattering directions and the convergence among the different-order HOSPMs. Comparisons of precision between *n*th-order HOSPMs and the MOM in the backscattering and forward scattering directions are given in the second and third rows of Table 1. At 1st order and above, the HOSPM shows high precision, with differences of less than 0.6 dB between the two methods.

Since HOSPM are expressed in the form of series of arbitrary orders, the order convergence should be discussed. The fourth row in Table 1 shows the iteration errors from the 2nd-order to the 8th-order HOSPM.

The relative errors for BSCs of different orders that are reported in the fourth row of Table 1 are denoted by Σ_n and are defined as:

$$\Sigma_n = \max\left|\frac{\sigma_n(\theta_i)-\sigma_{n-1}(\theta_i)}{\sigma_{n-1}(\theta_i)}\right|, (n \gg 2). \tag{30}$$

As seen from Table 1, the relative error Σ_n decreases as the order n increases. If we set 5% as the threshold for convergence, the values obtained for the 1st-order HOSPM and above are acceptable. Because the relative errors of the 2rd-order HOSPM and above are negligible, the terms of 2rd-order and above in the series can be ignored, consistent with the error property of power series.

These findings prove that our method is accurate and stable. Considering both the accuracy and convergence results, the BSCs obtained using the 1st-order HOSPM and above can be considered acceptable.

B. Time and memory consumption

Without the application of any acceleration algorithms, the MOM has a memory requirement of $O(N^2)$ and a computational complexity of $O(N^3)$, where N is the total number of sample points per interface. A precise analysis reveals that, the HOSPM requires $O[(n+1)N]$ memory and $O[(n+1)!n^3N]$ operations. Therefore, the HOSPM is theoretically superior to the MOM in both memory and complexity because of $n \ll N$. The HOSPM also exhibits computational advantages in practice, as shown in Table 2 and Fig. 3. Table 2 presents the time consumption data for the MOM and for the 2nd-, 3rd- and 4th-order HOSPMs, which vary with the number of points on the surface.

Table 2: The time cost by MOM and HOSPM of different orders (s)

N	2^8	2^9	2^{10}	2^{11}	2^{12}	2^{13}
t	2.13	6.51	25.13	103.70	491.51	2532.0
t_1	1.69	2.97	5.75	11.50	27.57	74.48
t_2	4.61	8.44	16.61	35.83	87.56	238.2
t_3	10.56	19.55	39.10	85.33	208.91	579.47
t_4	22.68	41.81	85.62	186.47	458.19	1239.8

t: the time cost by MOM.
t_1: the time cost by HOSPM1.
t_2: the time cost by HOSPM2.
t_3: the time cost by HOSPM3.
t_4: the time cost by HOSPM4.

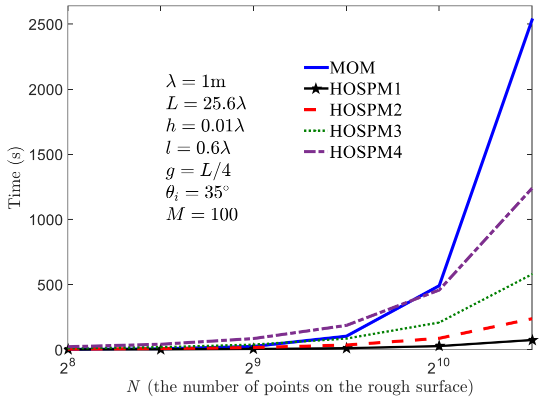

Fig. 3. Time cost by MOM and HOSPMs with 1st-, 2nd-, 3rd- and 4th-order (in the unit of second).

Figure 3 illustrates the data summarized in Table 2. The parameters used to generate the results presented in Fig. 3 and Table 2 are listed in the figure. Among the different-order HOSPMs, the 1st-order method exhibits the best time performance. Its time curve is nearly linear, whereas the MOM has a quadratic cubic time curve. As the order of the HOSPM increases, the curve becomes steeper, indicating worse efficiency. However, even the 4th-order HOSPM still shows better efficiency compared with the MOM when the number of points is greater than 2^{12}. Because of the use of FFT operations, the value of N must have the form 2^{N_1}, where N_1 is an integer. When N_1=10, the 1st- and 2nd-order HOSPM shows better time performance than the MOM; when N_1=11, the 1st-, 2nd- and 3rd-order HOSPMs perform better; and when N_1=13, the HOSPMs all perform better. Thus, we can conclude that our method shows good potential in terms of time efficiency for electrically large surfaces.

Considering the time efficiency, the 1st-order HOSPM is the best choice. Considering all the factor discussed above (the time efficiency, accuracy and convergency), the 2nd-order HOSPM is a better choice. Therefore, the following analysis will focus on the 2nd-order HOSPM.

C. Correlation length and RMS height

The correlation length is a fundamental quantity that describes a random rough surface. It provides a benchmark for estimating the level of independence between any two points on a random rough surface. If the distance between two points is larger than the correlation length l, the heights of these two points can be approximately regarded as independent. The RMS height h is a fundamental quantity that describes the roughness of a rough surface. The larger the RMS height is, the rougher the surface is. Therefore, the appropriate ranges of RMS heights and correlation lengths in which our method is applicable should be discussed.

Considering the analysis presented in subsection A, the HOSPM will be studied only at 2nd-order in this subsection and next for brevity. The regions of validity with regard to the backscattering and forward scattering angles for the 2nd-order HOSPM are examined based on two sets of simulations, as shown in Fig. 4. Each set consists of 325 different combinations of values of the varies from 0.1 to 2.5 in increments of 0.1 correlation lengths and RMS heights. The value of kl (0.16m≤l≤0.40m), whereas kh varies from 0.05 to 0.65 in increments of 0.05 (0.008m≤h≤0.104m).

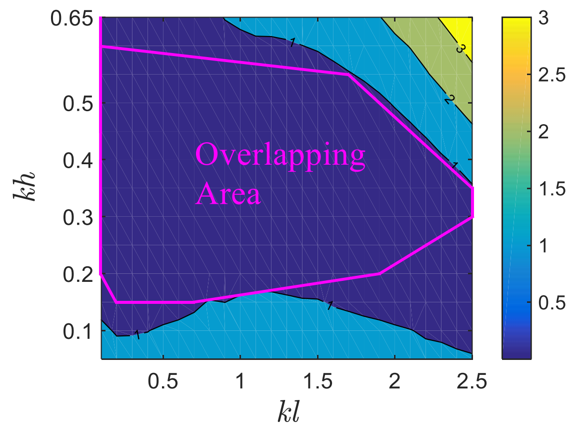

(a) Backscattering

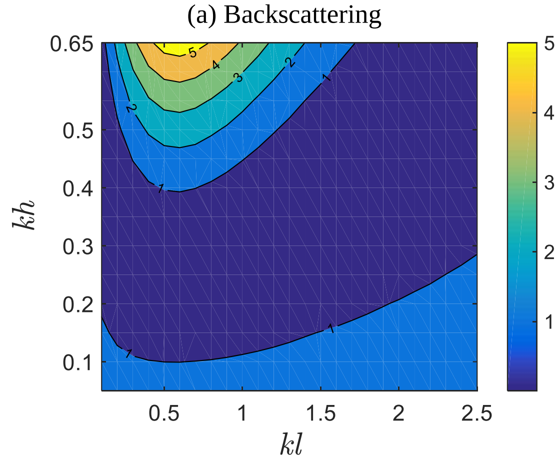

(b) Forward scattering

Fig. 4. Contour plot of $|\sigma_{MOM}-\sigma_{HOSPM2}|$ for backscattering and forward scattering direction when λ=1m, θ_i=45°, L=25.6λ, g=λ/4, N=256. Both σ_{MOM} and σ_{HOSPM2} are in decibels. The area enclosed by pink lines in (a) is the overlapping area for (a) and (b) under the condition $|\sigma_{MOM}-\sigma_{HOSPM2}|$≤1dB.

For the backscattering case, as illustrated in Fig. 4 (a), the 2nd-order HOSPM and the MOM show very good agreement in a broad region where kl spans the domain of the horizontal axis, and kh covers most the area of the figure, leaving only a little space in the upper right corner, where both kl and kh approach maximums.

In the small region near *kl*=2.5 and *kh*=0.65 (*l*=0.40m and *h*=0.104m), the difference between the two methods eventually grows to 3dB, indicating that the 2nd-order HOSPM is not suitable for the backscattering case when the RMS height and correlation length are both large.

For the forward scattering case, as illustrated in Fig. 4 (b), there is a large region in which the difference between the two methods is below 1dB. In this region, the value of *kl* ranges from 0 to 2.5 ($0\leq l\leq 0.40$m), and *kh* ranges from 0 to 0.65 ($0\leq l\leq 0.103$m). The error is approximately 5dB in a small region near *kl*=0.6 and *kh*=0.65 (*l*=0.10m and *h*=0.103m). This small region should be avoided when the HOSPM is used to estimate forward scattering.

The region enclosed by pink lines in Fig. 4 (a) represents the overlapping region for backscattering and forward scattering, where the condition $|\sigma_{MOM}-\sigma_{HOSPM2}|\leq 1$dB is satisfied for both cases. In this region, *kl* ranges from 0 to 2.5 ($0\leq l\leq 0.40$m), and *kh* ranges from 0.15 to 0.5 ($0.024\text{m}\leq l\leq 0.80$m). The overlapping area takes up most of the area under discussion. This provides a broad choice of suitable values when scattering data from both the backscattering and forward scattering directions are needed.

Table 3: The backscattering coefficients and forward scattering coefficients of different frequencies

f(Hz)	BC(dB)	FC(dB)	*f(Hz)*	BC(dB)	FC(dB)	*f(Hz)*	BC(dB)	FC(dB)
1.0G	–20.27	11.08	**15.0G**	-19.78	11.08	**300G**	-20.06	11.1
1.5G	–21.14	11.07	**30.0G**	-19.89	11.08	**333G**	-20.37	11.08
3.0G	–20.35	11.06	**33.3G**	-19.37	11.06	**375G**	-20.20	11.09
3.3G	–19.95	11.04	**37.5G**	-19.35	11.12	**429G**	-19.61	11.10
3.7G	–20.20	11.13	**42.9G**	-20.37	11.09	**500G**	-19.83	11.07
4.3G	–20.82	11.13	**50.0G**	-19.81	11.10	**600G**	-19.90	11.08
5.0G	–21.32	11.08	**60.0G**	-20.12	11.09	**750G**	-20.83	11.11
6.0G	–19.68	11.12	**75.0G**	-20.13	11.08	**1.0T**	-19.73	11.04
7.5G	–20.21	11.09	**100.0G**	-19.51	11.05	**1.5T**	-19.62	11.09
10.0G	–20.04	11.07	**150.0G**	-19.71	11.12	**3.0T**	-19.86	11.07

BC: the abbreviation of backscattering coefficient.
FC: the abbreviation of forward scattering coefficient.

D. Frequency robustness

As discussed above, the 2nd-order HOSPM has been proven to be good for both the backscattering and forward scattering angles. This section will focus on the frequency stability of the BSCs for these two angles. The analysis considers a range of frequencies from 1.0GHz to 3.0THz. A table and a figure are presented to illustrate the analysis. The univariate boxplot introduced by [29] is used to analyze the frequency robustness of the HOSPM, as shown in Fig. 5.

- Table of backscattering and forward scattering coefficients (Table 3). Both the backscattering and forward scattering coefficients are stable for frequencies from 1.0GHz to 3THz. The values of the backscattering coefficients vary only slightly. The difference between the largest and smallest values is less than 2dB. The values vary even less for the forward scattering coefficients, with a difference between the largest and smallest values of no more than 0.1dB.
- Box plot (Fig. 5). This plot visualizes the backscattering and forward scattering coefficients shown in Table 3 for different frequencies. The box plot displays the distributions of the sorted backscattering and forward scattering coefficients, where the observations along the x axis represent the different observation sets and the observations on the y axis represent the values obtained. For both sets, most values are very closely clustered, with no outliers. This plot also yields various statistical summary measures for the data in our sets. For the backscattering coefficients, the: minimum value is -21.14dB, the median is -20.26dB, and the maximum value is -19.65dB. For the forward scattering coefficients, the: minimum value is 11.03dB, the median is 11.09dB, and the maximum value is 11.16dB.

In brief, our method can be applied over a wide range of frequencies with high numerical stability.

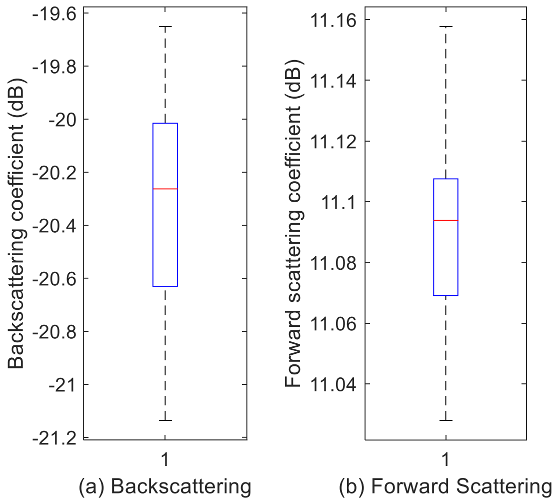

Fig. 5. Boxplot: backscattering and forward scattering coefficients by 2nd-order HOSPM among different frequencies.

V. DISCUSSION

The proposed method provides general explicit closed-form HOSPM expressions of arbitrary orders for solving the problem of the EM fields scattered from 1-D conducting random rough surfaces under TE incidence. The main contributions of this new method are four-fold: first, the surface field is treated as a function of the surface profile, allowing the total field to be expanded in power series form; second, the classic SPM is restricted to series of order two, whereas the applicability of our method extends to arbitrary orders; third, Faà di Bruno's formula is introduced into CEM for the first time to expand a tapered incident wave and its partial derivatives in power series form; and fourth, the obtained mathematical form is simple and easy to program and does not require any mathematical pretreatment.

In the context considered here, our method has been validated from many perspectives.

- In simulation A, the 1st-, 2nd-, 4th- and 8th-order HOSPMs were compared with the numerically exact MOM. The accuracy of the HOSPM at 1st-order and above was verified to be high. The convergency of the HOSPM was discussed with regard to the backscattering and forward scattering angles. The 1st-order form and above are considered to be satisfactory.
- In simulation B, the computational complexities of the 1st-, 2nd-, 3rd-, and 4th-order HOSPMs and the MOM were compared to investigate the efficiency of the proposed method. The results show that the larger the scale of the problem is, the better the HOSPM performs. Considering all factors mentioned above (accuracy, convergence, and time efficiency), the 2nd-order HOSPM applied to the backscattering and forward scattering angles was selected as a representative pair of cases for further study.
- In simulation C, the regions of validity of the 2nd-order HOSPM with respect to correlation lengths and RMS heights were investigated. It was shown that the HOSPM exhibits high precision and stability over a broad range of correlation lengths and RMS heights.
- In simulation D, the values of the backscattering and forward scattering coefficients were determined for 30 different frequencies. The method was confirmed to be stable over a broad frequency spectrum ranging from 1.0 GHz to 3.0 THz.

VI. CONCLUSION

We can conclude that HOSPM is a method with a rigorous mathematical form, high accuracy, high efficiency and greater suitability for application to a wide variety of different rough surfaces and different frequencies. Moreover, this model can further be used to study radar echoes from dynamic ocean surfaces and various inclusions in studies of composite EM scattering from targets and sea backgrounds. A fast and accurate forward model is necessary to ensure a successful inversion process. Therefore, our method is necessary and important for many inversion scenarios. It can be used in the retrievals of subsurface soil moisture measurements, in planetary exploration, and in the analysis of other natural scenes and can also serve as an important tool for radar system design. Hence, our future work will focus on higher-order solutions for dielectric or multilayer rough surfaces with an arbitrary number of rough interfaces under both TE and TM incidence.

ACKNOWLEDGMENT

This work is partly supported by National Nature Science Foundation of China [grant number 61601356], Shaanxi National Science Foundation [grant number 2016JQ6079] and Basic Scientific Research Foundation of Xidian University [JB180220/20101185311]. The authors would like to thank the reviewers for their valuable comments and constructive suggestions.

APPENDIX: EXPRESSIONS FOR THE PARTIAL DERIVATIVES OF A TAPERED INCIDENT WAVE

The computation of the derivatives of $e^{f(x)}$ is both useful and ubiquitous in analysis. Fà{a} di Bruno's formula, named after Francesco Faà di Bruno, is a mathematical identity for generalizing this problem.

Because a Thorsos tapered incident wave can be expressed as,

$$\psi_i(\mathbf{r}) = e^{\chi(\mathbf{r})}, \tag{31}$$

where

$$\chi(\mathbf{r}) = ik\left(x\sin\theta_i - z\cos\theta_i\right)\left(1+w(\mathbf{r})\right) - \frac{\left(x+z\tan\theta_i\right)^2}{g^2}, \tag{32}$$

the series expansion of this tapered incident wave can be derived using Faà di Bruno's formula[30]. This expansion has the form:

$$\psi_i^{(m)}(\mathbf{r}) = \sum_{k=1}^{m} \psi_i^{(k)}(\mathbf{r}) B_{m,k}\left(\chi'(\mathbf{r}), \chi''(\mathbf{r}), \cdots, \chi^{(m)}(\mathbf{r})\right). \tag{33}$$

Here, the $B_{m,k}\left(\chi'(\mathbf{r}), \chi''(\mathbf{r}), \cdots, \chi^{(m)}(\mathbf{r})\right)$ are the Bell polynomials, which have the form,

$$B_{m,k}\left(\chi'(\mathbf{r}), \chi''(\mathbf{r}), \cdots, \chi^{(m)}(\mathbf{r})\right) = \sum_{\substack{a_1+2a_2+\cdots+ma_m \\ a_1+a_2+\cdots+a_m=k}} \frac{n!\left[\chi'\right]^{a_1}\left[\chi''\right]^{a_2}\cdots\left[\chi^{(m)}\right]^{a_m}}{a_1!(1!)^{a_1}\, a_2!(2!)^{a_2}\cdots a_m!(m!)^{a_m}}, \tag{34}$$

where χ', χ'' and $\chi^{(m)}$ are used as abbreviations for $\chi'(\mathbf{r})$, $\chi''(\mathbf{r})$ and $\chi^{(m)}(\mathbf{r})$, respectively, and a_1, a_2, … and a_m are all integers greater than or equal to zero. The Bell polynomials also satisfy the following relation ($m \geqslant 1$):

$$kB_{m,k} = \sum_{l=k-1}^{m-1} \binom{m}{l} \chi^{(m-l)}(\mathbf{r}) B_{m,k-1}, \tag{35}$$

where $B_{m,k}$ and $B_{m,k-1}$ are used as abbreviations for $B_{m,k}\left(\chi'(\mathbf{r}), \chi''(\mathbf{r}), \cdots, \chi^{(m)}(\mathbf{r})\right)$ and $B_{m,k-1}\left(\chi'(\mathbf{r}), \chi''(\mathbf{r}), \cdots, \chi^{(m)}(\mathbf{r})\right)$, respectively. This relation is useful for programming the necessary calculations.

REFERENCES

[1] T. Wang and C. M. Tong, "An improved facet-based TSM for electromagnetic scattering from ocean surfacea," *IEEE Geosci. Remote Sens. Lett.*, vol. 15, no. 5, pp. 644-648, 2018.

[2] Y. Wang, K. S. Chen, L. Tsang, and L. Yu, "Depolarized backscattering of rough surface by AIEM model," *IEEE J. Sel. Top. Appl. Earth Observ. Remote Sens.*, vol. 10, no.~11, pp. 4740-4752, 2017.

[3] S. El-Bah, R. Dusséaux, and S. Afifi, "Some statistical and spatial properties of signal scattering by 2-D slightly rough random surfaces," *IEEE Trans. Antennas Propag.*, vol. 64, no. 2, pp. 721-729, 2016.

[4] T. H. Liao, L. Tsang, S. W. Huang, N. Niamsuwan, S. Jaruwatanadilok, and S. B. Kim, "Copolarized and cross-polarized backscattering from random rough soil surfaces from L-band to Ku-band using numerical solutions of Maxwell's equations with near-field precondition," *IEEE Trans. Geosci. Remote Sensing*, vol. 54, no. 2, pp. 651-662, 2016.

[5] C. A. Guérin and J. T. Johnson, "Cross-polarized backscattering under the secon-order small-slope approximation," *IEEE Trans. Geosci. Remote Sensing*, vol. 53, no. 11, pp. 6308-6314, 2015.

[6] A. Torabi, S. A. Zekavat, and K. Sarabandi, "Wideband directional channel characterization for multiuser MIMO systems over a random rough dielectric ground," *IEEE Trans. Wirel. Commun.*, vol. 15, no. 5, pp. 3103-3113, 2016.

[7] E. N. Grossman, N. Popovic, and R. A. Chamberlin, "Submillimeter wavelength scattering from random rough surfaces," *IEEE THz. Sci. Technol.*, vol. 7, no. 5, pp. 546-562, 2017.

[8] K. Li, L. X. Guo, and J. Li, "Investigation of bistatic scattering of a 2-D target coated with double negative materials above 1-D random rough surface by FDTD method," *Proc. Cross Strait Quad-Regional Radio Wireless Conf.*, Chengdu, Sichuan, pp. 435-438, 2013.

[9] S. Sung, N. Bajwa, W. S. Grundfest, and Z. D. Taylor, "Exploration of the Rayleigh roughness in THz medical imaging," *Proc. Int. Conf. Infrared, Millimeter and THz Waves*, Hong Kong, 2015.

[10] C. Yin, Y. L. Geng, Y. J. Pan, and H. Y. Jin, "Fast algorithm for rough surface scene simulation in passive millimeter wave imaging," *IEEE Access*, vol.~6, pp. 25051-25059, 2018.

[11] R. Wang, L. X. Guo, and Z. B. Zhang, "Scattering from contaminated rough sea surface by iterative physical optics model," *IEEE Geosci. Remote Sens. Lett.*, vol. 13, no. 4, pp. 500-504, 2016.

[12] H. Zamani, A. Tavakoli, and M. Dehmollaian, "Scattering by a dielectric sphere buried in a half-space with a slightly rough interface," *IEEE Trans. Antennas Propag.*, vol. 66, no. 1, pp. 347-359, 2018.

[13] S. Afifi, and R. Dusséaux, "Scattering from 2-D perfect electromagnetic conductor rough surface: analysis with the small perturbation method and the small-slope approximation," *IEEE Trans. Antennas Propag.*, vol.~66, no.~1, pp. 340-346, 2017.

[14] H. Zamani, A. Tavakoli, and M. Dehmollaian, "Scattering from two rough surfaces with inhomogeneous dielectric profiles," *IEEE Trans. Antennas Propag.*, vol.~63, no.~12, pp. 5753-5766, 2015.

[15] L. Tsang, J. A. Kong, and K. H. Ding, *Scattering of Electromagnetic Waves: Theories and Applications*. John Wiley & Sons, New York, 2000.

[16] O. Gilgert, C. Deumie, and C. Amra, "Angle-resolved ellipsometry of scattering patterns from arbitrary surfaces and bulks," *Opt. Express*, vol. 13, no. 7, pp. 2403-2418, 2005.

[17] J. E. Elson, "Infrared light scattering from surfaces covered with multiple dielectric overlayers," *Appl. Optics*, vol. 16, no. 1, pp. 2872-2881, 1977.
[18] C. D. Jones and D. R. Jackson, "Infrared light scattering from surfaces covered with multiple dielectric overlayers," *IEEE J. Oceanic ENG.*, vol. 26, no. 1, pp. 84-93, 2001.
[19] S. O. Rice, "Reflection of electromagnetic waves from slightly rough surfaces," *Commun. Pure Appl. Math.*, vol. 4, pp. 351-378, 1951.
[20] J. T. Johnson, "Third-order small-perturbation method for scattering from dielectric rough surfaces," *J. Opt. Soc. Am. A-Opt. Image Sci. Vis.*, vol. 16, no. 11, pp. 2720-2736, 1999.
[21] M. A. Demir, J. T. Johnson, and T. J. Zajdel, "A study of the fourth-order small perturbation method for scattering from two-layer rough surfaces," *IEEE Trans. Geosci. Remote Sensing*, vol. 50, no. 9, pp. 3374-3382, 2012.
[22] J. A. Kong, *Electromagnetic Wave Theory*. EMW Publishing, Cambridge, 2008.
[23] E. I. Thorsos, "The validity of the Kirchhoff approximation for rough surface scattering using a Gaussian roughness spectrum," *J. Acoust. Soc. Am.*, vol. 83, no. 11, pp. 78-92, 1988.
[24] L. Tsang, J. A. Kong, and K. H. Ding, *Scattering of Electromagnetic Waves: Numerical Simulation*. John Wiley & Sons, Inc., New York, 2001.
[25] H. X. Ye and Y. Q. Jin, "Parameterization of the tapered incident wave for numerical simulation of electromagnetic scattering from rough surface," *IEEE Trans. Antennas Propag.*, vol. 53, no. 3, pp. 1234-1237, 2005.
[26] J. T. Johnson and R. J. Burkholder, "A study of scattering from an object below a rough surface," *IEEE Trans. Geosci. Remote Sensing*, vol. 42, no. 1, pp. 59-66, 2004.
[27] J. T. Johnson, "A numerical study of scattering from an object above a rough surface," *IEEE Trans. Antennas Propag.*, vol. 50, no. 10, pp. 1361-1367, 2002.
[28] G. Macelloni, G. Nesti, P. Pampaloni, and S. Sigismondi, "Experimental validation of surface scattering and emission models," *IEEE Trans. Geosci. Remote Sensing*, vol. 38, no. 1, pp. 459-469, 2000.
[29] J. W. Tukey, "Mathematics and the picturing of data," *Proc. Int. Congress Mathematicians*, Vancouver, pp. 523-532, 1974.
[30] K. Drakakis, "On a closed formula for the derivatives of $e^{f(x)}$ and related finacial applications," *International Mathematical Forum*, vol. 4, no. 9, pp. 401-407, 2009.

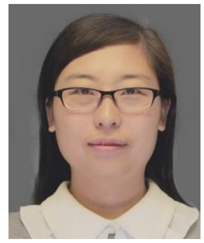

Qing Wang was born Shaanxi, China, in 1984. She received the B.Eng. degree in Measuring and Control Technology and Instrumentations from Xidian University, China, in 2006 and Ph.D. degree in Electromagnetic Field and Microwave Technology from Xidian University, China, in 2012. From 2009 to 2011, she was a visiting student in Clemson University, USA.

She is currently an Assistant Professor with the School of Electronic Engineering, Xidian University, Xi'an. Her research interests include computational electromagnetics and millimeter wave technology.

Chen Lin was born in Jiangsu, China, in 1982. He received the B.Eng. Degree in Measuring and Control Technology and Instrumentations from Xidian University, China, in 2006 and Ph.D. degree in Electromagnetic Field and Microwave Technology from Xidian University, China, in 2011.

He is currently a Senior Engineer with Yangzhou Marine Electronic Institute. His research interest contains radar system analysis and engineering, microwave engineering and electronically scanned arrays.

Zhen-Ya Lei was born in Shaanxi, China, in 1960. He received the B.Eng. degree in Computer Science from Xidian University, China, in 1981 and M.E. degree in Electromagnetic Field and Microwave Technology from Xidian University, China, in 1998. He was a visiting scholar in Ohio State University, U.S. in 2016.

He is currently a Professor with the School of Electronic Engineering, Xidian University, Xi'an. His research interest contains microwave circuits and microwave engineering, Rf/microwave transmitter and the receiver, antenna, system-level EM field analysis, target characteristics and stealth design.

Jian-Qiang Hou received the B.Eng. degree in Electromagnetic Field and Microwave Technology from Xidian University, China, in 1999, M.E. degree in Electromagnetic Field and Microwave Technology from Xidian University, China, in 2004 and Ph.D. degree in

Electromagnetic Field and Microwave Technology from Xidian University, China, in 2012.

He is currently an Associate Professor with the School of Electronic Engineering, Xidian University, Xi'an. His research interest contains microwave millimeter-wave circuits and systems and modeling and design of microwave devices.

Lei Li was born in 1980. He received the B.Eng. degree in Electronic Engineering from Shenyang Aerospace University, China, in 2001, M.E. degree in Electromagnetic Field and Microwave Technology from Xidian University, China, in 2005 and Ph.D. degree in Electromagnetic Field and Microwave Technology from Xidian University, China, in 2007. From 2015 to 2016, he was a visiting scholar in University of Montreal, Canada.

He is currently an Associate Professor with the School of Electronic Engineering, Xidian University, Xi'an. His research interest contains substrate integrated waveguide and target characteristics.

Electromagnetic Waves Interaction with a Human Head Model for Frequencies up to 100 GHz

Fatih Kaburcuk [1], Atef Z. Elsherbeni [2], Rachel Lumnitzer [2], and Allison Tanner [2]

[1] Department of Electrical-Electronics Engineering
Sivas Cumhuriyet University, Sivas, 58140, Turkey
fkaburcu@syr.edu – fkaburcuk@cumhuriyet.edu.tr

[2] Department of Electrical Engineering
Colorado School of Mines, Golden, CO 80401, United States
aelsherb@mines.edu, rachelgottlieb@mymail.mines.edu, tanner@mymail.mines.edu

Abstract **─** Specific absorption rate (SAR), penetration depth, and temperature rise in a one-dimensional (1D) dispersive human head model due to electromagnetic fields radiated by wireless communication systems operated up to 100 GHz are evaluated with the use of a Multiphysics model. In this model, the Debye model of human head tissue parameters is integrated into the finite-difference time-domain method with the use of the auxiliary differential equation to obtain solutions at multiple frequencies of interest using a single simulation. Then, the SAR, peneration depth, and temperature rise in the 1D head model are calculated for each frequency of interest. The effects of frequency on the SAR, penetration depth, and temperature rise in the head are investigated.

Index Terms **─** Dispersive tissues, FDTD method, human safety standard, penetration depth, millimeter-wave radiation, SAR, temperature rise.

I. INTRODUCTION

Due to the improvement in wireless communication applications such as fifth generation (5G) mobile systems [1], radar systems [2] for military and automotive industries, and medical treatment [3], the use of electromagnetic (EM) fields in centimeter and millimeter wave ranges is increasing day by day. For 3G mobile communication system, the frequency band was less than 6 GHz and for 5G mobile communication system the frequency band is between 24 GHz and 52 GHz. In the next few years, we start to enter into the 6G mobile communication system. Therefore, we should consider the effect of EM wave containing 100 GHz or higher frequency band on human tissues. It is important to investigate the absorption of EM energy and resulting temperature rise in human tissues due to EM fields in these frequency ranges.

In order to limit the temperature rise in the tissues resulting from the absorption of EM energy due to EM field exposure, international EM safety guidelines/ standards published by the Federal Communication Commission (FCC) [4], the International Commission on Non-Ionizing Radiation Protection (ICNIRP) [5], IEEE (C95.1–2005) [6], and Safety Code 6 (SC–6) [7] provide basic restrictions for the amount of absorbed EM energy in tissues and limits of incident power density (IPD). Table 1 gives maximum permissible exposure (MPE) limits of IPD, dependent on frequency range and exposure type (general public exposure (GPE) or occupational exposure (OE)).

The amount of EM energy absorbed by biological tissues is defined as specific absorption rate (SAR). The SAR presents an EM heat source for the tissues. The peak-spatial SAR averaged over 1 g of tissue (SAR_{1g}) has been used as a restriction for frequencies from 100 kHz to 6 GHz in FCC, SC–6, and old versions of IEEE standards. The specified limits of SAR_{1g} in head, neck, and trunk are 1.6 W/kg for GPE and 8 W/kg for OE, respectively. In the updated version of IEEE standards, the peak-spatial SAR is calculated over 10 g of tissues (SAR_{10g}) instead of 1 g and the upper frequency limit for evaluating SAR values has been changed from 6 GHz to 3 GHz. In ICNIRP, the SAR_{10g} value is a good measure for assessing absorbed energy up to 10 GHz. The specified limits of SAR_{10g} are 2 W/kg for GPE and 10 W/kg for OE, respectively. In the IEEE standard, the frequency range from 3 GHz to 6 GHz is considered as a transition region for SAR and IPD. At frequencies above 6 GHz for FCC and SC–6, above 3 GHz for IEEE standard, and above 10 GHz for ICNIRP, SAR is not considered appropriate for evaluating exposure, and thus IPD is considered as a restriction.

At frequencies below 6 GHz, effects of EM fields

Submitted On: March 30, 2020
Accepted On: May 11, 2020

due to near-field or far-field sources on the three-dimensional (3D) human head [8-15] and human eyes [16-19] have been investigated extensively using the finite-difference time-domain (FDTD) method. Furthermore, a one-dimensional (1D) multi-layered human head model [20-22] and body model [23-24] exposed to far-field sources at frequencies below 6 GHz have been studied using the FDTD method.

Table 1: MPE limits of safety standards/guidelines for GPE and OE

Safety Standards	Frequency (f:GHz) GPE / OE	MPE Limit for GPE (w/m^2)	MPE Limit for OE (w/m^2)
IEEE [6]	0.4 – 2 / 0.3 – 3	f / 0.2	f / 0.03
	2 – 100 / 3 – 300	10	100
FCC [4]	0.3 – 1.5	f / 0.15	f / 0.03
	1.5 – 100	10	50
ICNIRP [5]	0.4 – 2	f / 0.2	f / 0.04
	2 – 300	10	50
SC- 6 [7]	0.3 – 6 / 0.1 – 6	$0.02619\ f^{0.6834}$	$0.6455\ f^{0.5}$
	6 – 150	10	50

At frequencies above 6 GHz, effects of EM fields on the 3D human head and human eye models have not been well investigated using the FDTD method, except for a few studies [25-29]. A 3D anatomical eye model exposed to EM fields was investigated at frequencies of 6, 18, and 30 GHz in [26] and 77 GHz in [25]. In [27], a 3D human brain model and eye model exposed to EM fields were investigated at frequencies between 1 GHz to 10 GHz. In [28-29], a 3D human head model with a dipole antenna was analyzed at frequencies up to 30 GHz. For frequencies above 30 GHz, the minimum wavelength in head tissues are very small and thus the 3D human head model has not been studied using the FDTD method, due to excessively long computation times and large memory requirements when the FDTD cell size is in the order of 0.05 of the wavelength in the tissue. Therefore, the FDTD method has been used to analyze a 1D multi-layered human model in [29-30] for frequencies from 1 to 30 GHz and from 3 to 300 GHz, respectively, and a part of the 3D human face model included eye tissues in [31] for frequencies up to 100 GHz due to far-field sources. Furthermore, analysis of a 1D multi-layer human tissue model for frequencies up to 100 GHz in [25] and up to 300 GHz in [32] has been carried out using an analytical method.

All biological tissues are dispersive, thus their EM parameters such as relative permittivity and conductivity change with frequency. Therefore, the EM simulation of the human head must be repeated for each frequency of interest, which leads to a large increase in computation time. In all previous work, except for the studies in [13-14], each EM simulation has been performed for only one frequency of interest. In order to reduce the required computation time and get solutions for multiple frequencies of interest in a single simulation, an algorithm called a Multiphysics model was proposed in [13-14]. This model can be used to analyze the SAR, temperature rise, and radiation penetration depth in the human head at multiple frequencies in a single simulation. This model is based on the Debye representation of human head tissues which was conducted here for frequencies up to 100 GHz and is utilized in the FDTD formulation [33] for the dispersive tissues based on the auxiliary differential equation. Then, calculations of SAR and temperature rise using the Pennes bioheat equation [34] are performed. The Debye model of the tissues is constructed with three-term coefficients for three different frequency ranges: 100 MHz to 2 GHz, 2 GHz to 20 GHz, and 20 GHz to 100 GHz. These coefficients are determined by following the analysis in [35], based on data obtained from [36]. Therefore, the penetration depth, SAR and resulting temperature rise distributions in the human head model due to EM radiated fields can be calculated for a wide range of frequencies up to 100 GHz using the Multiphysics model.

In this paper, two 1D sections of the multi-layer head models based with and without eye tissues obtained from a 3D MRI images of the human head model are investigated using the Multiphysics model to show the effect of tissue types in the head model and to obtain the penetration depths, SAR and temperature rise distributions due to a far-field source at the frequencies up to 100 GHz using a single FDTD simulation. Eye tissues are chosen for investigation because, due to a lack of blood flow, they are most sensitive to EM heat sources. Numerical results obtained in this work are compared with published results for selective frequencies to assess the accuracy of the Multiphysics model and are useful for the development of EM safety guidelines/ standards at frequencies up to 100 GHz with faster simulation tool.

II. NUMERICAL METHOD AND MODELS

A. 1D multi-layer human head models

1D multi-layer head models analyzed in this work are obtained from a 3D realistic human head model [37]. The 3D head model consists of 21 biological tissues: skin, fat, bone, brain (grey and white matter), blood vessel, cartilage, cerebellum, cerebral fluid, cornea, lens, dura, eye sclera, gland, mucous membrane, muscle, nerve, tongue, tooth, trachea, and vitreous humor. Figure 1 shows a horizontal cross-section of the 3D human head model which consists of 2324(width)×3120(depth) cubic cells.

Two cuts (Layer-A and Layer-B) in Fig. 1 are leading to a planar 1D models for the investigation in this work. The Layer-A represented contains human head tissues without eye tissues, whereas the Layer-B contains human head tissues with eye tissues such as lens, cornea, eye sclera, and vitreous humor.

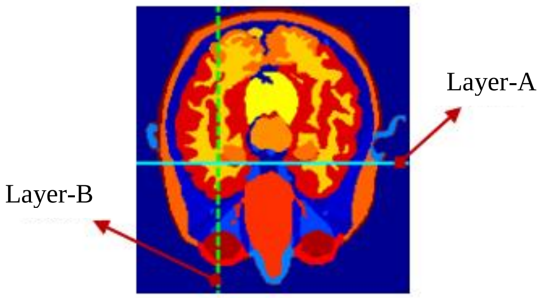

Fig. 1. Horizontal cross-section of a 3D human head model. (Layer A: solid line and Layer B: dashed line)

Table 2: Debye parameters of tissues for frequencies of 20GHz to 100GHz

Tissue	ε_∞	$\Delta\varepsilon_{s1}$	$\Delta\varepsilon_{s2}$	$\Delta\varepsilon_{s3}$	τ_1[ps]	τ_2[ps]	τ_3[ps]
Skin	4.030	0.125	32.419	22.833	1.449	7.233	160.7
Fat	2.566	0.339	1.182	1.424	1.321	4.985	16.95
B. Cortical	2.647	0.695	2.683	6.163	1.354	5.566	19.22
B. Marrow	2.565	0.335	1.158	1.407	1.305	4.911	16.16
Cartilage	4.371	2.030	11.251	25.934	1.489	6.305	20.23
Blood	4.498	3.684	32.111	26.674	1.668	6.403	20.63
Muscle	4.490	3.793	29.742	19.355	1.606	5.797	17.37
Tongue	4.451	3.348	27.925	21.646	1.609	6.059	17.37
Tooth	2.647	0.695	2.683	6.163	1.354	5.566	19.22
Trachea	2.851	2.590	21.581	16.693	1.619	6.103	18.07
Eye Sclera	4.460	3.447	28.933	22.031	1.641	6.169	19.10
Cornea	4.465	3.452	28.828	22.807	1.667	6.276	21.60
Lens	4.376	2.803	23.426	18.052	1.610	6.059	69.76
V. Humor	6.552	34.203	11.316	139.74	6.701	19.16	873.5
Nerve	4.251	1.827	15.117	11.972	1.628	6.155	19.21
Cerebellum	4.403	2.954	24.443	20.383	1.674	6.315	22.97
Dura	4.602	3.754	19.037	19.513	1.479	5.559	18.61
CSF	4.614	4.717	39.895	31.694	1.711	6.386	24.34
Gland	4.494	3.673	30.674	23.645	1.609	6.058	17.31
M. Membrane	4.368	2.711	22.538	17.662	1.629	6.146	18.93
W. Matter	4.315	2.212	18.093	14.502	1.594	6.058	17.77
G. Matter	4.428	3.123	25.887	20.355	1.622	6.128	18.66

B. Debye coefficients of human head tissues

The Debye coefficients of the tissues are needed to obtain solutions at multiple frequencies of interest in a single EM simulation. The three-term Debye coefficients obtained by using the numerical technique proposed in [35] are used to accurately fit the experimental data provided in [36] for the biological tissues in the frequency ranges of 100 MHz to 2 GHz, 2 GHz to 20 GHz, and 20 GHz to 100 GHz. The three-term Debye coefficients for the frequency range between 20 GHz and 100 GHz are tabulated in Table 2.

C. Incident plane wave and FDTD parameters

An incident plane wave with a Gaussian waveform containing all frequencies of interest up to 100 GHz is considered as the EM fields radiated by wireless communication systems. In this paper, the IPD of the incident plane wave are set to 100 W/m^2 and 10 W/m^2 which are maximum permissible exposure limits for occupational and public exposures [6], respectively.

The linearly polarized plane wave in the FDTD problem domain is generated on the total-field/scattered-field (TF/SF) boundary [33]. The convolution perfect matching layer (CPML) [33] is used as an absorbing boundary to truncate the FDTD problem domain. The Courant-Friedrichs-Lewy (CFL) condition is used to determine the numerical stability in the FDTD method. This condition depends on the cell size of the FDTD problem domain. Thus, the cell size should be less than $\lambda_{min}/20$, where λ_{min} is the wavelength of the highest frequency in the head model. In order to satisfy this criterion, the cell size of the 1D head model is set to 0.0625 mm.

D. SAR and temperature rise calculation for 1D multi-layered model

The electric field in time-domain is transformed to frequency domain by using the discrete Fourier transform (DFT) in each time-step of the FDTD simulation. After the FDTD simulation is completed, electric field (E) in the frequency domain is used to calculate the steady-state SAR distribution in the 1D head model at each frequency of interest. The SAR equation for the 1D multi-layered model is written at a specific frequency and location as follows:

$$SAR(i) = \frac{\sigma(i)}{2\rho(i)}(|E(i)|^2), \quad (1)$$

where σ and ρ are conductivity [S/m] and mass density [kg/m^3] of tissue, respectively, and i denotes the indexed cell. The algorithm specified in the IEEE C95.3 standard [38] is applied to calculate the SAR$_{1g}$ and SAR$_{10g}$ in the 1D head model.

The temperature rise in the 1D head model is calculated by using the Pennes bioheat equation in [34] and as implemented in [13-14]. The SAR$_{1g}$ distribution are used as EM heat source into the bioheat equation. All required thermal parameters for temperature rise calculations in the tissues are provided in [24].

III. NUMERICAL RESULTS AND DISCUSSIONS

First, the results obtained in this investigation are compared to the limited results available in the literature to confirm the validity of our 1D multi-layered head models with the use of the Multiphysics model. Then, the penetration depth, SAR, and temperature rise in Layer-A and Layer-B due to an EM plane wave are calculated using the Multiphysics model for three frequency ranges (100 MHz to 2 GHz, 2 to 20 GHz, and 20 to 100 GHz).

A. Comparison of results

In order to prove the validity of the Multiphysics model, the maximum local SAR, SAR_{1g}, SAR_{10g}, and temperature rise values in the Layer-A model obtained by the Multiphysics model at the frequencies of 3, 6, 24, 77, and 100 GHz are compared to those values obtained analytically for a 1D multi-layer model consisting of only skin, fat, and muscle in [25]. The results listed in Table 3 are obtained when the IPD is 10 W/m^2. Although the 1D multi-layered models in [25] and in this work have different tissue layer thickness, and the EM and thermal parameters of tissues used are different, the results in Table 3 are in a good agreement with acceptable differences. For IPD is 100 W/m^2, the measured and simulated temperature rise calculated by using the finite-element method (FEM) in [25] are 0.7 and 0.84 ºC at 77 GHz, respectively, whereas the temperature rise obtained using our Multiphysics model is 0.64 ºC.

Furthermore, a 3D eye model has been analyzed at 77 GHz using the traditional FDTD method with the IPD of 10 W/m^2 in [25]. The reported SAR_{1g} is 0.66 W/kg, whereas in this work, the SAR_{1g} for Layer-B model obtained by the Multiphysics model at 77 GHz is 0.55 W/kg. The SAR_{1g} values obtained in [25] and here are close to each other, even with the use of different dimensional models.

Table 3: Layer-A results compared with those from [25] when IPD =10 W/m^2

Freq. (GHz)	Methods	SAR_{max} (W/kg)	$SAR_{1g,max}$ (W/kg)	$SAR_{10g,max}$ (W/kg)	Temp. Rise (ºC)
3	Result in [25]	0.098	0.200	0.110	<0.1
	Multiphysics	0.548	0.154	0.101	0.074
6	Result in [25]	0.800	0.240	0.140	<0.1
	Multiphysics	0.888	0.260	0.144	0.038
24	Result in [25]	7.740	0.420	0.200	<0.1
	Multiphysics	8.022	0.465	0.215	0.057
77	Result in [25]	27.200	0.580	0.270	<0.1
	Multiphysics	24.511	0.581	0.270	0.064
100	Result in [25]	33.900	0.620	0.290	<0.1
	Multiphysics	28.982	0.616	0.286	0.067

B. SAR and temperature rise distribution on layer-A

The penetration depths, SAR, and temperature rise distributions on the Layer-A model due to the incident plane wave with an IPD of 100 W/m^2 are calculated up to 100 GHz using the Multiphysics model. However, one should point out that the data in [6] assumes 10 W/m^2, which is the maximum permissible limit for general public exposure. While, in this work, we assume that the incident power density is equal to 100 W/m^2 which is the maximum permissible limit for occupational exposure. That's why the results in Table-3 and those presented in the figures of this and the next section are having an approximately factor of 10 differences.

For Layer-A model, the maximum local SAR values and radiation penetration depths as a function of frequency are shown in Fig. 2. The penetration depths of an EM plane wave incident on the head model provide the distance where the local SAR values fall to 1% of their maximum. It has been realized that penetration depths decrease exponentially with the increase of frequency, whereas maximum local SAR values increase with frequency, because the permittivity of tissues decreases and the conductivity of tissues increases at higher frequencies. Decreased permittivity causes more incident power to reach deeper tissues, while increased conductivity works to prevent this power from entering deeper tissues. The penetration depth becomes gradually less than 1 mm when the frequency gets closer to 100 GHz. The maximum SAR_{1g} and SAR_{10g} values up to 100 GHz are shown in Fig. 3.

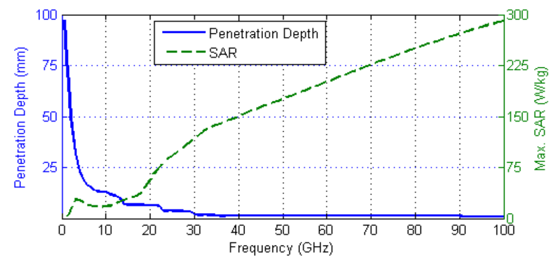

Fig. 2. Maximum local SAR and penetration depth as a function of frequency.

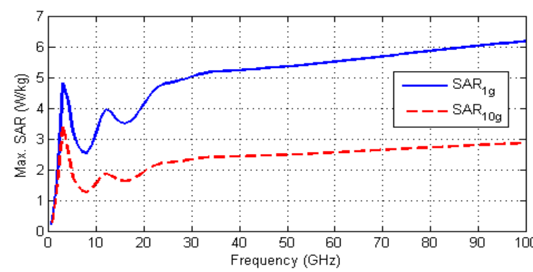

Fig. 3. Max. SAR_{1g} and SAR_{10g} as a function of frequency for Layer-A.

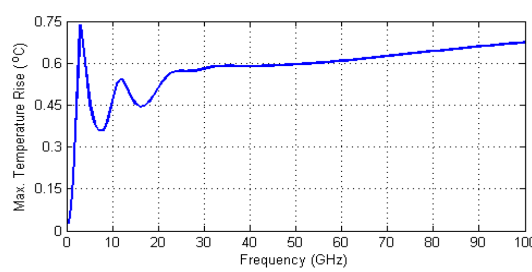

Fig. 4. Maximum temperature rise as a function of frequency for Layer-A.

These values are less than the specified limits of 8 W/kg for SAR_{1g} and 10 W/kg for SAR_{10g}. The calculated maximum temperature rise shown in Fig. 4 is less than 0.73 ºC at all frequencies of interest. The maximum SAR value occurs at 100 GHz, whereas the maximum temperature rise occurs at 3 GHz. This is because small penetration depths at high frequencies prevent incident power from entering deeper tissues and causing an increase in temperature. It has been realized that the maximum temperature rise at all frequencies of interest in the head model are linearly proportional to the maximum SAR_{1g} and SAR_{10g} values, whereas they are not directly proportional to the maximum local SAR shown in Fig. 2. The local SAR and temperature rise distributions on the Layer-A model at specified frequencies up to 100 GHz are shown in Fig. 5 and Fig. 6, respectively. It can be seen that the maximum values of local SAR generally occur at the skin surface of the head model, whereas the maximum temperature rise occurs at about 2.5 mm under the skin surface of the head model. Furthermore, the values of local SAR distributions exhibit faster decrease with the increase of the frequency, whereas the values of temperature rise distributions decrease gradually. Figure 7 shows the maximum temperature rise in Layer-A model at specified frequencies as a function of time. It can be seen that the maximum temperature rise is reached after 30 minutes of exposure.

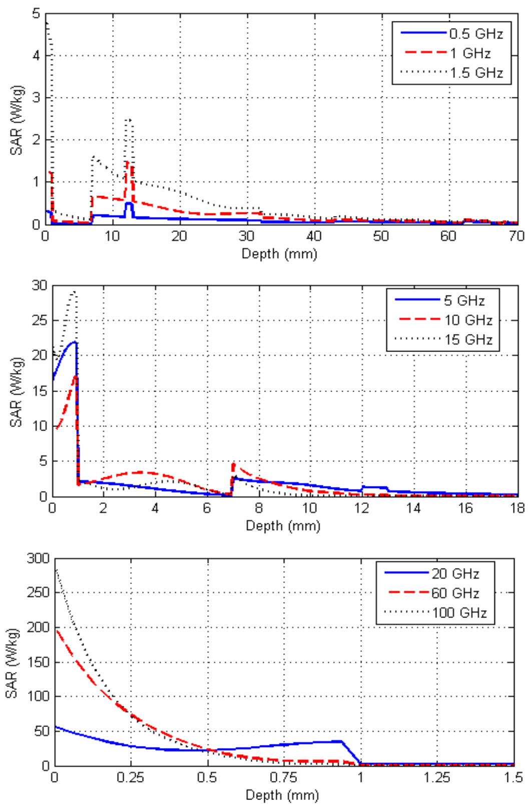

Fig. 5. Local SAR distributions on Layer-A at specified frequencies.

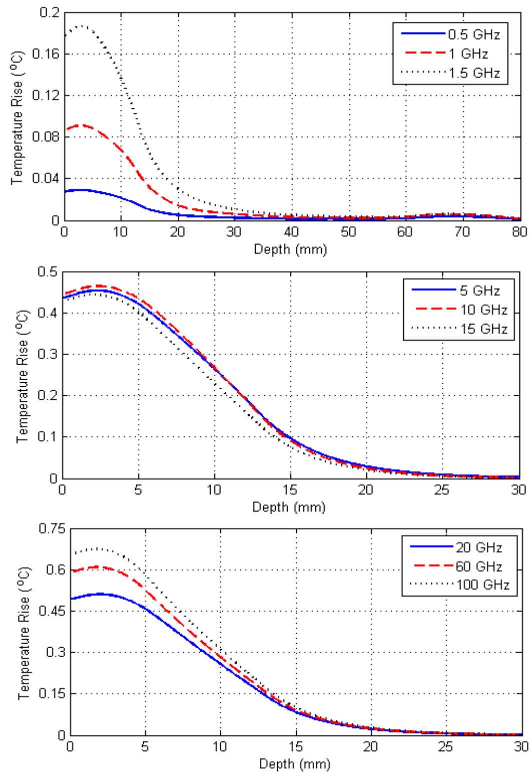

Fig. 6. Temperature rise distributions on Layer-A at specified frequencies.

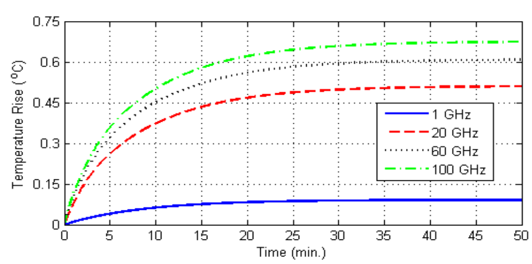

Fig. 7. Max. temperature rise as a function of time.

C. SAR and temperature rise distribution on layer-B

In order to show the effect of eye tissues on penetration depth, SAR, and temperature rise distributions, the Layer-B head model with eye tissues such as cornea, lens, sclera, and vitreous humor is analyzed using the Multiphysics model up to 100 GHz. The maximum local SAR values and radiation penetration depths as a function of frequency on the Layer-B model are shown in Fig. 8. The maximum SAR_{1g} and SAR_{10g} values up to 100 GHz shown in Fig. 9 are less than the specified limits of SAR_{1g} and SAR_{10g}. The calculated maximum temperature rise versus frequency are shown in Fig. 10. Numerical results show that the maximum local SAR values in Layer-B are slightly higher than those values in Layer-A, especially for higher frequencies, whereas the maximum SAR_{1g} and SAR_{10g} values in Layer-B are slightly smaller than those values in Layer-A. However, the maximum temperature rise values in Layer-B are much higher than those values in the Layer-A, because Layer-B contains the eye tissues. The maximum temperature rise in the 1D human eye model is not linearly proportional in everywhere to the maximum SAR_{1g} and SAR_{10g} values. This is the reason that the temperature rise distribution is affected not only by the SAR distribution, but also by thermal parameters of eye tissues and penetration depth of the EM radiation. The local SAR and temperature rise distributions on the Layer-B model at specified frequencies up to 100 GHz are shown in Fig. 11 and Fig. 12, respectively. It can be seen from Fig. 6 and Fig. 12 that Layer-B allows higher temperature into deeper tissues than Layer-A. Figure 13 shows the maximum temperature rise in Layer-B at specified frequencies as a function of time.

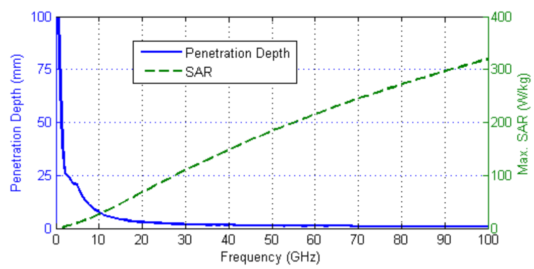

Fig. 8. Maximum local SAR and penetration depth as a function of frequency.

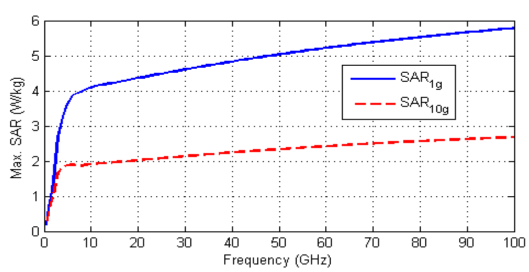

Fig. 9. Max. SAR_{1g} and SAR_{10g} as a function of frequency for Layer-B.

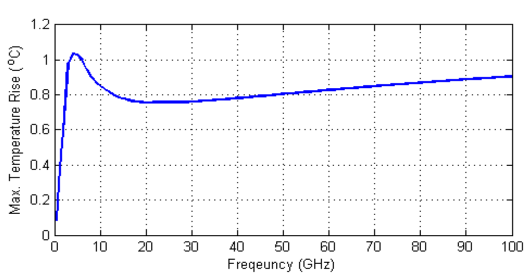

Fig. 10. Maximum temperature rise as a function of frequency for Layer-B.

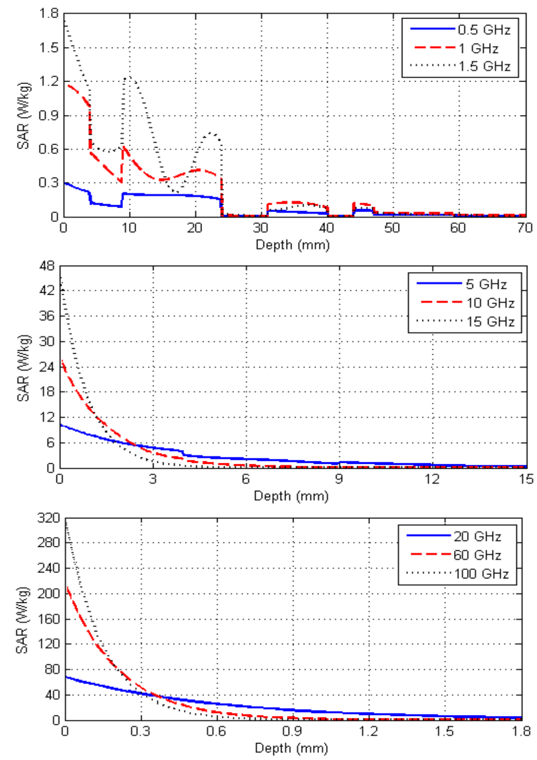

Fig. 11. Local SAR distributions on Layer-B at specified frequencies.

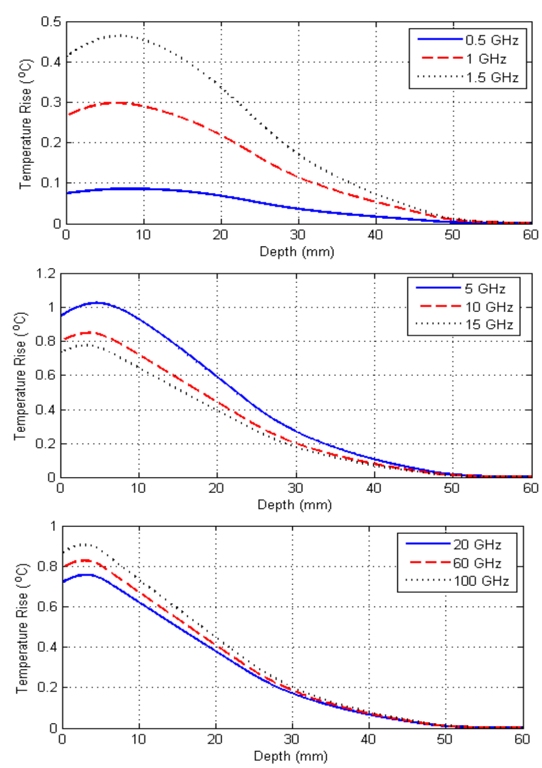

Fig. 12. Temperature rise distributions on Layer-B at specified frequencies.

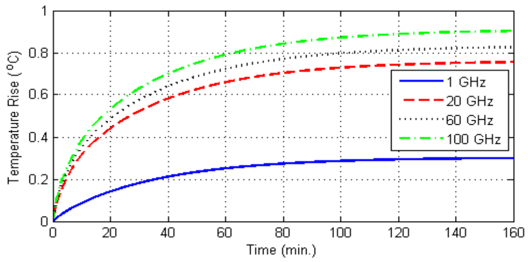

Fig. 13. Max. temperature rise as a function of time.

IV. CONCLUSION

The interaction between one-dimensional human head model and electromagnetic fields radiated by wireless communication systems up to 100 GHz has been investigated by using the Multiphysics model in a single simulation. Numerical results show that the maximum SAR values increase when the frequency gets closer to 100 GHz, whereas the penetration depths in the head model decrease exponentially. In order to show the effect of tissue types on the penetration depth, SAR and temperature rise distributions in the head model, two head models with and without eye tissues are investigated. For the layer-A model, the SAR_{1g} and SAR_{10g} values at 100 GHz are 6.16 and 2.86 W/kg, respectively. For the layer-B model, the SAR_{1g} and SAR_{10g} values at 100 GHz are 5.78 and 2.68 W/kg, respectively. These values are less than the specified limits of 8 W/kg for SAR_{1g} and 10 W/kg for SAR_{10g}. The resulting maximum temperature rise at 100 GHz is 0.67 °C for the layer-A model and 0.9 °C for the layer-B model. These values are less than the threshold temperature rise of 3–5 °C for cataract formation and physiological damage [39] in the tissues. Numerical results obtained in this work are useful to evaluate the effect of EM fields radiated from wireless communications systems operated up to 100 GHz on the human head.

REFERENCES

[1] International Wireless Industry Consortium (IWIC), "5G millimeter wave frequencies and mobile networks," July 2019.

[2] R. Ramasubramanian, K. Ramaiah, and A. Aginsky, "Moving from legacy 24 GHz to state-of-the-art 77 GHz radar," *Texas Instru.*, pp. 1-6, Oct. 2017.

[3] M. A. Rojavi and M. C. Ziskin, "Medical application of millimetre waves", *An International Journal of Medicine* (*QJM*), vol. 91, no. 1, pp. 57-66, Jan. 1998.

[4] Federal Communications Commission, "Evaluating compliance with FCC guidelines for human exposure to radio frequency electromagnetic fields," *Rep.*, Washington, DC, Tech. Rep. OET Bull. 65, 1997.

[5] International Commission on Non-Ionizing Radiation Protection (ICNIRP), "Guidelines for limiting exposure to time-varying electric, magnetic, and electromagnetic fields (up to 300 GHz)," *Health Phys*., vol. 74, pp. 494-522, 1998.

[6] IEEE C95.1. IEEE standard for safety levels with respect to human exposure to radio frequency electromagnetic fields, 3 kHz to 300 GHz, IEEE Standard C95.1-2005, 2006.

[7] Safety Code 6, Health Canada, "Limits of human exposure to radiofrequency electromagnetic energy in the frequency range from 3 kHz to 300 GHz," 2015.

[8] J. Wang and O. Fujiwara, "FDTD computation of temperature rise in the human head for portable telephones," *IEEE Trans. Microwave Theory Tech.*, vol. 47, pp. 1528-1534, Aug. 1999.

[9] P. Bernardi, M. Cavagnaro, S. Pisa, and E. Piuzzi, "Power absorption and temperature elevations induced in the human head by a dual-band monopole-helix antenna phone," *IEEE Trans. Microwave Theory Tech*., vol. 49, no. 12, pp. 2539-2546, Dec. 2001.

[10] A. Hirata and T. Shiozawa, "Correlation of maximum temperature increase and peak SAR in the human head due to handset antennas," *IEEE Trans. Microw. Theory Tech.*, vol. 51, no. 7, pp. 1834-1841, July 2003.

[11] A. Hirata, M. Morita, and T. Shiozawa, "Temperature increase in the human head due to a dipole antenna at microwave frequencies," *IEEE Trans. Electromag. Compat*., vol. 45, no. 1, pp. 109-116, Feb. 2003.

[12] M. Fujimoto, A. Hirata, J. Q. Wang, O. Fujiwara, and T. Shiozawa, "FDTD-derived correlation of maximum temperature increase and peak SAR in child and adult head models due to dipole antenna," *IEEE Trans. Electromagn. Compat.*, vol. 48, no. 1, pp. 240-247, Feb. 2006.

[13] F. Kaburcuk and A. Z. Elsherbeni, "Temperature rise and SAR distribution at wide range of frequencies in a human head due to an antenna radiation," *ACES Journal*, vol. 33, no. 4, pp. 367-372, Apr. 2018.

[14] F. Kaburcuk and A. Z. Elsherbeni, "Efficient computation of SAR and temperature rise distributions in a human head at wide range of frequencies due to 5G RF field exposure," *ACES Journal*, vol. 33, no. 11, pp. 1236-1242, Nov. 2018.

[15] O. Fujiwara, M. Yano, and J. Wang, "FDTD computation of temperature rise inside a realistic head model for 1.5-GHz microwave exposure," *Electron. Comm. Jpn. Pt. I*, vol. 82, no. 3, pp. 240-247, 1999.

[16] A. Hirata, S. Matsuyama, and T. Shiozawa,

"Temperature rise in the human eye exposed to EM waves in the frequency range 0.6-6 GHz," *IEEE Trans. Electromag. Compat.*, vol. 42, no. 4, pp. 386-393, Nov. 2000.

[17] A. Hirata, H. Watanabe, and T. Shiozawa, "SAR and temperature increase in the human eye induced by obliquely incident plane waves," *IEEE Trans. Electromag. Compat*., vol. 44, no. 4, pp. 592-594, Nov. 2002.

[18] A. Hirata, "Temperature increase in human eyes due to near-field and far-field exposures at 900 MHz, 1.5 GHz, and 1.9 GHz," *IEEE Trans. Electromag. Compat*., vol. 47, no. 1, pp. 68-76, Feb. 2005.

[19] C. Buccella, V. D. Santis, and M. Feliziani, "Prediction of temperature increase in human eyes due to RF sources," *IEEE Trans. Electromag. Compat*., vol. 49, no. 4, pp. 825-833, Nov. 2007.

[20] A. Drossos, V. Santomaa, and N. Kuster, "The dependence of electromagnetic energy absorption upon human head tissue composition in the frequency range of 300-3000 MHz," *IEEE Trans. Microwave Theory Tech*., vol. 48, no. 11, pp. 1988-1995, 2000.

[21] A. A. Omar, Q. M. Bashayreh, and A. M. Al-Shamali, "Investigation of the effect of obliquely incident plane wave on a human head at 900 and 1800 MHz," *Int. J. RF and Microwave Comp. Aid Eng*., vol. 20, no. 2, pp. 133-140, Mar. 2010.

[22] A. I. Sabbah, N. I. Dib, and M. A. Al-Nimr, "Evaluation of specific absorption rate and temperature elevation in a multi-layered human head model exposed to radio frequency radiation using the finite-difference time domain method," *IET Microwaves, Antennas & Propagation*, vol. 5, no. 9, pp. 1073-1080, 2011.

[23] T. Samaras, A. Christ, A. Klingenbock, and N. Kuster, "Worst case temperature rise in a one-dimensional tissue model exposed to radio-frequency radiation," in *IEEE Transactions on Biomedical Engineering*, vol. 54, no. 3, pp. 492-496, Mar. 2007.

[24] A. Hirata, O. Fujiwara, T. Shiozawa, "Correlation between peak spatial-average SAR and temperature increase due to antennas attached to human trunk," *IEEE Trans. Biomed. Eng.*, vol. 53, no. 8, pp. 1658-1664, 2006.

[25] F. Gustrau and A. Bahr, "W-band investigation of material parameters, SAR distribution, and thermal response in human tissue," in *IEEE Transactions on Microwave Theory and Techniques*, vol. 50, no. 10, pp. 2393-2400, Oct. 2002.

[26] P. Bernardi, M. Cavagnaro, S. Pisa, and E. Piuzzi, "SAR distribution and temperature increase in an anatomical model of the human eye exposed to the field radiated by the user antenna in a wireless LAN," *IEEE Trans. Microwave Theory Tech.*, vol. 46, no. 12, pp. 2074-2082, Dec. 1998.

[27] I. Laakso, "Assessment of the computational uncertainty of temperature rise and SAR in the eyes and brain under far-field exposure from 1 to 10 GHz," *Physics in Medicine and Biology*, vol. 54, pp. 3393-3404, 2009.

[28] R. Morimoto, I. Laakso, V. De Santis, and A. Hirata, "Relationship between peak spatial-averaged specific absorption rate and peak temperature elevation in human head in frequency range of 1-30 GHz," *Phys. Med. Biol.*, vol. 61, pp. 5406-5425, 2016.

[29] R. Morimoto, A. Hirata, I. Laakso, M. C. Ziskin, and K. R. Foster, "Time constants for temperature elevation in human models exposed to dipole antennas and beams in the frequency range from 1 to 30 GHz," *Phys. Med. Biol*., vol. 62, pp. 1676-1699, 2017.

[30] Y. Hashimoto, A. Hirata, R. Morimoto, S. Aonuma, I. Laakso, K. Jokela, and K. R. Foster, "On the averaging area for incident power density for human exposure limits at frequencies over 6 GHz," *Phys. Med. Biol.*, vol. 62, pp. 3124-3138, Mar. 2017.

[31] I. Laakso, R. Morimoto, J. Heinonen, K. Jokela, and A. Hirata, "Human exposure to pulsed fields in the frequency range from 6 to 100 GHz," *Phys. Med. Biol.*, vol. 62, pp. 6980-6992, 2017.

[32] A. Kanezaki, A. Hirata, S. Watanabe, and H. Shirai, "Parameter variation effects on temperature elevation in a steady-state, one-dimensional thermal model for millimeter wave exposure of one- and three-layer human tissue," *Phys. Med. Biol*., vol. 55, pp. 4647-4659, 2010.

[33] A. Z. Elsherbeni and V. Demir, *The Finite-Difference Time-Domain Method for Electromagnetics with MATLAB Simulations*, second edition, ACES Series on Computational Electromagnetics and Engineering, SciTech Publishing, an Imprint of IET, Edison, NJ, 2016.

[34] H. H. Pennes, "Analysis of tissue and arterial blood temperature in resting forearm," *J. Appl. Physiol.*, vol. 1, pp. 93-122, 1948.

[35] M. A. Eleiwa and A. Z. Elsherbeni, "Debye constants for biological tissues from 30 Hz to 20 GHz," *ACES Journal*, vol. 18, no. 3, Nov. 2001.

[36] http://niremf.ifac.cnr.it/tissprop/ [Online website 2020].

[37] http://noodle.med.yale.edu/zubal/ [Online website 2020].

[38] IEEE Recommended Practice for Measurements and Computations of Radio Frequency Electromagnetic Fields With Respect to Human Exposure to Such Fields, 100 kHz-300 GHz, IEEE Standard C95.3-2002, Annex E, 2002.

[39] A. C. Guyton and J. E. Hall, *Textbook of Medical*

Physiology. Philadelphia, PA: W. B. Saunders, chap. 73, 1996.

Fatih Kaburcuk received both the Master of Science and Doctor of Philosophy degrees from Syracuse University, Syracuse, NY, USA, in 2011 and 2014, respectively, all in electrical engineering. Since April 2020, he has been serving as an Associate Professor with the Department of Electrical-Electronics Engineering, Sivas Cumhuriyet University, Turkey. During his graduate studies, he worked as a Research Assistant with Syracuse University and PPC-Belden Inc. in Liverpool, NY, USA. He worked as a Visiting Research Scholar at the Department of Electrical Engineering, Colorado School of Mines, Golden, CO, USA in 2014. He joined the Erzurum Technical University in November 2015 and served as an Assistant Professor until May 2019. Kaburcuk is a member of ACES. His research interest includes numerical methods in electromagnetics, biological effect of electromagnetic radiation, finite-difference time-domain analysis of antennas.

Atef Z. Elsherbeni received an honor B.Sc. degree in Electronics and Communications, an honor B.Sc. degree in Applied Physics, and a M.Eng. degree in Electrical Engineering, all from Cairo University, Cairo, Egypt, in 1976, 1979, and 1982, respectively, and a Ph.D. degree in Electrical Engineering from Manitoba University, Winnipeg, Manitoba, Canada, in 1987. He started his engineering career as a part time Software and System Design Engineer from March 1980 to December 1982 at the Automated Data System Center, Cairo, Egypt. From January to August 1987, he was a Post-Doctoral Fellow at Manitoba University. Elsherbeni joined the faculty at the University of Mississippi in August 1987 as an Assistant Professor of Electrical Engineering. He advanced to the rank of Associate Professor in July 1991, and to the rank of Professor in July 1997. He was the Associate Dean of the college of Engineering for Research and Graduate Programs from July 2009 to July 2013 at the University of Mississippi. He then joined the Electrical Engineering and Computer Science (EECS) Department at Colorado School of Mines in August 2013 as the Dobelman Distinguished Chair Professor. He was appointed the Interim Department Head for (EECS) from 2015 to 2016 and from 2016 to 2018 he was the Electrical Engineering Department head. In 2009 he was selected as Finland Distinguished Professor by the Academy of Finland and TEKES. Elsherbeni is a Fellow member of IEEE and ACES. He is the Editor-in-Chief for ACES Journal, and a past Associate Editor to the Radio Science Journal. He was the Chair of the Engineering and Physics Division of the Mississippi Academy of Science, the Chair of the Educational Activity Committee for IEEE Region 3 Section, the General Chair for the 2014 APS-URSI Symposium, the President of ACES Society from 2013 to 2015, and the IEEE Antennas and Propagation Society (APS) Distinguished Lecturer for 2020-2022.

Rachel Lumnitzer is currently pursuing her B.S. and M.S. in Electrical Engineering from the Colorado School of Mines. Her research interests include the interaction of electromagnetic waves with biological tissues at high frequencies and identification of the tissue dielectric properties.

Allison Tanner received her B.S. in Electrical Engineering from the Colorado School of Mines in 2020. Her research interests include Time Reversal using the Finite Difference Time Domain (FDTD) method and characterization of electrical properties of biological tissues.

Acceleration of Dual Reflector Antenna Radiation Analysis using Double Bounce Physical Optics Accelerated using Multipole Method

Chunbang Wu and Jun Li

School of Electronic and Optical Engineering
Nanjing University of Science and Technology, Nanjing, Jiangsu Province 210094, China
13770328703@139.com

Abstract ─ The multipole method is firstly used to accelerate the radiation analysis of the dual reflector antenna with the double-bounce physical optics. The algorithm starts with physical optics to calculate the equivalent electric current on the subreflector. Then the equivalent electric current on the main reflector can be obtained through the current on the subreflector. It should be noted that the modified multilevel fast multipole method (MLFMM) is applied to accelerate the calculation between the main reflector and the subreflector. In this way, the computation complexity is reduced greatly, thus the computational time can be significantly saved. At last, numerical results are given to demonstrate the superior efficiency and accuracy of the proposed method.

Index Terms ─ Double-bounce physical optics, dual reflector antenna, MLFMM.

I. INTRODUCTION

Nowadays, the satellite communication has a wide application in both the military and civilian domains. The antenna technology plays a very important role in satellite communication. There are three kinds of satellite antennas, namely lens [1], phased array [2]-[3] and reflector [4]-[6] antennas. However, the weight of lens antenna is generally heavier than reflector antenna. Moreover, the phased array antenna generally need to hundreds of units in order to achieve the same gain of reflector antenna, which leads to exceed to the limit of the satellite. Therefore, the reflector antenna has a great advantage in volume and weight.

Full-wave simulation of electrically large size problems is impossible to be taken on conventional workstations due to their hardware limitations. Parallel technique provides a possibility through thousands of Giga Bytes (GB) of memory and processors connected by high-speed switches [7]. Moreover, it is an arduous task for the method of moments (MoM) for electrically large problems. In reference [8], a multi-level method based on near-field and far-field transformation of plane wave is proposed. This method uses diagonal translation operator and is available for evaluating electrically large antennas. In [9], it presents the multilevel fast multipole method has been adapted to speed-up the inverse solution process. To rapidly analyze the radiation pattern of electrically large parabolic reflector antenna, the MoM accelerated with MLFMM is proposed [10]-[12]. In [13], it shows excellent agreement of physical optics results in the main lobe and out to several lobes has been found with those of MLFMM accelerated MoM technique. In order to further improve the speed of calculation, it is preferred to combine MoM with physical optics (PO) to analyze reflector antenna problems [14]. For the antenna radiation problems, it is a key to get the gain of main lobe. PO method can provide the main lobe gain with high efficiency. Therefore, it can be used as a promising tool to simulate the radiation pattern of antenna. In [15], PO is used to analyze the radiation pattern of a monopole antenna mounted on an aircraft. In order to analyze the reflector antenna efficiently, [16] applied graphics processing units to PO in computing the radiated fields. In [17], it proposes a new algorithm about multilevel physical optics for the effective evaluation of the wide angle radiation pattern. Then an acceleration technique was presented in [18] to fast evaluate the monostatic radar cross section. In order to get higher gain with limited size, single reflected antenna is replaced by dual reflector antenna. Reference [19] demonstrates MLFMM is applied to accelerate multiple reflection Physical Optics significantly. Recently, multilevel sampling and interpolation of phase-compensated and amplitude-compensated is applied to the double bounce through physical optics [20]. In [21], it is first to use the MLFMM algorithm for internal field calculations, and consider effect of internal shadowing on the factorized version of the field evaluation matrix, without compromising speed and accuracy. Although the double-bounce physical optics is accelerated by the above technology, it is still time-consuming to optimize large aperture antennas, especially in high frequency. It is significant to develop more efficient approach for

Submitted On: November 19, 2019
Accepted On: April 18, 2020

dual reflector antenna.

A new DBPO (double bouncing physical optics) technique is proposed to evaluate the radiation pattern of the dual reflector parabolic antenna. It is a novel combination between DBPO and MLFMM. In order to obtain the equivalent current of main reflector high efficiently, the effect of the subreflector's equivalent electric current on the main reflector's equivalent electric current is accelerated by MLFMM. Because of the distance between the main reflector and subreflector is long, we use window function to further accelerate the operation of transfer. Suppose N_1 and N_2 are the number of unknowns on the sub and main reflectors respectively. The computational complexity of computing the bounce between reflectors, that can be reduced from $O(N_1{*}N_2)$ to $O(N_1+N_2)$ by using the new approach. With the increase of N_1 and N_2, the efficiency of new method is more evident. Several examples are presented to validate the superior efficiency and accuracy of the proposed method.

II. THEORY AND FORMULATION

A. Physical Optics

The radiation is obtained by the equivalent electric current on the surface of the metallic reflector. The equivalent currents are zero when the surface is not illuminated by incident plane wave, and it has the following expressions in the illuminated area:

$$\vec{J}(\vec{r}^{\,'}) = 2\hat{n}\times\vec{H}^{inc}(\vec{r}^{\,'}), \tag{1}$$

where $\hat{n}$ is the unit normal vector of the surface at point $\vec{r}^{\,'}$, $\vec{H}^{inc}(\vec{r}^{\,'})$ is the incident magnetic field. The radiation diagram of metallic surface as follows:

The radiation pattern is:

$$\vec{E}(\vec{r}) = -jk_0\eta_0(\bar{\bar{I}}+\frac{1}{k_0^2}\nabla\nabla)\iint_S \vec{J}(\vec{r}^{\,'})G(\vec{r}\,|\,\vec{r}^{\,'})ds, \tag{2}$$

where $\eta_0=\sqrt{\frac{\mu_0}{\varepsilon_0}}$ presents the free space wave impedance, $k_0=\omega\sqrt{\varepsilon_0\mu_0}$ presents the free space wave number.

According to the far field approximation, the Green's function is simplified as follows:

$$G(\vec{r}\,|\,\vec{r}^{\,'}) = \frac{e^{-jk\left|\vec{r}-\vec{r}^{\,'}\right|}}{4\pi\left|\vec{r}-\vec{r}^{\,'}\right|} \approx \frac{e^{-jkr}}{4\pi r}e^{jk\vec{r}^{\,'}\cdot\hat{R}}, \tag{3}$$

where $\hat{R}$ is the unit vector of the observed point in spherical coordinates in terms of the rectangular coordinates system, the expression is:

$$\hat{R} = \sin\theta\cos\phi\hat{x}+\sin\theta\sin\phi\hat{y}+\cos\theta\hat{z}\,. \tag{4}$$

The radiation field of the reflector antenna is expressed as:

$$\vec{E}(\vec{r}) = -jk_0\eta_0(\bar{\bar{I}}+\frac{1}{k_0^2}\nabla\nabla)\iint_S \vec{J}(\vec{r}^{\,'})\frac{e^{-jkr}}{4\pi r}e^{jk\vec{r}^{\,'}\cdot\hat{R}}ds^{'}. \tag{5}$$

Only the item of $1/r$ is retained in the far field of radiation, and electric filed intensity is:

$$\vec{E}(\vec{r}) = -jk_0\eta_0\frac{e^{-jkr}}{4\pi r}(\bar{\bar{I}}-\hat{R}\hat{R})\iint_S J(\vec{r}^{\,'})\frac{e^{-jkr}}{4\pi r}e^{jk\vec{r}^{\,'}\cdot\hat{R}}ds^{'}. \tag{6}$$

where $\bar{\bar{I}}$ represents the dyadic unit vector, and $\hat{R}\hat{R}$ represents the dyadic unit vector of $\hat{R}$.

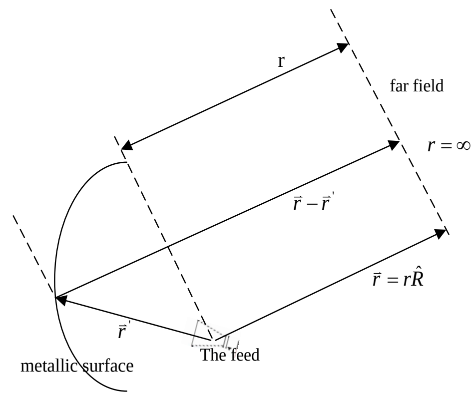

Fig. 1. Radiation of the single reflector antenna in PO.

In Fig. 2, for the dual reflector antenna, it is suitable to apply double bounce physical optics rather than PO. The radiation field of the main reflector is obtained through the equivalent electric current of the subreflector:

$$\begin{aligned}\vec{H}_{sc} &= \iint \vec{J}_s\times\nabla^{'}g\,dS \\ &= \frac{1}{4\pi}\iint\frac{e^{-jkr_m}}{r_m}(\vec{J}_s\times\vec{r}_m)(jk+\frac{1}{r_m})dS\end{aligned}, \tag{7}$$

where dS represents the area of each triangle in subreflector, and $\vec{J}_s$ represents the tangential equivalent electric current of each triangle in subreflector.

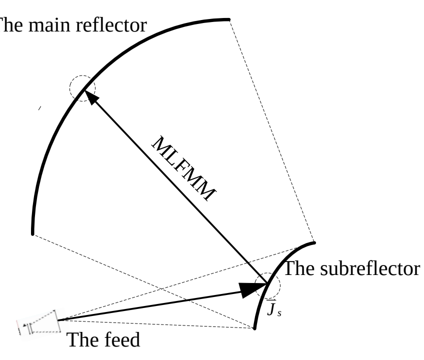

Fig. 2. Dual offset reflector antenna.

B. A novel method based on MLFMM

Triangles are usually used to fit the surface of the object, and $\lambda/10$ is taken as the mesh size. Where λ is the wavelength of the incident wave. It is time-consuming to get the incident field of the main reflector. Due to the fact that the distance between of the main reflector and the subreflector is farther than 10λ, where the main reflector regards as the far field for the subreflector. Therefore we speed up the process of (7) through a novel method, which modifies from MLFMM [22]-[24]. All the aggregations happen in subreflector, and all configurations appear in the main reflector. This is different from the MLFMM. In MLFMM, aggregation and configuration are determined by the distance between the groups. If the distance between two groups are close, the contribution of group is obtained by direct numerical calculation. Only the distance between two groups is long, it uses MLFMM to accelerate the contribution. In proposed algorithm, because the group of main reflector and the group of subreflector are far apart, all the contribution are evaluated by MLFMM. Through three processes of aggregation, transfer and configuration in Fig. 3, the acceleration of the computation is achieved. Firstly, the contribution of every source point is aggregated to the center of the corresponding group. In order to simplify the computation, the source point is defined as the center of the meshed triangle in the subreflector. The equivalent electric current of every point is considered as the basic function of corresponding triangle. Secondly, after finishing aggregation, the contribution of group of source point transfers to the group center of observed point. Thirdly, the contribution of observed point's group center is configured to the observed point, and the configuration is the inverse operation of aggregation.

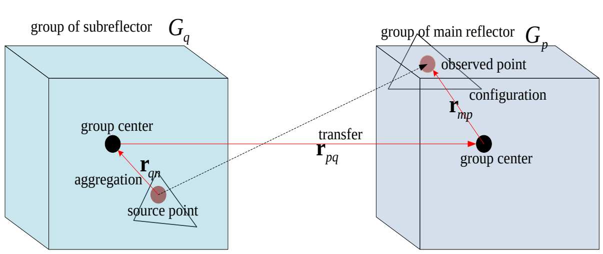

Fig. 3. Principle of accelerating the effect of the subreflector to the main reflector in single level.

The main reflector and the subreflector are surrounded by box through octree grouping. Then the two reflectors are divided into many groups, and (7) is the contribution of the current. The entire solution region is first enclosed in a large group (the red cube at n+1 level in Fig. 4), which is divided into eight smaller groups (the red cubs at n level in Fig. 4). Each sub-group is then recursively subdivided into smaller sub-groups until the finest group (the yellow cube in Fig. 4) contains a few current elements. The level of groups is determined by the distance between the two elements in MLFMM. In Fig. 4, every group of n-1 level transfers at the n-1 level. This is the operation of transfer. Meanwhile, every group of n-1 level gathers into the n level, which is the father group of n-1 level. This is the operation of aggregation. Then every group of n level is transferred at the n level. Every group of n level gathers into the n+1 level, which is the father group of n level. Above operation is aggregation and transfer, and configuration is reverse of aggregation. Every group of n+1 level is configurated to the n level. In MLFMM, the aggregation process stars from the bottom level, and the configuration process stars from the top level.

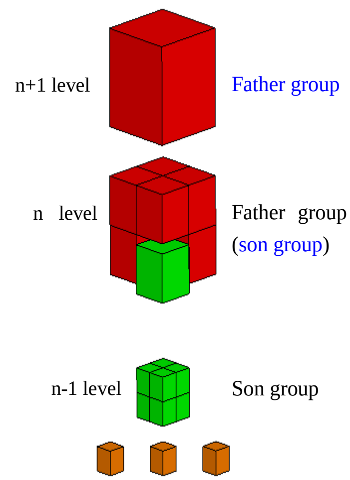

Fig. 4. Multi-level of aggregation, transfer and configuration.

If the distance between the main reflector and the subreflector, satisfying the following condition:

$$|\vec{r}_{pq}| > |\vec{r}_{mp}| + |\vec{r}_{nq}|, \tag{8}$$

Where $\vec{r}_{pq}$ is orientation that from source group center of subreflector to observed group center of main reflector, and $\vec{r}_{mp}$ is orientation that from source group center of main reflector to observed group center of main reflector. $\vec{r}_{pq}$ is orientation that from group center of subreflector to group center of main reflector.

Because the distance between the main reflector and subreflector is far, the main reflector is regarded as the far-field of the subreflector. In this case, the operation of aggregation-transfer-configuration is to accelerate this progress, which solving the equivalent electric current of main reflector from the equivalent current of subreflector.

The Green's function can be unfolded as:

$$g = \frac{e^{-jk\vec{r}_{mn}}}{r_{mn}} = -\frac{jk}{4\pi}\oiint e^{-jk\cdot\left(\vec{r}_{mp}+\vec{r}_{qn}\right)} T_L\left(\vec{k}\cdot\vec{r}\right) d^2k , \quad (9)$$

$$\nabla' g = \frac{k^2}{4\pi}\vec{k}\iint e^{-jk\cdot\left(\vec{r}_{mp}+\vec{r}_{qn}\right)} T_L\left(\vec{k}\cdot\vec{r}\right) d^2k , \quad (10)$$

$$T_L\left(\vec{k}\cdot\vec{r}\right) \approx \sum_{l=0}^{L}(-j)^l(2l+1)h_l^{(2)}(k_o r_{pq})P_l(\vec{r}\cdot\vec{k}) , \quad (11)$$

where multipole mode number L is infinite. In order to calculate the $T_L\left(\vec{k}\cdot\vec{r}\right)$, L is cut off. L has an empirical formula:

$$L = kd + \alpha\log(\pi + kd) , \quad (12)$$

$$\alpha = -\log(\varepsilon) , \quad (13)$$

$$\beta = 1.8(-\log(\varepsilon))^{2/3} , \quad (14)$$

where d represents the diagonal length of the group and ε represents the precision.

Through transforming the Green's function, (7) is expressed as:

$$\vec{H}_{sc} = \iint \vec{J}_s \times \nabla' g dS' = \frac{k^2}{4\pi}\iint \vec{J}_s \times \vec{k}\iint e^{-jk\cdot(\vec{r}_{mp}+\vec{r}_{qn})} T_L\left(\vec{k}\cdot\vec{r}\right) d^2k dS' , \quad (15)$$

$\vec{J}_s \times \vec{k}e^{-jk\vec{r}_{mp}}$ represents the factor of aggregation, $T_L\left(\vec{k}\cdot\vec{r}\right)$ represents the factor of transfer and $e^{-jk\vec{r}_{qm}}$ represents the factor of configuration.

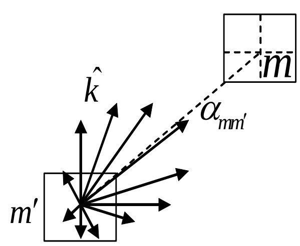

Fig. 5. Sketch map of window function.

In order to accelerate the operation of transfer, we add a window function to the transfer matrix:

$$w_l = \begin{cases} 1 & l \le J \\ \frac{1}{2}\left[1+\cos\left(\frac{l-J}{L-J}\pi\right)\right] & l > J \end{cases} . \quad (16)$$

In Fig. 5, after the transfer factor multiplied by upper window function, the window function, like a bandpass filter, filters out the area that is not concerned. The transfer component at a certain distance form the center of the group becomes smaller. Because of the long distance between source and observation. Through the window function, we omit many of the angular spectral components that have less influence on the transfer process. Thus this function makes the calculation more efficient.

C. NURBS modeling

The NURBS [25] surface is a bivariate piecewise rational function, which is P order in the direction of u and Q order in the direction of v. The basic expression is as follows:

$$\mathbf{S}(u,v) = \frac{\sum_{i=0}^{n}\sum_{j=0}^{m} w_{ij}N_{i,p}(u)N_{j,q}(v)P_{ij}}{\sum_{i=0}^{n}\sum_{j=0}^{m} w_{ij}N_{i,p}(u)N_{j,q}(v)} , \quad (17)$$

in which P and Q are the order, m and n are the number of control points in the direction of u and v. $N_{i,p}(u)$ is P cubic B spline basis function, which is obtained by the node vector $U = [u_0, u_1, ..., u_{n+k+1}]$ according to the de-Boor-Cox recurrence formula. P_{ij} represents the control points of surface, w_{ij} is the weight of every control point:

$$N_{i,0}(u) = \begin{cases} 1 \text{ if } u_i \le u \le u_{i+1} \\ 0 \text{ otherwise} \end{cases} , \quad (18)$$

$$N_{i,p}(u) = \frac{u-u_i}{u_{i+p}-u_i}N_{i,p-1}(u) + \frac{u_{i+p+1}-u_i}{u_{i+p+1}-u_{i+1}}N_{i+1,p-1}(u) . \quad (19)$$

The piecewise rational base function is:

$$R_{i,j}(u,v) = \frac{w_{ij}N_{i,p}(u)N_{j,q}(v)}{\sum_{k=0}^{n}\sum_{l=0}^{m} w_{ij}N_{k,p}(u)N_{l,q}(v)} . \quad (20)$$

The NURBS expression can be abbreviated as:

$$\mathbf{S}(u,v) = \sum_{i=0}^{n}\sum_{j=0}^{m} R_{i,j}(u,v)P_{ij} . \quad (21)$$

As is shown in Fig. 6, we change the model through changing the control points (red points), which are selected by Rhinoceros software. The weight of control points is set to 1.

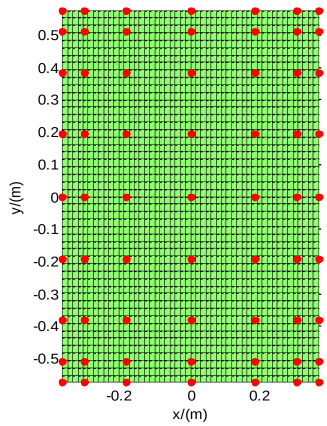

Fig. 6. NURBS fitting plane.

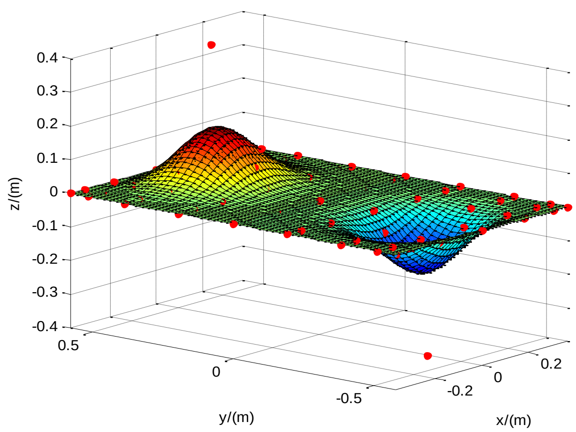

Fig. 7. Change value of two control points in Z coordinate to get the new surface.

In Fig. 6, the x axis represents the direction of V, and the y axis represents the direction of U. The surface around the control point varies with the control point and has no effect on the far curved surface. Through changing 7*9 control points, we can achieve different surface what we want. In Fig. 7, changing the value of two control points in Z coordinate constantly, we will get many surface with different shapes. In the optimization process of the reflector antenna, it has a fixed contour. Only the value of the control point is changed in Z coordinate, the projection shape of the surface in the XOY plane is not affected. Therefore, the outline of the reflector antenna does not have any change. This is why the NURBS modeling is chosen to apply in the shape optimization of the reflector antenna.

III. NUMERICAL RESULTS

The CPU has Intel core Q9500 and 8GB memory. The environment is based on the Fortran MPI.

In Fig. 8, it is the dual offset Cassegrain antenna with primary reflector diameter of 2.5m and rectangular secondary reflector diameter of 1.08m*1.06m, and the feed adopts the ideal horn feed with the right circular polarization. Since the antenna is a shared antenna, and it should be optimized simultaneously both at the receiving and transmitting frequency. The mesh size is 0.4 times the wavelength of the receiving frequency at 28GHz, and the triangle of the primary reflector with 927395, the secondary reflector with 150785. The phi of simulation is 0 degree and the theta ranges from -5 degree to 5 degree. The tangential plane pattern of DBPO, DBPO with MLFMM at 18GHz is shown in Fig.9, and DBPO and the proposed method is in good agreement in the main lobe, so is the near-sidelobe. The result of FEKO and the proposed method has difference in sidelobe. We pay attention to the main lobe and near-sidelobe in this problem. Therefore the proposed method meet the application requirements.

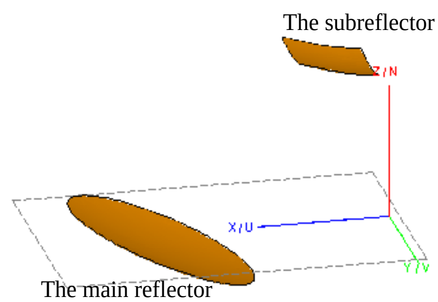

Fig. 8. Model of the dual offset Cassegrain antenna.

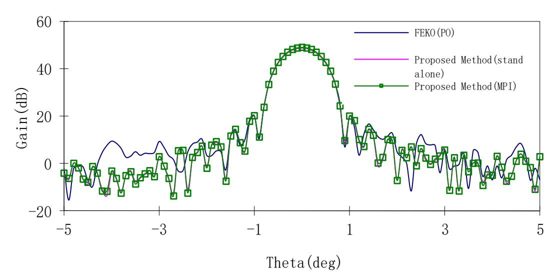

Fig. 9. Radiation pattern of the dual reflector antenna in different methods.

Table 1: Efficiency of different methods

	PO	Proposed Method (Stand-alone)	Proposed Method (MPI with 15 Core)
Time (s)	16214.32	156.84	15.49

The enormous advantage of the proposed method is shown in Table 1. The proposed method is 103.38 times faster than traditional method (DBPO). The presented method combined optimization algorithm applies to optimize the dual reflection antenna, especially for the large aperture antenna.

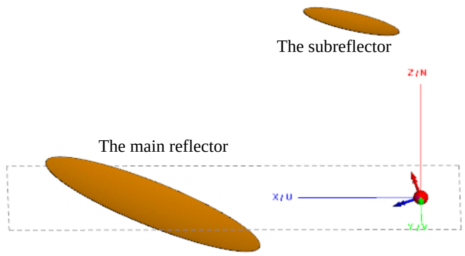

Fig. 10. Model of the dual offset Cassegrain antenna.

In Fig. 10, the diameter of the main reflector is 2.5m, the focal length is 3.74m, and the center offset height is 3.12m. The focal length of the subreflector is 1.456m, and the distance of the hyperbolic vertex is 1.248m. We model the main reflector and subreflector through NURBS, and select 9*9 control points to change the shape of the main reflector and subreflector. The shape of the initial reflector and the coordinates of the control points are shown in Fig. 11.

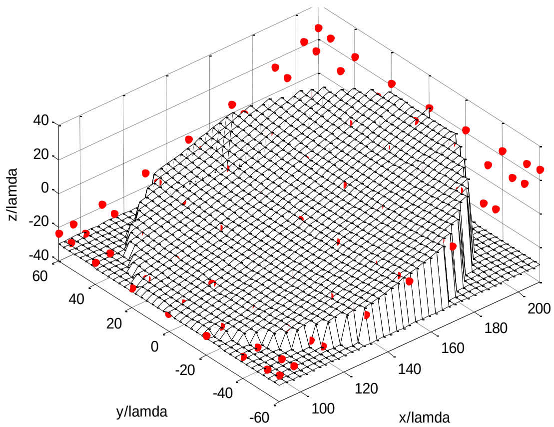

Fig. 11. Initial main reflector and control points.

In Fig. 12 and Fig. 13, the center frequency point of transceiver is 28GHz in Ka band. Since the performance of the 70 beams is approximately similar, it can only be optimized by taking several representative beams at the center and edge. For a high gain narrow beam antenna, we properly take less sampling point to the optimized target area. Here we take 8 sampling points form each edge of the beam and the symmetrical sampling points of equal distance, which guarantee the symmetry of the optimized beam. At the same time, a point is picked up at the center, which reduces the number of the sampling points and prevents the center of the radiation pattern from sinking. The optimization goal is that the directional coefficient of 0.8 degree beam is greater than 45dB.

By optimizing the shape of the reflector, we achieve the radiation pattern which meets 45dB as shown in Fig. 13.

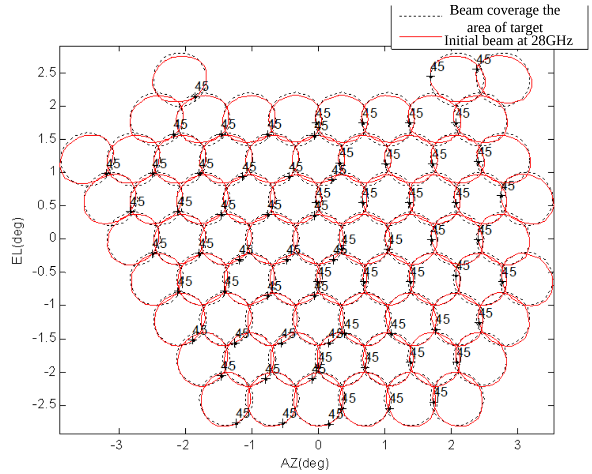

Fig. 12. Isoline pattern of the initial beam at the frequency of 28GHz.

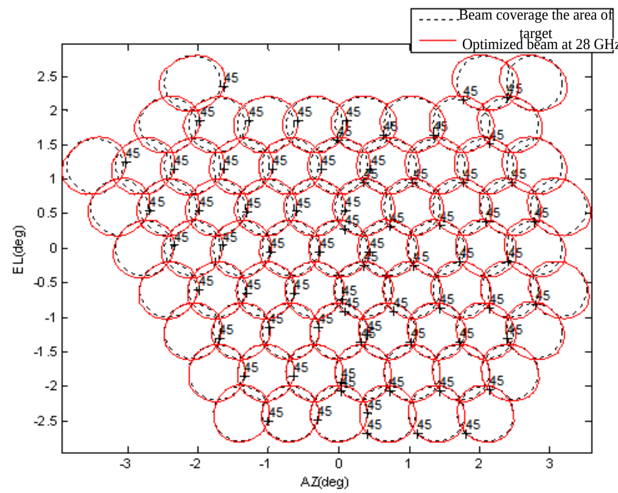

Fig. 13. Isoline pattern of the optimized beam at the frequency of 28GHz.

VI. CONCLUSION

An innovative MLFMM-DBPO approach for calculating the radiation pattern of the dual reflector antenna is proposed in this work. The new method reduces the computational complexity and expedites the simulation of antenna with DBPO fundamentally. It is significant for optimizing the shape of large aperture antenna and analyzing the radiation of large electrical objects, such as the satellite antenna. According to the numerical results, the new algorithm is more efficient than traditional DBPO with encouraging accuracy.

ACKNOWLEDGMENT

This work was supported in part by Natural Science Foundation of 61701232, 61431006, 61771246, Jiangsu Province Natural Science Foundation of BK20170854, the China Postdoctoral Science Foundation of 2017M620861.

The Authors are with the Department of Communication Engineering, Nanjing University of Science and Technology, Nanjing 210094, China. (E-mail: zihe@njust.edu.cn).

REFERENCES

[1] I. Aghanejad, H. Abiri, and A. Yahaghi, "Design of high-gain lens antenna by gradient-index metamaterials using transformation optics," *IEEE Transactions on Antennas & Propagation*, vol. 60, pp. 4074-4081, 2012.

[2] D. W. Boeringer and D. H Werner, "Particle swarm optimization versus genetic algorithms for phased array synthesis," *IEEE Transactions on Antennas and Propagation*, vol. 52, pp. 771-779, 2004.

[3] D. Pozar and D. Schaubert, "Scan blindness in infinite phased arrays of printed dipoles," *IEEE Transactions on Antennas and Propagation*, vol. 32, pp. 602-610, 1984.

[4] A. Molaei, J. H. Juesas, and W. J. Blackwell, "Interferometric sounding using a metamaterial-based compressive reflector antenna," *IEEE Transactions on Antennas & Propagation*, vol. 66, pp. 2188-2198, 2018.

[5] M. Albani, G. L. Cono, and R. Gardelli, "An efficient full-wave method of moments analysis for RLSA antennas," *IEEE Transactions on Antennas & Propagation*, vol. 54, pp. 2326-2336, 2006.

[6] C. H. Schmidt and T. F. Eibert, "Multilevel plane wave based near-field far-field transformation for electrically large antennas in free-space or above material halfspace," *IEEE Transactions on Antennas and Propagation*, vol. 57, pp. 1382-1390, 2009.

[7] T. F. Eibert and C. H. Schmidt, "Multilevel fast multipole accelerated inverse equivalent current method employing rao-wilton-glisson discretization of electric and magnetic surface currents," *IEEE Transactions on Antennas and Propagation*, vol. 57, pp. 1178-1185, 2009.

[8] F. T. Wu, "Design of a new millimeter wave paraboloidal reflector antenna using MLFMM," *IEEE Transactions on Antennas and Propagation*, 2014.

[9] Z. Zhao, L. Li, and J. Smith, "Analysis of scattering from very large three-dimensional rough surfaces using MLFMM and ray-based analyses," *IEEE Antennas & Propagation Magazine*, vol. 47, pp. 20-30, 2005.

[10] M. Chen, R. S. Chen, and X. Q. Hu, "Augmented MLFMM for analysis of scattering from PEC object with fine structures," *Applied Computational Electromagnetics Society Journal*, vol. 26, pp. 418-428, 2011.

[11] T. F. Eibert, "Modeling and design of offset parabolic reflector antennas using physical optics and multilevel fast multipole method accelerated method of moments," *IEEE Multitopic Conference*, 2006.

[12] A. Miura and Y. Rahmat-Samii, "Spaceborne mesh reflector antennas with complex weaves: Extended PO/periodic-MoM analysis," *IEEE Trans. Antennas Propag.*, vol. 55, pp. 1022-1029, 2007.

[13] M. Ariasacuna and T. Jost, "Physical optics analysis of the radiation pattern of an antenna mounted on an aircraft," *2015 9th European Conference on Antennas and Propagation (EuCAP)*, 2015.

[14] O. Borries, B. J. Dammann, E. Rgensen, et al., "Reflector antenna analysis using physical optics on graphics processing units," *The 8th European Conference on Antennas and Propagation (EuCAP 2014)*, 2014.

[15] C. Letrou and A. Boag, "Generalized multilevel physical optics (mlpo) for comprehensive analysis of reflector antennas," *IEEE Transactions on Antennas and Propagation*, vol. 60, pp. 1182-1186, 2012.

[16] Y. An, D. Wang, and R. Chen, "Improved multilevel physical optics algorithm for fast computation of monostatic radar cross section," *IET Microwaves Antennas & Propagation*, vol. 8, pp. 93-98, 2014.

[17] D. P. Xiang and M. M. Botha, "Acceleration of multiple reflection physical optics scattering analysis with the MLFMM," *2016 10th European Conference on Antennas and Propagation (EuCAP)*, 2016.

[18] M. Roudstein, Y. Brick, and A. Boag, "Multilevel physical optics algorithm for near-field double-bounce scattering," *IEEE Transactions on Antennas & Propagation*, vol. 63, pp. 5015-5025, 2015.

[19] D. P. Xiang and M. M. Botha, "Acceleration of multiple reflection physical optics scattering analysis with the MLFMM," *European Conference on Antennas & Propagation*, 2016.

[20] F. T. Wu, "Design of a new millimeter wave paraboloidal reflector antenna using MLFMM," *Proceedings of 2014 3rd Asia-Pacific Conference on Antennas and Propagation*, 2014.

[21] J. Cao, S. F. Tao, and R. S. Chen, "An efficient solution for volume integral equation based on meshfree scheme," *IEEE Antennas & Wireless Propagation Letters*, vol. 14, pp. 1618-1621, 2015.

[22] D. Z. Ding, R. S. Chen, and Z. H. Fan, "A novel hierarchical two-level spectral preconditioning technique for electromagnetic wave scattering,"

IEEE Transactions on Antennas & Propagation, vol. 56, pp. 1122-1132, 2008.

[23] J. Yan, J. Hu, and Z. Nie, "Calculation of the physical optics scattering by trimmed NURBS surfaces," *IEEE Antennas & Wireless Propagation Letters*, vol. 13, pp. 1640-1643, 2014.

Jun Li was born in Taizhou, China. He received the B. S. degree in Optical Engineering from the School of Electrical Engineering and Optical Technique, Zijin College of Nanjing University of Science and Technology, Nanjing, China, in 2013. He is currently pursuing his Ph.D. degree in Electronic Engineering at Nanjing University of Science and Technology.

The interest of his research are about antennas, high frequency method and computational electro-magnetics.

Chunbang Wu received the B.S. degree in Radio Propagation and Antenna of Wuhan University in 1992. He received the Master's degree in Insitut national de polytechnique-Toulouse. He mainly researches in space antenna technology and satellite payload technology.

Sparse Representation of Targets with Mixed Scattering Primitives

John Lee, Peter J. Collins, and Julie Ann Jackson

Department of Electrical and Computer Engineering
Air Force Institute of Technology, Dayton, OH 45433 USA
John.Lee.Ctr@afit.edu, Peter.Collins@afit.edu, Julie.Jackson@afit.edu

Abstract **─** A combination of two scattering primitives – wedge diffraction primitives and isotropic point scatterers – is used to reconstruct far-field monostatic scattering patterns of several target geometries and addresses shortcomings of traditional approaches that only use a single type of primitive (e.g., approximations in analytic solutions, slow convergence). An l_1-norm minimization technique is applied to determine a set of weights for the point scatterers. We show that combining these two types of primitives yields better reconstruction performance than when each primitive type is used individually.

Index Terms **─** Geometric Theory of Diffraction (GTD), l_1-norm minimization, Radar Cross Section (RCS), scattering primitives, sparse representation, Uniform Theory of Diffraction (UTD).

I. INTRODUCTION

It is well known that far-field scattering from a complex geometry can be estimated by decomposing the target into simple scattering primitives and summing their individual responses. Reconstruction of electromagnetic field quantities with isotropic point scatterers (IPSs) is a fundamental principle in SAR and ISAR processing [1]. The use of non-isotropic scattering primitives has also been investigated in [2,3]. Moreover, in [4], a dense array of IPSs is used as a part of an overcomplete dictionary. Sparse representations enable discrimination of target returns from nuisance returns that can arise from the measurement process.

In this work, we also seek to reduce the number of scattering centers required by introducing a wedge diffraction primitive (WDP) derived from GTD/UTD theory. We use the WDP to capture known scattering mechanisms based on the target's far-field pattern and allow the IPSs to recover the remaining coherent differences. We limit the analysis of this approach to planar cuts of 2D geometries and compare the results to reference data generated by a 3D Method of Moments (MoM) code. A normalization factor is applied to translate 2D echo width predictions to 3D RCS.

The use of multiple primitive types is also considered under the context of compressive sensing (CS). The theory states that the number of measurements required to successfully recover the sparse representation of a far-field pattern (via Basis Pursuit or other l_1-norm minimization algorithms) decreases substantially (even below the Nyquist sampling rate) as signal sparsity increases [5]. We posit that the sparsity of the far-field pattern representation can be improved by using WDPs to capture diffraction behavior and IPSs to capture the remaining difference between the diffraction contributions and the original far-field pattern. For example, a large portion of the monostatic response from a 2D flat plate can be accurately represented with two WDPs located at the ends of the plate. In contrast, a solution with two IPSs can only capture the specular response and would require significantly more points to accurately reconstruct the sidelobes of the monostatic return.

While sparsi ty can be satisfied, the efficacy of this technique as an application for CS is also dependent on the bounds of the Restricted Isometry Property (RIP) of the measurement matrix [6]. Determining these bounds explicitly is an NP-hard problem, but numerical experiments can provide a cursory and empirical assessment of its performance.

In the following sections, we describe the theory behind reconstruction via scattering centers and describe the framework that was developed to perform the reconstruction with a mixed set of primitives. We then present two simple cases to validate our approach, discuss the implications of their results and describe additional areas of investigation.

II. SCATTERING CENTER THEORY

Consider a collection of spatially distributed scattering centers, each associated with a complex coefficient that modulates its magnitude and phase [7]. By adjusting the location and the complex value of each scattering center, the superposition of every scattering center's far-field response may yield a pattern that matches the far-field response of an arbitrary target

Submitted On: August 29, 2019
Accepted On: March 26, 2020

geometry. This concept is illustrated in Fig. 1 (a) and concisely summarized as:

$$S_{IPS}^{pred}(k,\hat{\mathbf{r}})=\sum_{n=1}^{N}\gamma_n\, e^{-j2k\hat{\mathbf{r}}\cdot\mathbf{r}'_n}, \tag{1}$$

where S_{IPS}^{pred} is the far-field value synthesized with the wavenumber k and observed from direction $\hat{\mathbf{r}}$. S_{IPS}^{pred} is determined by the summation of N IPSs that are located at $\mathbf{r}'_n$ and modulated by the complex coefficient γ_n. The components of γ_n control the magnitude and phase delay applied to the IPSs, while the operating frequency and the locations of the scattering centers with respect to the phase origin affect the exponential term in (1) and alters the phase oscillation rate of the far-field pattern.

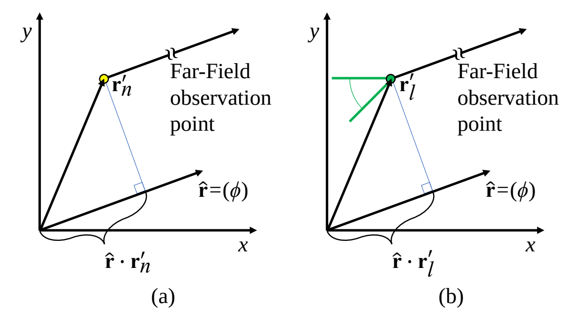

Fig. 1. Far-Field approximation of a (a) IPS and (b) WDP.

WDPs, shown in Fig. 1 (b), are coherently summed together in a similar fashion as IPSs to generate far-field patterns. From [8], UTD diffraction coefficients reduce to GTD coefficients when the surfaces of the wedge are flat and the observation angles are not in the transition regions near the shadow boundaries. We implement 2D WDPs as:

$$D^{s,h}(\phi,m)=\frac{-e^{j\pi/4}\sin(\pi/m)}{2m\sqrt{2\pi k}}\left[\left(\frac{1}{\cos\frac{\pi}{m}}\right)\mp\left(\frac{1}{\cos\frac{\pi}{m}-\cos\frac{2\phi}{m}}\right)\right], \tag{2}$$

where $m=(2\pi\text{-}\alpha)/\pi$, α is the wedge angle and ϕ is the monostatic observation angle. In the second term between the brackets, the negative term corresponds to the soft polarization, while the positive term corresponds to the hard polarization (in our case, θ and ϕ polarization, respectively). This 2D analytic solution assumes that the diffraction edge is always aligned along the z-axis and extends towards infinity. The RCS of a finite wedge of width w can be determined by multiplying the 2D echo width by $2\pi w^2/\lambda$, where wavelength $\lambda=2\pi/k$. The diffraction coefficient $D^{s,h}$ replaces the IPS coefficient γ_n in (1) and yields:

$$S_{WDS}^{pred}(k,\hat{\mathbf{r}})=\sum_{l=1}^{L}D_l^{s,h}\, e^{-j2k\hat{\mathbf{r}}\cdot\mathbf{r}'_l}, \tag{3}$$

to generate the far-field monostatic backscatter of the L diffracting wedges.

We note that the formulation in (2) is valid for wedge angles of up to 180° and does not address dihedral effects. Moreover, the scattering pattern arising from WDPs exhibit asymptotic behavior for monostatic angles that are normal to the faces of the wedge due to their vicinity to the shadow boundaries. These singularities occur in pairs for finite length wedges and additional considerations need to be made when geometries contain dihedral or concave regions.

III. OPTIMIZATION FRAMEWORK

We use the IPS and WDP formulations to estimate a solution S_{FF}^{est} for S_{FF}^{ref} by considering,

$$\begin{aligned} S_{FF}^{ref}&\approx S_{FF}^{est}=S_{WDS}^{pred}+\Delta p\\ &=S_{WDS}^{pred}+\left(S_{FF}^{ref}\text{-}S_{WDS}^{pred}\right)\\ &=S_{WDS}^{pred}+S_{IPS}^{pred}, \end{aligned} \tag{4}$$

where S_{WDS}^{pred} utilizes a priori information about the geometry to generate a coarse estimate of S_{FF}^{ref} and the coherent difference Δp is estimated with S_{IPS}^{pred}. An optimization framework, depicted in Fig. 2, was designed to determine S_{WDS}^{pred} in a preprocessing stage and S_{IPS}^{pred} with a sparse optimization stage.

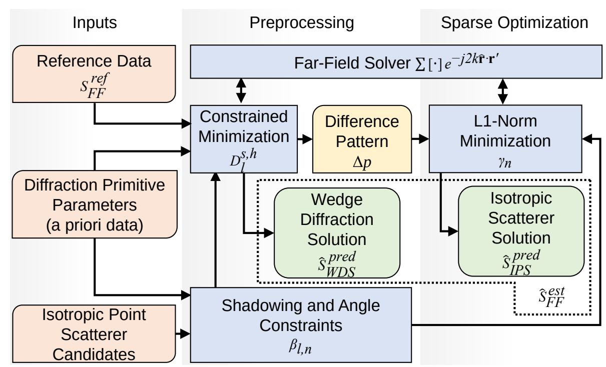

Fig. 2. Optimization framework.

The framework was generalized to use a constrained minimization routine to estimate appropriate parameter values for multiple types of non-isotropic scattering primitives (including the WDP utilized in this study). We note that the determination of $\mathbf{r}'_l$ and the dependent variables of $D_l^{s,h}$ in (3) can be a non-trivial problem with many local minima, especially when a priori information is limited. Because our investigation is focused on the feasibility of reducing the number of IPSs, we bypass the constrained minimization in these experiments and provide parameter values for the WDPs based on a priori knowledge of the scattering geometry as inputs instead.

The preprocessing stage synthesizes a far-field pattern from the WDPs and applies a global phase shift to the prediction that best matches the reference data. This is a necessary step in the event that the reference data and WDP prediction from the analytic geometry have different phase origins. The phase-shifted WDP solution is then coherently subtracted from the S_{FF}^{ref} to yield Δp.

Shadowed regions are also determined in the preprocessing stage of the framework to prevent WDPs and IPSs from radiating through the boundaries of the target geometry. This is performed by tracing a vector from each primitive and scattering center to all far-field observation points and determining whether the ray intersects a facet of the geometry [11].

Modifications to support shadowing and the phase shift of the WDP solution augment the model in (4) with additional modulation terms such that,

$$\begin{aligned}\hat{S}_{FF}^{est}(k,\hat{\mathbf{r}}) &= \hat{S}_{WDS}^{pred} + \hat{S}_{IPS}^{pred} \\ \hat{S}_{FF}^{est}(k,\hat{\mathbf{r}}) &= \sum_{l=1}^{L} \beta_l \, e^{j\psi} S_{WDS}^{pred} + \sum_{n=1}^{N} \beta_n \, S_{IPS}^{pred} \\ &= \sum_{l=1}^{L} \beta_l D_l^{s,h} \, e^{-j(2k\hat{\mathbf{r}}\cdot\mathbf{r}_l' - \psi)} + \sum_{n=1}^{N} \beta_n \gamma_n \, e^{-j2k\hat{\mathbf{r}}\cdot\mathbf{r}_n'},\end{aligned} \tag{5}$$

where $\beta_{l,n}$ represent the shadowing and angle constraints applied to the WDSs and IPSs respectively and $e^{j\psi}$ represents the phase shift applied to the WDP solution.

In the sparse optimization stage, determining appropriate values of r_n' and γ_n in (1) often relies on l_1-norm minimization techniques such as Basis Pursuit DeNoising (BPDN) in [4]. We note that BPDN provides a solution that minimizes the sum of the magnitudes of the complex coefficients, whereas an l_0-norm minimized solution minimizes number of complex coefficients contributing to the solution (true sparsity). A solution arising from an l_1-norm minimization routine is a good approximation to the l_0-norm minimized solution when compressive sensing characteristics are met, namely that the basis set that is used to represent the signal satisfies the RIP. Again, determining adherence to the RIP can be computationally intractable for non-random matrices, therefore we proceed to apply this technique with the understanding that l_1-norm minimized solutions may not strictly be the sparsest solution. In our framework, the SPGL1 library was leveraged to perform the BPDN optimization [9].

We note that primitive-based approaches are popular because generating far-field scattering from the primitives is straightforward. This is a key benefit and allows the optimization routine to iterate more quickly than in alternative approaches [10].

IV. NUMERICAL EXPERIMENTS

We first apply our framework on a single flat plate, to demonstrate that the WDPs are implemented correctly and that BPDN can recover an adequate solution to Δp. Next, the framework is applied to an angled plate, which includes a dihedral response that cannot be captured with the WDPs and shall be recovered with the IPSs. Figure 3 illustrates the two test geometries that are used to validate our approach.

The flat plate geometry is a 1m x 0.1m plate with zero thickness, while the angled plate geometry consists of a 1m x 0.125m and a 0.5m x 0.125m plate joined at one end to form a 90° angle (the latter dimension of each geometry is used to translate 2D echo width to 3D RCS). While the flat plate has no thickness, two variations of the angled plate were generated: one with zero thickness and one with 0.01m thickness. The significance of the angled plate variations is discussed in Section IV-B.

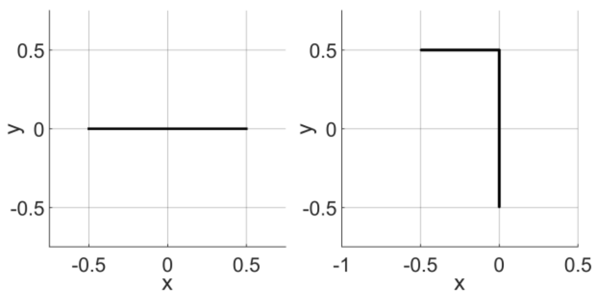

Fig. 3. Flat plate and angled plate test geometries.

For all cases, only the points on the z=0 plane were used since the far-field patterns were limited to the xy-plane (elevation θ=90°, azimuth ϕ=[0, 360°]) and there is no variation in either geometry in the z-direction. In all cases, we calculated the TM-polarized far-field backscatter response at 6 GHz (λ=0.05m), ensuring that both targets are electrically large and amenable to high frequency approximations. Several mesh discretizations were generated to assess sparsity requirements for a given BPDN solution. Lastly, the BPDN parameters for error tolerance and maximum iterations were set to 10^{-3} and 10^3, respectively, and were held constant over all experiments.

The reference data S_{FF}^{ref} in our comparisons was generated with a MoM-based code to mitigate any contribution from measurement artifacts. We utilize a relative error norm as our metric for comparison, calculated as $\sum_{k,\hat{\mathbf{r}}} \left\| S_{FF}^{ref} - \hat{S}_{FF}^{est} \right\|_2 / \left\| S_{FF}^{ref} \right\|_2$, where $\|\cdot\|_2$ is the l_2-norm.

A. Flat plate

Figure 4 illustrates our results from the flat plate geometry and compares the reference data against our method: the top plot compares the reference data S_{FF}^{ref} against the diffraction solution from the preprocessing stage $\hat{S}_{WDS}^{pred}$ as well as the combined solution $\hat{S}_{FF}^{est} = \hat{S}_{WDS}^{pred} + \hat{S}_{IPS}^{pred}$; the middle plot illustrates the performance of the sparse optimization stage by comparing the IPS solution $\hat{S}_{IPS}^{pred}$ with the difference pattern Δp that the optimization attempts to recover; finally, the bottom plot depicts the coherent difference between S_{FF}^{ref} and $\hat{S}_{FF}^{est}$.

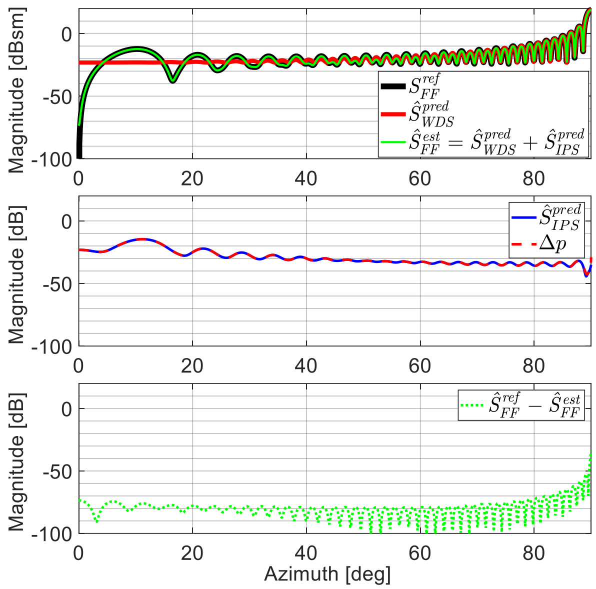

Fig. 4. Reference, WDP and IPS solutions for a flat plate (magnitude). Discrepancies between the reference and WDP solution (top) are corrected with an IPS solution (middle) to yield low reconstruction error (bottom).

$\hat{S}_{WDS}^{pred}$ was generated by defining two WDPs at the ends of the plate with α=0°. The singularities from each primitive sum to generate the specular lobe at ϕ=90°. We observe that the diffraction solution compares well with the reference data until the monostatic angle approaches the grazing angle of the flat plate (a known deficiency in GTD analytic solutions). The coherent difference from the preprocessing stage stays largely within the -20 and -40 dB range and yields a relative error of 0.0731.

After $\hat{S}_{WDS}^{pred}$ is generated, Δp is supplied to BPDN to synthesize $\hat{S}_{IPS}^{pred}$. The result of the sparse optimization stage shows a well-converged solution and has a coherent difference that is largely below -60 dB. When the WDP and IPS solutions are combined to yield $\hat{S}_{FF}^{est}$, we see overlay agreement with S_{FF}^{ref}. The combined solution achieves a relative error of 0.0011.

In contrast to our combined method, traditional scattering center reconstruction of far-field data utilizes IPSs exclusively to reconstruct the reference data rather than the delta pattern. We can assess the efficacy of the traditional approach by calculating the relative error as a function of the number of IPSs used to perform the reconstruction, as shown in Fig. 5. Using a λ/3 sampling to generate the IPSs candidates provides N=61 points. We see that both methods require all points to achieve the lowest errors, and the traditional method achieves a relative error of 0.0019, compared to 0.0011 when the combined method is used (the WDP solution does not vary as a function of the number of IPSs).

We also observe that when scattering centers with the smallest magnitudes are removed from contributing to the far-field pattern, the error of the traditional approach increases more quickly than the combined approach. In this example, the traditional approach exceeds the error of the WDP solution when fewer than N=60 points are used for the reconstruction.

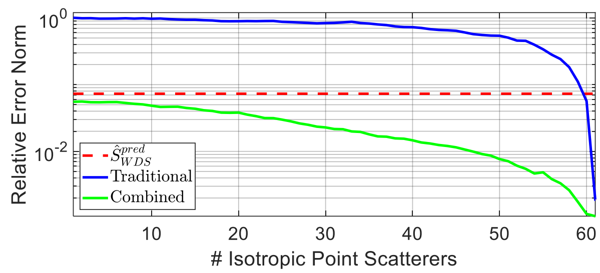

Fig. 5. Relative error norm of the flat plate.

These results indicate that a solution generated from a combination of WDPs and IPSs can achieve a more accurate reconstruction than either of the two separately. Moreover, for any desired level of error, the combined solution is sparser than the traditional method.

B. Angled plate

The angled plate geometry provides a more challenging far-field pattern to reconstruct than the flat plate. In addition to the flat plate responses, a strong dihedral response will occur in the far-field azimuth sector ϕ=(180°, 270°). Knowing that the current implementation of WDPs cannot reconstruct the dihedral response, we limit their contributions to angles exclusive of the dihedral sector via β_l in (5).

We note that even with the applied angle constraints, the WDPs may be inaccurate outside of the dihedral region, as well. According to [12], UTD WDPs fail near the shadow boundaries on concave shapes due to the fact that one of the WDPs is shadowed by obstructing geometry. The authors propose a separate type of diffraction coefficient to address dihedral effects by tracking rays that have multiple diffraction and reflection interactions on the target. Without introducing a third type of scattering center into the framework, we apply two additional WDPs located on the shared edge of the two plates (both with α=0°). This is analogous to two independent flat plates, where the additional WDPs complement the primitives on the open edges of the angled plate and compensate for the singularities that arise from those primitives. In total, five WDPs are used: two for each flat plate and one for exterior corner of the angled plate and with α=90°. This arrangement yields a good approximation when compared to the reference data. The relative error norm over the far-field sector where the WDP solution is valid was calculated to be 0.0992 and is similar to the relative error norm achieved by the WDP solution for the flat plate geometry.

We note that IPSs will also encounter issues in pattern reconstruction of the angled plate due to the dihedral sector. We observed that the IPSs on a zero-thickness angled plate failed to generate an adequate reconstruction since there is a large contrast in the far-field response of the dihedral and non-dihedral regions. Implementing a finite thickness model, shown in Fig. 6, and enforcing shadow boundaries mitigated these effects: an optimization of the zero thickness geometry resulted in an error of 0.7210, while the finite thickness geometry achieved an error of 0.0477.

However, even with the finite thickness geometry, additional non-physical aberrations are evident in the solution. We can observe the source of these errors by considering the angle sectors where each IPS contributes to the far-field. These sectors are discretized and plotted as vectors in Fig. 6.

Fig. 6. Active IPSs for ϕ=[0°, 270°] (red vectors) and ϕ=[270°, 360°] (green vectors).

The figure indicates that there are IPSs located in the interior region of the angled plate that contribute to both the dihedral and non-dihedral sectors of the far-field response. Moreover, the number of interior points contributing to the non-dihedral sector varies as the shadow boundary sweeps across the interior sector of the angled plate from ϕ=[116°,180°] and [270°, 296°]. This variation causes the discontinuities in the far-field pattern shown in Fig. 7 and we see that the severity of the discontinuities decrease when the rate of variation decreases, namely when angle approaches either of the normal incident angles (ϕ=180° and 270°).

If the IPSs from the finite thickness model are used in the proposed method to reconstruct Δp for the entire azimuth range ϕ=[0°, 360°], these discontinuities significantly degrade the reconstruction in the regions where the $\hat{S}_{WDS}^{pred}$ is already very good: under this arrangement, the method achieves a relative error norm of 0.0964 (0.0905 for λ/4, 0.0830 for λ/5). While it is a slight improvement over the solution generated by WDPs alone, it does not provide a better solution than the traditional method. We speculate that, in addition to the discontinuities, the dynamic range of the delta pattern increases because the WDPs are restricted from contributing to the dihedral sector of S_{FF}^{ref}. These effects ultimately make Δp more difficult to reconstruct with IPSs.

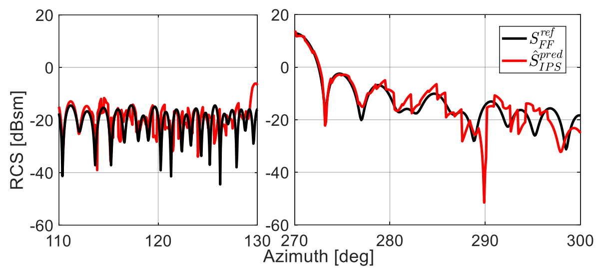

Fig. 7. Discontinuities in non-dihedral sector of IPS solution due to interior IPS contributions.

As an alternative, we enforce additional constraints on the finite thickness model via β_n such that the interior and exterior IPSs only contribute to the non-dihedral and dihedral sectors, respectively. Using this strict separation, $\hat{S}_{FF}^{est}$ from the combined method yields an improved relative error norm of 0.0238 and exceeds the performance of the traditional method. The results of this experiment are shown in Fig. 8.

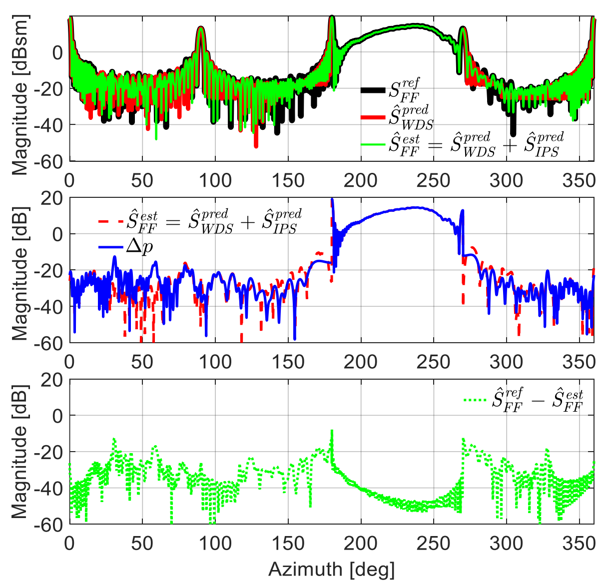

Fig. 8. Reference, WDP and IPS solutions for an angled plate (magnitude only). Discrepancies between the reference data and WDP solution (top) are corrected with an IPS solution (middle) to yield low reconstruction error (bottom).

The figure also clearly shows the large dynamic range of Δp where much of the dihedral sector stays above 0 dB and non-dihedral sector stays largely below -20 dB. With our proposed method of synthesizing $\widehat{S}_{FF}^{est}$, the errors achieved mostly fall below -20 dB.

Mirroring the analysis performed on the flat plate, we assess the trade between relative error norm and the number of IPSs used in the reconstruction of S_{FF}^{ref} and Δp, shown in Fig. 9. We note that the figure includes an additional dataset to show that, while the strict separation of the contributions of the inner IPSs to the dihedral sector and the outer IPSs to the non-dihedral sector was an effective strategy for synthesizing Δp, it was not effective when the IPSs were used to reconstruct S_{FF}^{ref}. We speculate that the configuration that enforces strict separation does not provide an adequate number of IPSs to generate the narrow lobes that are present near the edges of the dihedral region in the far-field reference pattern. Conversely, the more permissive shadowing scheme provides enough of these point scatterers to generate narrow (but discontinuous) peaks to match the far-field reference pattern well, but detrimentally impacts the solution when they are used to match Δp (which has lower and wider lobes).

We also observe a discontinuity in the solutions that rely exclusively on IPSs whereas the flat plate tests exhibited a monotonically decreasing error. This is because the magnitudes of the coefficients supporting the dihedral sector are significantly higher than those supporting the non-dihedral sector. For example, in the test case where Δp was recovered via IPSs only, the removal of the lowest magnitude coefficients from reconstruction will incrementally degrade the non-dihedral sector and only after the 39th largest coefficient is removed will the dihedral reconstruction degrade.

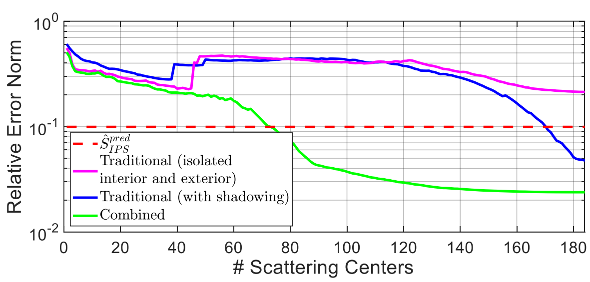

Fig. 9. Relative error norm of the angled plate.

Overall, the results are consistent with those in the flat plate experiment. That is, the traditional approach that utilizes only IPSs to reconstruct far-field reference data is unable to reach the error levels that are achieved with the proposed approach. Moreover, if the smallest (in magnitude) non-zero coefficients are discarded from the reconstruction, the degradation of the solution from the proposed method is more gradual than the traditional method.

Our numerical experiments are summarized in Table 1. We see with both geometries that a lower error is achieved when combining a WDP solution with an IPS solution to the delta pattern instead of the relying exclusively on WDPs or IPSs to reconstruct the far-field data. In the case of the angled plate, the result required manually setting boundaries on the range of angles where each primitive type contributes to the far-field pattern. Nonetheless, this is a valuable insight—if the primary goal is to find a compact representation of far-field data, this approach would prove to be very useful. With the proposed method, we can achieve a lower error with approximately the same number of point scatterers (WDPs and IPSs). Likewise, we have solutions that degrade more slowly with respect to how many IPSs are used to reconstruct the pattern when the IPSs are applied to a delta pattern rather than the far-field data.

Table 1: Relative error and (total point scatterer count) of $\lambda/3$ discretized geometries

	Flat Plate	Angled Plate*
WDS Only	0.0731 (2)	0.0992 (5)
IPS Only	0.0019 (61)	0.0477 (184)
Combined	0.0011 (63)	0.0238 (189)

* WDS case evaluated for non-dihedral sector only.

V. SPARSE RECONSTRUCTION CONSIDERATIONS FOR COMPRESSIVE SENSING

In addition to investigating the reconstruction accuracy of the proposed method, we seek to understand how well IPSs perform as a sparse basis in the context of CS. With both the flat plate and angled plate geometries, we tested for solution convergence and robustness.

Figure 10 depicts the results from multiple discretizations of the flat plate geometry and how their solutions degrade as the weakest scattering centers are incrementally removed from the solution.

CS literature states that the recovery of signal is robust to noise and reconstruction accuracy should degrade gracefully with a given basis set due to the RIP (more specifically, the Null Space Property) [13]. We can see that the IPS basis can used to reconstruct Δp in the proposed method and reconstruct S_{FF}^{ref} in the standard method. We noted previously that the degradation of $\widehat{S}_{FF}^{est}$ in the proposed method is more gradual than the far-field reconstruction in the standard method and we see that this remains true for other discretizations as well. However, the data also indicates that the solutions generated by the BPDN are not optimally sparse. The delta pattern and far-field pattern do not vary with respect to discretization, yet the number of IPSs required to reconstruct those patterns does vary with respect to discretization.

We also observe that the numbers of candidate IPSs are N=61, 81 and 101 for $\lambda/3$, $\lambda/4$ and $\lambda/5$, respectively. At 6 GHz, the plate is 20 λ long and the solutions are effectively using all of the available scattering centers to determine a solution, even though it is known that a sparser solution exists (because the coarse discretizations are able to recover an equally accurate solution with fewer IPSs). While BPDN determines solutions with the smallest $\sum_n |\gamma_n|$, it does not guarantee a solution that minimizes the cardinality of γ unless other CS criteria are met. These findings suggest that a basis set from IPSs does not satisfy the RIP.

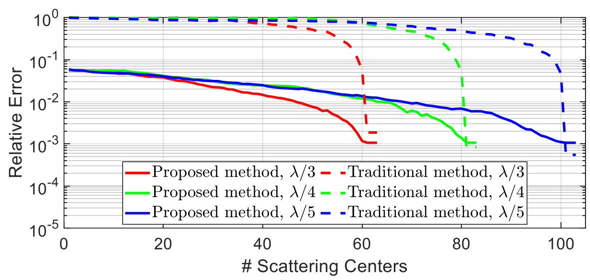

Fig. 10. Robustness of proposed and traditional method solutions for $\lambda/3$ to $\lambda/5$ discretizations of the flat plate.

A similar analysis is performed on the data for the angled plate dihedral region, depicted in Fig. 11. Again, the number of IPSs required to reach a given level of error depends on the number of available IPSs. The rate of degradation is different from the flat plate case, however: the presence of longer tails on the reconstructions with the proposed method suggest that they have converged and while they are not ideal and optimally sparse solutions, they seem to be sparser and more robust than the reconstructions with the traditional method.

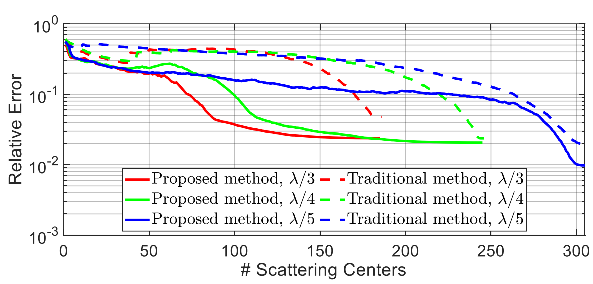

Fig. 11. Robustness of proposed and traditional method solutions for $\lambda/3$ to $\lambda/5$ discretizations of the angled plate.

These numerical experiments show that, while the technique is successful in generating point scatterer based (WDP and IPS) representations of the targets, there may be limited utility as a basis for compressive sensing applications. The results show empirically that when a sparse representation of the target is used to generate far-field patterns (the traditional approach), perturbations in the sparse representation will introduce excessively large errors for the purpose of interpolation and extrapolation. The sparsity is slightly improved when IPS are employed to reconstruct delta patterns (the proposed approach), but their efficacy seems to be geometry dependent.

These initial results reveal areas that merit additional investigation. It would be prudent to integrate solutions for dihedral scattering mechanisms [14] into the framework which would allow the IPSs to recover a more simplified delta pattern. Additionally, we observed that the number of shadowed IPSs can vary rapidly and would introduce unwanted discontinuities in synthesized solution. Tapering or adjusting the angles that an IPS contributes to may address this issue and would improve how the IPSs perform on concave targets. Lastly, the optimization framework can be expanded to support multiple frequencies, multiple polarizations, non-planar observation geometries and bistatic quantities to possibly aid the convergence of the optimization routines and expand its applicability to a wider variety of test cases.

VII. CONCLUSION

Using WDPs in conjunction with IPSs to reconstruct far-field patterns shows merit in simple cases and when they are applied judiciously. In our numerical experiments, we show that this approach can reduce the overall number of scattering centers required to replicate the scattering response of a flat and a right-angled plate. We also observed that l_1-norm minimization techniques may have difficulty finding maximally sparse solutions when IPSs are used as a basis set. Despite this, synthesized solutions are more robust when they are used to reconstruct a coherent difference pattern rather than the far-field data.

ACKNOWLEDGMENT

The views expressed in this paper are those of the authors, and do not reflect the official policy or position of the United States Air Force, Department of Defense, or the U.S. Government.

REFERENCES

[1] M. A. Richards, J. A. Scheer and W. A. Holm, *Principles of Modern Radar: Basic Principles*. SciTech Publishing, Edison, NJ, 2010.

[2] J. A. Jackson, "Parametric models for signature prediction and feature extraction," invited paper, *Applied Computational Electromagnetics Society (ACES) Journal*, vol. 34, no. 2, pp. 258-260, 2019.

[3] J. Halman and R. J. Burkholder, "Sparse

expansions using physical and polynomial basis functions for compressed sensing of frequency domain EM scattering," *IEEE Antennas Wirel. Propag. Lett.*, vol. 14, pp. 1048-1051, 2015.
[4] B. Fischer, I. Lahaie, M. Hawks, and T. Conn, "On the use of basis pursuit and a forward operator dictionary to separate specific background types from target RCS data," *AMTA 36th Annual Meeting and Symposium*, pp. 85-90, 2014.
[5] S. Foucart and H. Rauhut, *A Mathematical Introduction to Compressive Sensing*. Springer, New York, 2013.
[6] E. J. Candes, J. Romberg, and T. Tao, "Robust uncertainty principles: Exact signal frequency information," *IEEE Trans. Inf. Theory*, vol. 52, no. 2, pp. 489-509, 2006.
[7] R. Bhalla, H. Ling, J. Moore, D. J. Andersh, S. W. Lee and J. Hughes, "3D scattering center representation of complex targets using the shooting and bouncing ray technique: a review," *IEEE Antennas and Propagation Magazine*, vol. 40, no. 5, pp. 30-39, Oct. 1998.
[8] D. A. McNamara, C. W. I. Pistorius, and J. A. G. Malherbe, *Introduction to The Uniform Geometrical Theory of Diffraction*. Artech House, Boston, MA, 1990.
[9] E. van den Berg and M. P. Friedlander, "Probing the Pareto frontier for basis pursuit solutions," *SIAM J. on Scientific Computing*, vol. 31, no.2, pp. 890-912, November 2008.
[10] I. J. Lahaie, S. M. Cossmann, M. A. Blischke, V. Way, and A. Arbor, "A model-based technique with l1 minimization for defect detection and RCS interpolation from limited data," *Applied Computational Electromagnetics Society (ACES) Journal*, vol. 28, no. 12, pp. 1171-1179, 2013.
[11] J. Tuszynski, "Triangle/ray intersection," *Mathworks File Exchange*. https://www.mathworks.com/matlabcentral/fileexchange/33073-triangle-ray-intersection
[12] T. Griesser and C. A. Balanis, "Dihedral corner reflector backscatter using higher order reflections and diffractions," *IEEE Trans. Antennas Propag.*, vol. 35, no. 11, pp. 1235-1247, 1987.
[13] Y. C. Eldar and G. Kutyniok, *Compressed Sensing: Theory and Applications*. Cambridge University Press, NY, 2012.
[14] J. A. Jackson, "Analytic physical optics solution for bistatic, 3D scattering from a dihedral corner reflector," *IEEE Trans. Antennas Propag.*, vol. 60, no. 3, pp. 1486-1495, Mar. 2012.

John Lee Received his B.S. in Electrical and Computer Systems Engineering from Rensselaer Polytechnic Institute in 2005 and his M.S. in Electrophysics from New York University Tandon School of Engineering in 2012. He is currently pursuing his Ph.D. in Electrical Engineering at the Air Force Institute of Technology. He has previously worked for The Boeing Company in Southern California and is currently a Member of the Research Staff at Riverside Research in New York, NY. His current research interests are focused on electromagnetic applications of compressive sensing, RCS modeling, analysis and optimization.

Peter J. Collins is a Professor of Electrical Engineering with the Air Force Institute of Technology, Department of Electrical and Computer Engineering, Wright-Patterson AFB, OH. Collins' research interests are in the areas of low observables, electromagnetic materials design, and remote sensing along with the underlying foundational disciplines of electromagnetic theory, computational electromagnetics, and signature metrology.

Collins is a Fellow of the Antenna Measurement Techniques Association (AMTA), Senior Member of the Institute of Electrical and Electronic Engineers (IEEE), and is author or co-author of over 90 technical papers, 2 book chapters, and 1 US Patent.

Julie Ann Jackson is an Associate Professor of Electrical Engineering at the Air Force Institute of Technology (AFIT), where she joined the faculty in 2009. She earned the B.S.E.E. degree from Wright State University, Dayton, OH, in 2002 and the M.S. and Ph.D. degrees from The Ohio State University, Columbus, OH, in 2004 and 2009, respectively. Her graduate studies were funded with fellowships from the National Science Foundation, the Dayton Area Graduate Studies Institute, The Ohio State University, and the Ohio Board of Regents. Jackson has held internships at the Air Force Research Laboratory, Alphatech, Inc., Jacobs Sverdrup, and Bell Laboratories. She is a Senior Member of the

IEEE, member of Eta Kappa Nu and Tau Beta Pi, and Chief Advisor for the Ohio Eta Chapter of Tau Beta Pi. Jackson was elected in 2018 to the IEEE AES Society Radar Systems Panel and serves on the technical program committees of the IEEE Radar Conference and the MSS Tri-Service Radar Conference. Jackson's contributions have been recognized with mulitple awards including the 2019 IEEE Fred Nathanson Memorial Radar Award, the Air University Civilian Quarterly Award in 2018, the Southwestern Ohio Council for Higher Education (SOCHE) 2016 Faculty Excellence Award, and the 2012 Air Force Science, Technology, Engineering, and Mathematics Award for Outstanding Scientist/Engineer, Junior Civilian. Her research interests are in radar signal processing and imaging and exploitation of RF signals.

A Novel Omnidirectional Circularly Polarized Pagoda Antenna with Four Shorting Pins for UAV Applications

Zheyu Li, Yongzhong Zhu*, Yu Shen, Xiaoyu Liu, and Guohao Peng

School of Information Engineering
Engineering University of PAP, Xi'an, Shanxi, 710086, P. R. China
lzyewe@163.com, *bsbs1980@sina.com, 348511372@qq.com, lxywjgd@163.com, 302662481@qq.com, bsbs1980@sina.com

***Abstract* -** A novel omnidirectional circularly polarized (CP) pagoda antenna with four shorting pins is presented. In this structure, four curved branches are utilized to generate horizontal polarization, while coaxial cable and four shorting pins produce vertical polarization. Omnidirectional CP radiation is achieved by combining the radiation from the branches and the shorting pins. The curved branches loaded with shorting pins reduce the size of the antenna and the antenna is loaded with the lower substrate with two coupling patches to improve the bandwidth. The novel pagoda antenna is fabricated and measured. Its final dimensions are $0.42\lambda_0$*$0.42\lambda_0$*$0.33\lambda_0$ (λ_0 is the free-space wavelength at operating frequency). The impedance bandwidth (S_{11}≤-10dB) is 0.53GHz and the axial ratio (AR) bandwidth (AR≤3dB) is 0.95GHz, which can be used for unmanned aerial vehicles' diagram transmission in China.

***Index Terms* -** Circularly polarized (CP), coupling patch, curved branch, omnidirectional antenna, shorting pin.

I. INTRODUCTION

Omnidirectional circularly polarized (CP) antennas have attracted more and more attention from experts and scholars due to they widely used in wireless communication, remote sensing and telemetry and satellite communication systems. Omnidirectional antenna can radiate electromagnetic wave in any direction in a plane, which is suitable for multipoint simultaneous communication and communication in uncertain position during movement. The CP antennas can accept arbitrary polarized wave, reduce multipath interference, and have high polarization isolation. Having both advantages of omnidirectional antenna and CP antenna, omnidirectional CP antenna can meet the requirements of accurate signal transmission of unmanned aerial vehicle (UAV) systems and be used as its image transmission antenna, which can effectively reduce the signal blind area and polarization interference.

In recent years, many methods of realizing omnidirectional CP antennas have been proposed, which can be roughly classified into three categories. The first method is circular polarized method of omnidirectional antenna that a circular polarizer is loaded outside the omnidirectional antenna. In [1], the omnidirectional CP antenna is realized by using the parallelepiped medium element with high dielectric constant to embrace around the coaxial probe. In [2], the inner conductor is fed, while the spiral groove is opened on the outer cylinder conductor. The second method is element combination [3-6], which uses the combination of CP antenna elements to achieve omnidirectivity. In [3], circular open rings loaded with parasitic rings are used as CP antenna elements, and they are combined around cylinder to attain omnidirectivity. In [4], a rectangular ring is used as a CP antenna element.

However, omnidirectional CP antennas realized by these two methods are generally large in size and have high profile, which is difficult to install on small and lightweight UAVs. In order to reduce the size and profile, a third method is proposed, which combines the antenna that generates the vertical polarized wave with the antenna that generates the horizontal polarized wave [7-15]. In [7], a broadband omnidirectional CP antenna was proposed, in which two sets of dipoles were used to generate omnidirectional CP waves. In [8], capacitive feeding is used to widen the bandwidth of the antenna. The antenna's profile is greatly reduced, but the radius is still large. In [9], planar sector-shaped endfire elements are used to realize omnidirectional circular polarization of the antenna, which further reduces the antenna profile. V-shaped slot on the same principle was used in omnidirectional CP antenna [10], which also makes the size of the antenna even smaller. The profile and radius of this kind of antenna are small, but the bandwidth is too narrow to meet the actual needs.

Based on the comparison with the antenna mentioned above, this paper proposes an omnidirectional CP antenna suitable for UAV image transmission system. The antenna's size is relatively small and has an adequate bandwidth to ensure the transmission of information. Coaxial cable and four shorting pins

Submitted On: December 9, 2019
Accepted On: February 23, 2020

are used to generate vertical polarized waves, while four curved branches are used to generate horizontal polarized waves. The structure of curved branches loaded with shorting pins are used to reduce the size of the antenna, and the dielectric substrates at the bottom with two ring patches are coupled to extend the bandwidth. Finally, the antenna's size is $0.42\lambda_0$*$0.42\lambda_0$*$0.33\lambda_0$. The impedance bandwidth of the antenna ($S_{11}\leq$-10dB) ranges from 5.56GHz to 6.09GHz, and the axial ratio (AR) bandwidth (AR≤3dB) is from 5.07GHz to 6.02GHz, effectively covering UAVs' diagram transmission frequency in China at 5.8GHz. The configuration, principles, simulation used by Ansoft high-frequency structure simulator (HFSS) and results of the antenna are described detailedly in the following sections.

II. ANTENNA CONFIGURATION

Figure 1 shows the configuration of omnidirectional CP pagoda antenna. It consists of three dielectric substrates with a thickness of 1mm, a radiant patch, a reference ground, four shorting pins and four ring patches. The radiation patch and ground plane are located on the upper surface of the upper substrates and the middle substrates respectively, the material of which is FR-4 with the permittivity of 4.4 and the loss tangent of 0.002. The radiation patch and ground plane each contains four curved branches in opposite direction connected by shorting pins at the end, which are commonly used to reduce the size of antenna. The coaxial cable is in direct contact with the radiation patch for feeding. The inner conductor of coaxial cable and shorting pins are both made of copper.

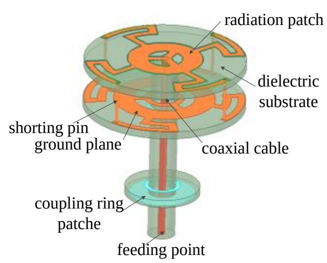

(a)

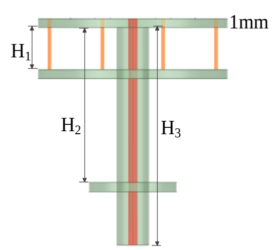

(b)

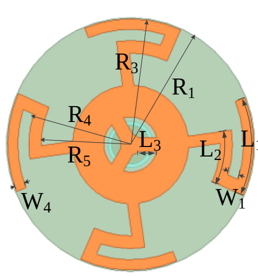

(c)

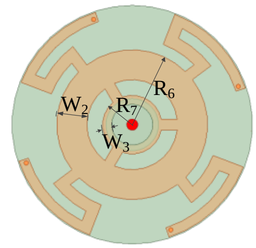

(d)

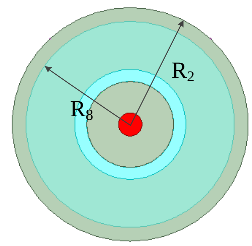

(e)

Fig. 1. Geometrical configuration of the proposed antenna. (a) Perspective view. (b) Side view. (c) Top view of the upper substrates. (d) Top view of the middle substrates. (e) Top view of the lower substrates.

The curved branches loaded with shorting pin reduce the size of the antenna, but the bandwidth is relatively narrow. In order to improve the bandwidth for better practicability, the antenna is loaded with the lower substrate with two ring patches on the upper surface and the lower surface respectively. The lower substrate with two ring patches acts as a choking coil, similar to a metal sleeve. Because it can be coupled with the radiation patch to enhance the radiation intensity, the lower substrate broadens both impedance bandwidth and AR bandwidth. The parameters of the antenna are listed as follows: R_1=11mm, R_2=5.1mm, R_3=10.9mm, R_4=9mm, R_5=8mm, R_6=6.9mm, R_7=2.7mm, R_8=4.5mm, W_1=1mm, W_2=2.75mm, W_3=0.82mm, W_4=0.9mm, L_1=8.74mm, L_2=5mm, L_3=3mm, H_1=4.65mm, H_2=17.09mm, H_3=24mm.

III. PRINCIPLE AND METHODOLOGY

For omnidirectional CP pagoda antenna is understand clearly, working principle and parameters analysis of the proposed antenna are discussed in this section.

A. Omnidirectional CP property

CP waves are composed of two orthogonal linearly polarized waves with a phase difference of 90°. According to the duality principle, the electric field ($\vec{E}$) in the far field generated by the magnetic currents on the pagoda antenna can be expressed as:

$$\vec{E} = \hat{\theta} E_\theta + \hat{\phi} E_\phi. \tag{1}$$

It is found that when there are more branches, omnidirectivity of the antenna is better, as shown in Fig. 2. And the operating frequency is reduced as the increase in the number of branches, which has the function of miniaturization, as shown in Fig. 3. However, considering the size of the antenna, four branches are finally chosen. The four branch elements are arranged in sequence and fed by coaxial cables, forming a clockwise current loop. The end of each branch element is connected to the ground plane by a shorting pin, that form a current path. According to the boundary condition, the clockwise current loop generates a vertical down magnetic pole ($\vec{J} = \vec{n} \times \vec{H}$), which forms a horizontal polarization component, the E_φ field. The radius of the current loop is R_1. The far field of the current loop E_φ can be expressed as [16]:

$$E_\varphi = \frac{[I] R_1 \omega \mu_0}{2r} J_1(\beta R_1 \sin\theta) \hat{\varphi}. \tag{2}$$

Where $[I]$ represents the magnitude of current on the loop, ω is the operating frequency, μ_0 is the free-space permeability, J_1 is Bessel's first order function, β is the propagation parameter of space and r is the distance between the antenna and the measuring point.

Vertical polarized waves are generated by coaxial cable and four shorting pins, which act as electrodes. What is more, the vertical polarized waves produced by the electrodes are omnidirectional. The height of the shorting pin can be seen as H_1. Its far field E_θ can be expressed as [16]:

$$E_\theta = j \frac{[I] H \omega \mu_0}{4\pi r} \sin\theta \ \hat{\theta}. \tag{3}$$

Based on (2) and (3), it is noted that as long as the current $[I]$ through coaxial cable, curved branch and shorting pin is uniform, there will be a 90° phase difference between the vertical polarized component and the horizontal polarized component. The CP radiation pattern will be generated when the magnitude of E_θ and E_ϕ are adjusted to be equal. As shown in the Fig. 4, it can be found that the current passing through does not change its direction in one time. Therefore, two polarization components exist 90° phase difference to each other in the far field. Due to the compact structure of the antenna, two polarization components have the same amplitude and orthogonal to each other in space at the same time. Finally, the omnidirectional CP pagoda antenna is realized in theory.

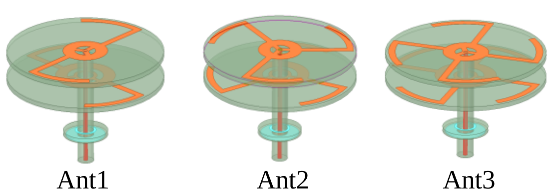

Fig. 2. Three improved prototypes of the proposed antenna.

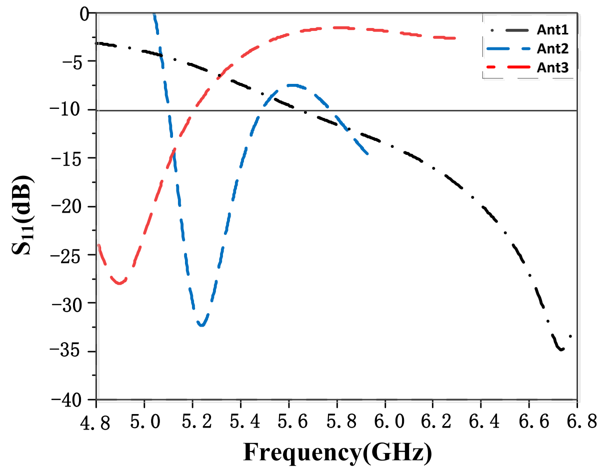

Fig. 3. Simulated $|S_{11}|$ of Ant 1, Ant 2 and Ant 3.

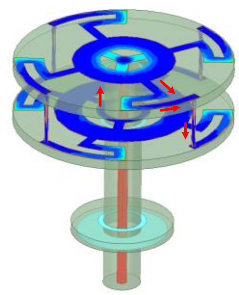

Fig. 4. Current distribution of the proposed antenna at 5.8GHz.

B. Parametric study and analysis

Curved branch can change the path of current, effectively reducing the size of the antenna. The length of the branches is approximately determined by:

$$\frac{R_6 \pi}{4} + L_2 + \frac{W_4}{2} + R_5 = \lambda. \tag{4}$$

Where λ is the operating wavelength. As shown in Fig. 5, the radius of the curved branch is much smaller than that of the straight branch by adjusting the width of the branches when the current passes through the same length.

The shorting pin at the end of the branch not only supports the upper and middle dielectric substrates, but also miniaturizes the antenna. The two ends of the radiation patch are open, and there must be zero potential points in the standing wave. Loading shorting pin at zero potential points, the original state of standing wave will be made from open circuit to short circuit state, equivalent to make $\lambda/2$ to $\lambda/4$ harmonic resonance. The antenna size (R) can be approximately calculated by [17]:

$$R = \frac{\lambda}{4} = \frac{c}{4 \times \sqrt{\varepsilon_{eq}} \times f}, \tag{5}$$

$$\varepsilon_{eq} = \frac{H_1 + H_2}{\frac{H_1}{\varepsilon_r} + \frac{H_2}{\varepsilon_{air}}}. \tag{6}$$

Where c is the speed of light in vacuum, and ε_{eq} is the equivalent dielectric constant of multilayered substrate. Figure 6 compares the *S* parameters of antenna with shorting pin and without shorting pin. As can be seen from Fig. 6, the impedance characteristic of the antenna with shorting pin is obviously better than that without shorting pin, and the resonant frequency of antenna reduces, thus achieving the miniaturization. Therefore, the antenna size is reduced due to the curved branch loaded with shorting pin.

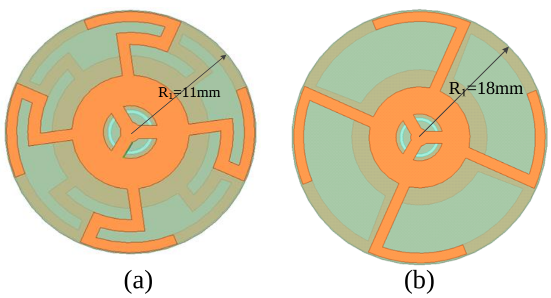

Fig. 5. Radius of (a) curved branch and (b) straight branch.

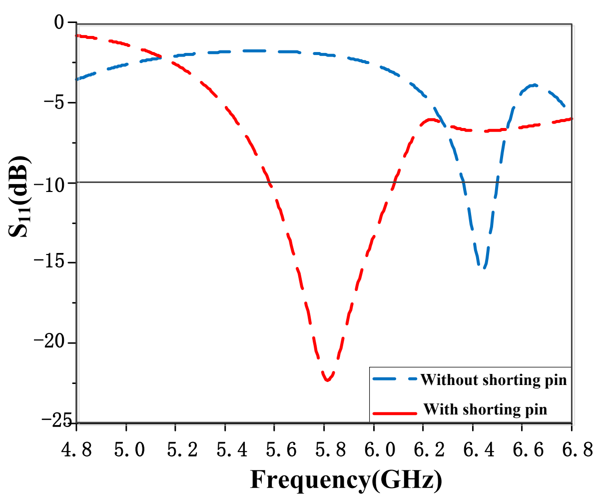

Fig. 6. Simulated $|S_{11}|$ of the proposed antenna with and without shorting pins.

The lower substrate with two coupling patches can adjust the resonance point and enlarge the bandwidth of the antenna. Figure 7 shows the comparison of *S* parameters and AR bandwidth of antennas with and without the coupling patches. It can be seen that the impedance bandwidth and AR bandwidth of the antenna both increase after the coupling patches loaded.

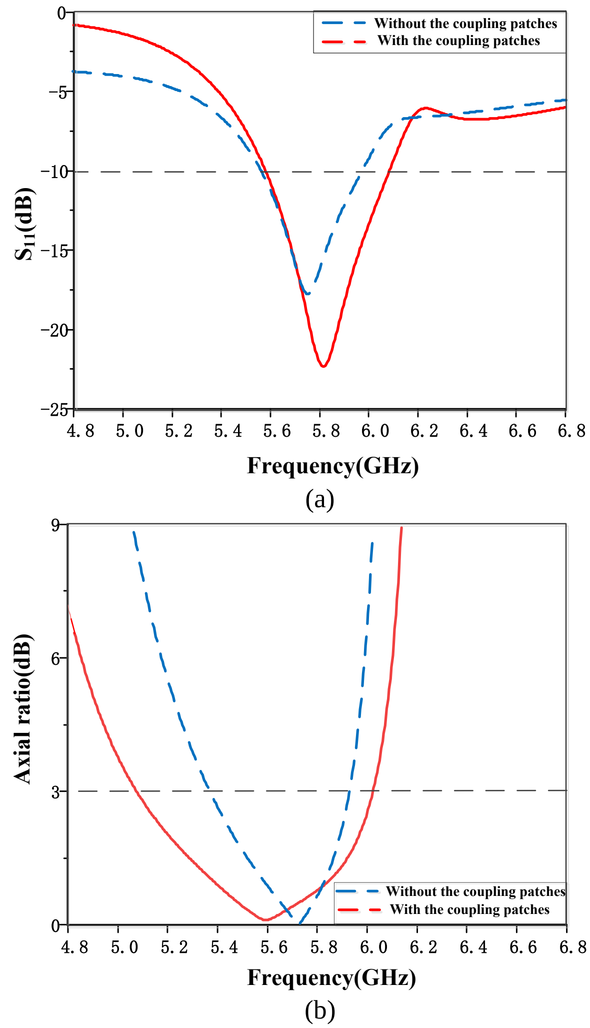

Fig. 7. Simulated (a) $|S_{11}|$ and (b) AR of the proposed antenna with and without coupling patches.

The coupling strength is affected by two factors [18], one is the distance between the upper substrate and the middle substrate H_1, the other is curved branch arc width of the radiation patch W_4. Figure 8 shows the influence of the distance H_1 on the operating frequency of the antenna. It can be seen from Fig. 8(a) that when the distance H_1 decreases, the resonant frequency of the antenna increases, while Fig. 8 (b) shows that AR points shift towards higher frequency. Figure 9 shows the effect of the width W_4. Figure 9 (a) shows that when W_4 decreases, the S-parameter curves of the antenna decrease while Fig. 9 (b) shows that the AR values have no obvious changes.

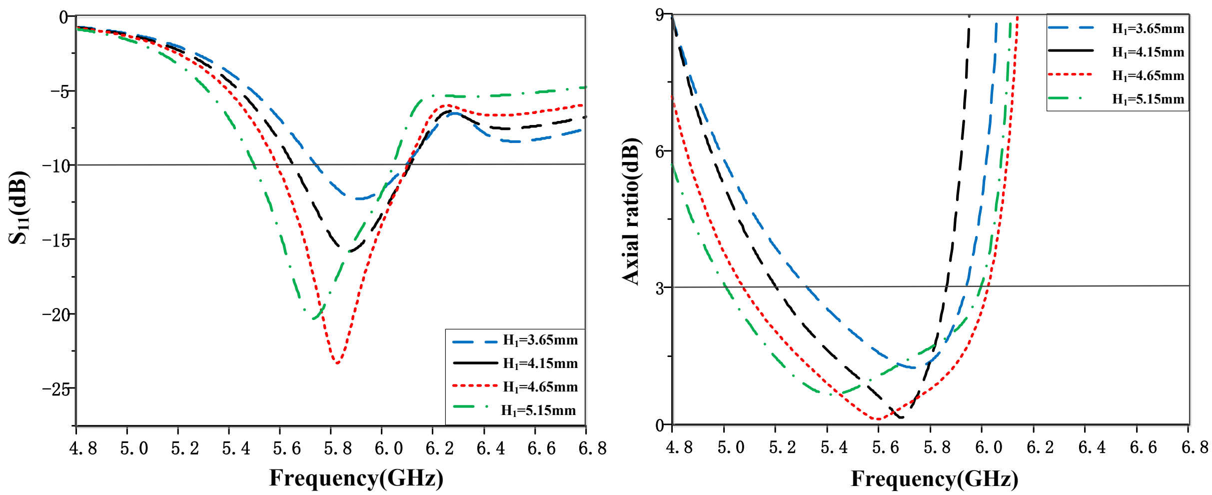

(a) (b)

Fig. 8. Simulated (a) $|S_{11}|$ and (b) AR of the proposed antenna with different H_1.

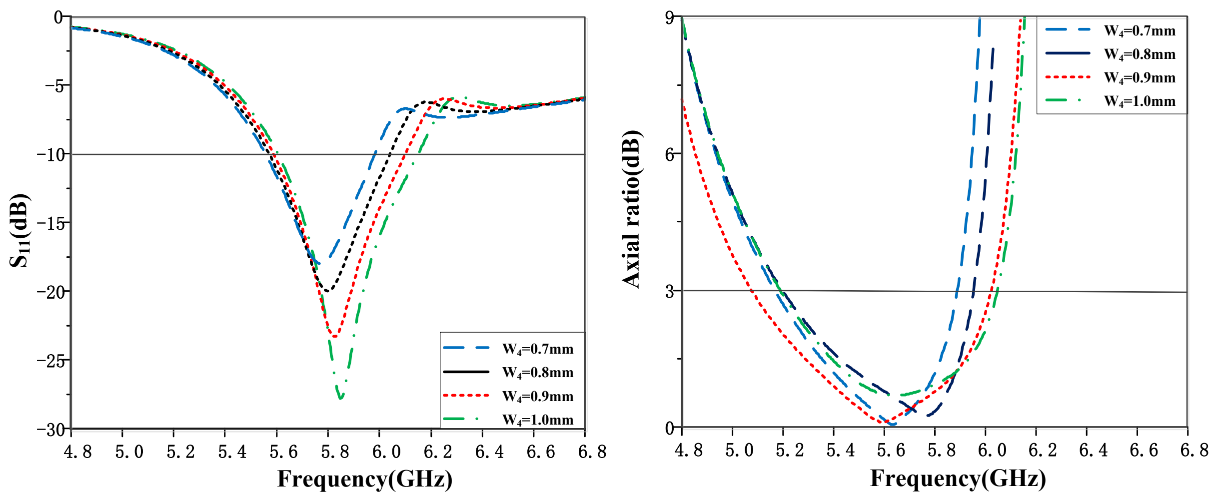

(a) (b)

Fig. 9. Simulated (a) $|S_{11}|$ and (b) AR of the proposed antenna with different W_4.

IV. EXPERIMENTAL RESULTS

In order to validate the proposed method, the antenna is fabricated, as shown in the Fig. 10. The antenna weighs only 4 grams, which makes it more suitable for UAVs diagram transmission because it's light enough. The measurements were implemented by an Agilent E8363B network analyzer and a far-field system in anechoic chamber.

Simulated and measured S parameters of antenna are shown in Fig. 11 (a). It can be seen that the measured S parameters agree with the simulated values well. The measured bandwidth of the antenna ($S_{11}\leq$-10dB) is 0.64GHz, from 5.56GHz to 6.21GHz, equivalent to 11% at 5.8GHz. Figure 11 (b) shows simulated and measured AR bandwidth of antenna. The AR bandwidth (AR$\leq$3dB) is 0.9GHz, from 5.10GHz to 6.00GHz, equivalent to 15.5%. It can be found that the overlapped bandwidth of Impedance and AR from 5.56GHz to 6.00GHz covers the UAVs diagram transmission frequency of 5.8GHz in China.

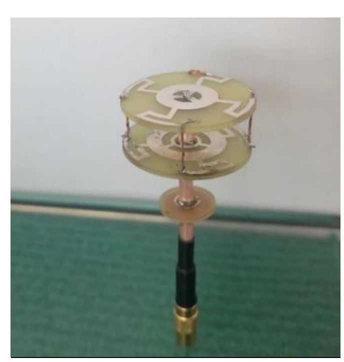

Fig. 10. Photograph of the fabricated antenna.

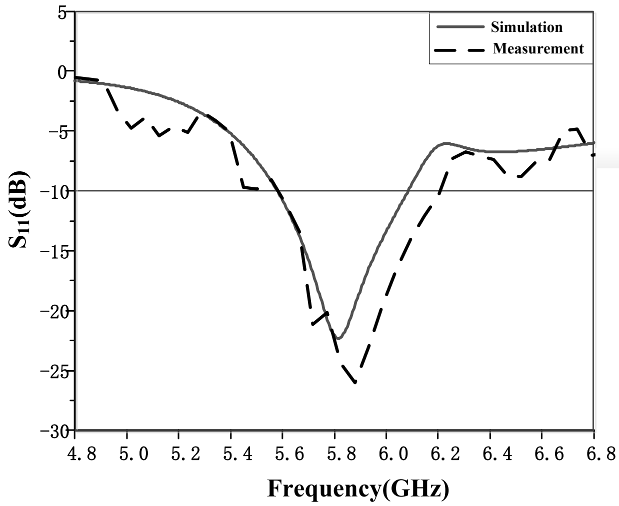

(a)

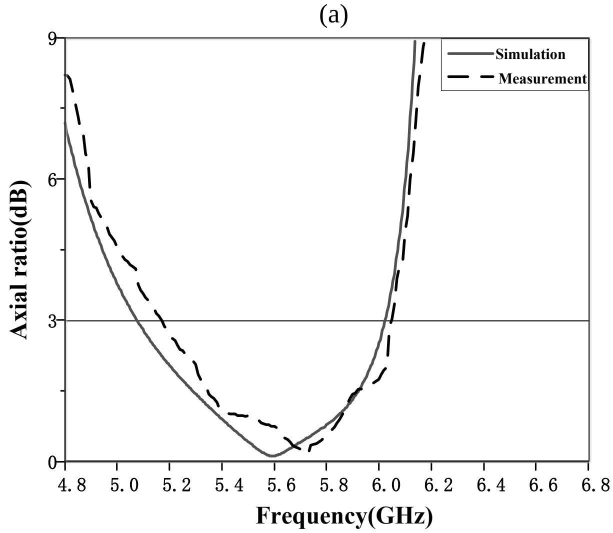

(b)

Fig. 11. Simulated and measured (a) $|S_{11}|$ and (b) AR of the fabricated prototype.

Figure 12 shows simulated and measured AR of the antenna in the azimuth plane (θ =90◦) at 5.8GHz. It can be seen that there are some small differences between the simulated and measured values due to fabrication errors. From the figure, when it is simulated, the ARs fluctuate within 1dB. The measured ARs are slightly higher than the calculated results in all directions, but they are all less than 3dB in the plane, the ripple of which is 0.7dB. Both the simulated and measured values meet the requirement of circular polarization, which indicates that the antenna has good CP characteristics at 5.8GHz.

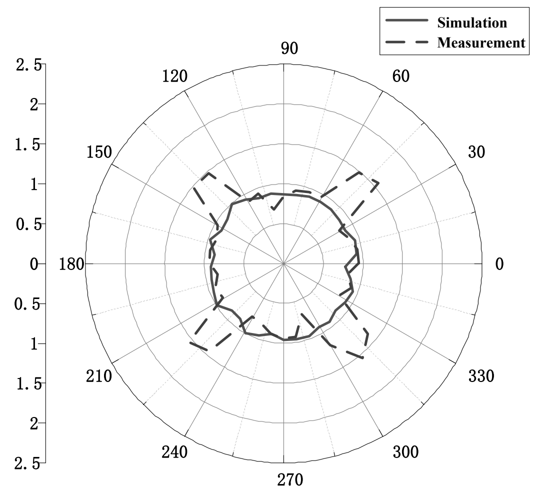

Fig. 12. Simulated and measured AR of the CP antenna in the azimuth plane (θ =90◦).

The simulated LHCP gain at 5.8 GHz is 1.12 dBic. Figure 13 shows the measured and calculated radiation patterns of the proposed antenna at 5.8 GHz in the azimuth (xy plane) and elevation (xz plane) planes, respectively. In xy plane, both the simulated and measured values of left-hand circularly polarized (LHCP) fluctuate around 1dB, while the simulated and measured values of right-hand circularly polarized (RHCP) are less than -15dB. In xz plane, it also can be seen that the results of the simulated and measured agree well with each other, and the level differences between the RHCP and LHCP are more than 15dB, that indicates the antenna is LHCP and has good omnidirectivity.

In order to show the advantage of the antenna, Table 1 compares the omnidirectional CP pagoda antenna with existing antennas in bandwidth and dimensions, from which the overall advantage of the novel pagoda antenna can be seen. Compared with the existing antenna, the overall size of novel pagoda antenna proposed is more advantageous. For the same size, the bandwidth is wider than that of the compared antenna.

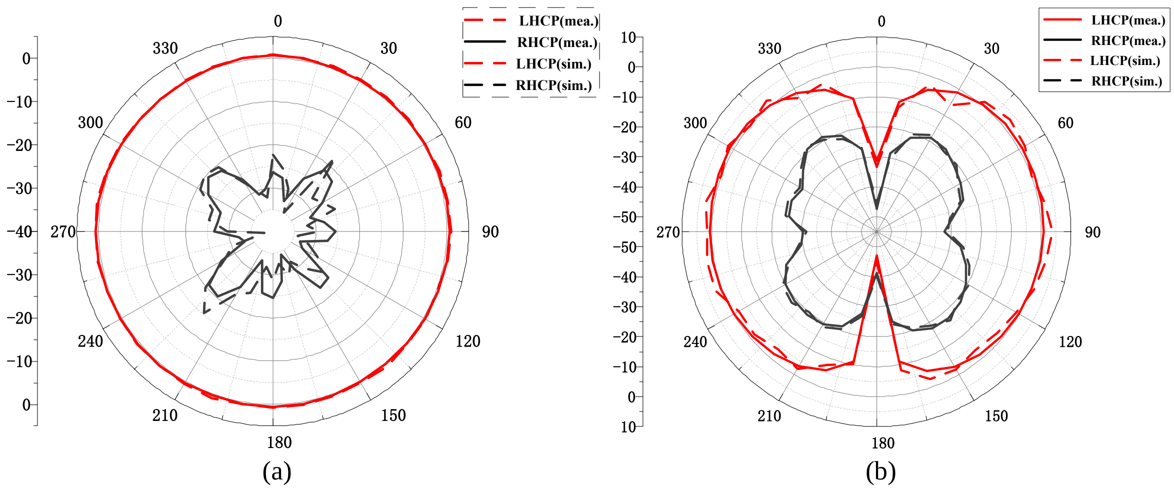

Fig. 13. Simulated and measured radiation patterns in (a) azimuth (xy plane) and (b) elevation (xz plane) planes at 5.8GHz.

Table 1: Performance comparison of reported omnidirectional CP antennas with existing antenna

Ref.	Dimensions (λ_0)	Imp. Bandwidth (%)	3dB AR Bandwidth (%)	Usable Bandwidth (%)
[7]	$1.63\lambda_0 \times 1.63\lambda_0 \times 0.28\lambda_0$	21.60	25.3	21.60
[9]	$0.62\lambda_0 \times 0.62\lambda_0 \times 0.029\lambda_0$	3.97	-	3.97
[10]	$0.52\lambda_0 \times 0.52\lambda_0 \times 0.026\lambda_0$	3.50	-	3.50
[15]	$0.24\lambda_0 \times 0.24\lambda_0 \times 0.12\lambda_0$	3.90	7.5	3.90
This work	$0.42\lambda_0 \times 0.42\lambda_0 \times 0.33\lambda_0$	9.00	16.4	9.00

V. CONCLUSION

A novel omnidirectional RHCP antenna is presented in this letter. The novel pagoda antenna loaded with the shorting pin and the lower substrate with two coupling patches achieves miniaturization in size with adequate bandwidth. The principle and experiment of the antenna are discussed in detail above. Finally, the impedance bandwidth of novel pagoda antenna is 0.53GHz, AR bandwidth is 0.95GHz and usable bandwidth is 0.53GHz, which can cover the UAVs diagram transmission frequency of 5.8GHz in China. With the final dimensions of $0.42\lambda_0 * 0.42\lambda_0 * 0.33\lambda_0$, the antenna has advantages compared with the existing antennas. At the same time, it can be found that the AR bandwidth of the antenna is wider than the impedance bandwidth, which provides a potential for the following research. Impedance bandwidth can be further broadened to achieve miniaturized broadband omnidirectional CP pagoda antenna.

ACKNOWLEDGMENT

This work was supported by the National Natural Science Foundation of China (No. 61771490), Shaanxi Natural Science Foundation Project (No. 2018JM6055), the Basic Research Program of ENGG University of the Chinese People Armed Police Force (No. WJY201606) and Research team project (KYTD201803).

REFERENCES

[1] Y. M. Pan and K. W. Leung, “Wideband circularly polarized dielectric bird-nest antenna with conical radiation pattern,” *IEEE Trans. Antennas Propag.*, vol. 61, no. 2, pp. 563-570, 2013.

[2] G. Zheng and B. Sun, “High-gain normal-mode omnidirectional circularly polarized antenna,” *IEEE Antennas and Wireless Propagation Letters*, vol. 17, no. 6, pp. 1104-1108, June 2018.

[3] Y. Fan, X. Y. Liu, and R. Li, “A broadband circularly polarized omnidirectional antenna with circular open-loops,” *2016 IEEE International Conference on Computational Electromagnetics (ICCEM)*, Guangzhou, pp. 200-201, 2016.

[4] X. Quan, R. Li, and M. M. Tentzeris, “A broadband omnidirectional circularly polarized antenna,” *IEEE Transactions on Antennas and Propagation*, vol. 61, no. 5, pp. 2363-2370, May 2013.

[5] Y. Fan, X. L. Quan, Y. Pan, Y. H. Cui, and R. L. Li, “Wideband omnidirectional circularly polarized

antenna based on tilted dipoles," *IEEE Trans. Antennas Propag.*, vol. 63, no. 12, pp. 5961-5966, Dec. 2015.

[6] C. Y. Liu and Q. X. Chu, "Omnidirectional circularly polarized antenna based on crossed dipoles," *2016 IEEE International Conference on Microwave and Millimeter Wave Technology (ICMMT)*, Beijing, pp. 731-733, 2016.

[7] L. Yang, N. W. Liu, Z. Y. Zhang, et al., "A novel single feed omnidirectional circularly polarized antenna with wide AR bandwidth," *Progress In Electromagnetics Research C*, vol. 51, pp. 35-43, 2014.

[8] J. Su and F. Zhang, "Capacitive probe fed broadband circularly polarized omnidirectional antenna," *2018 Cross Strait Quad-Regional Radio Science and Wireless Technology Conference (CSQRWC)*, Xuzhou, pp. 1-1, 2018.

[9] Q. X. Chu, Y. Mao, and X. R. Li. "A low-profile omnidirectional circularly polarized antenna using planar sector-shaped endfire elements," *IEEE Transactions on Antennas & Propagation*, PP(99):1-1, 2017.

[10] C. Guo, R. Yang, and W. Zhang, "Compact omnidirectional circularly polarized antenna loaded with complementary V-shaped slits," *IEEE Antennas and Wireless Propagation Letters*, vol. 17, no. 9, pp. 1593-1597, Sept. 2018.

[11] Q. Nie, Z. Zhang, and G. Fu, "A compact omnidirectional circularly polarized antenna for 5G communication system," *2018 International Conference on Microwave and Millimeter Wave Technology (ICMMT)*, Chengdu, pp. 1-2, 2018.

[12] H. H. Tran, N. Nguyen-Trong, and H. C. Park, "A compact wideband omnidirectional circularly polarized antenna using TM_{01} mode with capacitive feeding," *IEEE Antennas and Wireless Propa gation Letters*, vol. 18, no. 1, pp. 19-23, Jan. 2019.

[13] Y. Cai, S. Gao, Y. Yin, W. Li, and Q. Luo, "Compact-size low-profile wideband circularly polarized omnidirectional patch antenna with reconfigurable polarizations," *IEEE Transactions on Antennas and Propagation*, vol. 64, no. 5, pp. 2016-2021, May 2016.

[14] J. Li, Y. Huang, and G. Wen, "Design of a compact tri-band omnidirectional circularly polarized antenna," *2018 IEEE International Symposium on Antennas and Propagation & USNC/URSI National Radio Science Meeting*, Boston, MA, pp. 121-122, 2018.

[15] C. Y. Liu and Q. X. Chu, "A compact omnidirectional circularly polarized antenna" *European Conference on Antennas and Propagation (Eu CAP 2018)*. IET, 1-2, 2018.

[16] D. Wu, X. Chen, L. Yang, et al., "Compact and low-profile omnidirectional circularly polarized antenna with four coupling arcs for UAV applications," *IEEE Antennas and Wireless Propagation Letters*, PP (99):1-1, 2017.

[17] J. Liu, Q. Xue, H. Wong, H. W. Lai, and Y. Long, "Design and analysis of a low-profile and broadband microstrip monopolar patch antenna," *IEEE Transactions on Antennas and Propagation*, vol. 61, no. 1, pp. 11-18, Jan. 2013.

[18] Y. Z. Zhu, D. Su, W. Xie, et al., "Design of a novel miniaturized Vivaldi antenna with loading resistance for ultra wideband (UWB) applications," *Applied Computational Electromagnetics Society Journal*, vol. 32, no. 10, 2017.

Zheyu Li was born in Hubei, China. She received the B.S. degree in Communication Engineering from Engineering University of People's Armed Police in 2018, and she is now studying for a master's degree at Engineering University of People's Armed Police. Her research interests are mainly in microwave antennas.

Yongzhong Zhu was born in Anhui, China. He received the B.S. degree in Communication Engineering from Engineering University of People's Armed Police, the M.S. degree in Military Communication from Engineering University of People's Armed Police, and the Ph.D. degree in Electronic Science and Technology from Xidian University, in 2002, 2005 and 2008, respectively. From 2009 to 2011, he was a Postdoctoral Fellow with Northwestern Polytechnical University. Since 2012, he has been an Associate Professor of microwave engineering with Engineering University of People's Armed Police. His research interests are in microwave antennas and devices, wireless communications and information systems.

Shen Yu was born in Shanxi, China. She received the Bachelor degree in Military Communication from Engineering University of People's Armed Police in 2006 and the M.S degree in Military Communication from Engineering University of People's Armed Police in 2009. Since 2019, she has been an Associate Professor of Command Information System of Engineering University of People's Armed Police. Her research interests are in command information system.

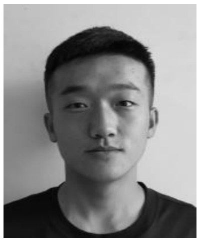

Xiaoyu Liu was born in Inner Mongolia, China. He received the B.S. degree in Communication Engineering from Engineering University of People's Armed Police in 2018, and he is now studying for a master's degree at Engineering University of People's Armed Police. His research interests are mainly in microwave antennas.

Guohao Peng was born in Sichuan, China. He received the B.S. degree in Electronic and Information Engineering from Wuhan University of Science and Technology in 2018,and he is now studying for a master's degree at Engineering University of People's Armed Police. His research interests are mainly in microwave antennas.

Performance of Aeronautical Mobile Airport Communications System in the Case of Aircraft at Final Approaching or Initial Climbing

Yuchu Ji [1], Yang Wang [2], and Yuan Sang [3]

[1] College of Electronic Information and Automation
Civil Aviation University of China, Tianjin 300300, China
jiyuchu@126.com

[2] Tianjin Key Lab for Advanced Signal Processing
Civil Aviation University of China, Tianjin, 300300, China
raynor63@163.com

[3] Inventec Group (Tianjin) Electronic Technology Co. LTD, Tianjin, 300070, China
dorisbps@163.com

Abstract ─ The aeronautical mobile airport communications system (AeroMACS) is proposed to support the communications between the tower and aircrafts or the service vehicles in the range of airport. In this paper, the working environment that the aircraft at final approaching or initial climbing (AFAIC) is researched. By considering the influence of Doppler frequency shift and the channel model in AFAIC case, we propose a transmission scheme which can obtain preferable transmission performance for low order modulation. Simulation results of the signal-to-noise ratio loss, the spectrum efficiency and the bit error rate are given, which indicate that the proposed scheme can meet the demand of AeroMACS and expand the zone of airport communication area.

Index Terms ─ Aeronautical mobile airport communications system, communication in aircraft at final approaching and initial climbing case, signal processing.

I. INTRODUCTION

The increase of air traffic in civil airports has led to a growth of data loads needed for both air traffic control (ATC) and airline operational communications (AOC) services. The new generation of air traffic management (ATM) system needs the support of a broadband communication structure able to satisfy the increasing application and service requirements foreseen by the Communications Operating Concept and Requirements (COCR) [1].

To satisfy the communication order, both international civil aviation organization (ICAO) and Eurocontrol identified a solution to provide dedicated aeronautical communications on the airport surface. This system is named aeronautical mobile airport communications system (AeroMACS), which supports the aircraft are in closest proximity to each other and to a wide variety of service and operational support aircrafts, vehicles, personnel, and infrastructures [2,3]. AeroMACS is based on the IEEE 802.16e standard, known as Mobile WiMAX [4].

The AeroMACS operates in the aeronautical C-band, which is with the frequency between 5091 MHz and 5150 MHz, and divided into 11 separated subchannels with the bandwidth of 5MHz. The transmission characteristics and the antenna design of the aeronautical C-band has been widely studied [5,6]. In particular, non-line-of-sight (NLoS) communications are supported by means of orthogonal frequency division multiplexing access (OFDMA) technology, which provides robustness against detrimental propagation effects and efficient use of resources, thus enabling high-data-rate services.

According to the AeroMACS profile, OFDMA frames follow a time division duplexing (TDD) structure, in which the downlink (DL) and uplink (UL) transmissions occur at different times and share the same frequency channel, and the AeroMACS frame occupies the entire 5 MHz channel during its 5 milliseconds duration.

In [2] and [3], the concept and the basic scheme of AeroMACS is introduced. The transmission efficiency and performance is analyzed in [4] and [7]. The typical transmission case, which considers different communication environment and variety kind of access node (i.e., aircrafts, vehicles and sensors), is discussed in [8]. The MIMO antenna configuration scheme is proposed and tested in [9] and [10], and the multi-hop relay scheme based on IEEE 802.16j is proposed in [11].

Submitted On: January 1, 2020
Accepted On: May 4, 2020

To describe different work environments in the airport, two typical working cases, the aircraft at hangar taxiway or runway (AHTR) and the aircraft at the gate (AG) are defined [8]. In AHTR case, there is few obstacles between the access nodes, and the channels between different nodes contain one LOS path and some NLOS paths. In AG case, there are several aircrafts and tens of vehicles in one communication cell, and the channels between different nodes do not have LOS path.

Beside the two abovementioned cases, aircraft at final approaching or initial climbing (AFAIC) progress plays an important part of ATM communication in AeroMACS. The aircraft operation data in AFAIC case is also important to realizing the high level advanced surface movement guidance and control system (A-SMGCS) or the automatic aircraft navigation such as automatic approaching or landing.

In AFAIC case, high approaching or climbing speed of aircraft leads to strong Doppler frequency shift in the communication system, which leads to intersubcarrier interference of the OFDMA scheme. Besides, the communication channel in the AFAIC case is with strong LOS path, which is different from the AG and AHTR cases.

To improve the transmission performance, many intersubcarrier interference cancellation schemes and transmission schemes are proposed [12-15]. In [16], a Doppler shift and timing error estimation and cancellation scheme is proposed for AeroMACS. However, it is with complicated decoding process, and the special channel between the base station and the aircraft in AFAIC case has not been considered.

In this paper, the transmission mode of AFAIC case in AeroMACS has been researched. By considering the influence of Doppler frequency shift and the channel model in AFAIC case, we propose a transmission scheme that the decoding process is similitude with the existing one in IEEE 802.16e. It is easy to be realized during the construction process of AeroMACS. Simulation results of the signal-to-noise ratio (SNR) loss, the spectrum efficiency and the bit error rate (BER) are also given at the end of this paper.

II. SYSTEM MODEL

As shown in Fig. 1, the AeroMACS network architecture is based on IEEE 802.16e [17], which is an all-IP network that decouples the access architecture from IP connectivity and allows modularity and flexibility.

The mobile station (MS) and the subscriber station (SS) are the end user devices. The MS nodes are moving nodes such as aircrafts, vehicles, and personal nodes in the airport. The SS nodes are fixed nodes such as radar, weather stations, and sensors in the movement area of the airport.

The base station (BS) is the access point to the network, implementing air interface and the access functionalities including UL and DL scheduler, radio resource management, and handover (HO) control. Each BS operates on an angular sector and is at a given frequency. During different transmission environments, the cover area of BS can be large (e.g., the macro cell for the AHTR scenery) or small (e.g., the micro cell for the AG scenery).

Access service network (ASN) is in charge of all the functions needed to provide radio access to AeroMACS subscriber, authentication, and resource management procedures. The connectivity service network (CSN) is a set of network functions that provide IP connectivity services to the AeroMACS subscriber. The ASN gateway, represents the link between the ASN and the CSN, described below, performing routing or bridging functions.

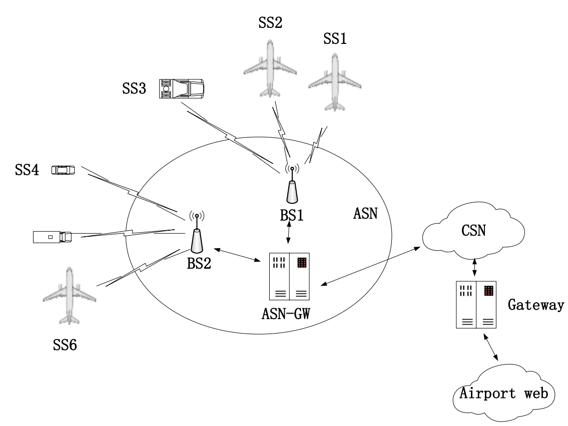

Fig. 1. Typical AeroMACS network, which includes BS node, MS nodes and SS nodes. The ASN, CSN and the ASN gateway realize the connection to the airport web.

In AFAIC case, the aircraft approaches to or climbs from the runway with the similar track. Considering that the minima taking-off interval or approaching interval in civil ATC rule is about 10 km, and the cover range of BS in macro cell reaches more than 10 km, as shown in Fig. 2, the number of MS node in AFAIC is limited (Normally, BS covers 2 aircrafts during both approaching and climbing cases).

Since the approaching speed or the climbing speed of aircraft is a dynamic value, which affected by aircraft type, load, oil quantity and wind speed, in [18], five categories, i.e., CAT A, B, C, D and E, of typical aircraft have been established by different approaching speed. In general, for normal civil aircraft, the speed range of AFAIC case is between 200km/h (kilometers per hour) and 400km/h [15]. The channel between BS and MS in AFAIC scenery is the fast fading channel with strong Doppler frequency shift. In the OFDM system, we take ε as the normalized offset frequency:

$$\varepsilon = N f_c T_S v / c \, , \tag{1}$$

where f_c is the carrier frequency, c is the light speed, and v is the moving speed of MS in meter per second, N is the number of the DFT point in OFDMA scheme and T_S is the symbol period duration time.

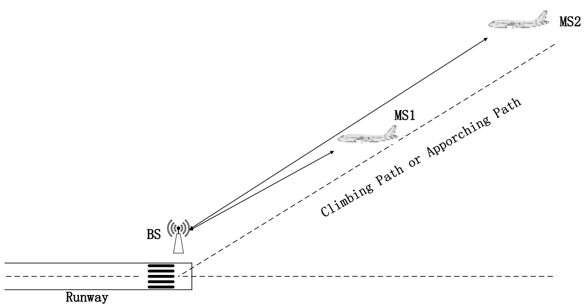

Fig. 2. The AFAIC case. The aircrafts are approaching or climbing with the similar track.

In the typical AeroMACS, considering the above-mentioned speed range in AFAIC case, and assuming that the carrier frequency is 5GHz, the number of DFT point is 512, and the symbol period duration time is 1.75×10^{-7} seconds, the range of ε is:

$$\varepsilon \in \left[4.97\times10^{-2}, 1.66\times10^{-1}\right]. \tag{2}$$

The channel model of AFAIC case is shown in Fig. 3, which is with one LOS path and some NLOS paths, and it is a typical Rice model.

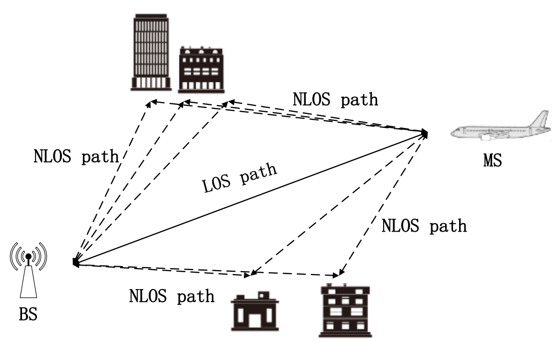

Fig. 3. Channel model of AFAIC case, which contains one LOS path and several NLOS paths.

Define the amplitude of the LOS path is a, the variance of the diffuse process with zero-mean quadrature components of NLOS path is c, The Rice factor, which is the power ratio between the LOS and the diffuse components is given by:

$$K_{\mathrm{RICE}} = 10\lg\left(\frac{a^2}{c^2}\right)\mathrm{dB} \, . \tag{3}$$

Define the number of NLOS path is N. Let f_D and be the Doppler shifting frequency of the LOS path. The phase shift, the Doppler shifting frequency and the time delay of the n-th NLOS path are θ_n, f_{D_n} and τ_n, respectively. The channel function of AFAIC is given by:

$$h(t) = ae^{j2\pi f_D t} + c\frac{1}{\sqrt{N}}\sum_{n=1}^{N} e^{j\theta_n} e^{j2\pi f_{Dn} t} e^{-j2\pi\tau_n} \, . \tag{4}$$

In (4), $ae^{j2\pi f_D t}$ denotes the channel function of the LOS path, and the rest parts denote the channel function of the NLOS paths where $e^{j\theta_n}$, $e^{j2\pi f_{Dn}}$ and $e^{-j2\pi\tau_n}$ represent the phase shifting component, the Doppler shift component and the time delay heft component of the n-th NLOS path, respectively.

As discussed in [15], in the typical AFAIC case, the parameter K_{RICE} is between 9dB and 20dB, and the typical value of K_{RICE} is 15dB. The typical number of NLOS path is 20.

III. TRANSMISSION MODEL IN AFAIC CASE

From the physical layer specifications, the DL of OFDMA scheme is essentially equivalent to an OFDM system that in one symbol period, BS can occupy the all subcarriers. Let $\boldsymbol{d}_i$ be the transmitted symbols of the BS node during DL in the i-th symbol period and N denotes the number of the subcarrier, where,

$$\boldsymbol{d}_i = \left[d_i(0) \quad d_i(1) \quad \cdots \quad d_i(N-1)\right]. \tag{5}$$

As noted in [12], the transmitted symbols are fed to a conventional OFDM modulator that consists of an N-point inverse discrete Fourier transform (IDFT) unit followed by the insertion of an N_g-point cyclic prefix (CP) to avoid interference between adjacent blocks. The output of IDFT unit is denoted as:

$$\boldsymbol{s}_i = \left[s_i(0) \quad s_i(1) \quad \cdots \quad s_i(N-1)\right], \tag{6}$$

where the CP is denoted as:

$$s_i(k) = s_i(k+N) \quad for \quad -N_g \le k \le -1 \, . \tag{7}$$

The modulated symbol on the k-th subcarrier is:

$$\begin{gathered} s_i(k) = \frac{1}{\sqrt{N}}\sum_{n=0}^{N-1} d_i(n) e^{\frac{j2\pi nk}{N}} \\ \text{for} -N_g \le k \le N-1 \end{gathered} \, . \tag{8}$$

The discrete-time downlink signal takes the form:

$$s^T(k) = \sum_i s_i(k - iN_T) \, , \tag{9}$$

where $N_T = N + N_g$.

By considering the time-variant frequency-selective fading channel between BS and MS, we denote the channel impulse response (CIR) of the l-th subcarriers as $h(l)$ and $l \in \{0, 1, \cdots, L-1\}$. The received signal on the k-th subcarriers of MS in the i-th symbol period is:

$$r_i(k) = P_{BS}\sum_{l=0}^{L-1} h(l)s_i(l) + w(k), \tag{10}$$

where P_{BS} is the transmission power of BS, and $w(k)$ is the complex-valued additive white Gaussian noise (AWGN). The received signal of MS during contiguous symbol period is:

$$r(k) = P_{BS}\sum_i\sum_{l=0}^{L-1} h(l)s_i(k-l-iN_T)+w(k). \tag{11}$$

At the receiver, $r(k)$ is divided into adjacent segments of length N_T, each corresponding to a transmitted OFDMA block. Assuming the CP is longer than the CIR duration, after removing the CP, the remaining N samples are passed to an N-point discrete Fourier transform (DFT) unit, and the output of the DFT unit is:

$$R_{i,n} = P_{BS}H_n d_{i,n} + w_{i,n}, \tag{12}$$

where

$$H_n = \sum_{l=0}^{L-1} h(l)e^{-\frac{j2\pi nl}{N}}, \tag{13}$$

and $w_{i,n}$ is the equivalent additive noise after DFT, which is with the complex Gaussian distribution.

By considering the frequency shift in AFAIC case calculated in (2), ε is less than the bandwidth of the subcarrier, the frequency shift only leads to the intersubcarrier interference. The received signal of the MS in (10) can be rewritten as:

$$R_{i,n} = P_{BS}e^{j\varphi_i}H_n f_N(\varepsilon)d_{i,n}+I_{i,n}(\varepsilon)+w_{i,n}. \tag{14}$$

Where

$$\varphi_i = \frac{2\pi\varepsilon_i N_T}{N}, \tag{15}$$

$$f_N(\varepsilon)=\frac{\sin(\pi\varepsilon)}{N\sin\left(\frac{\pi\varepsilon}{N}\right)}e^{\frac{j\pi\varepsilon(N-1)}{N}}, \tag{16}$$

and $I_{i,n}(\varepsilon)$ denotes the interference signal caused by the adjacent subcarriers. Since $I_{i,n}(\varepsilon)$ relates to the transmitted symbols on the adjacent subcarriers, we model it as a zero-mean random variable with its power denoted as

$$\sigma_I^2(\varepsilon) = P_{BS}\left[1-\left|f_N(\varepsilon)\right|^2\right]. \tag{17}$$

By considering the Rice channel model of the AFAIC case in (3), formula (14) can be rewritten as:

$$\begin{aligned} R_{i,n} &= P_{BS}ae^{j\varphi_i} f_N(\varepsilon)d_{i,n} \\ &+\sum_{l=0}^{N-1} P_{BS}ce^{\varphi_i}h(l)e^{-\frac{j2\pi nl}{N}} f_N(\varepsilon)d_{i,n} \\ &+I_{i,n}(\varepsilon)+w_{i,n} \end{aligned} \tag{18}$$

During the UL transmission of AeroMACS, the flexible OFDMA spectrum allocation schemes are allowed. Normally, there are two UL transmission cases.

The first case is that in one symbol period, all the subcarriers are allocated to one MS node, and this scheme befits for the case that there are small number of MS nodes in the coverage zone of BS. The transmission model is similar with the DL mode. This scheme does not fit in the AG and the AHTR cases since large number of MS nodes results in lower spectrum allocation efficiency and more time delay.

Another case is that in one symbol period, the subcarriers are allocated to u MS nodes ($MS_1, MS_2, \cdots, MS_u$), and we assume that the N_{us}-th to the N_{ue}-th subcarriers are allocated to the u-th MS. After IDFT, the modulated signal of the u-th MS at the k-th subcarrier is:

$$s_{i,u}(k) = \frac{1}{\sqrt{N}}\sum_{n=N_{us}}^{N_{ue}-1} d_{i,u,n}e^{\frac{j2\pi nk}{N}}. \tag{19}$$

$$\text{for } -N_{us} \le k \le N_{ue}-1$$

The received signal at the k-th subcarrier of BS can be denoted as:

$$r_i(k) = \sum_{u=0}^{U-1} P_u \sum_{k=N_{u1}}^{N_{u2}-1} h_u(k)s_{i,u}(k) + w_i(k), \tag{20}$$

where $h_u(k)$ is the CIR of the channel from MS_u to BS on the k-th subcarrier. The demodulated signal after DFT at BS node is:

$$R_{i,n} = \sum_{u=0}^{U-1} P_u \sum_{k=N_{us}}^{N_{ue}-1} h_u(k)e^{-\frac{j2\pi nk}{N}} d_{i,u}(k) + w_{i,n}. \tag{21}$$

Let,

$$H'_{n,u} = \sum_{k=N_{us}}^{N_{ue}-1} h_u(k)e^{-\frac{j2\pi nk}{N}} d_{i,u}(k), \tag{22}$$

and ε_u be the nominalized frequency shift of the u-th MS, the received signal at the MS can be described as:

$$R_{i,n} = \sum_{u=0}^{U-1} P_u e^{j\varphi_{i,u}} f_N(\varepsilon_u)H'_{n,u}d_{i,u}(k)+I_{i,n}(\varepsilon_u)+w_{i,n}. \tag{23}$$

By considering the Rice channel model in (3), formula (23) can be rewritten as":

$$\begin{aligned} R_{i,n} &= \sum_{u=0}^{U-1} a_u P_u e^{j\varphi_{i,u}} f_N(\varepsilon_u)d_{i,u}(k) \\ &+\sum_{u=0}^{U-1}\sum_{k=N_{us}}^{N_{ue}-1} c_u P_u e^{\varphi_i}h_u(k)e^{-\frac{j2\pi nk}{N}} f_N(\varepsilon_u)d_{i,u}(k). \\ &+\sum_{u=0}^{U-1} I_{i,n}(\varepsilon_u) + w_{i,n} \end{aligned} \tag{24}$$

A dramatic phenomenon is that, in the AFAIC case, the aircrafts are with the similar approaching speeds and the climbing speeds. The frequency shifts of different MS nodes are with the similar values.

During the decoding process at the receiver, we propose a rough CIR estimation and decoding (RCED) scheme. In this scheme, we estimate the affected CIR instead of the parameter ε by one precursor symbol. Then, the receiver treats the interference signal $I_{i,n}(\varepsilon)$ as the additional noise. The process of RCED scheme is similar with the normal decoding process, which can run under the IEEE 802.16e protocol receiver. So the RCED scheme can be realized by the limited improvement of the existing equipment.

In the DL process of AFAIC case, before transmission, we design a precursor symbol vector $\boldsymbol{d}_p$ which is known by the receiver. The precursor symbol is as follows:

$$\boldsymbol{d}_p = \left[\underbrace{1 \quad 1 \quad \cdots \quad 1}_{N}\right]. \tag{25}$$

The modulated symbol on the k-th subcarriers is:

$$s_p(k) = \frac{1}{\sqrt{N}} \sum_{n=0}^{N-1} e^{\frac{j2\pi nk}{N}} \quad \text{for} - N_g \le k \le N-1. \tag{26}$$

The received signal of the precursor period at the n-th output of DFT unit of MS node is:

$$R_{p,n} = P_{BS} e^{j\varphi_p} H_n f_N(\varepsilon) + I_{i,n}(\varepsilon) + w_{i,n}, \tag{27}$$

Let $T(n) = P_{BS} e^{j\varphi_p} H_n f_N(\varepsilon)$ be the transmission coefficient, it can be estimated during the precursor period as:

$$\hat{T}(n) = \underset{T(n)}{\arg\min} \left\{ \left| R_p(n) - T(n) \right| \right\}, \tag{28}$$

which also denoted as the received signal of the precursor slot at the n-th output of DFT unit.

The decoding process of the following symbol periods can be described as:

$$\hat{d}(n) = \underset{\hat{d}(n)\in\Delta}{\arg\min} \left\{ \left| R_i(n) - \hat{T}(n) d(n) \right| \right\}, \tag{29}$$

where Δ represents the possible symbol set of the transmitted signals.

The flow diagram of the RCED process is shown in Fig. 4. BS continual transmits one signal packet which includes $\{\boldsymbol{d}_p, \boldsymbol{d}_1, \boldsymbol{d}_2, \cdots, \boldsymbol{d}_I\}$. The packet length, which equals to I+1, depends on the time-variant characteristic of the transmission channel.

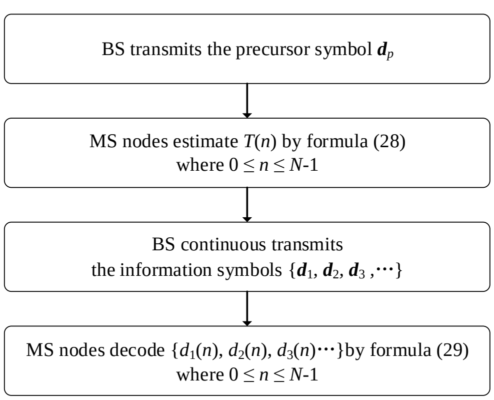

Fig. 4. Flow diagram of the RCED process.

In the UL process, to estimate the transmission coefficient, the known precursor periods are allocated to each MS node, respectively, and the transmission coefficient estimating and the decoding process are similar with the DL case.

IV. PERFORMANCES ANALYSIS

The performances of SNR loss, the spectrum efficiency and BER of the transmission scheme in AFAIC case are discussed in this part, and to simplify the analysis process, the DL transmission is considered.

Let SNR_{real} be the real SNR of the receiver at MS, and the channel gain is equalized, the real SNR is:

$$SNR_{\text{real}} = \frac{P_{BS} E\left\{ \left| f_N(\varepsilon) \exp^{j\varphi_i} \right|^2 \right\}}{\sigma_I^2(\varepsilon) + \sigma_w^2}, \tag{30}$$

where P_{BS} is the transmission power of the BS, $E\left\{ \left| f_N(\varepsilon) \exp^{j\varphi_i} \right|^2 \right\}$ is the coefficient of the transmitted signal, which represents the effect of the frequency shift of the signal, $\sigma_I^2(\varepsilon)$ and σ_w^2 are the power of the interference signal and the AWGN, respectively.

With the increase of the speed of MS node, the power of the signal, which equals to the primal signal power multiplied by the coefficient $E\left\{ \left| f_N(\varepsilon) \exp^{j\varphi_i} \right|^2 \right\}$, reduces and the power of intersubcarrier interference, which equals to $P_{BS}\left[1 - \left| f_N(\varepsilon) \right|^2\right]$, increases.

According to the typical AeroMACS system in [2], we assume that the FFT point is 512, the symbol period is 1.75×10^{-7} seconds, and N_g equals 64 (1/8 symbol period).

Without loss of generality, AWGN is assumed as a complex random variable, the mean and variance equal 0 and 1, respectively. Since the power of AWGN can be recognized as the variance of it, we set $\sigma_w^2 = 1$.

Let $SNR_{\text{sync}} = P_{BS} / \sigma_w^2$ be the ideal SNR of the synchronic communication system. Performances of SNR loss in AFAIC case with different SNR_{sync} values, i.e., 5dB, 10dB, 15dB, 20dB and 30dB, are shown in Fig. 5.

In the case that SNR_{sync} is low, which means that MS is far away from BS, the real SNR loss is small. When SNR_{sync}=5dB, the SNR loss is about 1dB for the case that the MS node moves at 400 km/h.

With the increase of SNR_{sync}, which indicates that the MS approaches BS, the influence of Doppler frequency shift is obvious. When the speed of MS is 250km/h, which is the most common approaching speed and the initial climbing speed of civil aircraft, the real SNR loss are 2dB, 7dB and 16dB in the case that SNR_{sync} equal 10 dB, 20 dB and 30 dB, respectively. For the case that the speed of MS is 400km/h, SNR_{real} reduces to less than 10dB.

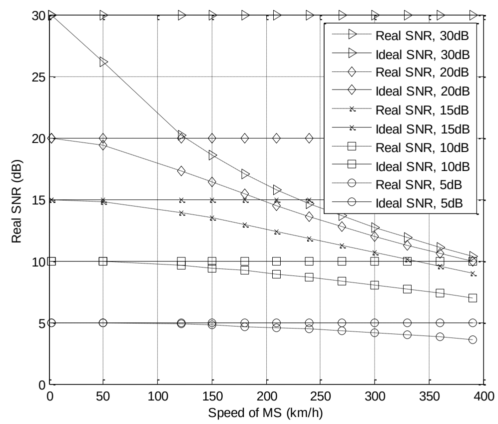

Fig. 5. SNR loss in AFAIC case, where SNR_{sync} is set to 5dB, 10dB, 15dB, 20dB and 30dB, and different move speeds of MS node are considered.

Simulation results of spectrum efficiency under different moving speeds of MS node are shown in Fig. 6. By considering that different modulation scheme will cause varying transmission performance, four common modulation schemes, i.e., binary phase shift keying (BPSK), quadrature phase shift keying(BPSK), 16-quadrature amplitude modulation(QAM) and 64-QAM are considered. Since the channel gain is equalized, the gain of LOS path does not affect the simulation results.

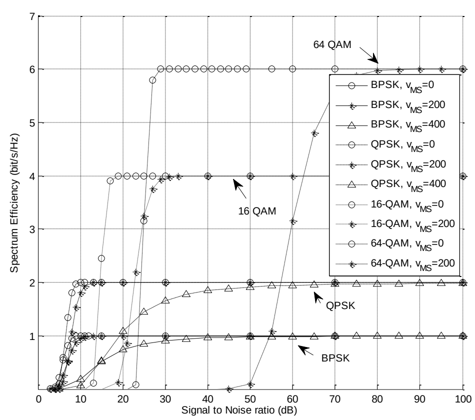

Fig. 6. Spectrum efficiency for BPSK, QPSK, 16-QAM and 64-QAM with different moving speed of MS node.

For the BPSK modulation, to reach half spectrum efficiency (0.5 bit/s/Hz), SNR_{sync} are 5dB, 7dB and 15dB for the speed of MS are 0km/h, 200km/h and 400km/h, respectively. For the QPSK modulation, to reach half spectrum efficiency (1 bit/s/Hz), SNR_{sync} are 6dB, 8dB and 20dB for the speed of MS are 0km/h, 200km/h and 400km/h, respectively.

For the 16-QAM modulation, to reach the half spectrum efficiency point (2 bit/s/Hz), SNR_{sync} are 14dB and 23dB for the speed of MS are 0km/h and 200km/h, respectively. For the 64-QAM modulation scheme case, to reach the half spectrum efficiency point (3 bit/s/Hz), SNR_{sync} are 25dB and 60dB for the speed of MS are 0km/h and 200km/h, respectively. For 16-QAM and 64-QAM modulation schemes, SNR_{sync} should be more than 100dB to reach the half spectrum efficiency in the case that the speed of MS is 400 km/h, which is not realistic in AeroMACS.

From the results, the spectrum efficiency loss of the higher order modulation scheme (i.e., 16-QAM and 64-QAM) is greater than the lower cases. The reason of huge spectrum efficiency loss in the high order modulation cases is that the high order modulated code is with smaller Euclidean distance, which is much easier to be affected by the interference signal and the AWGN.

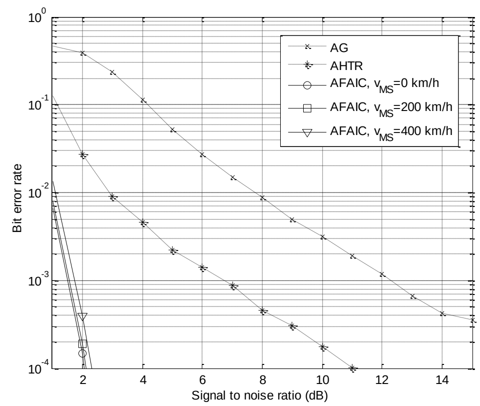

Fig. 7. BER performances of BPSK modulation.

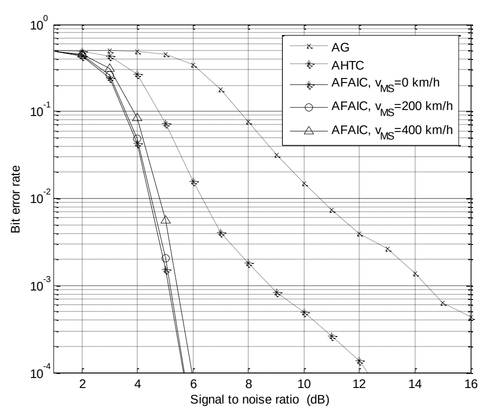

Fig. 8. BER performances of QPSK modulation.

BER performances of the abovementioned 4 modulation schemes are shown in Fig. 7 to Fig. 10, and the K_{RICE} is set to 15dB as the typical value in AFAIC case.

For BPSK and QPSK modulations, as shown in Fig.

7 and Fig. 8, when the moving speed of MS is 200km/h, the BER performances are similar with the case that MS node is stationary. In the case that the moving speed of MS reaches 400km/h, the BER performance loss is less than 0.5dB, which means that the proposed scheme can fit the AFAIC case for the low order modulation schemes.

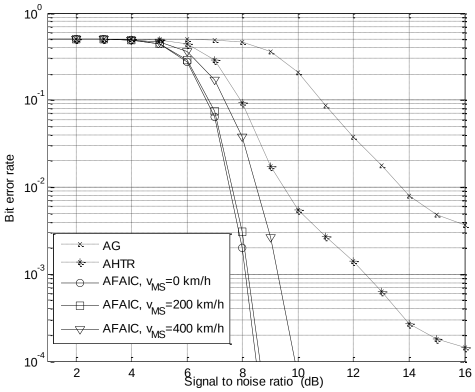

Fig. 9. BER performances of 16-QAM modulation.

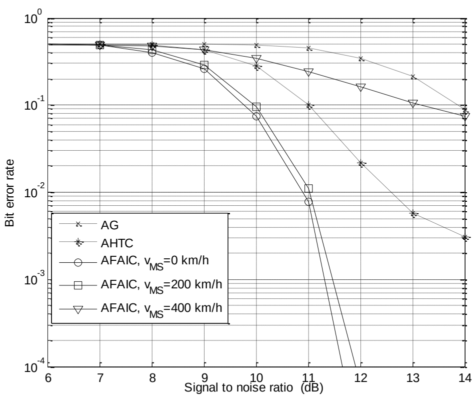

Fig. 10. BER performances of 64-QAM modulation.

As shown in Fig. 9, for 16-QAM modulation, compared with the case that MS node is stationary, the BER performance loss are 0.1dB and 1.5dB for the case that the moving speed of MS are 200km/h and 400km/h, respectively.

For 64-QAM modulation shown in Fig. 10, the BER performance loss is about 0.3dB for the case that the moving speed of MS is 200km/h. When the moving speed of MS is 400km/h, BER performance is with significant loss. The BER only reaches 10^{-1} when SNR is 14dB.

We also show the BER performances in the AG case and the AHTR case where K_{RICE} are set to 0 and 6.7dB, respectively [19]. Benefit from the strong gain of LOS path in AFAIC case, BER performances of BPSK, QPSK and 16-QAM modulation schemes in the AFAIC case with the moving speed of MS is 400km/h are better than the AG case and AHTR case significantly. For the 64-QAM modulation, the BER performance of the 400km/h moving speed case is with mightily loss, which is worse than the AHTR case and reaches the same BER with the AG case when SNR reaches 14dB.

Summarizing the simulation results in Fig. 5 to Fig. 10, we can get the transmission characteristics in AFAIC case. Firstly, the interference caused by the high moving speed of MS seriously affects the real SNR and the transmission efficiency, however, this interference signal is difficult to be cancelled. Secondly, the strong LOS path of the channel in AFAIC case can provide a stable transmission environment between BS and MS nodes, which can reduce BER of the transmission system. Third, increase the modulation order will lead to a sharp increase in BER. By using lower order modulation, the proposed RCED scheme can meet the communication requirements of AeroMACS in AFAIC case.

V. CONCLUSION

In this paper, to combat the Doppler frequency shift in AFAIC case, we propose a RCED scheme which estimates the affected CIR instead of the nominalized frequency shift at the receiver. It can run under the IEEE 802.16e protocol receiver, which can be realized by the limited improvement of the existing equipment. Simulation results of BER performance show that the proposed RCED scheme can meet the requirements of AeroMACS. From our research, the coverage zone of AeroMACS can be expanded from the ground part (which include the AG case and the AHTR case) to the takeoff and approaching strip (the AFAIC case), which is benefit to improve the ATM communication link. The data of aircrafts in approaching can also be used to estimate the grounding point and grounding time, which provides data support for guidance, collision avoidance and path planning of ground vehicles in the A-SMGCS.

ACKNOWLEDGMENT

This work was supported by the Research project of Tianjin education commission (No. 2018KJ239) and the open fund of Tianjin key lab for advanced signal processing (No. 2017ASP-TJ02).

REFERENCES

[1] Eurocontrol and FAA, COCRv2, *Communications Operating Concept and Requirements for the Future Radio System*, 2007.

[2] G. Bartoli, R. Fantacci, and D. Marabissi, "AeroMACS: A new perspective for mobile airport communications and Services," *IEEE Wireless Communications*, vol. 20, pp. 44-50, Dec 2013.

[3] C. Brian, "Service considerations for an AeroMACS

network reference model: Delivering next generation communications to the airport surface," *2015 Integrated Communication, Navigation, and Surveillance Conference (ICNS) IEEE*, pp. 1-21, June 2015.
[4] B. Giulio, et al., "An efficient subcarrier allocation method for AeroMACS-Based communication systems," *IEEE Transactions on Aerospace and Electronic Systems*, vol. 49, no. 2, pp. 786-797, Apr. 2013.
[5] O. Mohammad, O. Nasser, and G. Noradin, "Enhanced bandwidth small square slot antenna with circular polarization characteristics for WLAN/ WiMAX and C-band applications," *Applied Computational Electromagnetics Society Journal*, vol. 28, no. 2, pp. 156-161, Feb. 2014.
[6] R. Vahid, S. Hasan, and K. Saeid, "Circularly polarized aperture-coupled microstrip-line fed array antenna for WiMAX/ C bands applications," *Applied Computational Electromagnetics Society Journal*, vol. 32, no. 12, pp. 1117-1120, Dec. 2017.
[7] K. Morioka, et al., "EVM and BER evaluation of C band new Airport surface communication systems," *International Workshop on Antenna Technology: small Antennas, Novel Em Structures and Materials, and Applications IEEE*, Sydney, pp. 242-245, Mar. 2014.
[8] C. Antonio and N. Fistas, "AeroMACS: Impact of link symmetry on network capacity," *2016 Integrated Communications Navigation and Surveillance (ICNS) IEEE*, Piscataway, NJ, pp. 1-9, Apr. 2016.
[9] N. Kanada, et al., "MIMO effect evaluation for aeronautical WiMAX in airport at 5.1GHz," *Integrated Communications, Navigation & Surveillance Conference IEEE*, pp. 1-10, Apr. 2012.
[10] N. Kanada, et al., "Evaluation of antenna configuration for aeronautical WiMAX at 5.1GHz," *Wireless & Microwave Technology Conference IEEE*, pp. 1-4, Apr. 2012.
[11] K. Behnam and R. J. Kerczewski, "IEEE 802.16J multihop relays for AeroMACS networks and the concept of multihop gain," *2013 Integrated Communications, Navigation and Surveillance Conference (ICNS) IEEE*, Herndon, VA, pp. 1-7, Apr. 2013.
[12] M. Morelli, et al., "Synchronization techniques for orthogonal frequency division multiple access (OFDMA): A tutorial review," *Proceedings of the IEEE*, vol. 95, no. 7, pp. 1394-1427, July 2007.
[13] F. Romano, et al., "Adaptive modulation and coding techniques for OFDMA systems," *IEEE Transactions on Wireless Communications*, vol. 8, no. 9, pp. 4876-4883, Sep. 2009.
[14] M. Michele, L. Marchetti, and M. Moretti, "Maximum likelihood frequency estimation and preamble identification in OFDMA-based WiMAX systems," *IEEE Transactions on Wireless Communications*, vol. 13, no. 3, pp. 1582-1592, Mar. 2014.
[15] A. Biagioni, et al., "Adaptive subcarrier allocation schemes for wireless ODFMA systems in WiMAX networks," *IEEE Journal on Selected Areas in Communications*, vol. 27, no. 2, pp. 217-225, Feb. 2009.
[16] P. Paola, et al., "AeroMACS evolution-analysis during landing, takeoff, and approach phases," *IEEE Transactions on Aerospace and Electronic Systems*, vol. 50, no. 3, pp. 1899-1912, July 2014.
[17] WiMAX Forum Network Architecture — Stage 2: Architecture Tenets, Reference Model and Reference Points, *WIMAX Forum*, Tech. Rep., Feb. 2009.
[18] International Civil Aviation Organization, *Doc 9905: Required Navigation Performance Authorization Required (RNP AR) Procedure Design Manual.*
[19] E. Haas, "Aeronautical channel modeling," *IEEE Transactions on Vehicular Technology*, vol. 51, no. 2, pp. 254-264, Mar. 2002.

Yuchu Ji received his Ph.D. degree in School of Electronic Information Engineering, Tianjin University, Tianjin, China in 2014. Currently, he is a Lecturer at College of Electronic Information and Automation in Civil Aviation University of China. His research interests include 3 part, wireless sensor network and wireless communication system, cooperative communication, and intelligent airport.

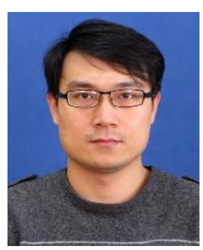

Yang Wang received his Ph.D. degree in Control Science and Engineering from Tianjin University, China in 2013. Currently, he is a Lecturer at Civil Aviation University of China. His research interests include artificial olfaction, mobile robotics and intelligent airport.

Yuan Sang received her master degree in School of Information and Control Engineering from China University of Mining and Technology in 2011. She is a Wireless Communication Engineer and also an Information Technology Engineer in Inventec Group (Tianjin) Electronic Technology Company.

Broadband Circularly Polarized Antenna by Using Polarization Conversion Metasurface

Zi-Jian Han [1,2], Wei Song [1*], and Xin-Qing Sheng [1]

[1] Center for Electromagnetic Simulation, School of Information Science and Technology
Beijing Institute of Technology, Beijing 100081, China
wsong@bit.edu.cn

[2] Beijing Institute of Space Long March Vehicle, Beijing 100076, China

Abstract **─** A compact and broadband circularly polarized antenna is proposed. A linear-to-circular polarization conversion metasurface is designed to broaden the 3-dB axial ratio bandwidth and the impedance bandwidth of the proposed antenna, with the mechanism of the metasurface investigated. Different with the conventional metasurface antenna designed by using uniform unit cells, this design makes use of two metasurface arrays with different unit cells. Full wave simulations show that the 10-dB impedance bandwidth of the proposed antenna is from 4.32 to 6.5 GHz (40.3%), and the 3-dB AR bandwidth is from 5 to 5.61 GHz (11.5%). Compared with that using the uniform elemental array, this design leads to more than 10% improvement in the 10-dB impedance bandwidth and more than 11.7% improvement in the axial ratio bandwidth. The proposed antenna has been fabricated and the simulated results have been verified with the measurements.

Index Terms **─** Circularly polarized antenna, linear-to-circular polarization conversion, metasurface.

I. INTRODUCTION

Metasurface (MS) has attracted much attention due to its unique properties in the past few years [1]. It is usually formed by regular or irregular periodic planner arrays and presents EM properties not found in natural materials. With advantages of planar structure and strong capability of manipulating electromagnetic waves, MS can be easily integrated on traditional antennas and provide a promising approach for new antenna designs with improved performances [2-13].

For radar, wireless, and satellite communication applications, circularly polarized (CP) antennas [14, 15] are widely used because of their immunities to multipath distortion and polarization mismatch losses. MS can be utilized to improve the CP performance or to convert a linearly polarized radiation from antennas to a circularly polarized one without deteriorating the radiation performance [3]. Dual-band conversion can also be realized by a single metasurface [4]. By properly combining the transmitted wave from the antenna and the reflected wave from the metasurface, broadband circular polarization can be obtained [5-7]. In [8-10], the metasurfaces work as polarization convertors and the E-field can be resolved into two orthogonal components. In this way, the circularly polarized wave can be possibly generated with wider bandwidth. In order to enhance the impedance-matching and the AR bandwidths, surface waves are excited on the MS to generate additional resonances with minimum AR points [11, 12]. Based on the mushroom antenna [1], a new wideband CP antenna can be realized by rotating the angle of the feed slot for a polarization-dependent MS superstrate [13].

The above MS antennas are all based on periodic MS arrays with the same unit cells. In this paper, we demonstrate by combining two linear-to-circular polarization conversion MS (PCMS) arrays, the 3-dB axial ratio (AR) bandwidth and impedance bandwidth can be further broadened. Simulation shows that the 10-dB impedance bandwidth for the proposed MS antenna is 40.3% from 4.32 to 6.5 GHz, and the 3-dB AR bandwidth is 11.5% from 5 to 5.61 GHz. Compared with the same element array, more than 10% improvement for 10-dB impedance bandwidth and more than 11.7% improvement for 3-dB AR bandwidth can be obtained. As the design verification, the proposed antenna is fabricated and measured. The measurement results agree with the simulation results.

II. ANTENNA DESIGN

A. Linear-to-circular polarization conversion MS

A linear-to-circular PCMS is made of arrays of the unit cell as shown in Fig. 1 (a). The unit cell consists of a metallic patch with a 45 degree-oriented rectangular slot and a substrate board with the thickness of 3 mm and the relative permittivity of 4.4. The dimensions of the unit cell specified in Fig. 1 (a) are as follows:

Submitted On: January 3, 2020
Accepted On: May 2, 2020

1054-4887 © ACES

$px = py = 11$mm, $l = w = 10$mm, $ls = 11$mm, and $ws = 0.65$mm. Consider an x-polarized plane wave normally illuminated on the bottom of the PCMS. This means the incidence only contains Ex component. The amplitudes of the transmitted E-field components are simulated by commercial software Ansoft HFSS. Master/slave boundaries are utilized based on a unit-cell model. The simulation results show that the amplitude intersections of Ex and Ey can be obtained and the corresponding frequency of the matching point varies with the length of the slots on the patch (Ref. Fig. 1 (b)).

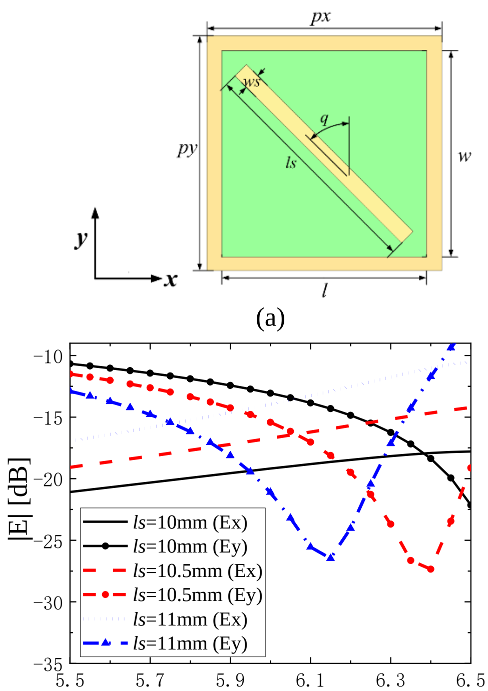

(a)

(b)

Fig. 1. (a) A unit cell of the PCMS, and (b) the amplitudes of the transmitted E-field components.

This indicates that, after the x-polarized plane wave transmits through the MS, both Ex and Ey components are generated with equal amplitudes in the transmitted wave. In this way, circularly polarized wave can be possibly generated when the MS array is properly designed. Accordingly, by considering the PCMS as a half-wavelength resonant cavity, the resonant length of slot can be qualitatively estimated by the following equation

$$ls = \lambda_e / 2 = \lambda / 2\sqrt{\varepsilon_r}, \quad (1)$$

where ls is the wavelength in the dielectric substrate and ε_r is the relative permittivity of the substrate.

As shown in Fig. 2, at 5.75GHz, the currents on slot with $ls = 11$ mm are better excited than that on slot with $ls = 10$mm, which further verifies the linear-to-circular polarization conversion function of the slot.

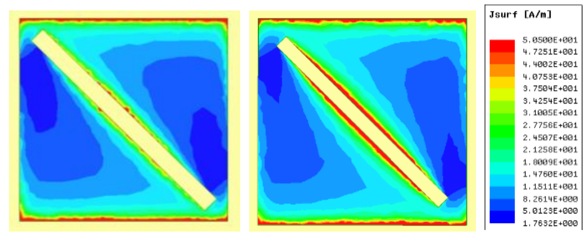

(a) $ls = 10$mm (b) $ls = 11$mm

Fig. 2. Simulated surface current amplitudes of the PCMS at 5.75 GHz for different slot lengths.

B. CP Antenna incorporating two CPMSs

Based on a MS-based broadband low-profile mushroom antenna as presented in [1], by simply replacing the mushroom EBG with the aforementioned PCMS arrays on a planar slot-coupling antenna, we obtain the proposed CP antenna. In order to obtain broader 3-dB AR and impedance bandwidths, the 4 by 4 PCMS array are separated into two 2 by 4 arrays as depicted in Fig. 3. After optimization, the dimension parameters of the PCMS arrays are determined as follows (in unit of mm): $l = 8.25$, $w = 8$, $px = 9.45$, $py = 9.2$, $ls1 = 9.45$, $ws1 = 0.65$, $ls2 = 8.8$, and $ws2 = 0.65$. The tilt angles for the two CPMSs are $q1 = 52.5^\circ$ and $q2 = 57^\circ$ respectively. The parameters of the feeding slot antenna are (in unit of mm): $le = 25$, $we = 2$, $lf = 27.5$, $wf = 2.1$, $lg = 16$, $wg = 5$, and $gf = 1.55$. Here, FR4 ($\varepsilon_r = 2.2$) is used as substrate for both the PCMS and the antenna. The thicknesses of the PCMS substrate and the antenna substrate are $h = 3$mm and $t = 1$mm respectively. A waveguide port is assigned to the coplanar waveguide as excitation in the HFSS model as shown in Fig. 3 (b). Figure 4 (a) shows the simulated S11 for the MS antenna. The simulated impedance bandwidth for S11< −10 dB is 4.32–6.5 GHz (40.3%). Figure 4 (b) shows the simulated axial ratio and gain in the boresight direction for the proposed antenna. It shows the PCMS array resulted in stable left-hand circular polarization (LHCP) radiation. The 3-dB AR bandwidth is from 5 to 5.61 GHz, about 11.5%. In Fig. 4 (c) the simulated radiation patterns of the proposed antenna at 5.3 GHz is provided.

The simulation results show that, as the time changes, the surface currents located at the azimuth angle turn in a clockwise manner. Figure 5 shows snapshots of the surface currents of the proposed antenna at 5.2 GHz for three different time phases (ωt), from 0° to 90°, with an interval of 45°. At $\omega t = 0^\circ$, the dominant surface current can be found in the y-direction, while as ωt changes to $\omega t = 45^\circ$ and then $\omega t = 90^\circ$, the dominant surface currents can be observed in the diagonal direction and then in the x-direction. Hence, the polarization characteristic is the LHCP in +z-direction.

It also can be seen in Fig. 5 that the current intensities on PCMS on different locations are different. It is understood that the discrepancy in the unit cells of CPMSs will decrease the resonance of the CPMSs in the center zone where strong mutual coupling occurs, however, strong resonance can still be formed on the edge of the structure, rendering the improved antenna performance.

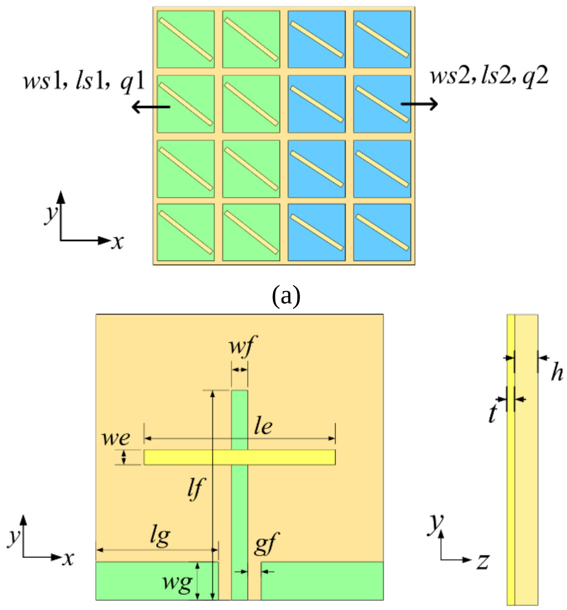

Fig. 3. Illustration of the geometry with the design parameters of the proposed antenna: (a) the top view; (b) the back view and the side view.

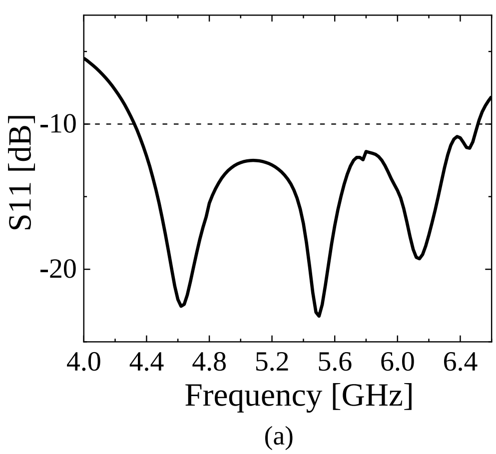

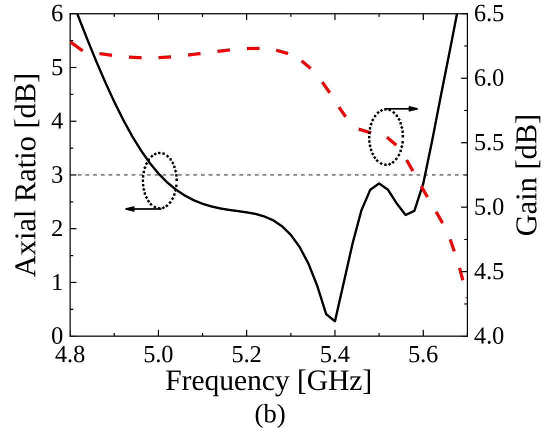

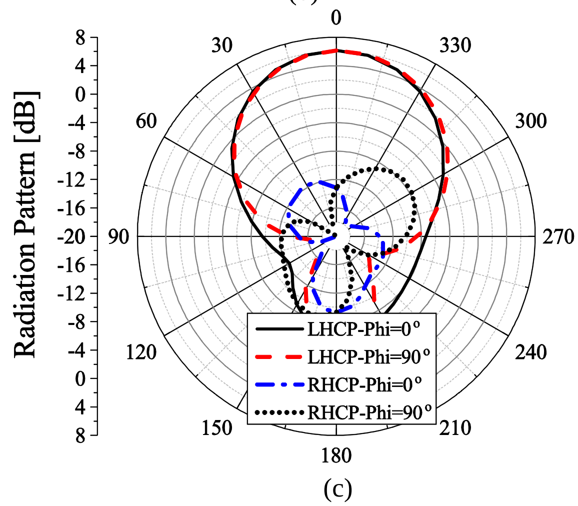

Fig. 4. (a) The simulated S11, (b) AR and broadside gain, and (c) the radiation pattern at 5.3GHz of the proposed antenna.

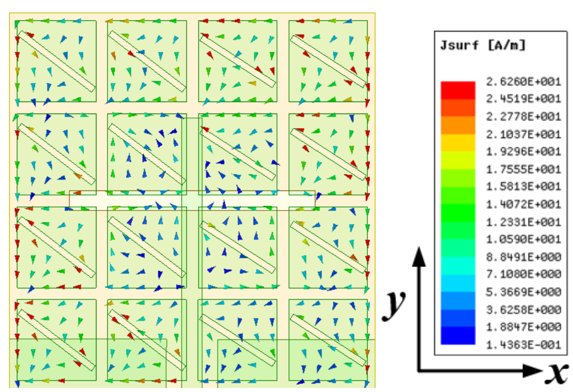

(a) $\omega t = 0^{\circ}$

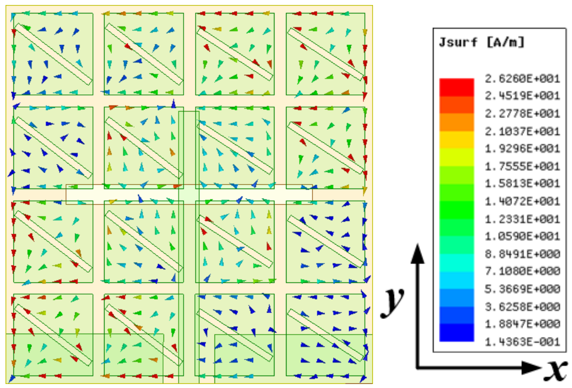

(b) $\omega t = 45^{\circ}$

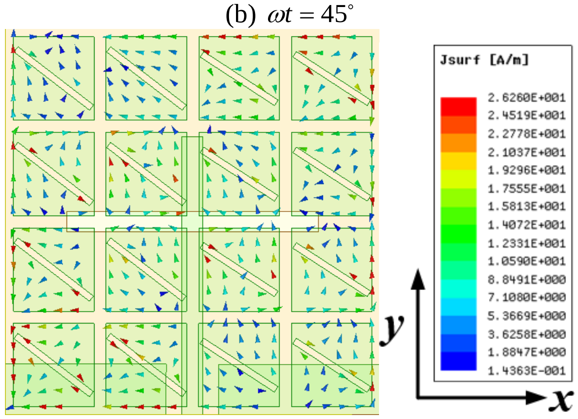

(c) $\omega t = 90^{\circ}$

Fig. 5. Simulated surface current distributions of the proposed antenna at 5.3 GHz for different time instants.

III. EXPERIMENTAL RESULTS

In Fig. 6, the simulated axial ratio (AR), the broadside gain, and the S11 parameter of the proposed antenna based on two different dimensions of PCMS arrays are compared with those of the two antennas with uniform PCMS arrays. The key parameters which are different among the three antennas are specified in the figure. The rest parameters are the same with those in Section II. It can be seen that wider 3-dB AR bandwidth and impedance bandwidth can be achieved by properly adjusting the length and rotating the angle (in degrees) of the rectangular slots without deteriorating the radiation performance. Parametric studies are performed to identify the effect of separating to two PCMS arrays on the impedance bandwidth, AR bandwidth in the boresight direction and the results provide a useful strategy to broaden the bandwidth for practical design. Compared with the antenna used by same elements with the wider bandwidth, more than 10% improvement for 10-dB impedance bandwidth and more than 11.7% improvement for 3-dB AR bandwidth can be obtained by adopting the combination of the two PCMS arrays.

The proposed antenna as shown in Fig. 7 is etched on FR4 substrate with a relative permittivity of 4.4 and a loss tangent of 0.02. Its characteristics are measured as design verification. As depicted in Figs. 8 (a) and (b), the measured results show that the 10-dB impedance bandwidth for the proposed MS antenna is 38.3% from 4.56 to 6.72 GHz, and the 3-dB AR bandwidth is 11.3% from 5 to 5.6 GHz. Figures 8 (c) and (d) show the simulated and measured radiation patterns at 5.3GHz. As can be found in Fig. 8, the measured results show good agreement with the simulated ones, and the deviations could be attributed to the fabrication and measurement tolerance.

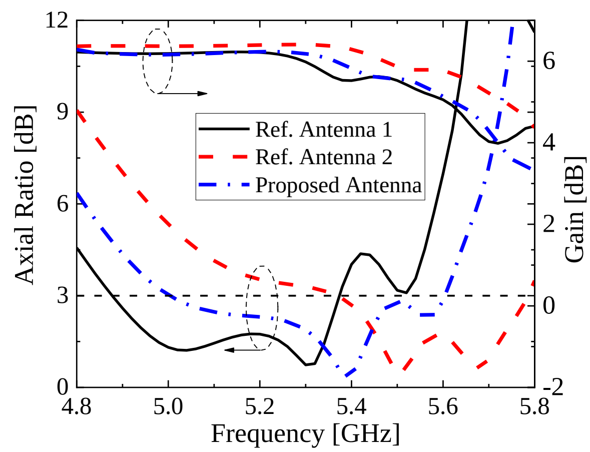

(a)

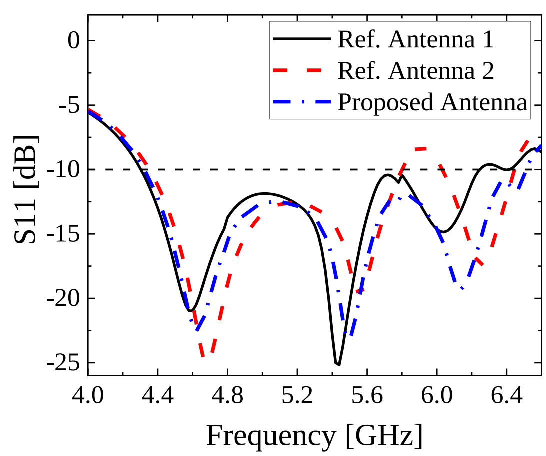

(b)

Fig. 6. (a) The AR, broadside gain and (b) the S11 of the proposed antenna and the two reference antennas with uniform PCMS array (the proposed antenna: (ls1,ls2,q1,q2)=(9.45mm, 8.80mm, 52.5º, 57º); Ref. Antenna 1: (ls1, q1)=(9.45mm, 52.5º); Ref. Antenna 2: (ls2, q2)=(8.80mm, 57º)).

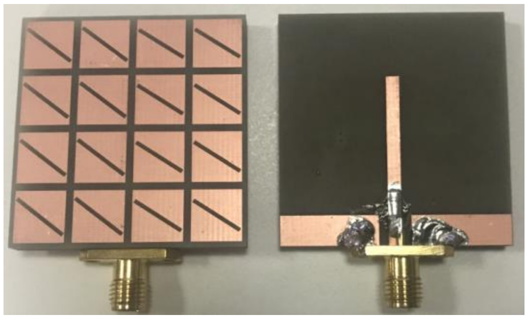

Fig. 7. Photographs of the fabricated antenna prototype.

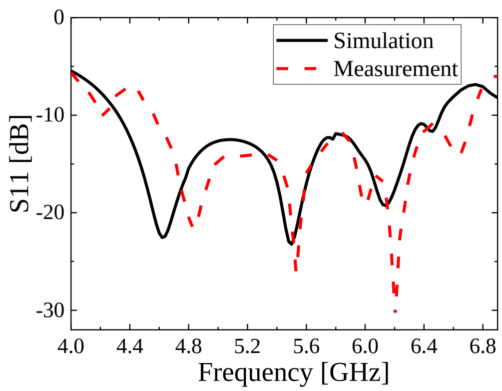

(a)

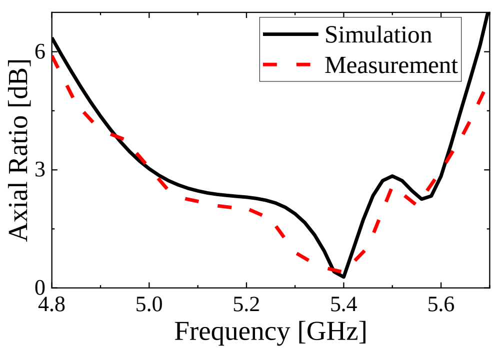

(b)

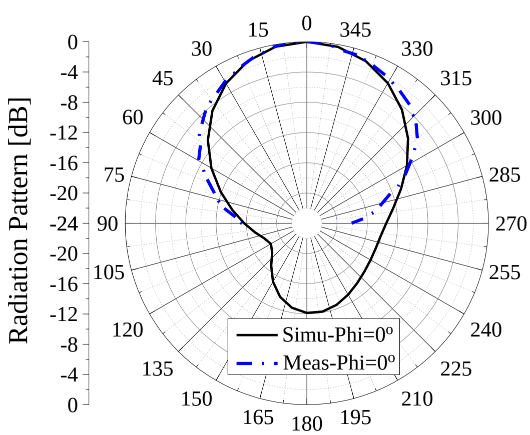

(c)

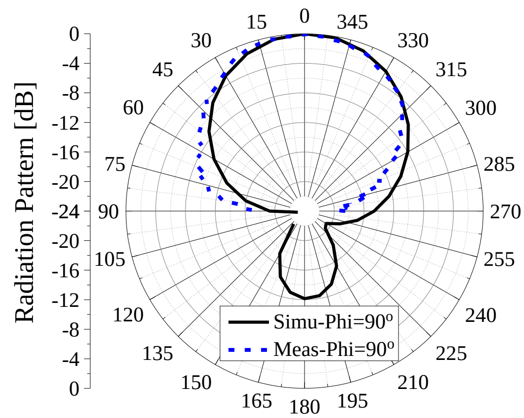

(d)

Fig. 8. (a) The S11, (b) the axial ratio, (c) the radiation patterns normalized by maxima at 5.3 GHz of the proposed antenna at $\varphi = 0^{\circ}$ plan, and (d) the radiation patterns normalized by maxima at 5.3 GHz of the proposed antenna at $\varphi = 90^{\circ}$ plan.

IV. CONCLUSION

An efficient method is presented to broaden the 3-dB AR bandwidth and the impedance bandwidth based on two PCMS arrays with different parameters in this paper. The proposed antenna design exhibits more than 10% improvement for 10-dB impedance bandwidth and more than 11.7% improvement for the 3-dB AR bandwidth compared with that composing the PCMS array with uniform elements. The simulated and measured results are in good agreement to verify the proposed antenna.

ACKNOWLEDGMENT

This work is supported by the National Key R&D Program of China under Grant 2017YFB0202500, and the NSFC under Grant No. 61601023 and U1730102.

REFERENCES

[1] W. Liu, Z.-N. Chen, and X. Qing, "Metamaterial-based low-profile broadband mushroom antenna," *IEEE Trans. Antennas Propag.*, vol. 62, no. 3, pp. 1165-1172, 2013.

[2] Z.-J. Han, W. Song, and X.-Q. Sheng, "Gain enhancement and RCS reduction for patch antenna by using polarization-dependent EBG surface," *IEEE Antennas Wireless Propag. Lett.*, vol. 16, pp. 1631-1634, 2017.

[3] F. Yang and Y. Rahmat-Samii, "A low profile single dipole antenna radiating circularly polarized waves," *IEEE Trans. Antennas Propag.*, vol. 53, no. 9, 3083-3086, 2005.

[4] H. Yi and S.-W. Qu, "A novel dual-band circularly polarized antenna based on electromagnetic band-

gap structure," *IEEE Antennas Wireless Propag. Lett*., vol. 12, pp. 1149-1152, 2013.

[5] H.-P. Li, G.-M. Wang, J.-G. Wang, and X.-J. Gao, "Wideband multifunctional metasurface for polarization conversion and gain enhancement," *Progress In Electromagnetic Research*, vol. 155, pp. 115-125, 2016.

[6] T. Nakamura and T. Fukusako, "Broadband design of circularly polarized microstrip patch antenna using artificial ground structure with rectangular unit cells," *IEEE Trans. Antennas Propag*., vol. 59, no. 6, pp. 2103-2110, 2011.

[7] S. Maruyama and T. Fukusako, "An interpretative study on circularly polarized patch antenna using artificial ground structure," *IEEE Trans. Antennas Propag*., vol. 62, no. 11, pp. 5919-5924, 2014.

[8] H.-L. Zhu, S.-W. Cheung, K.-L. Chung, et al., "Linear-to-circular polarization conversion using metasurface," *IEEE Trans. Antennas Propag*., vol. 61, no. 9, pp. 4615-4623, 2013.

[9] H.-L. Zhu, S.-W. Cheung, K.-L. Chung, et al., "Design of polarization reconfigurable antenna using metasurface," *IEEE Trans. Antennas Propag*., vol. 62, no. 6, pp. 2891-2898, 2014.

[10] C. Chen, Z. Li, L.-L. Liu, J. Xu, P. Ning, B. Xu, X. Chen, and C.-Q. Gu, "A circularly-polarized metasurfaced dipole antenna with wide axial-ratio beamwidth and RCS reduction functions," *Progress In Electromagnetics Research*, vol. 154, pp. 79-85, 2015.

[11] S.-X. Ta and I. Park, "Low-profile broadband circularly polarized patch antenna using metasurface," *IEEE Trans. Antennas Propag*., vol. 63, no. 12, pp. 5929-5934, 2015.

[12] S.-X. Ta and I. Park, "Compact wideband circularly polarized patch antenna array using metasurface," *IEEE Antennas Wireless Propag. Lett*., vol. 16, pp. 1932-1936, 2017.

[13] Z. Wu, L. Li, Y. Li, et al., "Metasurface superstrate antenna with wideband circular polarization for satellite communication application," *IEEE Antennas Wireless Propag. Lett*., vol. 15, pp. 374-377, 2016.

[14] M. I. Sabran, S. K. A. Rahim, P. J. Soh, C. Y. Leow, and G. Vandenbosch, "A simple electromagnetically fed circularly-polarized circular microstrip antenna," *Applied Computational Electromagnetics Society Journal*, vol. 30, no. 11, pp. 1180-1187, 2015.

[15] M. Shokri, S. Asiaban, and Z. Amiri, "Study, design and fabrication of a cpw fed compact monopole antenna with circular polarization for ultra wide band systems application," *Applied Computational Electromagnetics Society Journal*, vol. 32, no. 9, pp. 749-753, Sep. 2017.

Numerical Analysis of Wideband and High Directive Bowtie THz Photoconductive Antenna

Amira Dhiflaoui [1], Ali Yahyaoui [1,2], Jawad Yousaf [2,3], Shahid Bashir [4], Bandar Hakim [2], Toufik Aguili [1], Hatem Rmili [1,2], and Raj Mittra [2,5]

[1] University of Tunis El Manar (UTM), National Engineering School of Tunis (ENIT)
Communications Systems Laboratory (SysCom), BP 37, Belvédère 1002 Tunis, Tunisia

[2] Electrical and Computer Engineering Department, Faculty of Engineering, King Abdulaziz University
P.O. Box 80204, Jeddah 21589, Saudi Arabia

[3] Department of Electrical and Computer Engineering, Abu Dhabi University, United Arab Emirates
hmrmili@kau.edu.sa

[4] Department of Electrical Engineering, University of Engineering & Technology, Peshawar, Pakistan

[5] Electrical and Computer Engineering Department, University of Central Florida, EMC Lab, Orlando, FL 32816 USA

***Abstract* –** This paper presents a novel wideband and high directivity Bowtie photoconductive antenna (PCA) for THz frequency applications. The radiation properties of proposed PCA were analyzed by varying important design parameters, such as substrate thickness, conductor thickness, bowtie antenna width, length and gap. The optimized values of these parameters are then used to design a wideband PCA THz antenna which exhibits impedance bandwidth of 3 THz, 3 dB AR bandwidth of 6 THz, peak directivity of about 18.2 dBi and peak radiation efficiency of 98% within the operating band. To improve the directivity of the proposed antenna, a silicon-based lens is added in the structure and the effect of silicone lens on THz antenna directivity is also studied for enhanced directivity of proposed antenna. The proposed THz antenna can be a prospective candidate for future THz applications such as spectroscopy, imaging, sensing and indoor communication.

***Index Terms* –** Bowtie antenna, high directivity, photoconductive THz antenna, wideband.

I. INTRODUCTION

Due to an increased demand for high data rate and wide bandwidth applications there has been a consistent trend of moving towards higher frequency bands in the electromagnetic spectrum. The recent emergence of 5G technology has commercialized the use of millimeter waves (30GHz to 300GHz) for high data rate communication [1-3]. Now, there has been an ongoing attempt to use THz waves or submillimeter waves having frequency from 0.3 THz to 10 THz for specialized applications like brain imaging, tumor detection, security screening, material characterization using spectroscopy, bio-sensing, high data rate indoor communication and non-invasive imaging [4-9].

However, antenna design for THz is a big challenge in itself. Antenna design techniques used at low frequency are not applicable at THz range. Due to very small operating wavelength, the size of antenna becomes very small making it impossible to feed such an antenna using conventional feeding mechanism [3]. However, loss in THz signal power as it propagates is a serious challenge. This necessitates high gain THz antenna to compensate the losses and polarization insensitivity characteristics, particularly for imaging and sensing applications.

THz antennas working on the principle of photoconduction are getting attention by researchers working in the field of THz systems. However, their limitation is reduced radiated THz power and thus low efficiency [10-12]. Also, as compared to microwave antennas THz antennas require different excitation and current generation process that involve losses. A wideband on-chip dielectric resonator antenna (DRA) operating at sub-THz frequencies was proposed with a bandwidth of 65 GHz [4]. Low directivity is another constraint in THz antenna design. A bowtie-shaped antenna combined with a silicon-based lens and with an artificial magnetic conductor (AMC) was proposed to enhance its directivity properties [5]. The other reported examples of THz PCA designs are dipole planner array [13], Yagi-Uda [14], bow tie [11, 12, 15, 16], conical

Submitted On: January 12, 2020
Accepted On: April 20, 2020

horn [17] and spiral-shaped [18]. The authors used the antireflection coatings [11, 19], integration of lens [11, 12, 20-23] and metasurfaces [5, 13, 15] with antenna structures to enhance THz antennas directivity.

In this paper we have proposed a novel ultra wideband (UWB) and high directivity bowtie photoconductive antenna for THz band. The radiation properties of proposed antenna have been optimized after parametric analysis of critical design parameters. From full-wave EM simulations, the proposed antenna achieves the -10 dB impedance bandwidth of 3 THz with peak gain of about 15 dBi and radiation efficiency of 98% within the operating band. The antenna exhibit impedance matched behavior across 2 THz to 5 THz band. The directivity of antenna has also been enhanced using lens with optimized design parameters. The design, shape and structure of the added lens is selected carefully to ensure the wideband operation as well as improved directivity from the realized design. The designed antenna shows superior performance in terms of impedance bandwidth and efficiency as compared to the designs proposed in [10-18]. The detailed analysis of the design procedure, parametric study, effect of the added lens on the antenna performance and discussion about the obtained results is given in the following sections.

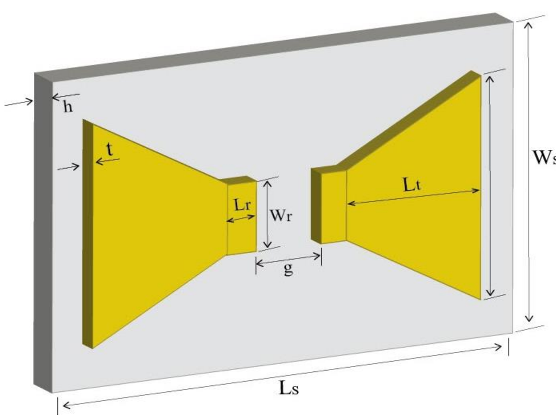

Fig. 1. Design of bowtie THz antenna.

Table 1: Initial design dimensions of Bowtie THz antenna

Parameters	Values (μm)
L_s	347
h	1.3
t	0.02
W_s	340
L_t	103
W_t	220
W_r	7
L_r	12
g	7.6

II. DESIGN PROCEDURE

A. Antenna design

The proposed antenna design is shown in Fig. 1. It is basically a bowtie antenna printed on a photoconductive substrate. DC bias is applied across the bowtie antenna. In order to generate THz radiation from this bowtie antenna, optical pulse is incident on the antenna gap (*g*), which propagates into the photoconductor and generate photocarriers inside the photoconductor. The generated photocarriers are accelerated in the DC bias field, producing a transient photocurrent, which drives the bowtie antenna and ultimately re-emits as a THz frequency pulse [24]. The metal conductor of the designed bowtie antenna has thickness of '*t*' and is made of gold conductor whereas the substrate is made of quartz. The relative permittivity and loss tangent of the used substrate material is 3.78 and 0.0001, respectively. The full-wave numerical analysis of the proposed bowtie THz antenna is performed in CST MWS. The initial dimensions of the designed antenna are given in Table 1.

In order to increase the directivity of this antenna a hemispherical lens is placed on bottom side as shown in Fig. 2.

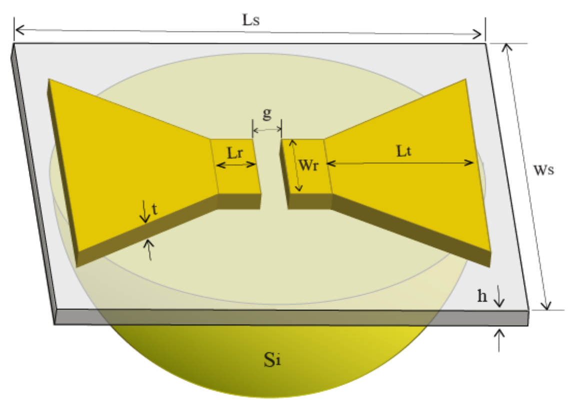

Fig. 2. Design of Bowtie THz antenna with lens.

B. Optimization of the UWB THz antenna

Firstly, the parametric analysis of the antenna design parameters of Fig. 1 is performed to obtain the optimized design parameters for the ultra-wideband (UWB) impedance matching characteristics. The major issues in the modeling are about the extensive analysis of the effect of the different antenna design parameters on its performance. For this purpose, a parametric analysis was performed to obtain the optimized design parameters for the ultra-wideband impedance matching characteristics. The variation ranges of the various design parameters for the parametric study are selected carefully keeping in view the fabrication constrains to minimize the extensive memory requirements of the numerical models with various design parameters

The upper and lower limit of each parameter is chosen by covering the maximum range of values without affecting the shape of the proposed antenna. In all parametric analysis we present only the important parameters values which give us significant behavior keeping in view the fabrication constrains.

1) Effect of Substrate Thickness (h)

Because the thickness of the substrate (h) is usually larger than the wavelength of THz waves, surface/ substrate modes may be generated and the effect of the substrate cannot be ignored. For this purpose, parametric study was conducted by varying the substrate thickness from 1.3 µm to 4.3 µm. The effect on S_{11} is shown in Fig. 3. As thickness increases the impedance matching behavior slightly degrades at upper operating frequencies. The results depict that for the optimal value of substrate thickness, *i.e.*, 2.3 µm, the -10 dB impedance bandwidth of the designed antenna is around 3 THz (2 to 5 THz).

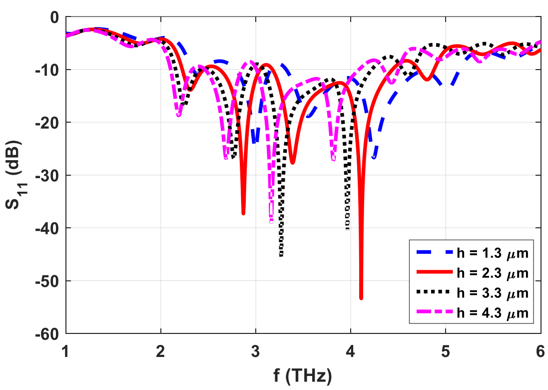

Fig. 3. S_{11} of THz antenna without lens with the variations in substrate thickness (h).

Normally, the antennas having -10 dB impedance bandwidth of greater than equal to 500 MHz or fractional bandwidth (FBW) of more than 20% are referred as ultra-wideband (UWB) antennas [25] [26]. As depicted in Fig. 3, the -10 dB impedance bandwidth ($|S_{11}| \leq -10\ dB$) and FBW of our proposed antenna is around 3 THz and 50% respectively, that's why we are using the term of UWB THz antenna for the proposed antenna structures.

2) Effect of Gold Thickness (t)

The effect of metal thickness (t) of top layer of proposed THz antenna is studied parametrically as shown in Fig. 4. The metal thickness is varied from 0.02 µm to 0.05 µm and only slight variation in the impedance matching characteristics across the band is observed.

3) Effect of L_s

The parametric study on L_s is also conducted and the variations in S_{11} are shown in Fig. 5 which depicts that this parameter has also no effect on S_{11} as like metal thickness variations.

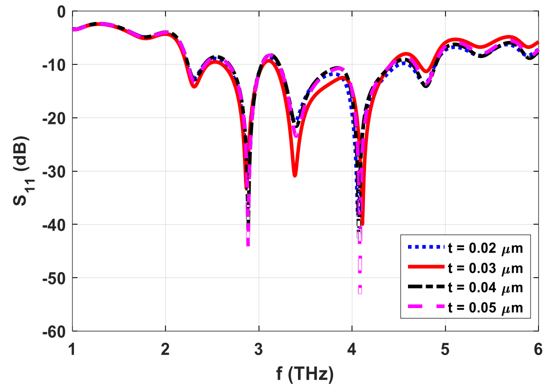

Fig. 4. S_{11} of THz antenna without lens with the variations in metal thickness (t).

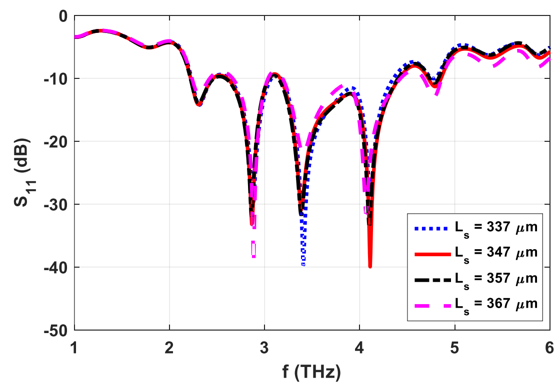

Fig. 5. S_{11} of THz antenna without lens with the variations in substrate length (L_s).

4) Effect of L_t

The effect of variation in L_t on antenna S_{11} is shown in Fig. 6. This parameter is varied from 103 µm to 124 µm and it is observed that matching behavior slightly drift towards lower frequency with increasing L_t values.

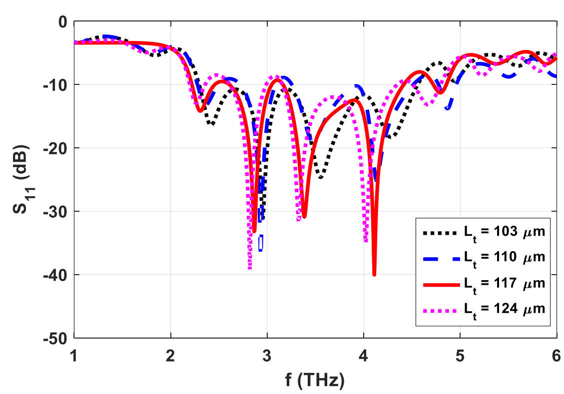

Fig. 6. S_{11} of THz antenna without lens with the variations in L_t.

5) Effect of W_r

As this parameter is varied between 7 µm to 19 µm, significant variation in S11 is observed as shown in Fig. 7. The best result is obtained for W_r =13 µm.

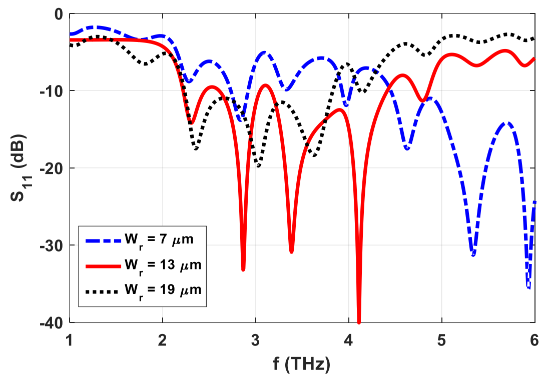

Fig. 7. S_{11} of THz antenna without lens with the variations in W_r.

6) Effect of Bowtie Aram Width (W_t)

The parameter W_t (bowtie arm width or flare angle) is varied from 220 µm to 280 µm. Figure 8 shows the effect of this variations on the reflection coefficient of the antenna. It can be noted from Fig. 8 results that the increase in W_t brings a minor shift (towards lower frequencies) in the resonance frequencies of the antenna.

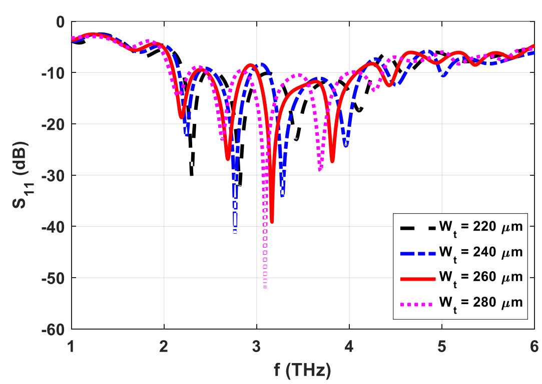

Fig. 8. S_{11} of THz antenna without lens with the variations in W_t.

7) Effect of Growth W_s

The change in reflection properties of the designed THz bowtie antenna when the parameter W_s (width of the substrate) is varied from 340 µm to 370 µm is depicted in Fig. 9. The change in the width of the substrate mainly effects the dips of the resonance frequencies without any significant change in the impedance bandwidth of the antenna.

8) Effect of g

The gap between the bowtie antenna poles is also varied from 1.6 µm to 7.6 µm to analyze its impact on S_{11} characteristics as shown in Fig. 10. As the gap width is increased from 1.6 µm to 3.6 µm the impedance matching improved. However, when *g* is increased further the impedance matching started degraded again.

Table 2 lists the optimized design parameters of the proposed bowtie THz antenna based on the conducted parametric study. The performance of the antenna is further analyzed with the addition of the lens in the antenna structure with the optimized antenna parameters of Table 2.

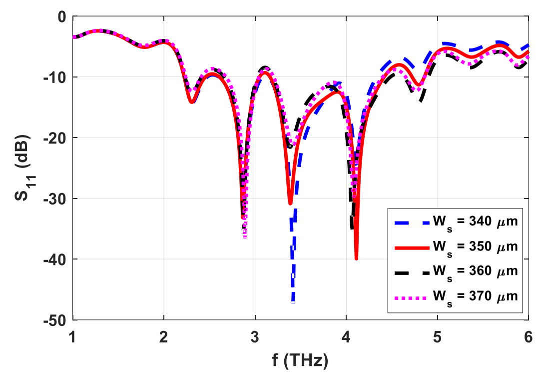

Fig. 9. S_{11} of THz antenna without lens with the variations in W_s.

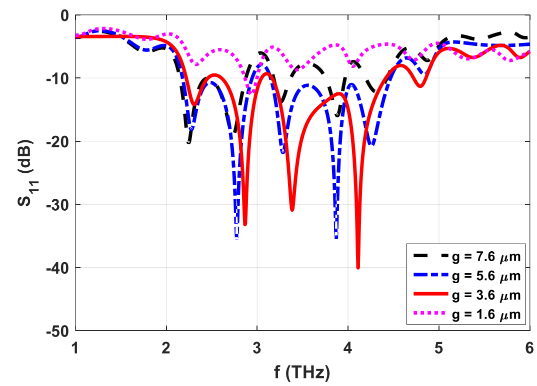

Fig. 10. S_{11} of THz antenna without lens with the variations in *g*.

Table 2: Optimized design dimensions of Bowtie THz antenna

Parameters	Values (µm)
L_s	347
h	2.3
t	0.03
W_s	350
L_t	117
W_t	260
W_r	13
L_r	8
g	3.6

III. ANALYSIS OF UWB THZ ANTENNA WITH LENS

This section describes the analysis of the change in the diameter (R_L) of the added silicon lens on the antenna performance. The performance of the antenna is analyzed in terms of the impedance matching, directivity, axial ratio and efficiency of the antenna. Following sections illustrates the conducted analysis.

A. Impedance matching

Figure 11 shows the variations in the reflection coefficient of the antenna when the diameter of the added silicon lens is changed from 80 µm to 160 µm with a step size of 40 µm. The results depict that the -10 dB impedance bandwidth of the proposed antenna improves with the increase in the diameter of the silicon lens.

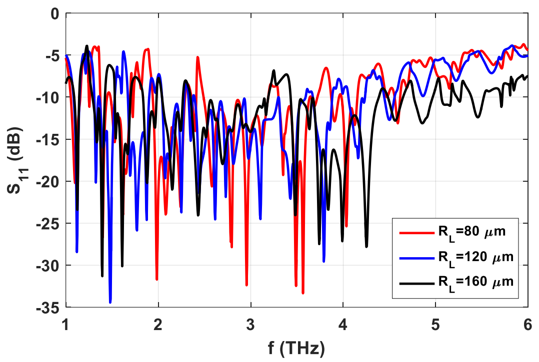

Fig. 11. Effect of variations in R_L on S_{11} of THz antenna with lens.

B. Directivity

In order to increase the directivity of proposed THz antenna, hemispherical silicone lens is placed over the bowtie antenna. The effect of radius of silicone lens on directivity is shown in Fig. 12. The best performance is observed for R_L =120 µm with consistently high directivity across the whole operating band. The directivity of the antenna decreases in higher frequency band when the diameter of the silicon lens is increased to 160 µm.

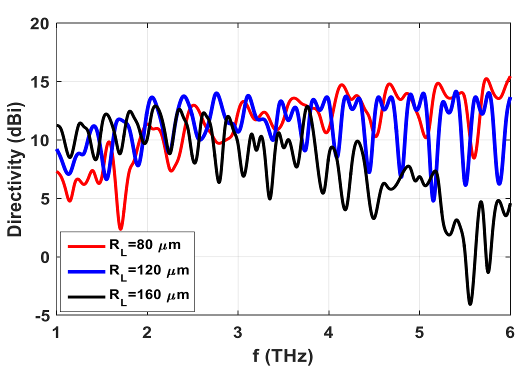

Fig. 12. Effect of variations in R_L on directivity of THz antenna with lens.

C. Axial ratio

In order to study the polarization behavior of proposed THz antenna, the axial ratio is observed for different values of R_L as shown in Fig. 13. The antenna generally exhibits linear polarization behavior. However, for R_L =160 µm circular polarization behavior is observed near 5.5 THz. It can be observed from the Fig. 13 that the 3 dB AR bandwidth of the proposed antenna is 6 THz.

The presence of the lens affects the polarization of the radiated electromagnetic fields because this lens generates a phase shift due to the wave propagation within it. This phase shift depends on the shape and the permittivity of the propagation medium constituting the lens, and thus explains the variation of the antenna polarization with the radius of the added lens. However, the polarization changes from linear to circular for a specific size of the lens means that the lens acts as a Quarter-Wavelength Plate (QWP) at certain frequency ranges, and the introduced phase shift is equal to $\pi/2$.

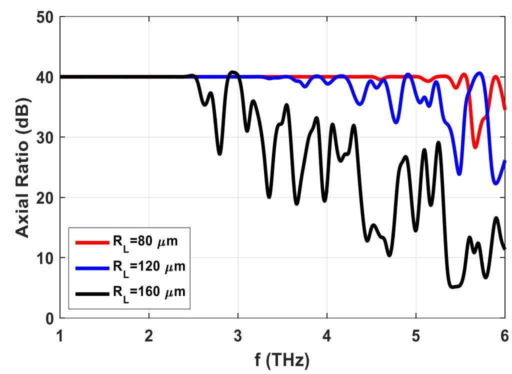

Fig. 13. Effect of variations in R_L on axial ratio of THz antenna with lens.

D. Efficiency

The effect of R_L on proposed THz antenna efficiency is also studied. Figure 14 shows the total efficiency results of the analyzed antenna for the three different diameters of silicon lens. The overall efficiency of the proposed antenna is more than 55% in the entire analyzed frequency band of 1 to 6 THz. The best efficiency is observed for R_L = 160 µm with peak value of 98%.

IV. RESULTS AND DISCUSSIONS

This section discusses the radiation pattern characteristics of the designed antenna with and without lens. The radiation pattern of proposed antenna was simulated for the three different values of RL. Figure 15 shows the 2D polar radiation pattern for R_L = 80 µm for proposed THz antenna with and without lens. It can be observed that lens significantly increased the directivity by focusing the radiation pattern towards it. The addition of the lens increases the level of the distributed current around the source location of the antenna which results in the enhancement of the infrared (IR) coupling and thus the increase of the directivity of the antenna. The peak directivity for R_L =80 µm lens in both planes is given in Table 3.

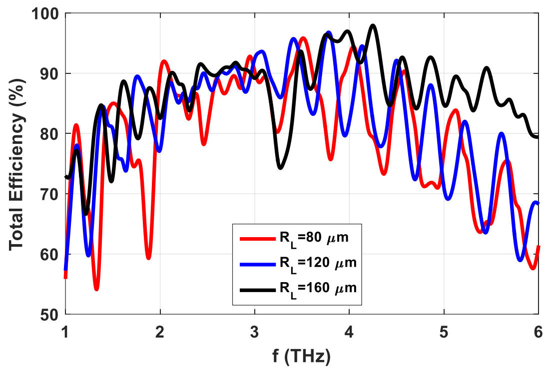

Fig. 14. Effect of variations in R_L on efficiency of THz antenna with lens.

Table 3: Increase of the antenna directivity (in dB) at different frequencies for R_L =80 µm

Frequency (THz)	Phi = 0º	Phi = 90 º
2	13.4	13.4
2.95	17.5	17.5
3.5	14.4	14.4
4.05	13.1	13.1

Figure 16 shows the 2D polar radiation pattern of the proposed THz antenna with and without lens with R_L =120 µm. Table 4 depicts the peak directivities of the designed antenna with lens which has diameter of 120 µm.

Table 4: Increase of the antenna directivity (in dB) at different frequencies for R_L =120 µm

Frequency (THz)	Phi = 0º	Phi = 90 º
1.75	18.2	18.2
2.1	15.7	15.7
3.8	16.6	16.6
4.5	11	11

The 2D polar radiation pattern of the analyzed antenna with (R_L =160 µm) and without lens is shown in Fig. 17 for different frequencies in both azimuth and elevation planes. Table 5 illustrates the increase in the peak directivity of the antenna with the addition of the lens in its structure.

The 3D patterns of proposed THz antenna with different size lens are given in Fig. 18. It can be noted from Fig. 18 that the radiation pattern is completely opposite-pointed. To increase the performance of the proposed antenna, a silicon lens is added on the backside of the structure. The structure was excited from the upper side and the target from the installed lens is to concentrate the main beam in the back side of the structure whereas reduce the lobes on the upper side. The highly directive main beam can easily be observed in all cases. It can be noted from Tables 3, 4 and 5 results that the maximum peak directivity of the designed antenna with lens diameter of 80 µm, 120 µm, and 160 µm is 17.5 dBi (@ 2.95 THz), 18.2 dBi (@ 1.75 THz) and 16.6 dBi (@ 2.15 THz). The directivity of the antenna increases with the enhancement of the lens diameter from 80 µm to 120 µm. However, a slight degradation in the directivity performance is observed with the further enhancement of the lens diameter to 160 µm.

V. COMPARISON WITH LEGACY DESIGNS

The comparison of the proposed wideband bowtie THz antenna with the available PCA designs in the literature is performed. The comparison of the proposed design is performed in terms of the antenna type, antenna substrate, antenna electrode material, lens type, -10 dB impedance bandwidth, maximum directivity, and 3dB AR bandwidth of the reported designs. The summary of the performed comparison with legacy designs in illustrated in Table 6. The authors in [10-12, 15, 17] used the hemispherical based silicon lenses to enhance the directivity of the proposed different kinds of antenna types. Malhotra *et al*. [13] and Zhu *et al*.[15] integrated the frequency selective surface (FSS) with the antenna electrodes to increase the directivity of the proposed dipole planner array and bow-tie PCAs, respectively. However, as can be noted from Table 6 that the reported maximum directivity of all compared legacy designs is less than the achieved peak directivity of proposed THz antenna. In addition, the -10 dB impedance and 3 dB AR bandwidth of the proposed bowtie antenna design is highest among all the compared legacy designs [10-18]. This comparison reflects that the proposed THz antenna can be a prospective candidate for future THz applications such as spectroscopy, imaging, sensing and indoor communication due to its wideband impedance and AR bandwidth characteristic as well as high directivity.

Table 5: Increase of the antenna directivity (in dB) at different frequencies for R_L =160 µm

Frequency (THz)	Phi = 0º	Phi = 90 º
1.6	16.4	16.4
2.15	16.6	16.6
2.45	14.8	14.8
3.75	15.7	15.7

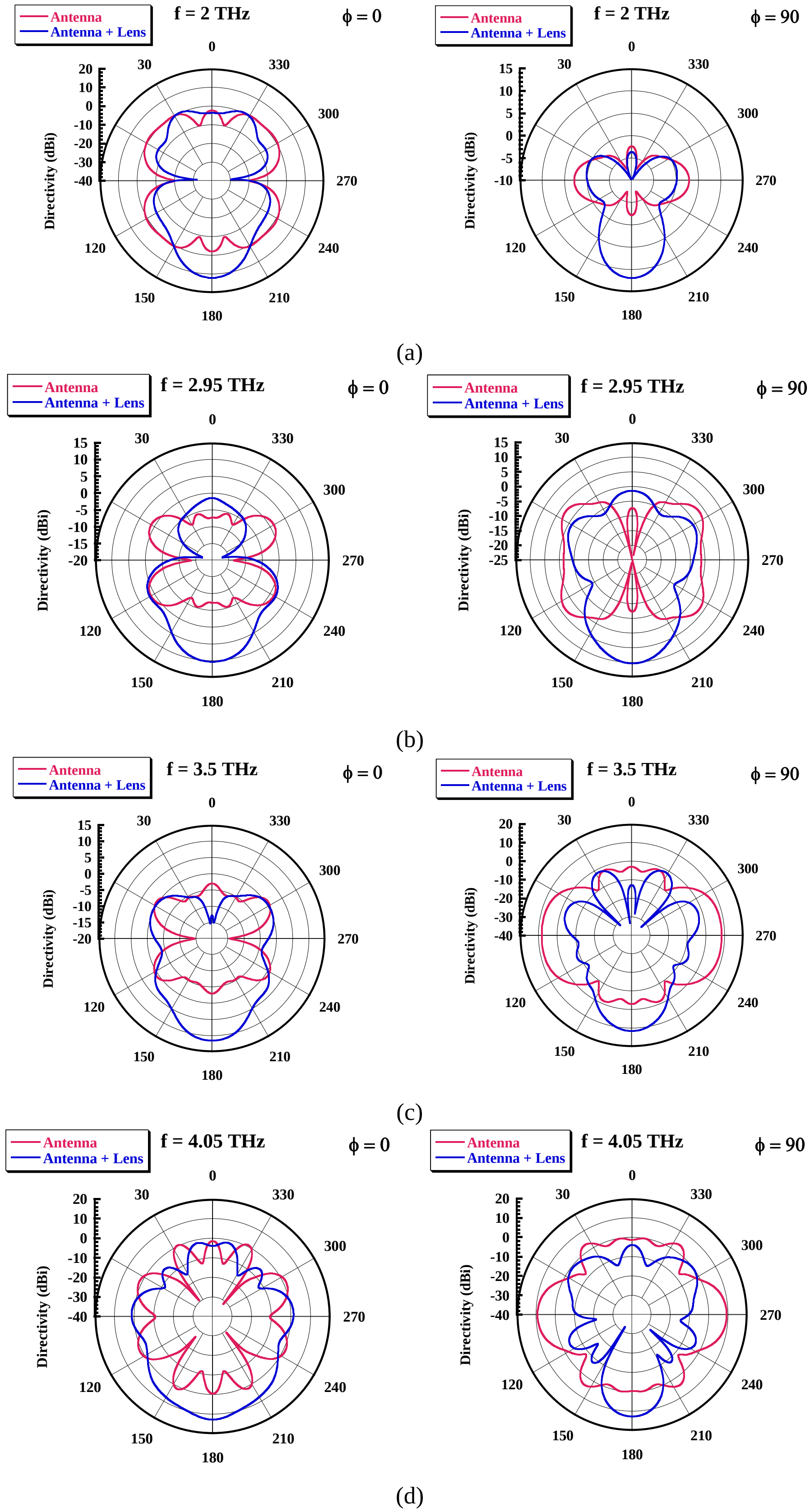

Fig. 15. 2D radiation pattern for R_L =80 μm: (a) 2 THz, (b) 2.95 THz, (c) 3.5 THz, and (d) 4.05 THz.

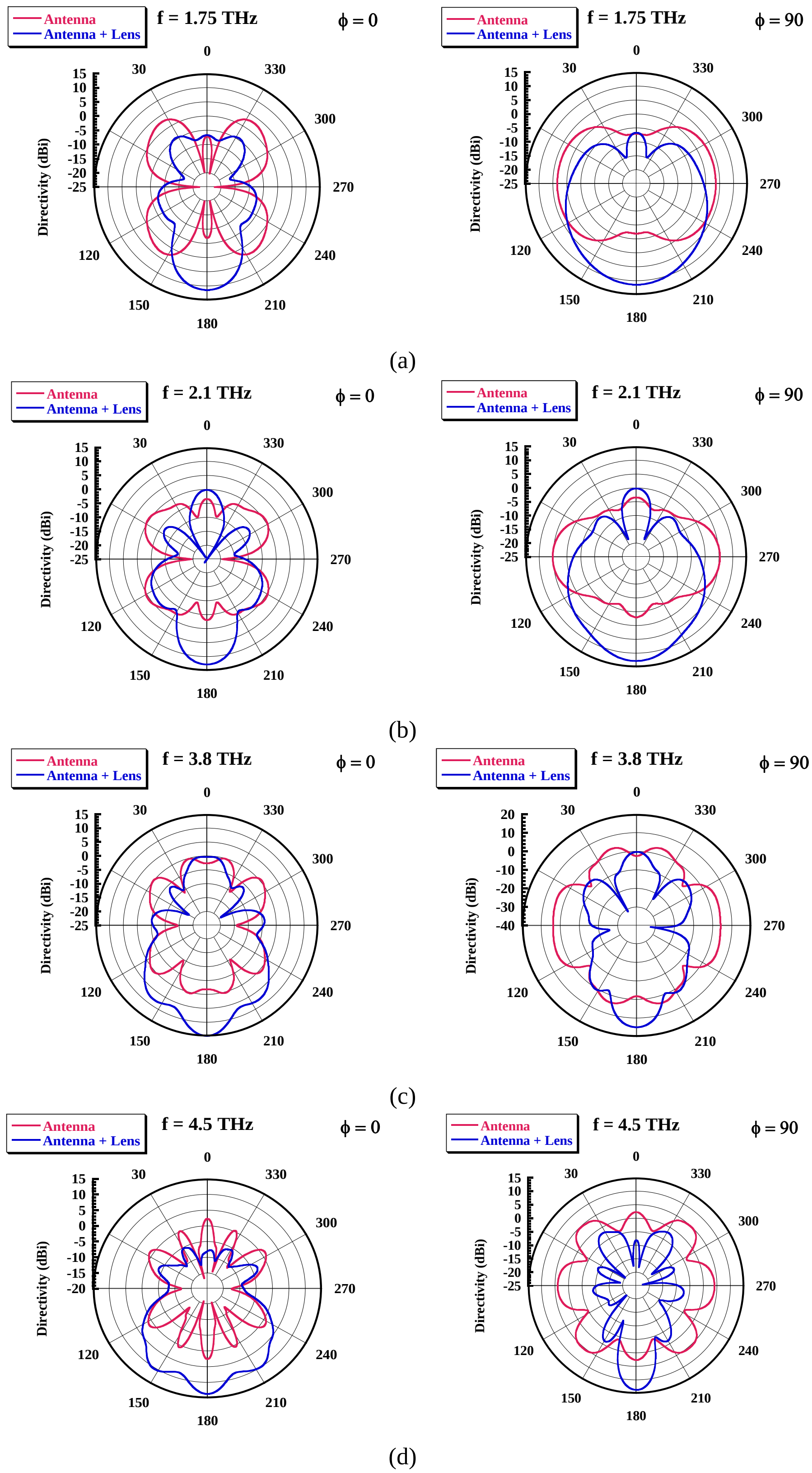

Fig. 16. 2D radiation pattern for R_L =120 µm: (a) 1.6 THz, (b) 2.15 THz, (c) 2.45 THz, and (d) 3.75THz.

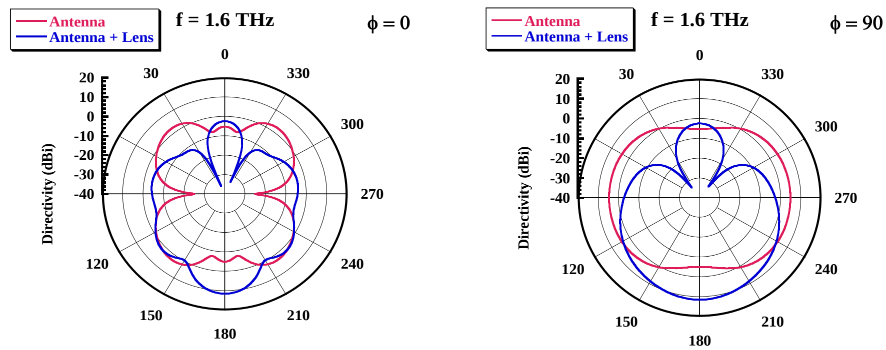

(a)

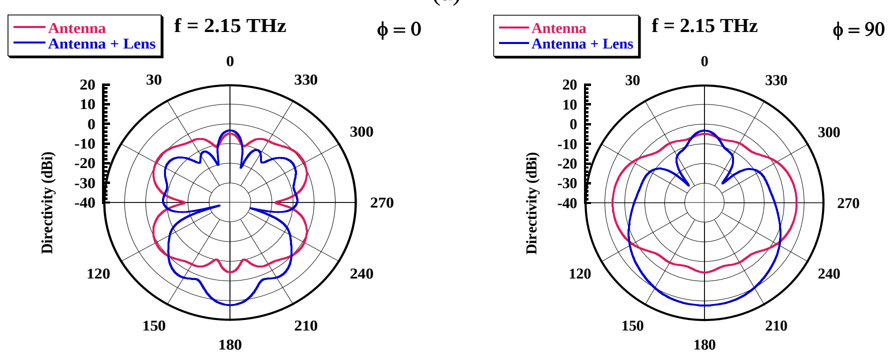

(b)

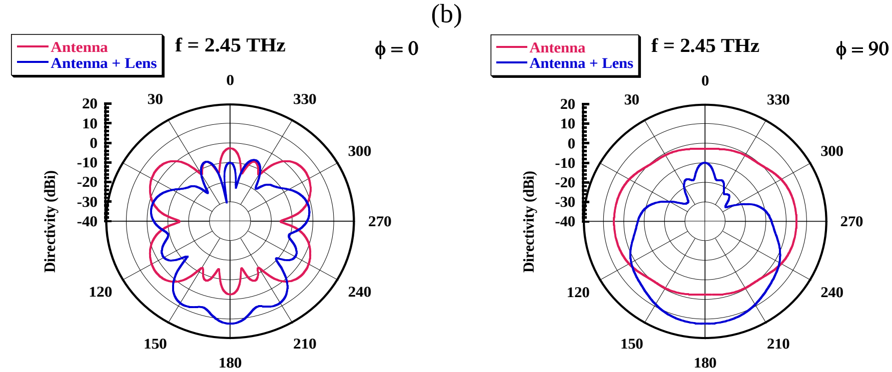

(c)

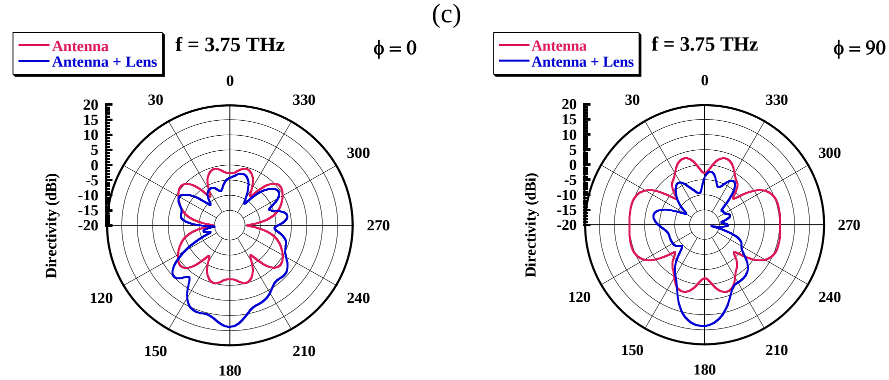

(d)

Fig. 17. 2D Radiation patter for R_L =160 μm: (a) 1.75 THz, (b) 2.1 THz, (c) 3.8 THz, and (d) 4.5THz.

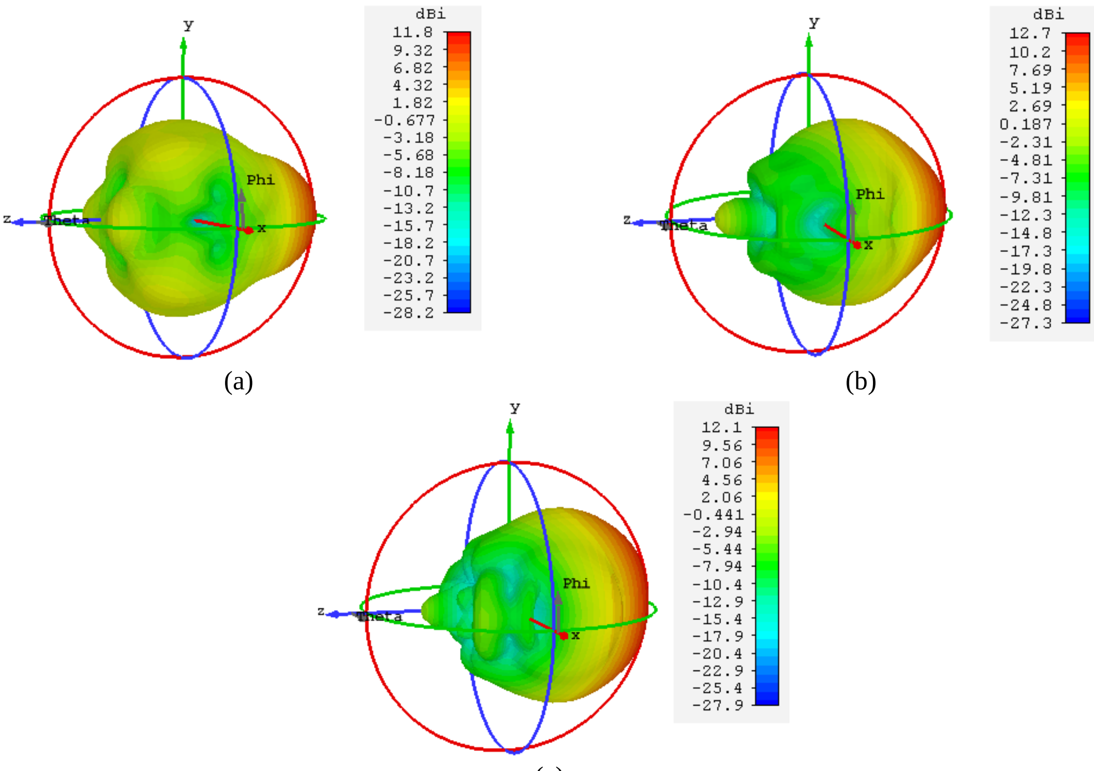

Fig. 18. 3D radiation patterns for different R_L values: (a) R_L = 80 µm at f = 2 THz, (b) R_L = 120 µm at f = 2.1 THz, and (c) R_L = 160 µm at f = 2.15 THz.

Table 6: Comparison of proposed UWB Bowtie PCA design with the legacy design

References	**Antenna Type**	**Substrate**	**Antenna Electrode Material**	**Lens/FSS**	**-10 dB Impedance Bandwidth (THz)**	**Maximum Directivity (dBi)**	**3dB AR Bandwidth (THz)**
Jyothi [12]	Bow-tie PCA	GaAs	TiAu /AuGe / AuCr	Si hemispherical lens	0.20	10.85	-
Malhotra [13]	Dipole planner array	LT-GaAs	Ti-Au	FSS	0.37	13.2	-
Gupta *et al.*[11]	Bow-tie PCA with dielectric coating	SI-GaAs	AuGe	HRFZ-Si lens	-	-	-
Zhu [15]	Bow-tie PCA	LT-GaAs	Ti-Au	No lens	0.18	8.0	-
	Bow-tie PCA			Si hemispherical lens		11.8	
	Bow-tie PCA with lens and combined with metasurface superstrate			FSS		11.9	
Han [14]	Yagi-uda	GaAs	Ti-Au	No lens	0.02	10.9	
Singh *et al.* [18]	Spiral-shaped	Si	Al	No lens	0.25	-	-
Formanek [10]	Dipole-type PCA	GaAs	Gold	Aspheric lens	0.80	-	-
Deva [17]	Conical horn	GaAs	-	Si-lens	-	18.5	-
Park [16]	Nanoplasmonic bow-tie PCA	GaAs	Cr/Au	No lens	1.00	-	-
Proposed Work	Bowtie	Quartz	Gold	Si hemispherical lens	3.00	18.2	6.00

IV. CONCLUSION

This research study has presented the full-wave numerical results of a wideband and high directivity bowtie PCA for THz frequency sensing and imaging applications. The detailed parametric analysis of the antenna design parameters was performed in CST MWS to obtain the optimal design parameters of the proposed antenna. The designed optimized bowtie PCA exhibits wideband impedance matching characteristics of 3 THz as well as 3 dB axial ratio bandwidth of 6 THz. The addition of the silicon lens with different diameters in the antenna structures increases its peak directivity to 18.2 dBi and overall efficiency of more than 55 % with peak value of 98% in the analyzed frequency band of 1 to 6 THz.

ACKNOWLEDGMENT

The project was funded by the Deanship of Scientific Research (DSR), King Abdulaziz University, Jeddah, Saudi Arabia under grant no. KEP-23-135-38. The authors, therefore, acknowledge with thanks DSR technical and financial support

REFERENCES

[1] P. U. Jepsen, D. G. Cooke, and M. Koch, "Terahertz spectroscopy and imaging – Modern techniques and applications," *Laser & Photonics Reviews*, vol. 5, no. 1, pp. 124-166, 2011/01/03 2011.

[2] I. Kasalynas, R. Venckevicius, and G. Valusis, "Continuous wave spectroscopic terahertz imaging with InGaAs bow-tie diodes at room temperature," *IEEE Sensors Journal*, vol. 13, no. 1, pp. 50-54, 2013.

[3] Y. C. Shen, T. Lo, P. F. Taday, B. E. Cole, W. R. Tribe, and M. C. Kemp, "Detection and identification of explosives using terahertz pulsed spectroscopic imaging," *Applied Physics Letters*, vol. 86, no. 24, p. 241116, 2005/06/13 2005.

[4] G. Rana, *et al.*, "A polarization-resolved study of nanopatterned photoconductive antenna for enhanced terahertz emission," *IEEE Transactions on Terahertz Science and Technology*, vol. 9, no. 2, pp. 193-199, 2019.

[5] B. M. Fischer, M. Walther, and P. U. Jepsen, "Far-infrared vibrational modes of DNA components studied by terahertz time-domain spectroscopy," *Physics in Medicine and Biology*, vol. 47, no. 21, pp. 3807-3814, 2002/10/16 2002.

[6] K. Serita, *et al.*, "Scanning laser terahertz near-field imaging system," *Optics Express*, vol. 20, no. 12, pp. 12959-12965, 2012/06/04 2012.

[7] S. Yu, B. J. Drouin, and J. C. Pearson, "Terahertz spectroscopy of the bending vibrations of acetylene 12C2H2," *The Astrophysical Journal*, vol. 705, no. 1, pp. 786-790, 2009/10/15 2009.

[8] W. Zhang, A. K. Azad, and D. Grischkowsky, "Terahertz studies of carrier dynamics and dielectric response of n-type, freestanding epitaxial GaN," *Applied Physics Letters*, vol. 82, no. 17, pp. 2841-2843, 2003/04/28 2003.

[9] I. Malhotra, K. R. Jha, and G. Singh, "Terahertz antenna technology for imaging applications: A technical review," *International Journal of Microwave and Wireless Technologies*, vol. 10, no. 3, pp. 271-290, 2018.

[10] F. Formanek, M.-A. Brun, T. Umetsu, S. Omori, and A. Yasuda, "Aspheric silicon lenses for terahertz photoconductive antennas," *Applied Physics Letters*, vol. 94, no. 2, p. 021113, 2009/01/12 2009.

[11] A. Gupta, *et al.*, "Enhanced optical-to-THz conversion efficiency of photoconductive antenna using dielectric nano-layer encapsulation," *APL Photonics*, vol. 3, no. 5, p. 051706, 2018/05/01 2018.

[12] A. Jyothi, C. Saha, B. Ghosh, R. Kini, and C. Vaisakh, "Design of a gain enhanced THz bow-tie photoconductive antenna," in *2016 International Symposium on Antennas and Propagation (APSYM)*, pp. 1-3, 2016.

[13] I. Malhotra, K. R. Jha, and G. Singh, "Design of highly directive lens-less photoconductive dipole antenna array with frequency selective surface for terahertz imaging applications," *Optik*, vol. 173, pp. 206-219, 2018/11/01/ 2018.

[14] K. Han, Y. Park, S. Kim, H. Han, I. Park, and H. Lim, "A terahertz Yagi-Uda antenna for high input impedance," in *2008 33rd International Conference on Infrared, Millimeter and Terahertz Waves*, pp. 1-2, 2008.

[15] N. Zhu and R. W. Ziolkowski, "Photoconductive THz antenna designs with high radiation efficiency, high directivity, and high aperture efficiency," *IEEE Transactions on Terahertz Science and Technology*, vol. 3, no. 6, pp. 721-730, 2013.

[16] S.-G. Park, Y. Choi, Y.-J. Oh, and K.-H. Jeong, "Terahertz photoconductive antenna with metal nanoislands," *Optics Express*, vol. 20, no. 23, pp. 25530-25535, 2012/11/05 2012.

[17] U. Deva and C. Saha, "Gain enhancement of photoconductive THz antenna using conical GaAs horn and Si lens," in *2016 International Symposium on Antennas and Propagation (APSYM)*, pp. 1-3, 2016.

[18] R. Singh, *et al.*, "Spiral-type terahertz antennas and the manifestation of the Mushiake principle," *Optics Express*, vol. 17, no. 12, pp. 9971-9980, 2009/06/08 2009.

[19] C. Headley, *et al.*, "Improved performance of GaAs-based terahertz emitters via surface

passivation and silicon nitride encapsulation," *IEEE Journal of Selected Topics in Quantum Electronics*, vol. 17, no. 1, pp. 17-21, 2011.

[20] G. Matthäus, *et al.*, "Large-area microlens emitters for powerful THz emission," *Applied Physics B*, vol. 96, no. 2, pp. 233-235, 2009/08/01 2009.

[21] A. Singh and S. S. Prabhu, "Microlensless interdigitated photoconductive terahertz emitters," *Optics Express*, vol. 23, no. 2, pp. 1529-1535, 2015/01/26 2015.

[22] L. Hou and W. Shi, "An LT-GaAs terahertz photoconductive antenna with high emission power, low noise, and good stability," *IEEE Transactions on Electron Devices*, vol. 60, no. 5, pp. 1619-1624, 2013.

[23] A. Jooshesh, *et al.*, "Plasmon-enhanced LT-GaAs/AlAs heterostructure photoconductive antennas for sub-bandgap terahertz generation," *Optics Express*, vol. 25, no. 18, pp. 22140-22148, 2017/09/04 2017.

[24] N. M. Burford and M. O. El-Shenawee, *Review of Terahertz Photoconductive Antenna Technology* (no. 1, J. Optical Engineering), SPIE, pp. 1-20, 20, 2017.

[25] M. N. Hasan and M. Seo, "High-gain 2 × 2 UWB antenna array with integrated phase inverter," *Electronics Letters*, vol. 54, no. 10, pp. 612-614

[26] M. Amin, J. Yousaf, and S. Iqbal, "Single feed circularly polarised omnidirectional bifilar helix antennas with wide axial ratio beamwidth," *IET Microwaves, Antennas & Propagation*, vol. 7, no. 10, pp. 825-830, 2013.

Mathematical Modelling on the Effects of Conductive Material and Substrate Thickness for Air Substrate Microstrip Patch Antenna

Abdullahi S. B. Mohammed [1], Shahanawaz Kamal [1], Mohd Fadzil bin Ain [1], Roslina Hussin [1], Zainal Arifin Ahmad [2], Ubaid Ullah [3], Mohamadariff Othman [4], and Mohd Fariz Ab Rahman [5]

[1] School of Electrical and Electronic Engineering, Universiti Sains Malaysia, Nibong Tebal 14300, Malaysia
abdulsbauchi@gmail.com, shahanawazkamal@gmail.com, eemfadzil@usm.my, eeroslina@usm.my

[2] School of Materials and Mineral Resources Engineering, Universiti Sains Malaysia, Nibong Tebal 14300, Malaysia
srzainal@usm.my

[3] Networks and Communication Engineering Department, Al Ain University, Abu Dhabi, UAE
ubaid.ullah@aau.ac.ae

[4] Department of Electrical Engineering, University of Malaya, Kuala Lumpur 50603, Malaysia
mohamadariff@um.edu.my

[5] Faculty of Bioengineering and Technology, Universiti Malaysia Kelantan, Jeli 17600, Kelantan, Malaysia
mohdfarizabrahman@yahoo.com

Abstract **─** The use of microstrip patch configuration in the 5th generation (5G) wireless network is expected to fulfill the demands of smartphone users by significantly increasing the capacity of the communication technology. The main aim of this paper is to disclose the development of a mathematical model on the effects of conductive material and substrate thicknesses on the centre frequency for the performance evaluation of a low profile, cost-effective antenna in 5G devices applications. This mathematical model is proposed for an antenna system operated with air substrate resonating at a bandwidth range of 5 GHz - 38 GHz. The effects of different thickness of conductive material and substrate on the antenna's bandwidth, gain, and efficiency for 5G applications were studied. Antennas were fabricated and tested in this study to evaluate the robustness of the proposed mathematical model at 28 GHz, 24 GHz, and 10 GHz. Gains of 9.55 dBi, 9.53 dBi and 10.1 dBi, impedance bandwidths of 2.12 GHz, 2.14 GHz and 0.41 GHz, with input reflection coefficients of 42.75 dB, 25.33dB and 21.51 dB, and performance efficiencies of 98.91, 87.4 and 83.2% were obtained for the respective resonances. For validation of results, the experimental results and the simulation results from the proposed mathematical model were made into comparison, and excellent correlation between the measured and simulated results was obtained.

Index Terms **─** 5G technology, conductive material thickness, mathematical model, microstrip patch inset-fed antenna.

I. INTRODUCTION

The fifth-generation (5G) wireless technology is expected to overcome the drawbacks of the previous generations of networks by supporting higher frequency bands as well as providing more benefits. Considering the end user's demand, it is necessary to design novel antenna systems for modern compact devices. To support the expected requirements for a higher data traffic, intensive researches were carried out on the fifth-generation (5G) cellular system [1]. Since 5G cellular systems are anticipated to work at a frequency band of 30 - 300 GHz close to millimeter-wave, it will become available in the future technologies [1-4]. The 26 GHz, 28 GHz, 38 GHz, and 50 GHz bands are the four frequency bands currently being investigated for 5G applications by academia and industry worldwide [5]. The extreme free space path loss that occurs at these frequencies is one of the drawbacks in using mm-wave frequencies for mobile communication. To solve potential path loss issues, a highly directional arrayed antenna is needed. A 5G antenna must have two distinct characteristics – high gain and wide bandwidth. Both properties depend strongly on the thickness of radiating patch and substrate used in fabricating antennas. Recent trends lead to the development of an antenna that transmits and receives the broadband characteristics and high gains that can be operated at high frequencies. In this way, size reduction and bandwidth enhancement have become major design issues for sensible applications of microstrip antennas [4-6].

Submitted On: January 18, 2020
Accepted On: April 18, 2020

Much research has been focused on modeling, designing and optimizing 5G antennas in the last eight years. However, most of the published work focused on a) investigating different configurations of (massive) Multiple Input Multiple Output (MIMO) antennas [7-12] as well as methods for reducing antenna element isolation [13-14]; b) new 5G mm-wave antennas with a wide range of polarizations like circular polarization [15-17] dual polarization [18-19] and polarization configurability [20]; c) study of multiple dual-band antenna structures (covering the proposed 28 GHz and 38 GHz band for 5G application) like rectangular slot patch [21], integrated substrate waveguide [22], printed slot [23-25], slot waveguide [26] and PIFA [27] are proposed.

Based on available literatures in this domain, no research findings have reported on the effects of the thickness of conductive material and substrate on the production of 5G antennas for their extensive performance. Therefore, this paper demonstrates the formulation of a mathematical model based on the effects of conductive material thickness and substrate height on a single rectangular microstrip patch inset-fed antenna operates from 1 - 40 GHz resonance for 5G wireless communication applications. The influences of these parameters were quantified on the antennas' impedance bandwidth, efficiency and gain. The use of air substrate was integrated in the designs to greatly reduce the cost of antenna manufacturing. The approach used in this work involved three phases summarizing the following: data acquisition and analysis, parameter substitution and optimization, and model development and optimization. The detailed explained in section (iv). The antennas were designed and tested, and the performance results are summarized in Table 1. An excellent correlation between the measured and mathematical modelled (simulation) results was obtained.

Table 1: Performance of the proposed mathematical model antennas

Frequency (GHz)	Gain (dB)		Bandwidth (GHz)		Return Loss (dB)		Efficiency (%)
	Sim.	Mea.	Sim.	Mea.	Sim.	Mea.	
28	9.58	9.45	2.12	2.00	42.75	38.53	83.2
24	9.53	9.40	2.14	2.01	25.33	25.13	87.4
10	10.1	9.87	0.41	0.39	21.51	21.73	98.9

II. ANTENNA CONFIGURATION AND DESIGN

The material used for this proposed antenna's radiation patch is copper. Typically, the dimensions of an inset-fed microstrip patch antenna are determined using the equations regarded to the microstrip antenna as provided in references [28-29]. Air substrate which has a dielectric constant (ε_r) of 1 and a negligible loss tangent was used. To achieve the goals, optimization of the antenna dimensions is necessary. The optimized design parameters at 28 GHz are listed in Table 2.

Table 2: Dimensions of the proposed antenna

Parameter	Value (mm)
Length of patch (L_p)	4.54
Width of patch (W_p)	5.34
Length of ground plane (L_g)	9.08
Width of ground plane (W_g)	10.68
Thickness of substrate (h_s)	0.50
Conductive thickness (h_t)	1.00
Length of inset-fed (f_i)	1.45
Width of feedline (W_f)	2.45
Gap between patch and inserted-fed (G_{pf})	0.50
Feedline length (L_f)	2.68

The geometric configurations of the proposed antennas with the following necessary dimensions; width of the patch (W_p), length of the feeder (L_f), inset depth (d), gap width (g), and feeder length from the left edge of a patch (L_1) are illustrate in Fig. 1.

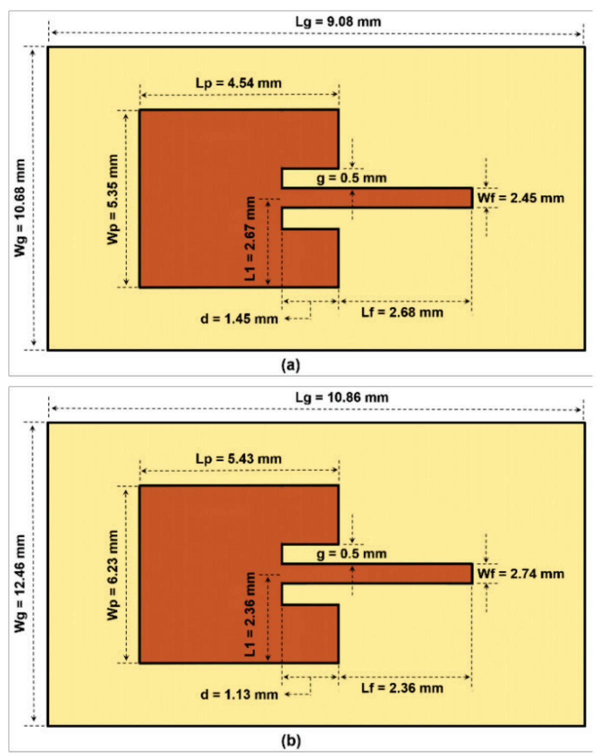

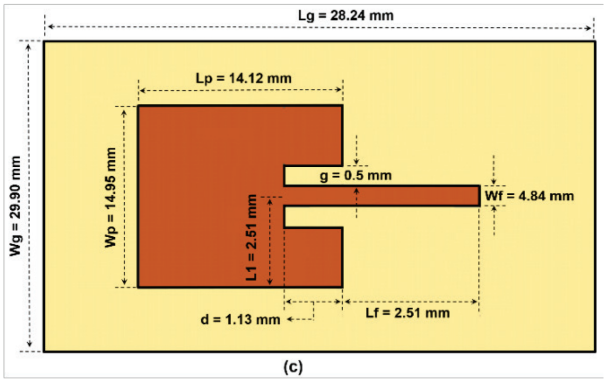

Fig. 1. Geometry of the proposed antennas with required dimensions at: (a) 28 GHz, (b) 24 GHz, and (c) 10 GHz.

III. PARAMETRIC ANALYSIS ON THE PERFORMANCE OF ANTENNA

Several design parameters affecting the bandwidth of the operating impedance were studied to comprehend the design guidelines of the proposed antenna. The radiating rectangular patch was designed using a standard formula applied in any conventional resonant frequency design. The key design parameters, which are useful in maximizing the bandwidth of an antenna, are the thickness of conductive material (h_c) and the substrate height (h_s). Parametric analysis was carried out at a thickness variation of 0.1 mm to 2 mm with varying antenna parameters. The simulated results are as shown in Table 3, and it is observed that with increasing conductor thickness (h_c) and constant width of patch and length of inserted-fed, the bandwidth increases but the length of the patch slightly decreases from the thickness of 1.1 to 2.0, as well as the centre operating frequency which shifts away from the desired resonant frequency. The resonant frequency resonated at 28 GHz at thickness of 0.1 mm to 1 mm. The most appropriate conductor thickness for this proposed antenna is 1 mm.

The selection of a proper substrate thickness is another important task in the development of microstrip patch antennas. In choosing the most appropriate substrate thickness (h_s), a developer needs to have knowledge on the effect of substrate thickness variation on the resonant frequency. In this case, h_s is varied from 0.4 mm to 1 mm with other varying antenna design parameters and the simulated results are as shown in Table 4. From the results, it is observed that when the air substrate thickness is increased while keeping the dimensions of the other parameters as in Table 2, there is a shift in the resonant frequency and the effective dielectric constant changes; which leads to a change in the effective dimensions of the patch. In this set of observation, as the height increases, a volume of fringing effect occurs, and this leads to the increase in the bandwidth. With greater height of substrate, higher amount of modes is excited, resulting in the degradation of the gain. The most appropriate height for this proposed antenna design at 28 GHz is 0.5 mm. However, surface waves are generated as the height of the substrate increases. These waves extract power in the direction of radiation from the total available power. Reduction in the parameters of the antenna design is therefore observed.

IV. DEVELOPMENT OF MATHEMATICAL MODEL

In this work, the effect of the variation of the resonance frequency (F_r); patch Length (L_p); patch width (W_p); and dielectric permittivity (ε_r) on the antenna parameters (gain, directivity, impedance bandwidth and input reflection coefficient), were studied with respect to conductor thickness (h_c) and substrate height (h_s), using computer simulation technology (CST) studio 2016 Software package However, the simulated data obtained where used to develop mathematical models which are father described in this manuscript MATLAB V19 Software package was used as the modeling environment.

In order to develop a mathematical model for the conductor thickness (h_c) and substrate height (h_s), simulated data were obtained from the CST studio suit 2016 for different center frequencies based rectangular microstrip inset patch antenna which are shows in Table 3 and Table 4 respectively. However, due to the limited amount of data, artificial neural networks (ANNs) toolbox in MATLAB was used to train a model and used to generate the desired amount of data to enable model creation. The steps involved in the proposed model development can be summarized as follows:

i. Data Acquisition and Preparation;
ii. Parameter Substitution and Optimization;
iii. Model Development and Optimization [30].

i. Data Acquisition and Preparation

This stage can be described using the following block diagram.

Obtained h_c, h_s, W_p, L_p, F_r and ε_r from the design analysis and simulated results

↓

Interpolate missing data based on antenna theory formulation using Newton Rapson's method

↓

Design an ANN model and generate 10,000 Data samples with varying h_c, h_s, W_p, L_p, F_r and ε_r

↓

Store data in a file for later use

Fig. 2. Data acquisition and preparation block diagram.

ii. Parameter Substitution and Optimization

However, since the width and length (W_p and L_p) of patch are dependent on other parameters of the model, based on antenna theory formulations, these parameters can be substituted for. To achieve that, the following stages were further executed.

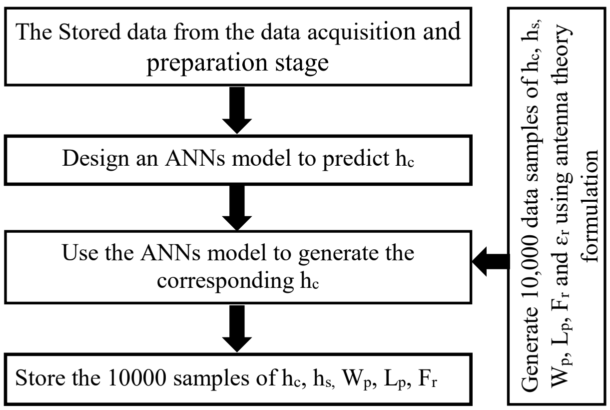

Fig. 3. Parameter substitution and optimization.

iii. Model Development and Optimization

This represents the main stage of this work, and it presents the strategy used in developing the set of mathematical function that could be used to evaluate a suitable value for h_c and h_s for a given antenna design specification. In this work, h_s is chose to be defined using the following simplified mathematical expressions in equation (1):

$$h_S = \left(\frac{\alpha F_r \sqrt{\varepsilon_r + 1} + \beta \sqrt{2C_O}}{\sqrt{2C_O} + \gamma F_r \sqrt{\varepsilon_r + 1}} \right), \tag{1}$$

where the α, β, and γ can be found using an optimization technique. However, the particle swarm optimization (PSO) techniques was chosen. The objective function of the optimization was to minimize the difference between the estimation and true value of the h_s. After the optimization, it was found that the model was inaccurate when α and β are fixed at constant values, however, γ can be fixed at 0.5053. In order to make α and β vary with change in parameter specification, let α and β be as shown in equations (2) and (3), respectively:

$$\alpha = X_1 \begin{pmatrix} X_2 (W_p)^{X_3} - X_4 (F_r)^{X_5} - X_6 (F_r)^{X_7} \\ + X_8 (E_r)^{X_9} - X_{10} (E_r)^{X_{11}} + X_{12} \end{pmatrix}, \tag{2}$$

$$\beta = Y_1 \begin{pmatrix} Y_2 (W_p)^{X_3} - Y_4 (F_r)^{X_5} - Y_6 (F_r)^{X_7} \\ + Y_8 (E_r)^{X_9} - Y_{10} (E_r)^{X_{11}} + Y_{12} \end{pmatrix}. \tag{3}$$

The set of parameters X and Y are unknown variables that can be determined using PSO. The resulting mathematic model for substrate height was determined as presented in the following equations (4) and (5) respectively:

A. Substrate height model (h_s)

The substrate height of a rectangular patched antenna can be calculated using equation (4),

$$h_S = \left(\frac{7.6904 \alpha F_r \sqrt{\varepsilon_r + 1} + 1.4142 \beta C_O}{1.4142 C_O + 0.5053 F_r \sqrt{\varepsilon_r + 1}} \right), \tag{4}$$

where, α and β are represented in equation (5) and (6) respectively:

$$\alpha = \begin{pmatrix} 0.8525 \left(\dfrac{C_O}{2F_r \sqrt{\varepsilon_r + 1}} \right)^{1.041} \\ -0.7464 (F_r)^{0.3993} - 0.3902 (F_r)^{0.6572} \\ +0.0817 (E_r)^{0.3679} - 0.5217 (E_r)^{-0.5611} \\ +4.4398 \end{pmatrix}, \tag{5}$$

$$\beta = \begin{pmatrix} 2.4846 \left(\dfrac{C_O}{2F_r \sqrt{\varepsilon_r + 1}} \right)^{-0.1202} \\ -0.3713 (F_r)^{0.4138} + 3.1339 (F_r)^{-0.223} \\ -0.4411 (E_r)^{-0.3029} - 1.2403 (E_r)^{-8.1344} \\ +0.6557 \end{pmatrix}. \tag{6}$$

Based on this model, the mathematical model for computing the conductive material thickness can be generated. Finally, the mathematical model of the conductor thickness was found to be in equation (7).

B. Conductive material thickness model (h_c)

The height of conductive mat Height of conductive material thickness of a rectangular patch antenna can be calculated using equation (7):

$$h_C = \begin{pmatrix} \left(\dfrac{F_r \varepsilon_r \sqrt{2\varepsilon_r + 2}}{C_O} \right)^{(\varepsilon_r - 1)} \times \\ \begin{pmatrix} 1.3703 h_S + 83.1872 (h_S)^{8.2891} \\ -172.286 (h_S)^{11.07824} - 0.3501 \end{pmatrix}^2 \end{pmatrix}, \tag{7}$$

where, C_o is the speed of light in air (mm/s); F_r is the desired center frequency (GHz) and h_S is the substrate height (mm) and it can be evaluated using the mathematical formulation. Table 5 shows the optimized dimensional parameters of the proposed mathematical modelled antennas.

V. RESULTS AND DISCUSSION

A. Input reflection coefficients

In reference to the optimized antennas dimensions as well as the developed mathematical model, prototypes of the proposed antennas were fabricated and tested to validate their operational performances through the mathematical model. The antennas were made excited using a long pin SMA connector by connecting its coaxial probe to the rectangular patch. Figure 4 displays a photograph of the fabricated antenna prototype. The S-parameters of the antennas were tested using the Agilent Vector Analyser (N5245A). On the other hand, Fig. 5 presents the input reflection coefficient characteristics of the simulated and measured results. The simulated input reflection coefficients are lower than -10 dB (VSWR< 2), measurably around 42.75 dB, 25.33 dB and 21.51 dB at frequencies of 28 GHz, 24 GHz and 10 GHz with bandwidths of 2.12 GHz, 2.14 GHz and 0.41 GHz, respectively. The measured return losses of 38.53 dB, 25.13 dB and 21.73 dB with bandwidths of 2.00 GHz, 2.01 GHz and 0.39 GHz respectively are found enough for proper impedance matches. However, it is pointed out that the bandwidth differences for 0.12 GHz, 0.13 GHz and 0.02 GHz constitute about 5.83%, 6.27% and 5.00% respectively between the simulated and measured bandwidth. These differences arise from the manufacturing sensitivity and the effect of the coaxial feed connector. An excellent correlation was observed between the measured and simulated results.

Table 3: Variation of antenna parameters with thickness of conductive material (simulated)

h (mm)	**d (mm)**	**W_p (mm)**	**L_p (mm)**	**F_r (mm)**	**D (dB)**	**G (dB)**	**R (dB)**	**BW (GHz)**
0.1	1.45	5.34	4.38	28.00	10.150	10.10	24.47	1.0930
0.2	1.45	5.34	4.78	28.00	10.130	10.10	25.69	1.1269
0.3	1.45	5.34	4.73	28.00	10.090	10.10	27.57	1.2092
0.4	1.45	5.34	4.70	28.00	10.040	10.00	26.70	1.2586
0.5	1.45	5.34	4.67	28.00	9.970	9.97	27.86	1.3566
0.6	1.45	5.34	4.63	28.00	9.880	9.88	35.94	1.4225
0.7	1.45	5.34	4.61	28.00	9.790	9.79	33.88	1.5158
0.8	1.45	5.34	4.57	28.00	9.694	9.69	33.54	1.6091
0.9	1.45	5.34	4.55	28.00	9.589	9.59	32.65	1.7025
1.0	1.45	5.34	4.54	28.002	9.474	9.47	31.49	1.7245
1.1	1.45	5.34	4.54	27.907	9.373	9.37	30.17	1.8852
1.2	1.45	5.34	4.51	27.809	9.211	9.22	26.78	1.9895
1.3	1.45	5.34	4.50	27.850	9.086	9.06	25.06	2.0609
1.4	1.45	5.34	4.46	27.880	8.940	8.94	20.63	2.0983
1.5	1.45	5.34	4.44	27.800	8.766	8.77	18.69	2.0928
1.6	1.45	5.34	4.42	27.744	8.620	8.62	17.47	2.1642
1.7	1.45	5.34	4.41	27.728	8.473	8.47	16.66	2.2411
1.8	1.45	5.34	4.40	27.728	8.306	8.31	16.03	2.2840
1.9	1.45	5.34	4.39	27.760	8.164	8.16	15.50	2.3830
2.0	1.45	5.34	4.36	27.760	7.992	7.99	14.36	2.3940

Table 4: Variation of antenna design parameters with substrate thickness (simulated)

h_s (mm)	**L_p (mm)**	**W_p (mm)**	**d (mm)**	**F_r (GHz)**	**D (dBi)**	**G (dB)**	**R (dB)**	**BW (GHz)**
0.4	4.54	5.34	1.45	28.576	9.585	9.58	19.323	1.5471
0.5	4.54	5.34	1.45	28.024	9.451	9.45	42.648	2.1180
0.6	4.54	5.34	1.45	27.696	9.310	9.31	28.001	2.3009
0.7	4.54	5.34	1.45	26.696	9.188	9.19	25.616	2.3512
0.8	4.54	5.34	1.45	26.467	9.064	9.06	28.118	2.3725
0.9	4.54	5.34	1.45	26.008	8.932	8.93	40.162	2.4405
1.0	4.54	5.34	1.45	25.656	8.785	8.79	32.600	2.5075

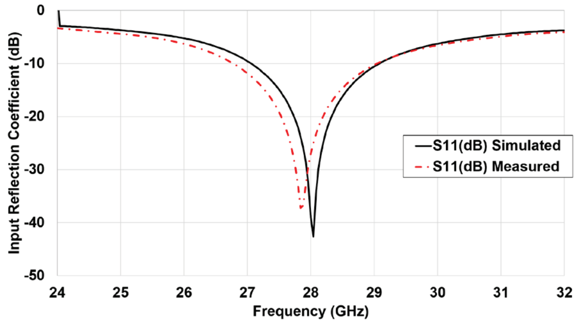

(a)

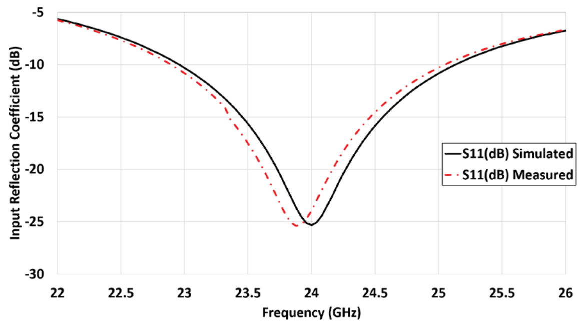

(b)

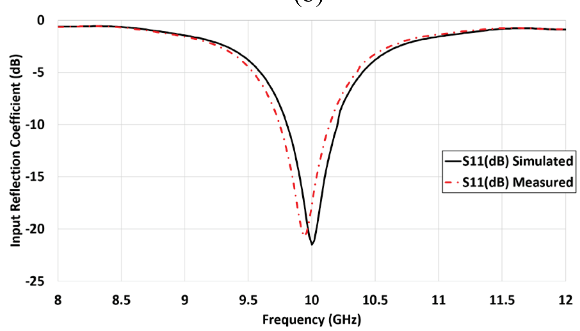

(c)

Fig. 5. Comparison of the measured and simulated results “input reflection coefficient” of a fabricated air substrate patch at: (a) 28 GHz, (b) 24 GHz, and (c) 10 GHz resonances.

B. Radiation pattern

Radiation patterns were measured using a swept frequency measurement conducted in an anechoic chamber. The measured radiating patterns of the proposed antennas were plotted at 28 GHz, 24 GHz and 10 GHz resonances and are presented in Fig. 6. The measured input impedance was 50.401–j1.02, which is approximate to 50Ω. Since both the real and imaginary parts of the measured input impedance were close to the Smith chart centre, it therefore indicates a maximum power transfer has occurred. Figures 6 (a), (b) and (c) show the normalized measured and simulated radiation patterns of the proposed linearly omnidirectional polarized antennas at 28 GHz, 24 GHz and 10 GHz resonances respectively in the E- and H-planes obtained using a swept frequency measurement in an anechoic chamber. The simulated patterns are reasonably in agreement with the measured patterns, and this shows that the antenna is rather of the directional type. Nonetheless, the contrast between the measured and simulated radiation patterns indicates some variations between these patterns. The measured E-plane radiation pattern indicates a reasonable degree of variation. This is probably due to the coaxial feed probe's effect on the height variability. It is important to note that the pattern of a radiation is mainly generated due the current of excitation from a coaxial probe to the radiating element and the current in the probe. Regarding the H-plane, both the simulated and measured patterns of radiation show a constant good agreement, but with a minor difference and a good directivity in both frequencies. The actual measured radiation patterns and gains of the proposed antennas are in close agreement with the simulated results.

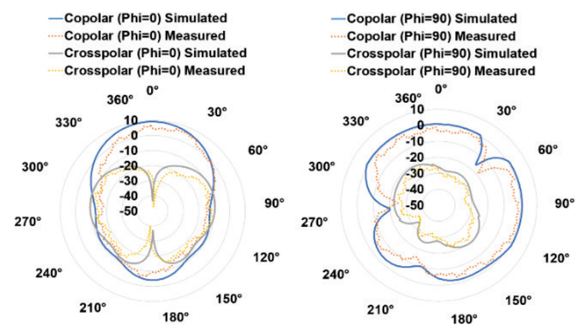

(a)

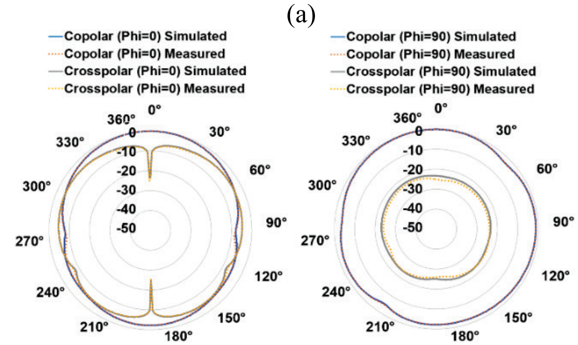

(b)

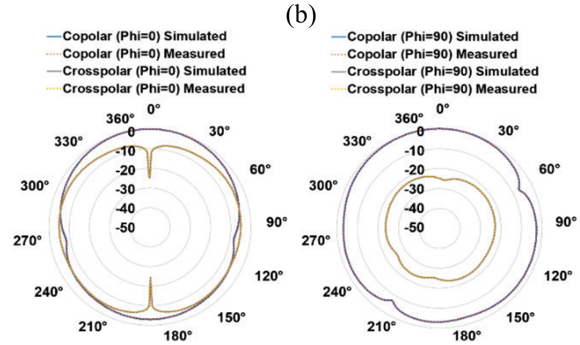

(c)

Fig. 6. Measured radiation patterns (E & H planes) of the proposed antennas at: (a) 28 GHz; (b) 24 GHz, and (c) 10 GHz.

C. Comparison of the proposed mathematical model

Table 6 provides a contrast between the published works performance profile comparisons with proposed antennas in terms of resonant frequency overall size and measured values, gain, radiation efficiency, return loss as well as bandwidth. This comparison shows that the proposed mathematical model antennas operating at 28 GHz, 24 GHz and 10 GHz has a wider bandwidth and a high gain compared to other antennas published previously.

The proposed mathematical model has the following advantages:

i. Ability to predict resonance frequency faster and more accurately compared to many advanced simulation tools that are available commercially
ii. Simplifies and save the simulation time to analyses parameters and process parametric result data compared to many advanced simulation tools that are available commercially
iii. It reduced the cost of optimum performance requirements for electromagnetic simulation (such as high clock speed and core count CPU, an efficient GPU workstation, and fast RAM.

Table 6: Publish works performance profile comparison with proposed antennas

Frequency (GHz)	Size (mm^2)	Gain (dB)	Bandwidth (GHz)	Efficiency (%)	Return loss (dB)	Ref. Antenna
28	04.42 × 3.47	8.58	0.63	N/A	44.46	[31]
28	04.40 × 4.20	4.47	1.55	94.00	N/A	[32]
28	20.00 ×16.50	9.33	0.45	N/A	23.50	[33]
28	**05.34 × 4.54**	**9.45**	**2.00**	**83.20**	**38.53**	**Proposed Antenna**
24	07.27 × 7.27	3.24	1.87	90.00	32.50	[34]
24	13.80 × 11.40	3.00	0.40	N/A	32.00	[35]
24	28.00×20.00	8.20	2.00	93.00	23.00	[36]
24	**5.20× 7.00**	**9.40**	**2.01**	**87.40**	**25.13**	**Proposed Antenna**
10	N/A	N/A	1.18	66.30	41.50	[37]
10	50× 25	8.76	1.14	82.32	27.77	[38]
10	20×18	3.14	0.80	N/A	34.50	[39]
10	**13.6× 07**	**9.87**	**0.39**	**98.90**	**21.73**	**Proposed Antenna**

VI. CONCLUSION

Evaluation of the effects of conductive material and substrate thickness, as well as the development of a mathematical model of a single element rectangular microstrip patch inset-fed antenna for 5G wireless communication application are presented in this paper. Microstrip patch antennas operated using air substrate at 28, 24 & 10 GHz resonance were designed, simulated, optimized and analysed accordingly. The conductive patch materials and substrate techniques used to produce mm-wave integrated antennas have a significant impact on the antennas' impedance and radiation characteristics. Therefore, the effects of conductive patch material and substrate technology on the performance of an antenna must be thoroughly defined and properly understood prior to the designing of a 5G antenna. The validity of the proposed model equations is verified by comparison with the measured results. The measured results obtained from the fabricated antennas prototypes are in good agreement with the simulated (model equations) results. The implementation of this proposed mathematical modelling approach will minimize the time required to obtain the best resonant frequency design compared to the parametric studies using a simulation software. The proposed antennas support a very low profile, which is an excellent in the integrated low-cost millimeter-wave applications.

ACKNOWLEDGMENT

This work was supported by Ministry of Higher Education, Malaysia under Fundamental Research Grant Scheme 203.PELECT.6071429.

REFERENCES

[1] A. Benjebbour, K. Saito, Y. Saito, and Y. Kishiyama, "5G radio access technology," *NTT Technical Journal*, vol. 17, no. 4, pp. 16-28, 2016.
[2] I. Fitri and T. A. A. Akbar, "A new gridded parasitic patch stacked microstrip antenna for enhanced wide bandwidth in 60 GHz band," *IEEE Trans. Antennas Propag.*, vol. 38, no. 5, pp 1-4, 2017.
[3] J. R. James, "Handbook of microstrip antennas," *IET*, vol. 1, 1989.
[4] F. Ahmad and B. Tillie, "Design and analysis of millimeter wave double F slot patch antenna for

future 5G wireless communications," *Proc. IEEE*, vol. 36, no. 7, pp 1-4, Nov. 2017.

[5] N. Kalambe, D. Thakur, and S. Paul, "Design of microstrip patch antenna for wireless communication devices," *International Journal of Science and Research*, vol. 4, no. 3, pp. 1149-1154, 2015.

[6] S. Choudhury, "Effect of dielectric permittivity and height on a microstrip fed rectangular patch antenna," *International Journal of Electronics & Communication Technology*, vol. 5, no. 2, pp. 1-2, 2014.

[7] B. Yang, Z. Yu, Y. Dong, J. Zhou, and W. Hong, "Compact tapered slot antenna array for 5G Millimeter-wave massive MIMO systems," *IEEE Trans. Antennas and Propag*., vol. 65, no. 12, pp. 6721-6727, 2017.

[8] M. M. Ali and A. Sebak, "Design of compact millimeter wave massive MIMO dual-band (28/38 GHz) antenna array for future 5G communication systems," *Proc. IEEE*, vol. 62, no. 10, pp. 1-2, July 2016.

[9] N. O. Parchin, M. Shen, and G. F Pedersen, "End-fire phased array 5G antenna design using leaf-shaped bow-tie elements for 28/38 GHz MIMO applications," *Proc. IEEE*, vol. 29, no. 10, pp. 1-4, Oct. 2016.

[10] O. Naser, M. Shen, and G. Fr, "Multi-layer 5G mobile phone antenna for multi-user MIMO communications," *IEEE*, vol. 31, no. 5, pp. 559-562, 2015.

[11] O. M. Haraz, M. Ashraf, and S. Alshebeili, "Single-band PIFA MIMO antenna system design for future 5G wireless communication applications," *Proc. IEEE Trans. Antennas Propag.*, pp. 608-612, 2015.

[12] K. Yu, Y. Li, and X. Liu, "Mutual coupling reduction of a MIMO antenna array using 3-D novel metamaterial structures," *Appl. Comput. Electromagn. Soc. J.*, vol. 33, no. 7, pp. 758-763, 2018.

[13] D. T. T. Tu, N. G. Thang, N. T. Ngoc, N. T. B Phuong, and V. Van Yem, "28/38 GHz dual-band MIMO antenna with low mutual coupling using novel round patch EBG cell for 5G applications," *In 2017 International Conference on Advanced Technologies for Communications (ATC)*, Oct. 2017, pp. 64-69.

[14] S. Luo, Y. Li, Y. Xia, and L. Zhang, "A low mutual coupling antenna array with gain enhancement using metamaterial loading and neutralization line structure," *Appl. Comput. Electromagn. Soc. J.*, vol. 34, no. 3, 2019.

[15] H. Aliakbariabar, A. Abdipour, A. Mirzavand, A. Costanzo, and P. Mousavi, "A single feed dual-band circularly polarized millimeter-wave antenna for 5G communication," *in 2016 IEEE European Conference on Antennas and Propagation (EuCAP)*, pp. 1-5, Apr. 2016.

[16] M. Nosrati and T. Tavassolian, "A single feed dual band, linearly/circularly polarized cross-slot millimeter-wave antenna for future 5G networks," in *IEEE International Symposium on Antennas and Propagation and USNC/URSI National Radio Science Meeting*, pp. 2467-2468, July 2017.

[17] W. Lin, R. W. Ziolkowski, and T. C. Baum, "28 GHz compact omnidirectional circularly polarized antenna for device-to-device communications in the future 5G systems," *IEEE Trans. Antennas and Propag.*, vol. 65, pp. 6904-6914, 2017.

[18] Y. Li, W. Li, and W. Yu, "A multi-band/UWB MIMO/diversity antenna with an enhance isolation using radial stub loaded resonator," *Appl. Comput. Electromagn. Soc. J.*, vol. 28, no. 1, pp. 8-20, 2012.

[19] Y. Li, W. Li, and W. Yu, "A switchable UWB slot antenna using SIS-HSIR and SIS-SIR for multi-mode wireless communications applications," *Appl. Comput. Electromagn. Soc. J.*, vol. 27, no. 4, pp. 340, 2012.

[20] J. K. Du, K. So, Y. Ra, S. Y. Jung, J. Kim, S. Y Kim, and W. Paik, "Dual-polarized patch array antenna package for 5G communication systems," *in 2017 IEEE European Conference on Antennas and Propagation (EUCAP)*, pp. 3493-3496, Mar. 2017.

[21] E. Al Abbas, A. T. Mobashsher, and A. Abbosh, "Polarization reconfigurable antenna for 5G cellular networks operating at millimeter waves," *in 2017 IEEE Asia Pacific Microwave Conference (APMC)*, pp. 772-774, Sept. 2017.

[22] M. M. Amin, M. F. Mansor, N. Misran, and M. T. Islam, "28/38GHz dual band slotted patch antenna with proximity-coupled feed for 5G communication," *in 2017 IEEE International Symposium on Antennas and Propagation (ISAP)*, pp. 1-2, May 2017.

[23] N. Ashraf, O. Haraz, M. A. Ashraf, and S. Alshebeili, "28/38-GHz dual-band millimeter waves SIW array antenna with EBG structures for 5G applications," *in 2015 IEEE International Conference on Information and Communication Technology Research (ICTRC)*, pp. 5-8, May 2015.

[24] O. M. Haraz, M. M. Ali, S. Alshebeili, and A. R. Sebak, "Design of a 28/38 GHz dual-band printed slot antenna for the future 5G mobile communication Networks," *in 2015 IEEE International Symposium on Antennas and Propagation & USNC/URSI National Radio Science Meeting*, pp. 1532-1533, July 2015.

[25] I. F. da Costa, S. A. Cerqueira, and D. H. Spadoti, "Dual-band slotted waveguide antenna array for adaptive mm-wave 5G networks," *in 2017*,

IEEE European Conference on Antennas and Propagation (EUCAP), pp. 1322-1325, 2017.

[26] W. Ahmad and W. T. Khan, "Small form factor dual band (28/38 GHz) PIFA antenna for 5G applications," *in 2017 IEEE MTT-S International Conference on Microwaves for Intelligent Mobility (ICMIM)*, pp. 21-24, Mar. 2017.

[27] J. R. James and P. S. Hall, (Eds.), "Handbook of microstrip antennas," *IET*, vol. 1, 1989.

[28] F. Ahmad and B. Tlili, "Design and analysis of millimeter wave double F slot patch antenna for future 5G wireless communications," *in 2017 IEEE International Conference on Electrical and Computing Technologies and Applications (ICECTA)*, pp. 1-4, Nov. 2017.

[29] Y. Huang and K. Boyle, "Antennas: From theory to practice," 2008.

[30] H. Kabir, Y. Cao, and Q. Zhang, "Advances of neural network modeling methods for RF/ microwave applications," *Appl. Comput. Electromagn. Soc. J.*, vol. 25, no. 15, pp. 423, 2010.

[31] M. A. Rahim, I. M. Ibrahim, R. A. A. Kamaruddin, Z. Zakaria, and N. Hassim, "Characterization of microstrip patch array antenna at 28 GHz," *Journal of Telecommunication, Electronic and Computer Engineering* (*JTEC)*, vol. 9, no. 2-8, pp. 137-141, 2017.

[32] W. Ahmad, A. Ali, and W. T Khan, "Small form factor PIFA antenna design at 28 GHz for 5G applications," *in 2016 IEEE International Symposium on Antennas and Propagation (APSURSI)*, pp. 1747-1748, June 2016.

[33] A. Abdelaziz and E. K. Hamad, "Design of a compact high gain microstrip patch antenna for tri-band 5 G wireless communication," *Frequenz*, vol. 73, no. 1-2, pp. 45-52, 2019.

[34] P. Sravani and M. Rao, "Design of 3d antennas for 24 GHz ISM band applications," *in 2015 IEEE* International *Conference on VLSI Design*, pp. 470-474, July 2015.

[35] S. Mandal, H. Singh, S. Mandal, S. K. Mahapatra, and A. K. Mal, "Design of a compact monopole on-chip antenna for 24 GHz automotive radar application," *in 2019 IEEE International Workshop on Antenna Technology (iWAT)*, pp. 115-117, Mar. 2019.

[36] R. A. Alhalabi and G. M. Rebeiz, "High-efficiency angled-dipole antennas for millimeter-wave phased array applications," *IEEE Transac. Antennas and Propag.*, vol. 56, no. 10, pp. 3136-3142, 2008.

[37] D. Feng, H. Zhai, L. Xi, S. Yang, K. Zhang, and D. Yang, "A broadband low-profile circular-polarized antenna on an AMC reflector," *IEEE Antennas and Wireless Propag. Letts.*, vol. 16, pp. 2840-2843, 2017.

[38] R. A. Siddiqui, B. Mishra, and M. R. Tripathy, "Conformal SIW feed tapered antenna array for the 10 GHz frequency applications," *in 2018 IEEE Indian Conference on Antennas and Propogation (InCAP)*, pp. 1-5, Dec. 2018.

[39] M. A. Ullah, F. B. Ashraf, T. Alam, M. S. Kibria, and M. T. Islam, "A compact triangular shaped microstrip patch antenna with triangular slotted ground for UWB application," *in 2017 IEEE International Conference on Innovations in Science, Engineering and Technology (ICISET)*, pp. 1-4, Oct. 2016.

Abdullahi S.B. Mohammed received the B.Eng. degree in Electrical Engineering from Bayero University Kano, Nigeria in 2008, and the M.Sc. degree in Electrical Engineering with prime focus on Telecommunication from Ahmadu Bello University, Nigeria in 2014. He is currently working toward the Ph.D. degree in Microwave Engineering with the School of Electrical and Electronic Engineering, Universiti Sains Malaysia, Malaysia. His research interests include the design of MIMO, printed, and microstrip patch antennas.

Shahanawaz Kamal was born in Mumbai, India. He received the B.E. and M.E. degrees in Electronics and Telecommunication Engineering from the University of Mumbai, India in 2013 and 2017, respectively. He is currently working with the School of Electrical and Electronic Engineering, Universiti Sains Malaysia, Malaysia.

He joined Vedang Cellular Services Pvt. Ltd., India as an IBS Engineer in 2014. He was a Visiting Lecturer at the Department of Information Technology, M. H. Saboo Siddik Polytechnic, India in 2016. His research interests include the design of MIMO, printed and quasi-lumped element resonator antennas.

Mohd Fadzil bin Ain received the B.S. degree in Electronic Engineering from Universiti Teknologi Malaysia, Malaysia in 1997; the M.S. degree in Radio Frequency and Microwave from Universiti Sains Malaysia (USM), Malaysia in 1999; and the Ph.D. degree in Radio Trequency and Microwave from the University of Birmingham, United Kingdom in 2003.

In 2003, he joined the School of Electrical and

Electronic Engineering, USM. He is currently a Professor with VK7 grade, the Dean of Research, Postgraduate and Networking, and the Director of Collaborative Microelectronic Design Excellence Centre (CEDEC). He is actively involved in technical consultancy with several companies in repairing microwave equipment. His current research interests include MIMO wireless system on FPGA/DSP, Ka-band transceiver design, dielectric antenna, RF characterization of dielectric material, and microwave propagation study.

Ain's awards and honors include International Invention Innovation Industrial Design and Technology Exhibition, International Exposition of Research and Inventions of Institutions of Higher Leaning, Malaysia Technology Expo, Malaysian Association of Research Scientists, Seoul International Invention Fair, iENA, Best Paper for the 7th WSEAS International Conference on Data Networks, Communications, Computers, and International Conference on X-Ray & Related Techniques in Research and Industry.

Zainal Arifin Ahmad received the B.S. degree in Materials Engineering from Universiti Sains Malaysia, Malaysia; the M.S. degree from the University of Manchester Institute of Science and Technology, United Kingdom; and the Ph.D. degree from the University of Sheffield, United Kingdom.

He is currently a Senior Professor with the School of Materials and Mineral Resources Engineering, Universiti Sains Malaysia, Malaysia. His current research interests include ZTA ceramic for cutting insert, low-temperature-cofired-ceramics-based circuits, metal–ceramic joining, crystal glaze ceramic, TCP bioceramic, and dielectric ceramic for antennas.

Ubaid Ullah received the B.S. degree in Electrical Engineering from CECOS University of IT and Emerging Sciences, Pakistan in 2010; the M.S. and Ph.D. degrees in Electronic Engineering from Universiti Sains Malaysia, Malaysia in 2012 and 2017, respectively.

He is currently a Post-Doctoral Researcher at the School of Science and Engineering, Reykjavik University, Iceland. He has published several articles in ISI indexed journals and some well-reputed international conferences. His current research interests include dielectric resonator antennas (DRAs), wideband DRAs, microwave circuits, low-temperature-cofired-ceramics-based antenna in package, applied electromagnetics, and small antennas.

Mohamadariff Othman received his Bachelor in Electronic Engineering from Multimedia University, Malaysia in 2006; the M.Sc. degree in RF and Microwave Field from Universiti Sains Malaysia (USM), Malaysia in 2008; and the Ph.D. degree in Antenna and Propagation Field from USM in 2015.

He joined the Department of Electrical Engineering, University of Malaya, Malaysia as a Senior Lecturer in 2016 after serving a private university for almost one and half year. His research interests include 5G antenna, dielectric characterization, dielectric resonator antenna design, and optimization of antenna design.

Roslina Hussin received the B.Sc. degree in Electrical Engineering from the University of Tulsa, United States of America in 1994, and the M.Sc. degree in Communication Engineering from Universiti Sains Malaysia (USM), Malaysia in 2016.

She joined the School of Electrical and Electronic Engineering, USM as a Research Officer in 2011.

Mohd Fariz Ab rahman was born in Kota Bharu, Malaysia. He received the B.Eng. (Hons) degree in Materials Engineering from Universiti Malaysia Perlis, Malaysia in 2010; the M.Sc. and Ph.D. degrees in Materials Engineering from Universiti Sains Malaysia (USM), Malaysia in 2014 and 2017, respectively. In 2018, he joined the School of Electrical and Electronic Engineering, USM as a Research Assistant under the supervision of Professor Ir. Dr. Mohd Fadzil Ain. He has authored or co-authored more than 20 articles. His research interests include materials engineering, materials science and electro-ceramics which include the development of ceramic materials for electronic devices.

A Dual-polarized UWB Antenna Fed by a New Balun for Electronic Reconnaissance System Application

Jian Wu [1, 2] and Xiaojin Zhu [1]

[1] School of Mechatronic Engineering and Automation
Shanghai University, Shanghai 200072, P.R. China
qcxyhb@163.com, shzhuxj@163.com

[2] Shanghai Microwave Equipment Research Institute
Shanghai 201802, P.R. China

Abstract **─** For a practical engineering application, a printed ultra-wide band (UWB) antenna with dual polarization is presented in this paper. An integrated Balanced-to-unbalanced (Balun) transformer from microstrip line to coplanar stripline (CPS) is designed, which is employed to feed the symmetrically coplanar Vivaldi radiator. Two substrates are used to support the Vivaldi radiators which are orthogonally mounted. The proposed antenna can build two orthogonal UWB channels and receive two polarization components of incident electromagnetic signal. By bending the balanced coplanar striplines, the cross placement of two polarization radiators can be easily realized, which is suitable for the engineering application. A dual-polarized Vivaldi antenna with the frequency range from 2.5GHz to 6GHz was simulated and fabricated. The measured indicated that the average return loss of designed antenna is less than -10dB and the port isolation degree is about 20dB with the operational frequency range, the gains are about larger than 3dB and the average cross polarization levels are about -20dB. The research results verify the feasibility of the proposed antenna scheme. The presented dual-polarized antenna has the advantages of easy design, high port isolation and convenient engineering application, which can be used in the fields such as electronic reconnaissance system.

Index Terms **─** Balun, CPS, dual polarization, electronic reconnaissance system, UWB, Vivaldi.

I. INTRODUCTION

Radar electronic reconnaissance system usually adopts ultra-wideband antenna to receive various radar signals, and uses signal processing algorithms to realize radar signal detection, feature extraction, target recognition and other functions[1-2]. Ultra-wideband antennas play an important role in radar electronic reconnaissance systems. In order to obtain more comprehensive information on the radar signal, the polarization-sensitive reconnaissance system is the future development trend. The dual-polarization UWB antenna is a key component of the polarization-sensitive radar reconnaissance system. Research on dual-polarization UWB antenna suitable for engineering application has important practical significance [3-4]. The dual-polarized antenna unit provides two polarized signal receiving ports, and simultaneously receives two orthogonal polarization components of the incident electromagnetic wave, thereby sensing the fully polarized information of the electromagnetic wave [5-7]. For dual-polarized UWB antennas, good polarization port isolation and low cross-polarization levels are important considerations, which require antennas with lower return loss over the ultra-wideband range and smooth radiation pattern [8-10]. In the design and development of dual-polarized UWB antennas, antenna types of various types of structures have emerged, such as dual-polarized ridged horn antennas, dual-polarized sinusoidal antennas [11-12], and dual-polarized logarithmic periodic antennas [13-14], dual-polarized slot antenna [15-16]. The dual-polarized Vivaldi antenna has been paid more and more attention and widely used due to its advantages of low cost and simple structure. Vivaldi antennas are broadband tapered slot antennas with ultra-wideband impedance radiation pattern performance. The dual-polarized UWB Vivaldi antenna is usually composed of a printed medium substrate. Two symmetric dielectric substrates are placed at the intersection, and two polarization ports are formed by mechanical assembly. In actual operation, the output port is usually a coaxial connector. In order to solder easily, the output port is generally a microstrip transmission line on the printed medium substrate. Since the microstrip transmission line is an unbalanced structure, it is necessary to introduce an unbalanced device to balanced conversion feeding structure, this unbalanced device is balun [17-19]. Balun is usually used as the conversion from microstrip line to slot line, based on

Submitted On: January 31, 2020
Accepted On: April 23, 2020

electromagnetic coupling, the excitation of tapered slots and space electromagnetic radiation are realized. The traditional microstrip-slot broadband balun structure is complex and has many design parameters, which results in a large amount of design work. For the cross structure of two dielectric substrates, it is difficult to assemble the antenna, it is easily results in the occlusion of two polarization ports and poor assembly consistency. In addition, due to the cross between polarization ports, the isolation degree of polarization ports becomes worse, and the electromagnetic coupling between polarization channels becomes stronger, which makes the measurement error larger [21-22].

Based on the above considerations, this paper proposes an integrated balun-fed dual-polarization UWB antenna based on microstrip line to coplanar stripline conversion. The balun design is simple and easy to connect and match with the Vivaldi radiator. The occlusion of orthogonal polarization ports bends and vertically isolates the coplanar strip lines, which effectively reduces the assembly difficulty and improves the isolation of the polarization ports, which lays a good foundation for engineering applications. In this paper, the structure of the specific dual-polarized antenna is designed and implemented for the frequency range of 2.5GHz~6GHz. According to the working frequency range and technical indicators, the size parameters of the antenna were preliminarily calculated. Finally, the full wave electromagnetic simulation software was used for numerical calculation and performance optimization, and then the structure and size that meet the requirements were determined to complete the design and implementation of the antenna. The research results of antenna processing and test work show that the design of the polarization diversity antenna is effective.

The paper is organized as follows. Section 2 gives the structure of the designed dual-polarized UWB antenna and discusses the simulation and optimization of the dual-polarized UWB antenna. Section 3 describes the test results. Finally, the research conclusion is provided.

II. ANTENNA DESIGN

The schematic diagram of the ultra-wideband dual-polarized Vivaldi antenna designed in this paper is shown in Figure 1. The dielectric substrate of the entire antenna is selected from FR4 plates, and the thickness of the dielectric substrate is 1 mm. Two dielectric substrates of the same size are placed orthogonally, each polarized port corresponds to an ultra-wideband Vivaldi radiator, the feed transmission line is a coplanar strip line, and the Vivaldi radiator uses two exponential curves to constrain its shape in the middle region. An exponentially graded gap is formed to realize an ultra-wideband radiation field. In order to facilitate assembly of the dielectric substrate, the excited coplanar strip line is bent, and in the vertical direction, the two coplanar strip lines are kept at a certain interval, which can improve the port isolation. The input terminal of the antenna is a microstrip line, which is suitable for soldering with the coaxial line. An integrated printing balun is added between the microstrip line and the coplanar strip line to complete the conversion between the unbalanced and balanced structures, at the same time, it can achieve impedance matching. The Balun is a kind of microstrip line-coplanar stripline conversion Balun.

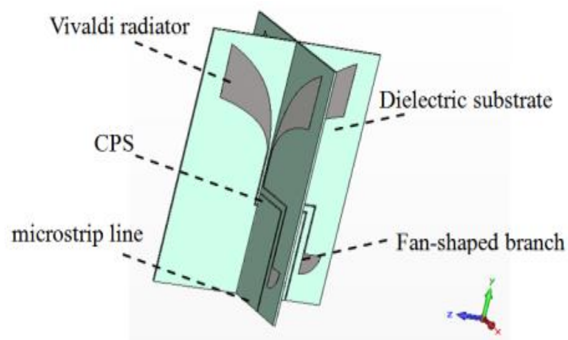

Fig. 1. The structure diagram of dual-polarized UWB antenna.

The geometrical models of the two dielectric substrates of the dual-polarized Vivaldi antenna are shown in Fig. 2 and Fig. 3 respectively. The designed Vivaldi radiator is a symmetrical structure, and the spacing between the excited coplanar strip lines is a_1, the width of the dielectric substrate is w_gnd. The designed microstrip line-coplanar stripline ultra-wideband Balun consists of the microstrip line at the input end, the coplanar strip line at the output end, the fan-shaped mating branch and the partially printed ground plane. The radius of the fan-shaped branch is r_fan.

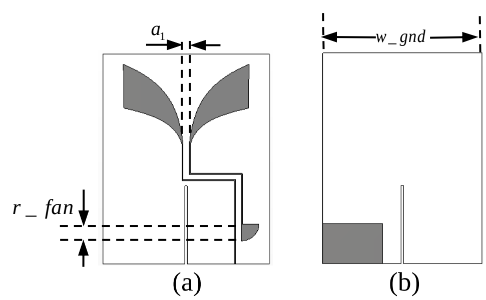

Fig. 2. The structure model of the first antenna radiator: (a) front view and (b) back view.

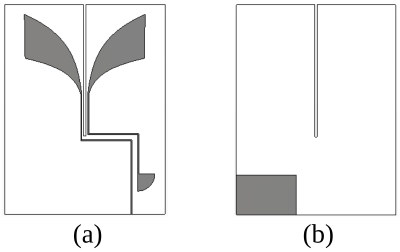

Fig. 3. The structure model of the second antenna radiator: (a) front view and (b) back view.

At the output of the Balun, the coplanar stripline excites the balanced Vivaldi radiator, the radiation impedance of the radiator is matched with the output impedance of the Balun, and the full-wave electromagnetic simulation technique is used to complete the parameter design. The curve equation of Vivaldi antenna as follows:

$$x = ae^{ry}. \tag{1}$$

The characteristic impedance of CPS can be calculated by the following formula [20]:

$$Z_0 = \frac{120\pi}{\sqrt{\varepsilon_{re}}}\frac{K(k_1)}{K'(k_1)}(\Omega), \tag{2}$$

$$\varepsilon_{re} = 1 + \frac{\varepsilon_r - 1}{2}\frac{K'(k_1)}{K(k_1)}\frac{K(k_2)}{K'(k_2)}, \tag{3}$$

$$k_1 = \frac{s}{s+2W} = \frac{a}{b}, \tag{4}$$

$$k_2 = \frac{\sinh\left(\dfrac{\pi a}{2h}\right)}{\sinh\left(\dfrac{\pi b}{2h}\right)}, \tag{5}$$

$$W_S = W_C = W_0. \tag{6}$$

Where, ε_r is the dielectric constant of the dielectric plate, ε_{re} is the relative dielectric constant, K is the elliptic integral function, h is the thickness of the dielectric plate, W and g are the width of the stripline and the gap between them, respectively.

According to formula (2)-(6), the characteristic impedance of coplanar stripline is calculated, and the structure of Balun and impedance matching is designed and optimized.

The simulated performance curves of polarization isolation for the designed antenna varying with the parameter of r_fan are shown in Fig. 4. It can be seen that the radius of the fan-shaped branch has little effect on port isolation of the low frequency band. In the high frequency band, as the radius of the fan-shaped branch becomes larger, the isolation between the ports is greatly undulated, and the size is preferably 10 mm.

The simulated curves of polarization isolation for the antenna varying with the parameter of a_1 are shown in Fig. 5. It can be seen that with the increase of a_1, the polarization port isolation of the two ports both show a good trend. When a_1 becomes 1.5 mm, it continues to increase by a_1.

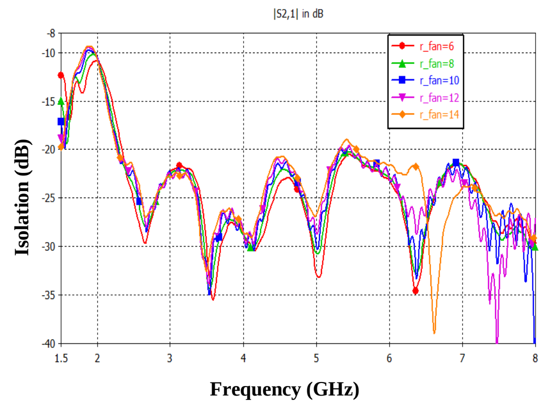

Fig. 4. Port isolation curves varying with r_fan.

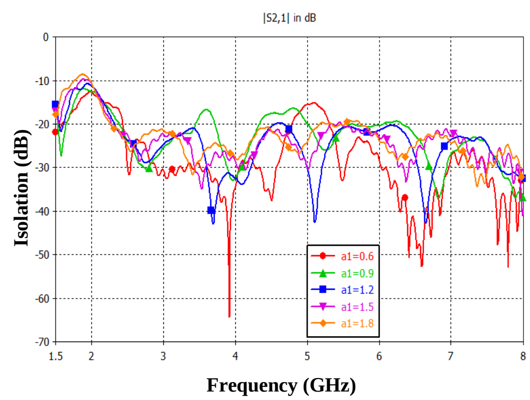

Fig. 5. Port isolation degree curves varying with a_1.
5

The dimensions of the dual-polarized UWB Vivaldi antenna are determined as follows: a_1 is 1.5 mm, r_fan is 10 mm, and w_gnd is 80 mm. The simulation results of the return loss and port isolation of the dual-polarized Vivaldi antenna designed in this paper are shown in Figure 6. In the frequency range of 3 GHz to 4 GHz, the average return loss of the two polarization ports of the antenna is about 8 dB, and the average isolation of the polarization port of the antenna is about 20 dB. The performance of the two port circuits is basically symmetrical.

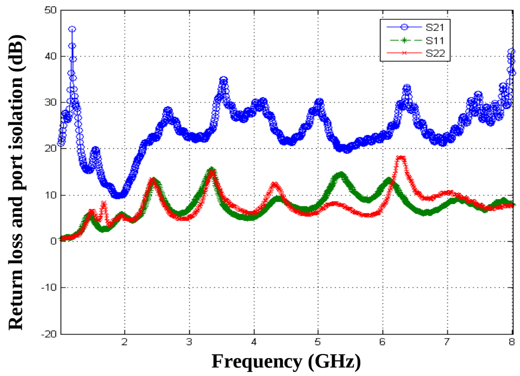

Fig. 6. The simulated return loss and port isolation degree of dual-polarized antenna.

Figure 7 shows the simulation results of the impedance characteristics of the two polarization ports. It can be seen that the average value of the resistance part of the input impedance of the two polarization ports is about 50 ohms in the working frequency band, and the reactance part is small. The mutual impedance value fluctuates near zero, and the average value is close to zero, which reveals the impedance characteristics of ultra wideband.

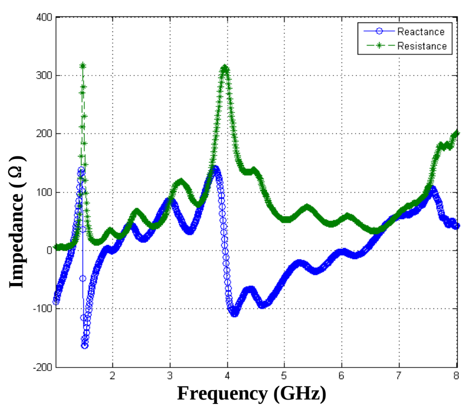

(a)

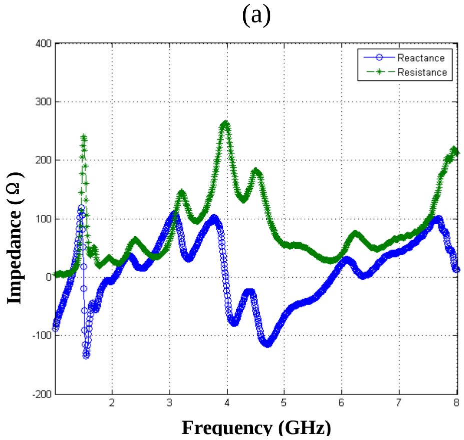

(b)

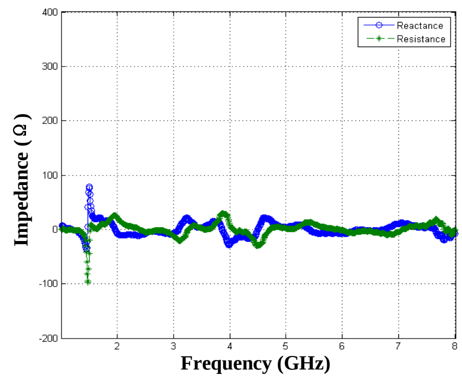

(c)

Fig. 7. The simulation results of the impedance characteristics of the two polarization ports: (a) the self impedance of port 1, (b) the self impedance of port 2, and (c) the mutual impedance between the port 1 and the port2.

Figure 8 shows the current distributions on the surface at 3GHz and 6GHz, respectively. It can be seen that the current distribution on the surface of the antenna changes smoothly with the frequency, the current distribution on the two polarization ports is symmetrical, and the current distribution is concentrated on the slot edge of the radiation dipole. The radiation fields of the two polarization ports are orthogonal, which shows the effectiveness of the design scheme.

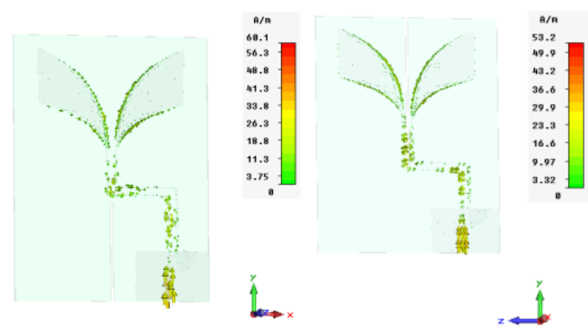

(a) Port 1 at 3GHz (b) Port 2 at 3GHz

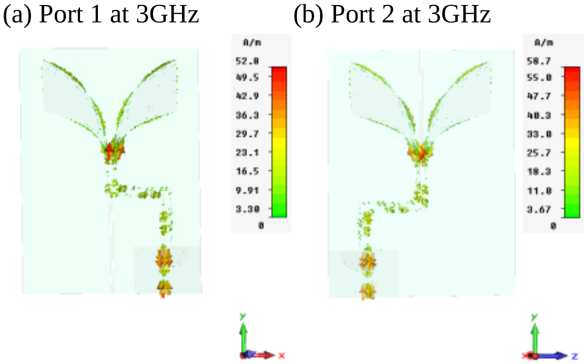

(c) Port 1 at 6GHz (d) Port 2 at 6GHz

Fig. 8. The current distributions of the impedance characteristics of the two polarization ports.

Figure 9 and Fig. 10 show the simulated three dimension gain patterns of two polarized ports at four typical frequencies, respectively. According to Fig. 9 and Fig. 10, the wide beam performances of two polarized ports within the whole working frequency range are observed.

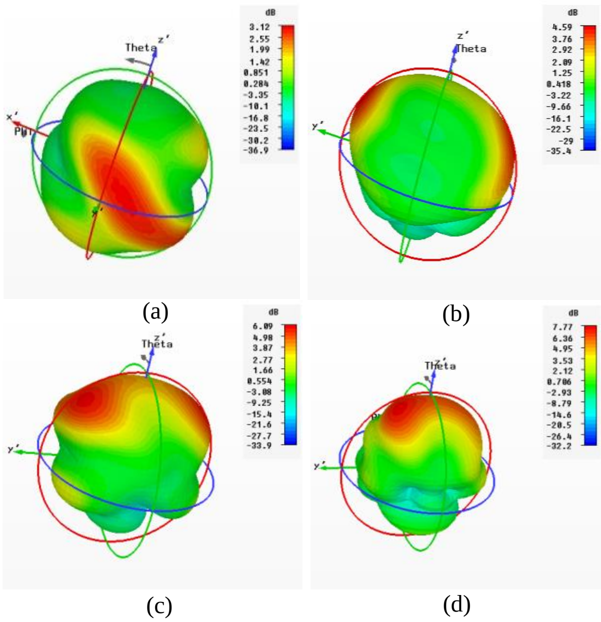

Fig. 9. The simulated three dimension gain patterns of port 1: (a) pattern at 3GHz, (b) pattern at 4GHz, (c) pattern at 5GHz, and (d) pattern at 6GHz.

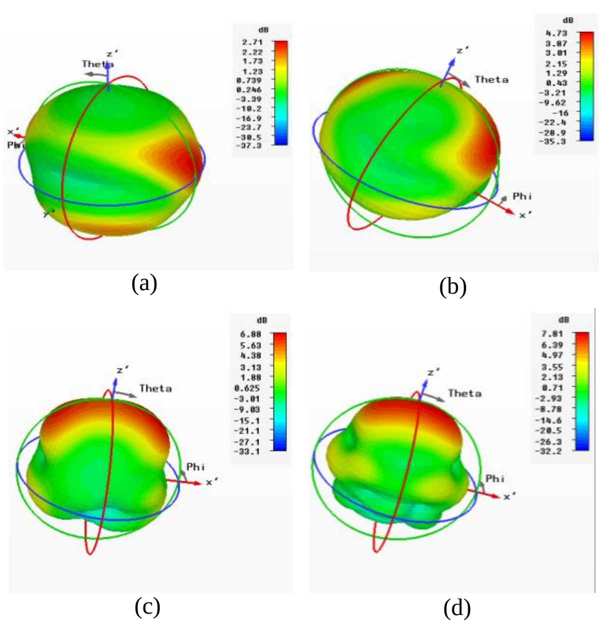

Fig. 10. The simulated three dimension gain patterns of port 2: (a) pattern at 3GHz, (b) pattern at 4GHz, (c) pattern at 5GHz, and (d) pattern at 6GHz.

III. RESULTS AND DISCUSSIONS

According to the design result of the dual-polarized UWB Vivaldi antenna, an antenna prototype was fabricated and tested. The antenna performance experiment was carried out in the microwave anechoic chamber. The processed antenna photo is shown in Fig. 11. The test results of return loss and port isolation of the dual-polarized Vivaldi antenna in this paper are shown in Fig. 12. The return loss in the frequency range of 3GHz~6GHz is less than 10dB, and the port isolation is less than 20dB. The return loss and isolation index meet the expected specifications of the dual-polarized antenna.

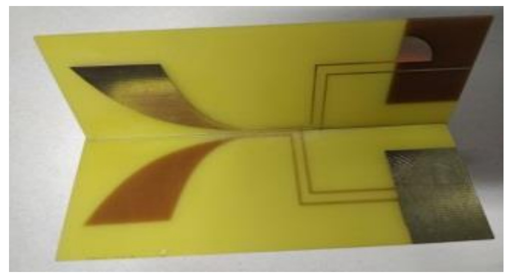

Fig. 11. The photo of the fabricated dual-polarized UWB antenna.

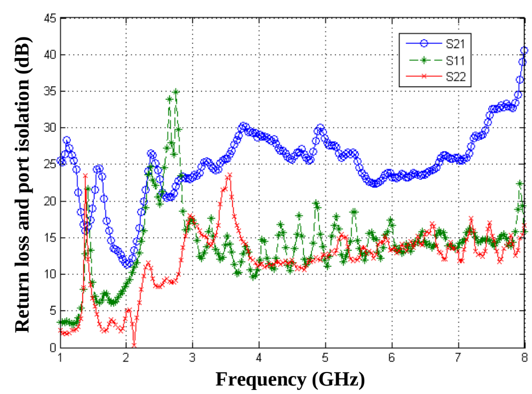

Fig. 12. The measured return loss and port isolation degree of dual-polarized antenna.

Figure 13, Fig. 14, Fig. 15 and Fig. 16 show the radiation pattern tested results at 3GHz, 4GHz, 5GHz and 6GHz, respectively. At each frequency point, the radiation directions of the E and H planes are given respectively. All test results are summarized in Table 1. The test results show that the test direction of the antenna is basically consistent with the simulation results, which verifies the effectiveness of the design. The tested gains are lower than the simulated results. The radiation pattern has a certain fluctuation, which is due to the environmental interference of the test site and machining errors.

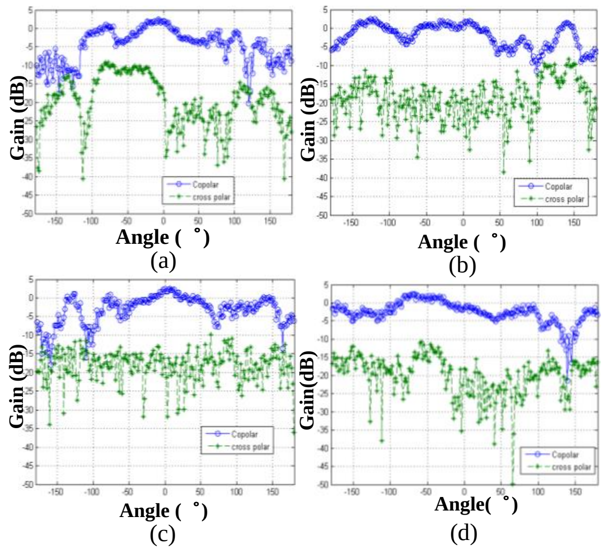

Fig. 13. The measured patterns of the antenna at 3GHz: (a) Port 1 at E plane, (b) Port 1 at H plane, (c) Port 2 at E plane, and (d) Port 2 at H plane.

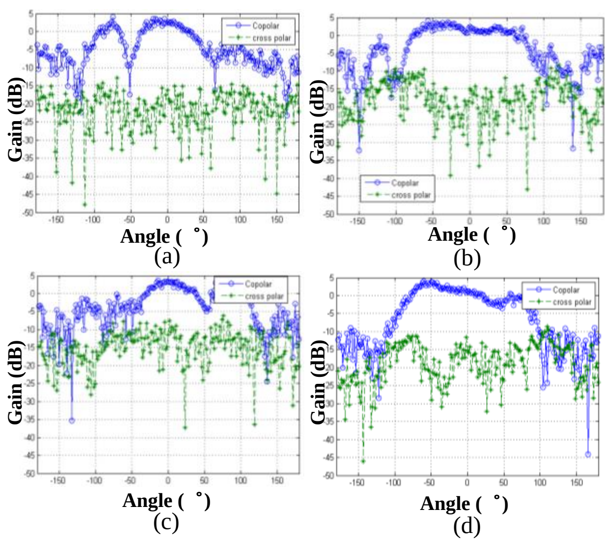

Fig. 14. The measured patterns of the antenna at 4GHz: (a) Port 1 at E plane, (b) Port 1 at H plane, (c) Port 2 at E plane, and (d) Port 2 at H plane.

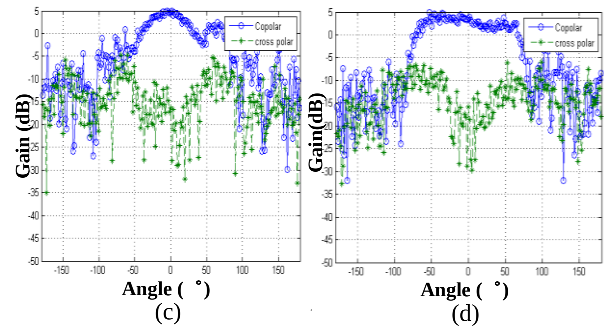

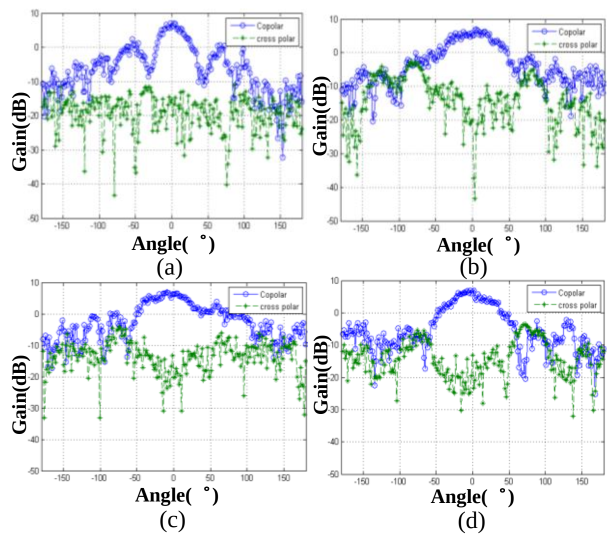

Fig. 15. The measured patterns of the antenna at 5GHz: (a) Port 1 at E plane, (b) Port 1 at H plane, (c) Port 2 at E plane, and (d) Port 2 at H plane.

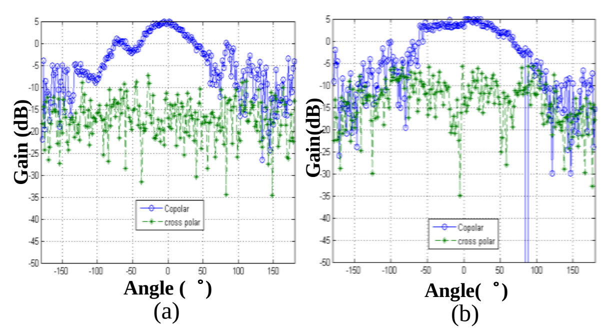

Fig. 16. The measured patterns of the antenna at 6GHz: (a) Port 1 at E plane, (b) Port 1 at H plane, (c) Port 2 at E plane, and (d) Port 2 at H plane.

Table 1: The test results of designed antenna

Frequency (GHz)	2.5	3	4	5	6
$\lvert S_{11}\rvert$ **for port 1 (dB)**	-19	-16	-10	-12	-16
Gain for port 1 (dB)	4	3.5	4.5	6	7.5
$\lvert S_{22}\rvert$ **for port 2 (dB)**	-9	-16	-11	-11	-12
Gain for port 2 (dB)	3.5	3	4.6	6.7	7.6
Isolation degree (dB)	-22	-23	-29	-30	-23

IV. CONCLUSION

This paper researched a dual-polarized UWB Vivaldi antenna, which employs an integrated Balun from microstrip line to coplanar stripline to feed the Vivaldi antenna radiator. The bended coplanar strip-lines were used to improve isolation degree of polarization ports. The traditional dual-polarized of the Vivaldi antenna isolation features have greatly improved. The design and fabrication difficulty of dual-polarized antenna have been reduced. It is easy to be used in the practical engineering. A UWB Vivaldi antenna working at 2.5GHz~6GHz is designed by full-wave electromagnetic simulation software. The simulation and experimental results verified the proposed dual-polarized UWB Vivaldi antenna scheme.

ACKNOWLEDGMENT

The authors would like to thank all anonymous reviewers and editors for their helpful suggestions for the improvement of this paper. The authors thank Dr. P. Lizhong Song for their help in simulation.

REFERENCES

[1] R. Sehroer, "Electronic warfare," *IEEE Aerospace Electronic Systems Magazine*, vol. 18, no. 7, pp. 49-54, Nov. 2003.

[2] B. Baseghi, "Characterizing radar emissions using a robust countermeasure receiver," *IEEE Transactions on Aerospace and Electronic Systems*, vol. 28, no. 3, pp. 109-117, Aug. 1992.

[3] T. Dang, H. Zheng, W. Cui, W. Wang, and G. Wang, "Research on UWB antenna elements and arrays with gradient balun feed," *Journal of Radio Science*, vol. 33, no. 3, pp. 357-364, Jan. 2018.

[4] Z. Chen, W. Niu, and Q. Cao, "Planar sinusoidal antenna and its miniaturized feed balun," *Aviation Weapons*, vol. 13, no. 5, pp. 44-46, June 2009.

[5] S.-G. Zhou, Z.-H. Peng, G.-L. Huang, J.-Y. Li, and C.-Y.-D. Sim, "Design of wideband and dual polarized cavity antenna planar array," *IEEE Transactions on Antennas and Propagation*, vol. 64, no. 10, pp. 4565-4569, Oct. 2009.

[6] H. Nawaz and I. Tekin, "Compact dual-polarised microstrip patch antenna with high interport isolation for 2.5GHz in-band full-duplex wireless applications," *IET Microwaves, Antennas & Propagation*, vol. 11, no. 7, pp. 976-981, Jan. 2017.

[7] H. Liu, Y. Liu, and S. Gong, "Design of a compact dual-polarised slot antenna with enhanced gain," *IET Microwaves Antennas & Propagation*, vol. 11, no. 6, pp. 892-897, Jan. 2017.

[8] H. Zhai, L. Xi, Y. Zang, and L. Li, "A low-profile dual-polarized high-isolation MIMO antenna arrays for wideband base-station applications," *IEEE Transactions on Antennas and Propagation*, vol. 66, no. 1, pp. 191-202, Nov. 2018.

[9] W. Yang, D. Chen, and W. Che, "High-efficiency high-isolation dual-orthogonally polarized patch antennas using nonperiodic RAMC structure," *IEEE Transactions on Antennas and Propagation*, vol. 65, no. 2, pp. 887-892, Nov. 2018.

[10] W.-Q. Deng, X.-S. Yang, C.-S. Shen, J. Zhao, and B.-Z. Wang, "A dual-polarized pattern reconfigurable Yagi patch antenna for microbase stations," *IIEEE Transactions on Antennas and Propagation*, vol. 65, no. 10, pp. 5095-5102, Aug. 2017.

[11] F. Jiang, "Four-arm sinusoidal antenna design," *Modern Radar*, vol. 28, no. 2, pp. 64-67, Aug. 2006.

[12] M. Vahdani and X. Begaud, "Wideband integrated feeding system for a dual polarisation sinuous antenna," *IET Microwaves, Antennas & Propagation*, vol. 4, no. 11, pp. 1704-1713, Dec. 2010.

[13] F. Zhang, X. Ding, S. Lu, and Y. Zhang, "Ultra-wideband dual-polarization logarithmic periodic single-pulse antenna," *Chinese Journal of Radio Science*, vol. 22, no. 5, pp. 751-754, May 2007.

[14] H. Shirinabadi, M. Ahmadi-Boroujeni, E. Arbabi, and K. Mohammadpour-Aghdam, "Design of a printed non-planar dual-polarised log-periodic dipole array," *IET Microwaves, Antennas & Propagation*, vol. 11, no. 4, pp. 490-494, Oct. 2007.

[15] C. Wu, C. Lu, and W. Cao, "Wideband dual-polarization slot antenna with high isolation by using microstrip line Balun feed," *IEEE Antennas and Wireless Propagation Letters*, vol. 16, no. 2, pp. 1759-1762, Feb. 2017.

[16] X. Chen and S. Liu, "Design of a dual-polarized MIMO ultra-wideband square-ring slot antenna," *Electronic Components and Materials*, vol. 36, no. 9, pp. 15-17, Jan. 2017.

[17] P. L. Carro and J. de Mingo, "Analysis and synthesis of double-sided parallel-strip transitions," *IEEE Transactions on Microwave Theory and Techniques*, vol. 58, no. 2, pp. 372-380, Mar. 2010.

[18] C. Icheln, J. Krogerus, and P. Vainikainen, "Use of Balun chokes in small-antenna radiation measurements," *IEEE Transactions on Instrumentation and Measurement*, vol. 53, no. 2, pp. 498-506, May 2004.

[19] M. Bemani, S. Nikmehr, and H.-R. Takfallah, "Dual-band microstrip-to-coplanar stripline Wilkinson balun using composite right- and left-handed transmission lines and its application in feeding dual-band bow-tie antenna," *IET Microwaves, Antennas & Propagation*, vol. 8, no. 7, pp. 532-540, May 2014.

[20] W. Guo, J.-S. Xiao, and M.-T. Li, "A novel high gain coplanar strip-line rectenna design," *Information and Electronic Engineering* (Chinese), vol. 6, no. 7, pp. 545-549, Mar. 2009.

[21] S. Karamzadeh. "A novel compact polarization diversity ultra-wideband MIMO antenna," *Appl. Comp. Electro. Society (ACES) Journal*, vol. 32, no. 1, pp. 75-79, Jan. 2017.

[22] R. Azim, M. T. Islam, and N. Misran, "Design of aplanar UWB antenna with new band enhancement technique," *Appl. Comp. Electro. Society (ACES)*

Journal, vol. 26, no. 10, pp. 856-862, Oct. 2011.

Jian Wu was born in Shiyan, China 1985. He received his M.Sc. degrees in National Defense Key Laboratory of Electronic Measurement Technology from North University of China in 2012. From 2012 he was an Assistant Engineer and now he is a Senior Engineer in the Shanghai Microwave Equipment Research Institute, Shanghai, China. He is currently Ph.D. student at Shanghai University, Shanghai, China. His primary research interests are in dual-polarized antenna, microwave circuits, electronic reconnaissance system.

Xiaojin Zhu was born in 1965. He is a Full Professor, Ph.D. Supervisor of the School of Mechatronic Engineering and Automation at Shanghai University. He received his B.S. degree from Xi'an University of Technology in 1985, his master degree from Tongji University in 1992, his Ph.D. degree from Nanjing University of Aeronautics and Astronautics in 1998. His present research interests are on electronic reconnaissance system, active vibration control, testing technology and signal processing, computer measurement and control technology.

A Wideband Wide-beam Dual Polarized Dipole Antenna and its Application in Wideband Wide-angle Scanning Array

JianYong Yin [1,2], HouJun Sun [1*], and Lei Zhang [1]

[1] The School of Information and Electronics
Beijing Institute of Technology, Beijing, 100081, China
13581869724@139.com, sunhoujun@bit.edu.cn*, txdy519@163.com

[2] Space Star Technology Co., Ltd
China Academy of Space Technology, Beijing, 100081, China

Abstract **─** A wideband wide-beam dual polarized dipole antenna is proposed in this paper. The antenna has a compact size ($0.48\lambda_0\times0.48\lambda_0\times0.154\lambda_0$) and can operate in a wide frequency range from 1.7GHz to 2.4GHz with a half power beam-width more than 100° in the H-plane for dual polarization. Furthermore, the proposed antenna is employed in two linear arrays. The main beam of the configured arrays can scan from -60° to +60° with a gain fluctuation less than 4dB over the entire band for dual polarization. The antenna is fabricated and measured in an anechoic chamber. The measured results have a good agreement with the simulated results.

Index Terms **─** Dipole antenna, dual polarization, wideband, wide beam, wide-angle scanning.

I. INTRODUCTION

In recent years, with the rapid development of modern wireless communication technology, high performance antennas have attracted more and more attentions. In order to improve the communication network capacity, achieve the high rate communication and minimize the multiple fading, the antenna should have the characteristics of the wide bandwidth, dual polarization, high cross polarization discrimination (XPD) and high front to back ratio (FBR) [1-3]. What is more, the emergence, progress and development of new technologies, such as 5G technology, Internet of things, low orbit satellite communication and so on, have stimulated researchers' enthusiasm on the large-scale electronically scanned array (ESA) [4-6]. As a result, a wide beam-width antenna is demanded for phased array to improve the gain at the wide scanning angle [7].

To meet the above requirements, various kinds of antennas have been proposed [8-10]. Owing to its merits of low profile, easy fabrication and light weight, the microstrip antenna has been used widely. Many methods involving wide band [11], dual polarization [12], wide beam-width [13] and wide scanning angle [14,15] have been reported, but only one or some aspect is referred. [14] proposes a wide-beam microstrip element by optimizing a parasitic pixel layer and achieves a 2-D planar wide-angle scanning from -75° to +75°. But it only works at 5.2GHz for single polarization. A wide-angle scanning linear phased array antenna is proposed in [15]. By employing a wide-beam microstrip antenna element, the proposed array can achieve ±75° scanning with a gain fluctuation less than 3dB in a frequency band from 3.2GHz to 3.8GHz for single polarization, indication a fractional bandwidth of 17%. The planar dipole antenna is another popular radiator and it has advantages of wide bandwidth, dual polarization and low cost, which makes it suitable for 2G/3G/4G base station [16,17]. But the narrow half power beam-width (generally 65°±5°) and high profile (generally 0.25λ) make the traditional planar dipole antenna mismatch the requirement of ESA, such as the large-scale ESA for 5G base station. The magneto-electric (ME) dipole antenna proposed by Luk and Wong is an attractive antenna owing to its excellent electrical characteristics, such as wideband, symmetric radiation patterns, low cross polarization, low back radiation and stable gain over the entire operating band [18]. [19] shows a wide-beam circularity polarized (CP) microstrip magnetic-electric dipole antenna and it is applied to achieve a wide-angle CP scanning from -66° to 66°. But it is only effective at 5.6GHz. As a result, to the knowledge of the author, an antenna, which can achieve wide-angle scanning in a wide bandwidth for dual polarization, is rarely presented.

In order to address problems mentioned above, a wideband wide-beam dual polarized dipole antenna is proposed. By employing the proposed antenna as an element, two wide-angle scanning linear arrays can be obtained. The main beam of arrays can scan from -60° to

Submitted On: February 4, 2020
Accepted On: April 18, 2020

$+60^{\circ}$ with a gain fluctuation less than 4dB from 1.7GHz to 2.4GHz for dual polarization, which makes it a promising candidate for 5G base station, radar and satellite communication systems.

II. DESIGN OF PROPOSED ANTENNA ELEMENT

A. Antenna configuration

The configuration of the proposed antenna is shown in Fig. 1. It consists of four layers from up to down. On the top layer, it is a Taconic TLY-5A substrate with the permittivity of 2.2 and the loss tangent of 0.0009. The size is 70mm×70mm×1.524mm. Two shaped dipoles are printed on the bottom of the substrate along the $\pm 45^{\circ}$ diagonal direction to form dual polarized radiation, while two microstrip lines and loop-structures are printed on the other side of the substrate to excite dipoles by coupling. Two vias are employed to avoid the intersection between the two feeding microstrip lines. There are two 50Ω coaxial cables are used to feed the antenna. The inner conductors are connected to the microstrip lines, while the outer conductors are soldered with the dipoles on the bottom of the substrate. As we all know, the height between the dipole and the PEC reflector is usually set as $0.25\lambda_0$ to form a directional radiation with high gain. In order to obtain a lower profile, here we make a compromise between bandwidth and profile and two layers are employed in the middle of the antenna. The upper one is an 8mm-thick foam layer, while the lower one is a Taconic FR-60 substrate with dielectric constant of 6.15 and thickness of 13mm. They are used to support the dipole antenna and reduce the overall height of proposed antenna lower than $0.25\lambda_0$. The bottom layer is a metal plane, which is as a reflector to form directional radiation. There are four plastic screws on the periphery of the antenna to form a solid structure.

Table 1: The parameters of proposed antenna (unit:mm)

Parameter	W1	W2	W3	W4
Value	4	8	3	3.5
Parameter	W5	W6	L1	L2
Value	1	9.32	15	21.5
Parameter	L3	L4	L5	L6
Value	3	4.75	7.07	2
Parameter	r1	r2	r3	G
Value	1	1.13	0.5	70
Parameter	H1	H2	H3	
Value	1.524	8	13	

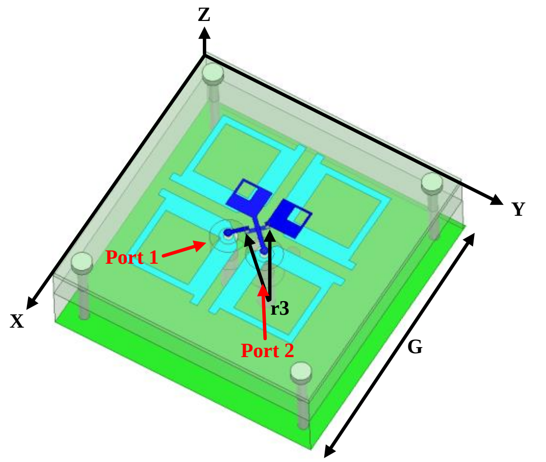

(a) Perspective view

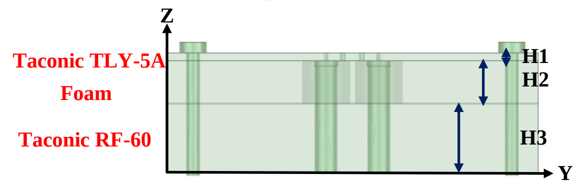

(b) Side view

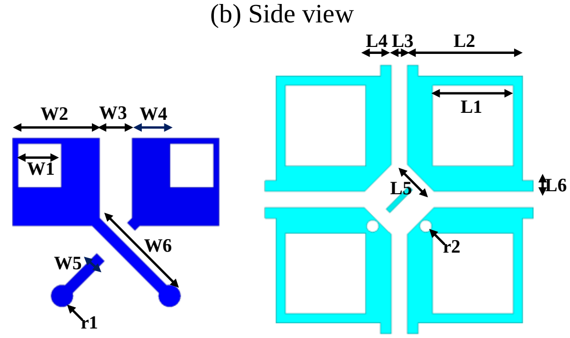

(c) Top view and bottom view of the top layer

Fig. 1. Configuration of the dual polarized antenna.

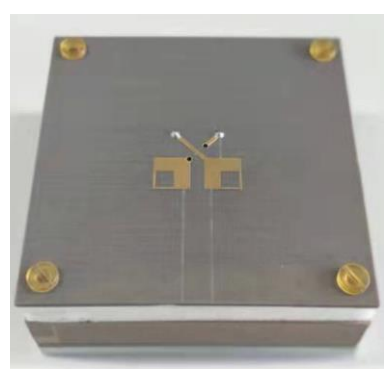

Fig. 2. Prototype of the proposed antenna.

The overall size of the proposed antenna is 70mm×70mm×22.524mm and is corresponding to $0.48\lambda_0 \times 0.48\lambda_0 \times 0.154\lambda_0$ (where λ_0 is the wavelength of the center operating frequency), which indicates a simple, compact structure and a low profile.

B. Numerical study and discussion of parameters

The proposed antenna is modeled in High Frequency Structure Simulator (HFSS) and optimized with the Finite Element Method (FEM). The detailed parameters of the proposed antenna are listed in Table 1. A prototype based on the optimized parameters is fabricated to verify the validity of the proposed antenna and it is exhibited in Fig. 2.

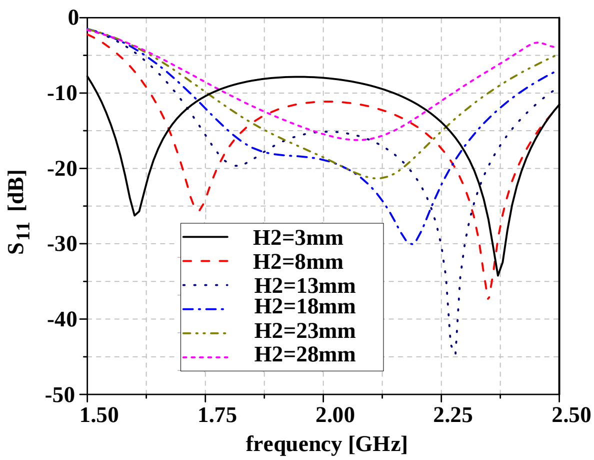

(a) Numerical study of parameter H2

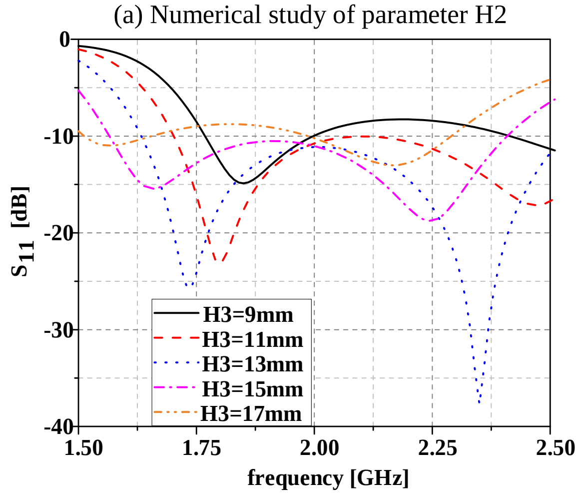

(b) Numerical study of parameter H3

Fig. 3. Numerical study of parameters.

Because the hybrid substrate has a great influence on the impedance bandwidth, here the key parameter H2 and H3 are numerically studied and shown in Fig. 3, while the other parameters remain unchanged. It can be seen that as H2 goes down, the single resonance gradually turns into the dual resonance and the bandwidth is enhanced. When the H2 gets smaller, the two resonant points are far apart, which leads to a dual band antenna. As a result, H2 is selected as 8mm to obtain a relatively wide bandwidth.

It can be seen from Fig. 3 (b) that the variation of parameter H3 will lead to the different resonance strength of two resonant points. Considering the balance between them, bandwidth and the profile, the parameter H3 is chosen as 13mm here.

C. Performances of the proposed antenna

The simulated S-parameters of the proposed antenna are illustrated in Fig. 4. It can be seen that a -10dB frequency band covering 1.7GHz to 2.4GHz can be observed, which means a fractional bandwidth of 34%. The isolation between two ports is greater than 25dB over the entire frequency band, indicating a good isolation. The measured S11 and S22 are consistent with the simulated ones and a lower port-to-port measured isolation than -25dB can be observed over the entire operating band.

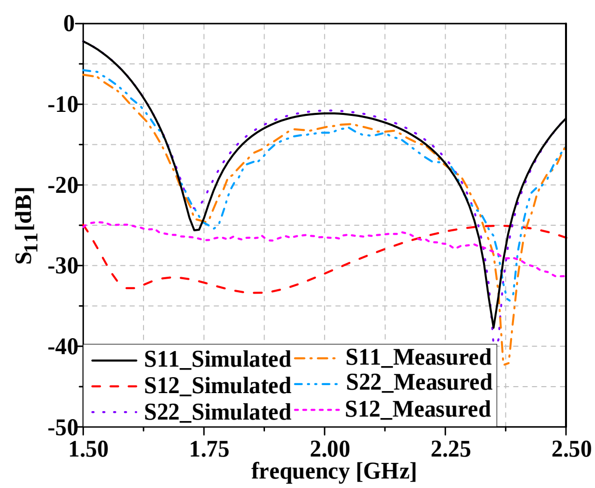

Fig. 4. S-parameters versus frequency.

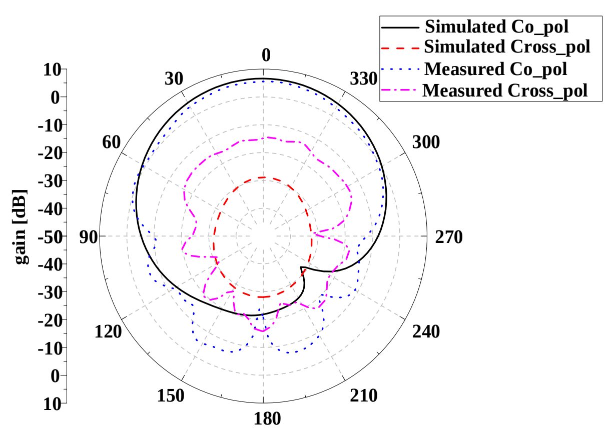

(a) E-plane (1.7GHz)

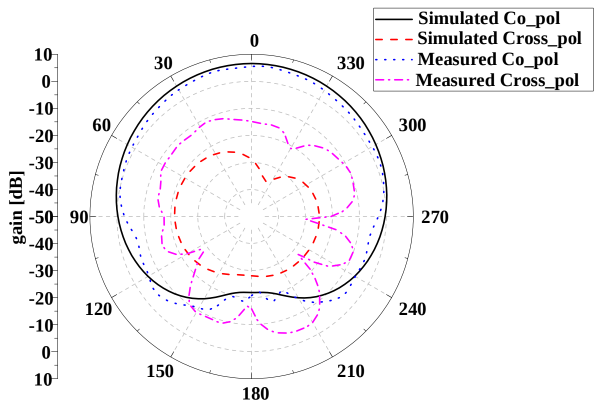

(b) H-plane (1.7GHz)

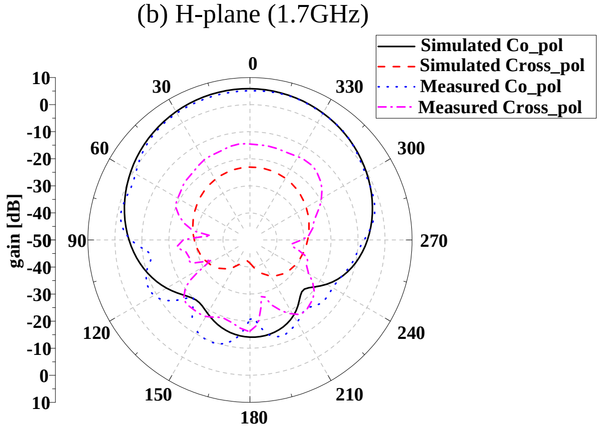

(c) E-plane (2GHz)

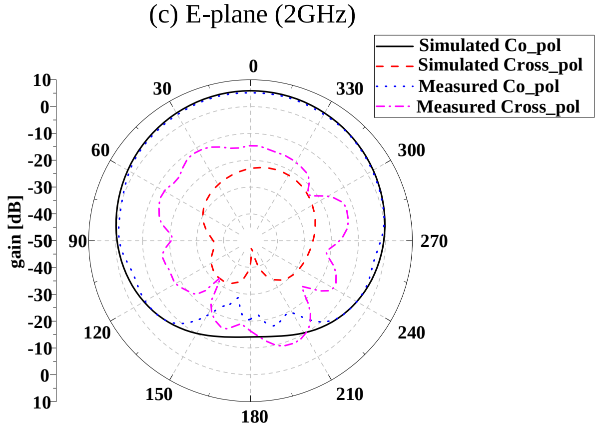

(d) H-plane (2GHz)

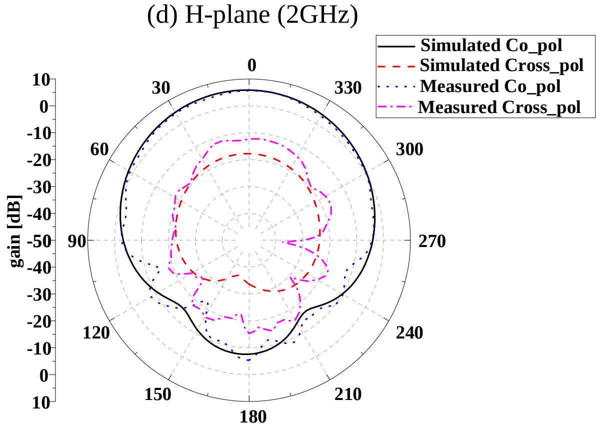

(e) E-plane (2.4GHz)

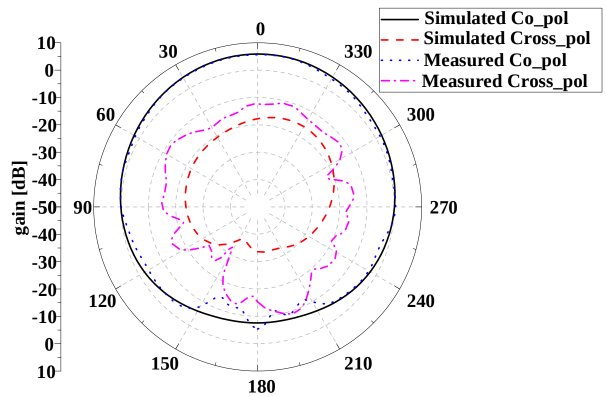

(f) H-plane (2.4GHz)

Fig. 5. Radiation patterns at 1.7GHz, 2 GHz and 2.4GHz for -45° polarization.

Considering the symmetry of the proposed antenna, only E-plane and H-plane radiation patterns with Port 1 excited at different operating frequency are exhibited in Fig. 5. It can be seen that a stable radiation pattern can be obtained over the entire operating band. The beam-width of the proposed antenna in the E-plane is 84° at 1.7GHz, 86° at 2GHz, and 92° at 2.4GHz, while the beam-width of the proposed antenna in the H-plane is 113° at 1.7GHz, 112° at 2GHz, and 106° at 2.4GHz. It is obvious that the beam-width of the proposed antenna is wider than that of the reported planar dipole antennas used in base station (The beam-width is usually 65°±5°). The measured results agree with the simulated ones, especially for the principle polarization component. The discrimination between them may come from the fabrication tolerance and imperfection of measurement environment.

III. THE PROPOSED ELEMENT FOR WIDE-ANGLE SCANNING ARRAY

A. Geometry of scanning linear array

In order to verify the effect of the proposed antenna in the ESA, two scanning linear arrays are designed as shown in Fig. 6. Each array consists of eight proposed elements and the spacing between the adjacent element is set as 64mm, which approximately corresponds to 0.5λ at 2.4GHz.

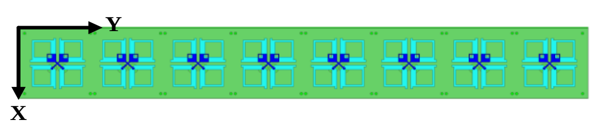

(a) Configuration array 1

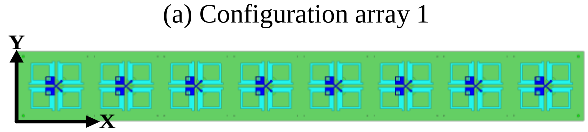

(b) Configuration array 2

Fig. 6. Configuration of scanning linear array.

B. Simulation of the scanning linear array

The simulated performances of two scanning linear arrays are exhibited in Fig. 7 and Fig. 8, respectively. It can be seen that the main beam of two arrays can scan from -60° to +60° with a gain fluctuation less than 4dB over the entire frequency band, especially less than 3dB at 1.7GHz and 2GHz. Compared with the tradition phased array antenna, which usually can scan from -45° to +45° with a gain fluctuation of 4-5dB [7], the proposed array has an excellent wide-angle scanning performance. The relevant scanning performances are concluded in Table 2 and Table 3.

C. Measured performances of the scanning linear array

The proposed array is fabricated and its prototype is shown in Fig. 9. Because of the similar scanning performances for configuration array 1 and array2, only the performances of configuration array 1 are measured in an anechoic chamber. A power divider with one input port and eight output ports and eight analog phase shifters are employed to achieve beam-steering. The measured results for configuration array 1 are presented in Fig. 10.

The measured results show that the main beam can steer from -60°to 60°at 1.7GHz, 2GHz and 2.4GHz. Compared with the normal direction, the gain degradation at ±60°elevation angle is 1.9dB, 2dB and 3.6dB, which is basically consistent with the simulation. The measured results are concluded in Table 4.

The difference between simulated and measured results may come from the fabrication and assembly error. Meantime, the imperfect measured environment and errors introduced by work divider and phase shifter also make the simulated results deviate from measured ones.

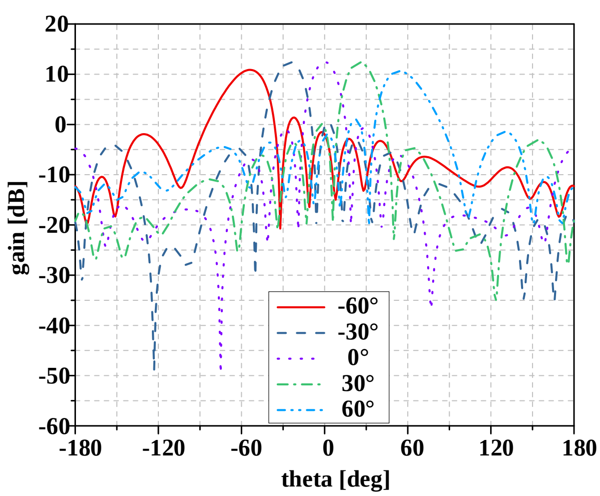

(a) 1.7GHz

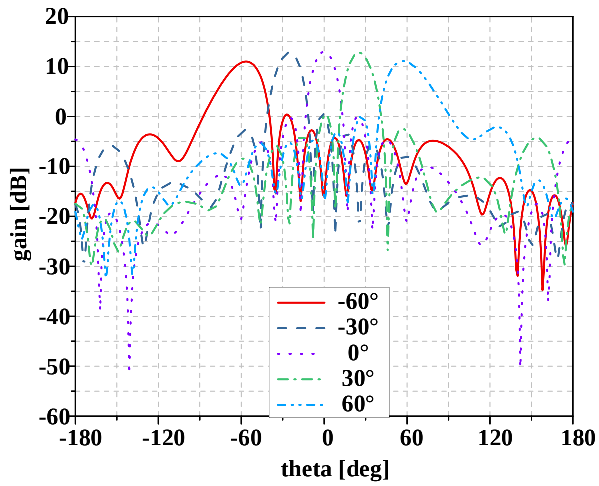

(b) 2GHz

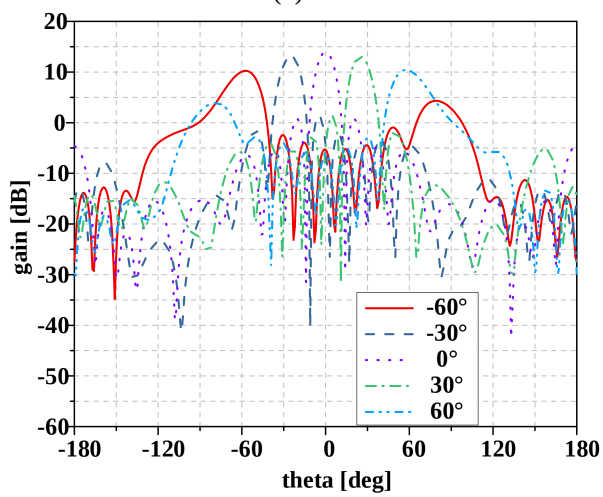

(c) 2.4GHz

Fig. 7. Scanning performances of configuration array 1 for -45° polarization at different frequency.

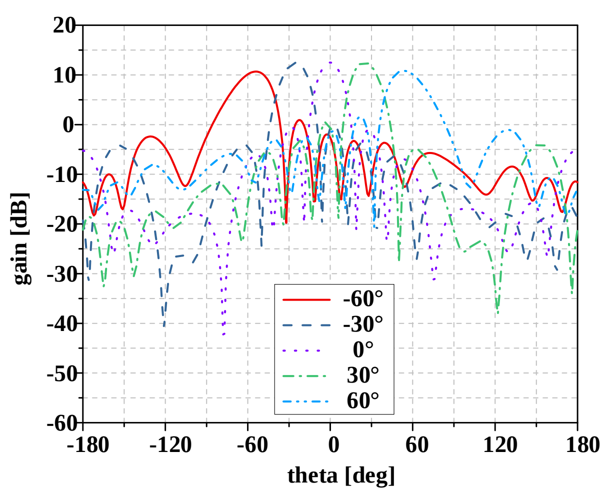

(a) 1.7GHz

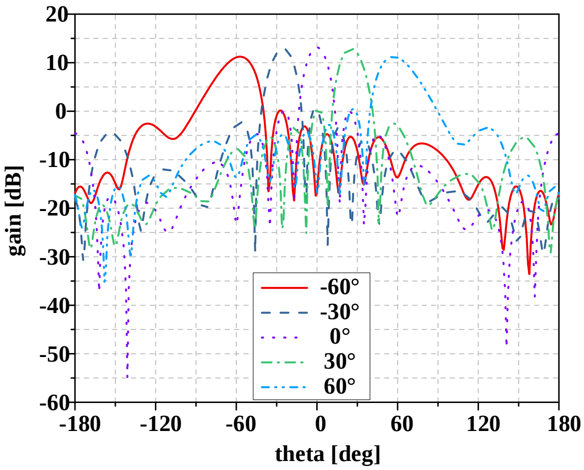

(b) 2GHz

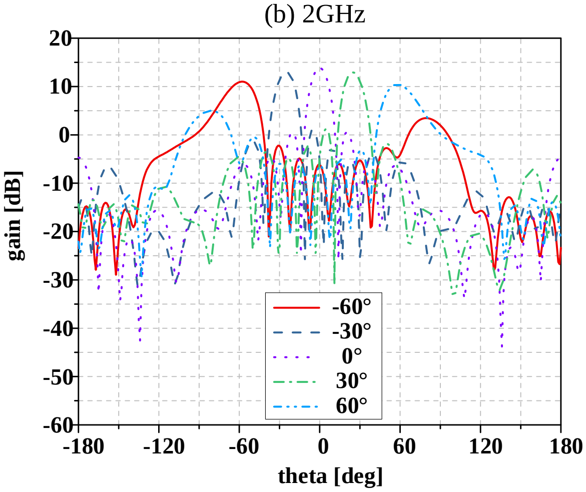

(c) 2.4GHz

Fig. 8. Scanning performances of configuration array 2 for -45° polarization at different frequency.

Table 2: The scanning performances of configuration array 1 for -45° polarization at different frequency in YOZ plane

Array 1		-60°	-30°	0°	30°	60°
1.7 GHz	Gain (dB)	10.2	11.6	12.4	11.6	10
	SLL (dB)	-8.8	-12	-13.5	-11.7	-9
2 GHz	Gain (dB)	10.7	11.8	13	11.8	10.9
	SLL (dB)	-10.3	-11.5	-12.8	-11.6	-10.8
2.4 GHz	Gain (dB)	10.1	11.4	13.9	11.4	10.3
	SLL (dB)	-5.8	-10	-13	-10.1	-6.4

Table 3: The scanning performances of configuration array 2 for -45° polarization at different frequency in XOZ plane

Array 2		-60°	-30°	0°	30°	60°
1.7 GHz	Gain (dB)	10.1	11.7	12.5	11.7	10.1
	SLL (dB)	-9.2	-11.7	-13	-11.1	-8.8
2 GHz	Gain (dB)	11.1	11.9	13.2	11.9	11
	SLL (dB)	-10.9	-11.4	-13.1	-11.4	-10.5
2.4 GHz	Gain (dB)	10.9	11.3	13.8	11.2	10.4
	SLL (dB)	-7.6	-10.2	-13.2	-10	-5.4

Fig. 9. Prototype of the scanning array.

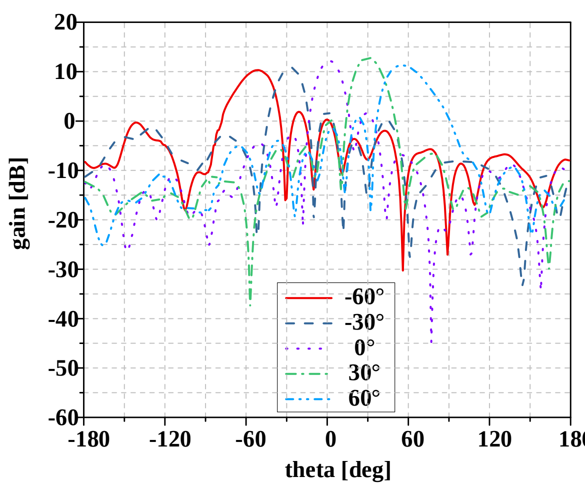

(a) 1.7GHz

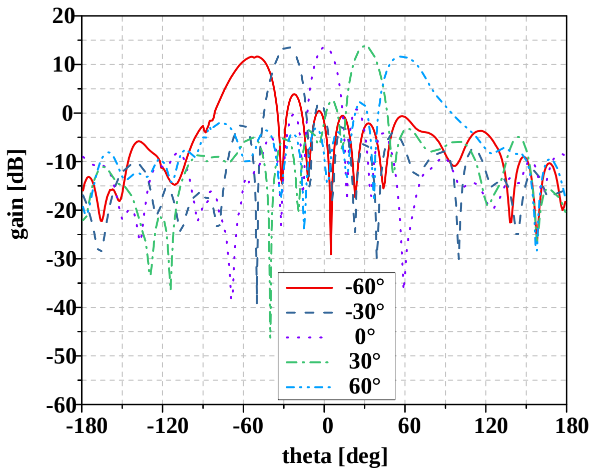

(b) 2GHz

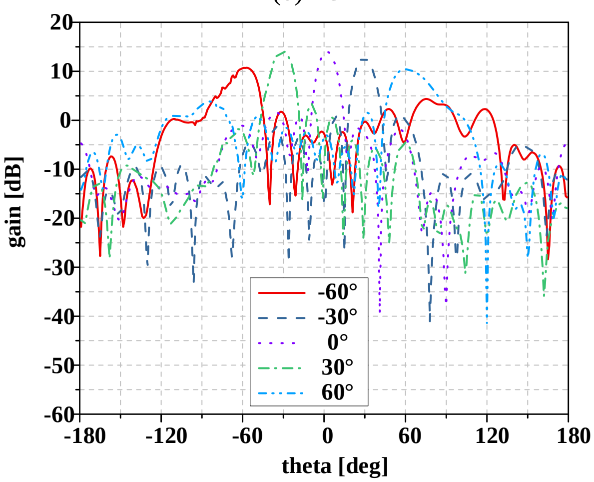

(c) 2.4GHz

Fig. 10. Measured scanning performances of configuration array 1 for -45° polarization at different frequency.

Table 4: The measured scanning performances of configuration array 1 for -45° polarization at different frequency in YOZ plane

Array 1		-60°	-30°	0°	30°	60°
1.7 GHz	Gain (dB)	10.3	10.8	12.2	12.5	11.2
	SLL (dB)	-8.4	-8.9	-13.5	-12.6	-10.5
2 GHz	Gain (dB)	11.6	13.7	13.6	13.7	11.6
	SLL (dB)	-7.7	-11.5	-13.8	-11.2	-9.3
2.4 GHz	Gain (dB)	10.4	14	14	12.6	10.7
	SLL (dB)	-6.4	-10.7	-12.4	-11	-6.5

IV. CONCLUSION

In this paper, a novel dipole antenna is designed. Owing to its merits of wide bandwidth, wide beam-width and dual polarization, the proposed antenna is employed as an element and two linear arrays with eight elements are proposed. Compared with the traditional phased array, the main beam of the proposed arrays can scan from -60° to +60° with a gain fluctuation less than 4dB in a wide frequency band, covering from 1.7GHz to 2.4GHz with a fractional bandwidth of 34%. The element and array are fabricated and measured for validity and measured results agree well with the simulated ones. The antenna has a simple, compact structure and a low profile, and can be applied to 5G base station, radar and satellite communication systems.

REFERENCES

[1] H. Huang, Y. Liu, and S. X. Gong, "A broadband dual-polarized base station antenna with sturdy construction," *IEEE Antennas Wireless Propagat. Lett.*, vol. 16, pp. 665-668, 2017.

[2] J. F. Jiang, Y. F. Xia, and Y. S. Li, "High isolated X-band MIMO array using novel wheel-like metamaterial decoupling structure," *Applied Computational Electromagnetics Society Journal*, vol. 34, no. 12, pp. 1829-1836, 2019.

[3] E. Sunday, B. Adebisi, A. Sabagh, and A. Well, "Gain enhancement of acoustic beamforming arrays in complex dynamic systems," *30th Annual Review of Progress in Applied Computational Electromagnetics*, Jacksonville, Florida, USA, 2014.

[4] J. X. Li, X. K. Zhang, Z. Wang, X. M. Chen, J. Chen, Y. S. Li, and A. X. Zhang, "Dual-band eight antenna array design for MIMO application in 5G mobile terminals," *IEEE Access*, vol. 7, pp. 71636-71644, 2019.

[5] J. Guo, F. Liu, L. Y. Zhao, Y. Z. Yin, G. L. Huang, and Y. S. Li, "Meta-surface antenna array decoupling designs for two linear polarized antennas coupled in H-plane and E-plane," *IEEE Access*, vol. 7, pp. 100442-100452, 2019.

[6] G. L. Huang, J. J. Liang, L. Y. Zhao, D. P. He, and C. Y. D. Sim," Package-in-dielectric liquid parch antenna based on liquid metal alloy," *IEEE Antennas Wireless Propagat. Lett.*, vol. 18, pp. 2360-2364, 2019.

[7] Y. Q. Wen, B. Z. Wang, and X. Ding, "Wide-beam SIW-slot antenna for wide-angle scanning phased array," *IEEE Antennas Wireless Propagat. Lett.*, vol. 15, pp. 1638-1641, 2016.

[8] B. Kaur, A. Marwaha, and S. Rani, "Characterization of 4 element compact microstrip patch antenna array for efficient null steering," *Applied Computational Electromagnetics Society Journal*,

vol. 32, no. 12, pp. 1105-1112, 2017.
[9] C. Craeye and R.Sarkis, "Finite array analysis through combination of macro basis function and array scanning methods," *Applied Computational Electromagnetics Society Journal*, vol. 23, no. 3, pp. 255-261, 2008.
[10] M. C. Tang, S. Q. Xiao, C. J. Li, C. L. Wei, and B. Z. Wang, "Scan blindness elimination using composite defected ground structures and edge coupled split ring resonators," *Applied Computational Electromagnetics Society Journal*, vol. 26, no. 7, pp. 572-583, 2011.
[11] W. J. Lu, Q. Li, S. G. Wang, and L. Zhu, "Design approach to a novel dual-model wideband circular sector patch antenna," *IEEE Trans. Antennas Propagat*., vol. 65, no. 10, pp. 4980-4990, 2017.
[12] Y. J. He, C. Li, and J. Yang, "A low profile dual polarized stacked patch antenna for micro-base-station applications," *2018 IEEE MTT-S International Wireless Symposium*, 2018.
[13] X. Chen, L. Yang, J. Y. Zhao, and G. Fu, "High-efficiency compact circularly polarized microstrip antenna with wide beamwidth for airborne communication," *IEEE Antennas Wireless Propagat. Lett.*, vol. 15, pp. 1518-1521, 2016.
[14] Y. F. Cheng, X. Ding, W. Shao, M. X. Yu, and B. Z. Wang, "2-D planar wide-angle scanning-phased array based on wide-beam elements," *IEEE Antennas Wireless Propagat. Lett.*, vol. 16, pp. 876-879, 2017.
[15] G. W. Yang, J. Y. Li, D. J. Wei, and R. Xu, "Study on wide-angle scanning linear phased array antenna," *IEEE Trans. Antennas Propagat*., vol. 66, no. 1, pp. 450-455, 2018.
[16] Y. H. Cui, L. J. Wu, and R. L. Li, "Bandwidth enhancement of a broadband dual-polarized antenna for 2G/3G/4G and IMT base station," *IEEE Trans. Antennas Propagat*., vol. 66, no. 12, pp. 7368-7373, 2018.
[17] Z. Zhou, Z. H. Wei, Z. Y. Tang, and Y. Z. Yin, "Design and analysis of a wideband multiple microstrip dipole antenna with high isolation," *IEEE Antennas Wireless Propagat. Lett.*, vol. 18, no. 4, pp. 722-726, 2019.
[18] K. M. Luk and H. Wong, "A new wideband unidirectional antenna element," *Int. J. Microw. Opt. Technol.*, vol. 1, no. 1, pp. 35-44, June 2006.
[19] Y. Q. Wen, B. Z. Wang, and X. Ding, "Wide-beam circularly polarized microstrip magnetic-electric dipole antenna for wide-angle scanning phased array," *IEEE Antennas Wireless Propag. Lett.*, vol. 16, pp. 428-431, 2017.

Jianyong Yin was born in Jiangsu Province, China, in 1986. He received the B.S. and M.S degree in Information Engineering from Beijing Institute of Technology (BIT). He is currently pursuing the Ph.D. degree in the Electromagnetic Field and Microwave Technology from BIT, Beijing, China. His research interests include antennas, arrays and phase array system.

Houjun Sun received his Ph.D. degree in Communication and Electronic Systems from BIT in 1997. He is currently a Professor in BIT, the Director of the Institute of Microwave Technology, and the Director of the Beijing Key Laboratory of Millimeter Wave and Terahertz Technology. His current research interests include the integration and application of the millimeter-wave and terahertz communication system, active antenna arrays, millimeter-wave imaging.

Lei Zhang received his M.S. degree in Communication and Information Systems from China Academy of Space Technology in 2017. He is currently pursuing the Ph.D. degree in the Electromagnetic Field and Microwave Technology from BIT, Beijing, China. His research interests include wideband antennas, wide-angle scanning phase array and electromagnetic meta-materials.

Metamaterial Based Compact Branch-Line Coupler with Enhanced Bandwidth for Use in 5G Applications

Arshad K. Vallappil [1], Mohamad Kamal A. Rahim [1], Bilal A. Khawaja [2,3], and Murtala Aminu-Baba [1]

[1] Advance RF and Microwave Research Group (ARFMRG), School of Electrical Engineering
Faculty of Engineering, Universiti Teknologi Malaysia, UTM Johor Bahru, Johor, 81310, Malaysia
kvarshad2@graduate.utm.my, mdkamal@utm.my, limaminkobi@yahoo.com

[2] Faculty of Engineering, Department of Electrical Engineering
Islamic University of Madinah, Madinah, 41411, Saudi Arabia
7166@iu.edu.sa

[3] Department of Electronics and Power Engineering, PN-Engineering College (PNEC)
National University of Sciences and Technology (NUST), Habib-Rahmatullah Road, Karachi, Pakistan
khawaja.bilal@pnec.nust.edu.pk

Abstract **─** A novel compact 5G branch-line coupler (BLC) based on open-circuit coupled-lines and interdigital capacitor structure is presented in this paper. The proposed BLC shows the composite right/left handed (CRLH) metamaterial transmission-line (TL) operation. The proposed BLC is designed and simulated using CST microwave studio. The designed BLC is then fabricated using the FR4 substrate (ε_r = 4.3 and h = 1.66mm). The proposed 5G BLC with coupled-lines and the interdigital capacitor has achieved the fractional bandwidth of ~ 40.2% and the size reduction of 54% as compared to the conventional BLC. The fabricated BLC operates at 2.74 – 4.15GHz frequency band with a coupling factor of -3 ± 0.2dB and the phase difference of 88° between the output ports. The BLC measurements are performed at the operating frequency of 3.5GHz. The simulated and measured scattering parameters and phase difference results are in good agreement with each other. The proposed design is suitable for use in future butler-matrix based beamforming networks for antenna array systems in 5G wireless applications.

Index Terms **─** 5G, beamforming network, branch-line coupler, butler-matrix, Composite Right/Left Handed (CRLH) Transmission-Line (TL), interdigital capacitor.

I. INTRODUCTION

In the 5G wireless communication systems, the multi-beam and beam-scanning smart antennas [1] are playing a crucial role to get the desired output. The use of multi-beam antenna array systems and beamforming network (BFN) is an important means of achieving high directivity and improved coverages for 5G [2]-[3]. The BFNs are used for the adjustment of the amplitude and phase distribution of the multi-beam antenna array system [4]-[5]. Most studies so far have concentrated on the BFNs as a significant part of the 5G system. The butler-matrix (BM) is the most commonly used BFNs, due to its compact design, easy and low-cost fabrication process. There is no requirement of external bias in the BM operation. Moreover, it works like a reciprocal network (used for receiving/transmitting signals) and can be used for the BFN for 5G communication system. The development of the conventional BM consists of three main components, which are; 1) 3-dB couplers, 2) Crossovers and 3) 45° phase shifters. So, this paper focusses on the design of a compact branch-line coupler (BLC) with enhanced bandwidth that can achieve improved coverage for 5G application.

A quadrature coupler is one in which the input is split into two signals (usually with a goal of equal magnitudes) that are 90 degrees apart in phase. Types of quadrature couplers include BLCs (also known as quadrature-hybrid couplers), lange couplers and overlay couplers [6]. The BLCs are used in several 5G communication applications which include BM based antenna arrays, and radio frequency (RF) transceiver systems, and wideband six-port reflectometer design formed by enhanced BLCs [7]–[9]. The 5G technology has many advantages for the end-user, like providing wide coverage, high data-rates and improved spectral efficiency compared to their predecessors [9]. In addition to the above challenges, the 5G technologies have reported limited resources and the paucity of the new

Submitted On: January 20, 2020
Accepted On: April 18, 2020

structure for antenna and passive devices like BLCs, power divider, etc. [1].

In [10], the use of coupled-line unit-cells shows the same properties as dual composite right/left-handed (D-CRLH) unit-cells, and it reduces the BLC size by 52% and improves the bandwidth by 18.9%. In [11], a miniaturized BLC is developed by using the square-split ring resonators that reduces the overall area of 39.82% without much improvement in the bandwidth. In [12], a novel miniaturized BLC based on CRLH-TL structure is presented. Interdigital structure and double-spiral-defected resonant cell are used to get the properties of CRLH. In [13], the authors designed a compact structure of BLC using open stubs and meandered TL.

This paper, therefore, aims to propose, design, fabricate and characterize a new BLC, which is considered one of the main components for the construction of the 5G BM. It is envisioned that the BLC proposed in this paper can be used in the future 5G antenna array BFNs. The 3.5GHz frequency band has been chosen in this study for 5G technology [14]. Moreover, the 700 MHz, 3.5 GHz and 26/28 GHz have also been identified as potential frequency bands for the initial deployment of 5G technology in Malaysia [15]. In the next section, the design methodology of the proposed BLC will be discussed. The configuration is approximately similar to a basic BLC with the *λ/4* length with additional open-circuits coupled-lines technique, and interdigital capacitor (IDC) achieves metamaterial properties. Lai *et al.* [16] first proposed the CRLH-TL structure. The proposed 5G coupler is designed by using the CST microwave studio software which uses the finite-difference time-domain (FDTD) techniques for the 3D electromagnetic field analysis. The proposed coupler is designed using the low-cost FR4 substrate [17]. The agreement between the simulation and measured results suggest that the designed coupler performs well and can be used in the future 5G systems.

The rest of the paper is organized as follows: Section II gives a brief overview of the proposed BLC geometry and design process. The BLC fabrication and characterization are discussed in Section III. The simulated and measured results in terms of BLC parameters like reflection coefficient (S_{11}), insertion loss (S_{12}, S_{13}) and isolation loss (S_{14}) are summarized in Section IV, and then a comparison of the results is presented. Finally, Section V draws conclusions.

II. BRANCH-LINE COUPLER DESIGN

The proposed design of the new BLC is depicted in Figs. 1 (a-b). As shown in Fig. 1 (a), the BLC consists of four ports [18]. The port-1, port-2 and port-3 are input-port, through port and the coupled-port, respectively. Whereas, the port-4 is an isolated port that has no or very negligible output power. The impedance of the horizontal and vertical TL is $Z_0/\sqrt{2}$ and Z_0, respectively. Whereas, Z_0 indicate the characteristic impedance. In the proposed BLC, the value of Z_0 is chosen as 50Ω. The length of the line impedance at each branch is shown in Eq. (1). The IDC unit-cell used in the vertical arm of the BLC is shown in Fig. 1 (b). The width (*W*) and feed length of the BLC can be calculated by using the following equations [18] shown in Eqs. (1-7), respectively. The substrate is chosen to be FR4 with the relative permittivity (ε_r) of 4.3, and the thickness (*h*) of 1.66mm, respectively.

$$Feed\ length = \frac{\lambda}{4\sqrt{\varepsilon_r}} \ . \tag{1}$$

$$A = \frac{Z_o}{60}\left(\frac{\varepsilon_r+1}{2}\right)^{1/2} + \frac{\varepsilon_r-1}{\varepsilon_r+1}\left(0.23+\frac{0.11}{\varepsilon_r}\right) = 1.5, \tag{2}$$

$$B = \frac{60\pi^2}{Z_o\sqrt{\varepsilon_r}}, \tag{3}$$

$$W/h < 2, \tag{4}$$

$$W/h = \frac{8\exp(A)}{\exp(2A)-2} \ , \tag{5}$$

$$W/h > 2, \tag{6}$$

$$W/h = \frac{2}{\pi}\{B-1-\ln(2B-1)\} + \frac{\varepsilon_r-1}{2\varepsilon_r}\left[\ln(B-1)+0.39-\frac{0.61}{\varepsilon_r}\right]. \tag{7}$$

The value of *A* is 1.5 and 1.1 by substituting impedance equal to 50Ω and 35Ω, respectively for vertical and horizontal arms of the BLC. Based on Eq. (1-7), the BLC-TL width (W_{35}) and (W_{50}) is optimized to 5mm and 2.8mm for the fabrication of BLC, as shown in Fig. 1 (a), respectively. The dimensions of the horizontal and vertical IDC unit-cell are summarized in Table 1. The difference of dimensions in the horizontal and vertical unit-cell finger length is due to the impedance matching and the S-matrix requirements for the four-port BLC [18]. Figure 1 (b) also shows that the gap *'s'* between the fingers and at the end of the fingers are same. The fingers have a width of '*m*', and length '*l'* which are also specified. The top surface of the substrate is a copper conductor with a thickness of 0.035mm.

The substrate properties will also affect the BLC performance. Due to the ease of design and fabrication, the IDC often uses planar microstrip TL. Many authors have studied the properties of this type of capacitor [19]–[23]. There are many assumptions made for the calculation of capacitance, some of which are: (1) finger and gap width are considered (2) capacitance also depends on the number of fingers (3) the capacitor dimensions are much less than a quarter wavelength; (4) metallization thickness and (5) the capacitance is neglected at the end of the finger. An enhanced model where the capacitor is divided into its core components is studied briefly in [24].

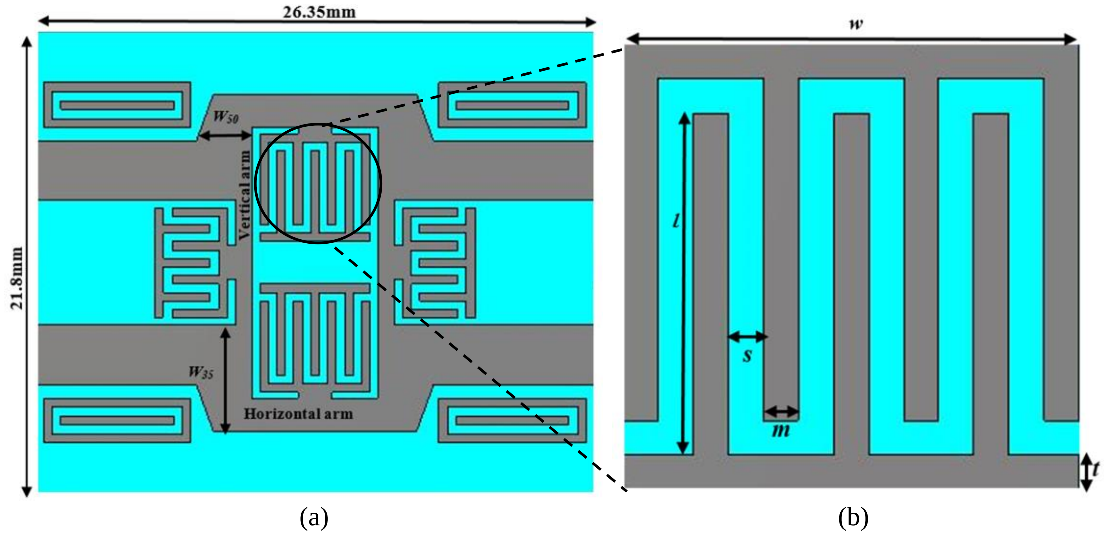

Fig. 1. (a) Proposed BLC showing Interdigital capacitor unit-cell and open-circuits coupled-lines, and (b) zoom-in of IDC unit-cell.

Table 1: Dimensions of horizontal and vertical IDC unit-cell

Description	Notation	Dimension (mm)
Horizontal Arm		
Finger Width	*m*	0.4
Finger Length	*l*	3.9
Width of IDC	*w*	5.2
Finger Gap	*s*	0.4
Exterior Finger Width	*t*	0.4
Vertical Arm		
Finger Width	*m*	0.4
Finger Length	*l*	2.2
Width of IDC	*w*	5.2
Finger Gap	*s*	0.4
Exterior Finger Width	*t*	0.4

Figures 2 (a-b) shows the proposed equivalent circuit model of the IDC. Alley *et al.* [19] have developed the most popular model. The effect of interdigital fingers capacitance is taken into account in this model. The total capacitance is given by Eq. (8) [24]:

$$C = (\varepsilon_r + 1)l\,[(N-3)A_1 + A_2]\ (\text{pF}). \tag{8}$$

In Eq. (8), N represents the number of fingers and the relative permittivity of substrate material represented as ε_r. The constant A_1 and A_2 in Eq. (8) are represented by Eqs. (9-10) [25], respectively:

$$A_1 = 4.409 \tanh\left[0.55\left(\frac{h}{w}\right)^{0.45}\right] \times 10^{-6} (\text{pF}/\mu\text{m}), \tag{9}$$

$$A_2 = 9.92 \tanh\left[0.52\left(\frac{h}{w}\right)^{0.5}\right] \times 10^{-6} (\text{pF}/\mu\text{m}). \tag{10}$$

The constant A_1 and A_2 represented IDC interior and exterior finger in terms of h and w. The w is the width of the overall IDC conductor, and the h represents the thickness of the substrate material. Based on Eqs. (8-10), the capacitance of IDC is equal to 0.14pF. Figures 2 (a-b) represent the IDC's lumped equivalent circuits (EC) for the low- and high-frequency applications, respectively**.** Finally, the series parasitic resistance due to conductor loss is given by Eq. (11):

$$R = \frac{4}{3}\frac{l}{mN} R_s\ (\Omega). \tag{11}$$

Where, R_s is the sheet resistivity of the conductor. The capacitance (C_s) and inductance (L) in eq. (12-13) are calculated for the m/h << 1 approximations. The magnetic field lines are also considered not to loop around each finger, but to loop around the cross-section of the interdigital width, as shown previously in Fig. 2(a). The c indicates the velocity of light in free space.The L and C_s are represented as [22]:

$$L = \frac{Z_0\sqrt{\varepsilon_{eff}}}{c}\, l\ (\text{H}), \tag{12}$$

$$C_s = \frac{1}{2}\frac{\sqrt{\varepsilon_{eff}}}{Z_0 c}\, l\ (\text{F}). \tag{13}$$

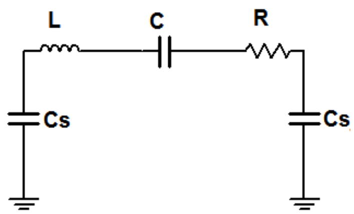

(a)

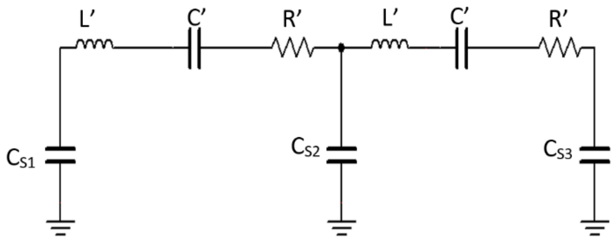

(b)

Fig. 2. EC of the IDC: (a) low frequency and (b) high frequency model, respectively.

The parameters l and w of the IDC unit-cell, as shown in Fig. 1 (b) are calculated in multiple steps which are described below by using Eqs. (14-15), respectively [26]:

Step-1: Choose center frequency (f_o) = 3.5 GHz.

Step-2: Calculate the width of IDC required to achieve BLC horizontal arm impedance of $Z_o/\sqrt{2}$. Based on Eqs. (2-7), the value of 'w' is found to be 5.2 mm.

Step-3: Set the number of fingers, '$N = 7$' (as per BLC design shown in Figs. 1 (a-b)). Then, by using Eq. (14), determine the required parameter 'm' and 's = 2m / 3':

$$m \approx \frac{w}{\left(\frac{5N}{3} - \frac{2}{3}\right)}. \tag{14}$$

Step-4: Optimize the value of 'm' and 's' to 0.4mm.

Step-5: Calculate the value of 'l' and optimize it to 3.9mm by using Eq. (15):

$$l \approx \frac{\lambda_g}{8} \approx \frac{c}{8 f_o \sqrt{\varepsilon_r}}. \tag{15}$$

The different techniques such as double quarter-wave transformer, series open-circuited stubs, open-circuited capacitively coupled lines, and arbitrary power division ratio have been implemented in conventional BLC design to overcome the bandwidth limitation. From these techniques, capacitively coupled $\lambda/4$ open-circuited lines achieve a much improved fractional bandwidth of 63% [27]. So, in this work, it was decided to insert four capacitively coupled open-circuited $\lambda/4$ lines at each port of the proposed BLC by adopting proper characteristic impedances for arbitrary power coupling. This will provide wide bandwidth with DC block capability and flat coupling characteristics [28]. The wideband characteristics of BLC can be analyzed by the equivalent admittance approach of the matched BLC and by the characteristics impedance calculation of the coupled lines as described in [29]. The dimensions of the coupled-lines are summarised in Fig. 3. The IDC make a shunt capacitor, and the coupled lines generate series gap capacitance with respect to the TL, which is acting as an inductor. Therefore, it has series and parallel LC circuit that makes a metamaterial TL.

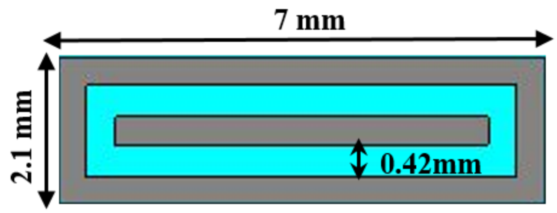

Fig. 3. Geometry of an open-circuit coupled-line used in the proposed BLC design with its dimensions

III. BLC FABRICATION AND CHARACTERISATION

The proposed and designed BLC is then fabricated using the FR4 substrate. Figure 4 (a) shows the fabricated BLC PCB and its dimensions, which are 27mm x 23mm, respectively and highlight the compact size of the BLC. The SMA connectors are then used with the fabricated BLC prototype for measurements. The fabricated BLC with detailed port information and dimensions are shown in Fig. 4 (b). It is important to note in Fig. 4 (b) that the central conductor of the SMA connector is only soldered to the transmission line for the measurement purposes. The S-parameter measurements of the fabricated BLC are then performed using Keysight (Agilent Technologies) FieldFox N9925A vector network analyzer (VNA).

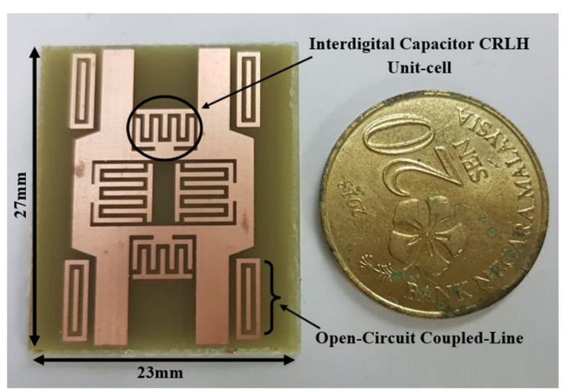

(a)

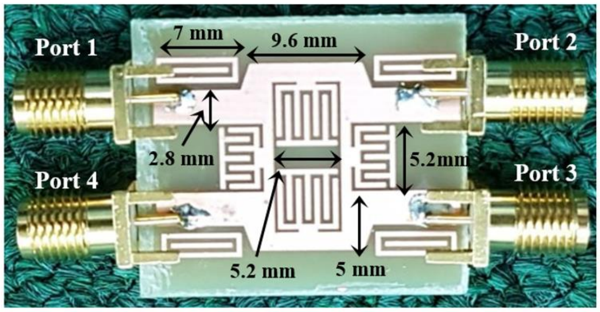

(b)

Fig. 4. FR4 substrate based fabricated prototype of the proposed BLC: (a) without connectors and (b) corresponding BLC ports and PCB dimensions are shown with SMA connectors

IV. RESULTS AND DISCUSSION

This section discusses the simulated and measured results of the BLC. Figure 5 (b) and Fig. 6, illustrate the performance of the proposed 5G BLC in terms of S-parameters and phase differences between the output ports, respectively. The simulation results in Fig. 5 (b), show that the proposed BLC is operating between 2.87GHz to 4.17GHz frequency band with a coupling factor of -3dB, respectively. The proposed simulated BLC return-loss (S_{11}) and isolation loss (S_{14}) characteristics were achieved better than 10dB and the bandwidth of 37.2% at 3.5GHz as compared to the conventional BLC result shown in Fig. 5 (a). Meanwhile, the proposed BLC design consideration in terms of insertion loss (S_{12}) and the coupling loss (S_{13}) should be -3dB to achieve equal power splitting across the port-2 and port-3. The simulated S_{12} and S_{13} results, as shown in Fig. 5 (b) are -3.04dB and -3.17 dB, respectively, also lying in the same frequency range. The insertion and coupling loss error (LE) is 0.04dB and 0.17dB, respectively, for the desired value of -3dB.

The phase difference between port-3 and port-2 should be 90° as per the design consideration of the proposed BLC. The comparison of simulated and measured results are shown in Fig. 6. It can be observed from Fig. 6 that when port-1 is excited, the simulated phase difference between port-3 and port-2 are 169.37° (S_{13}) and 78.47° (S_{12}), respectively, at 3.5GHz frequency band. In the simulation results, the phase difference between port-3 and port-2 is 90.9° as per the Eq. (16). So, the phase error is 0.9° with respect to the desired value of 90°:

$$\angle S_{13} - \angle S_{12} = \varphi. \tag{16}$$

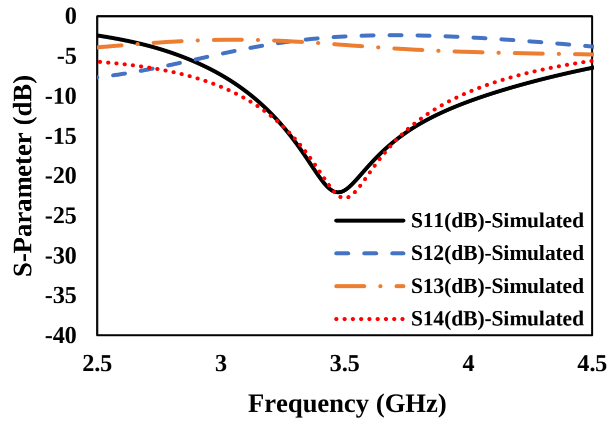

(a)

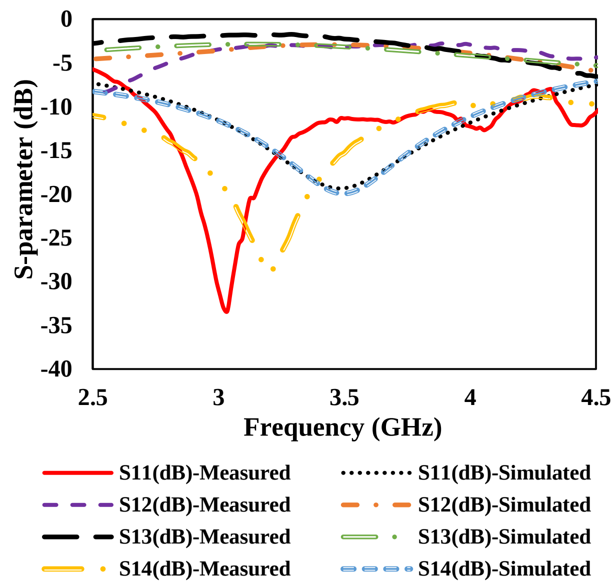

(b)

Fig. 5. S-Parameter response of: (a) conventional BLC (simulated response), and (b) proposed designed and fabricate BLC (both simulated and measured response).

The designed BLC has an overall area of 21.8mm x 26.65mm = 580.97 mm^2. Since, the conventional BLC area is 30mm x 41.7mm = 1251 mm^2 at 3.5 GHz, without degradation in performance, the proposed BLC only occupies 46% of the conventional design area. Figure 5 (a) shows the conventional BLC S-Parameter response. Compared to the conventional BLC [18], the proposed design is highly competitive, as shown in Table 2.

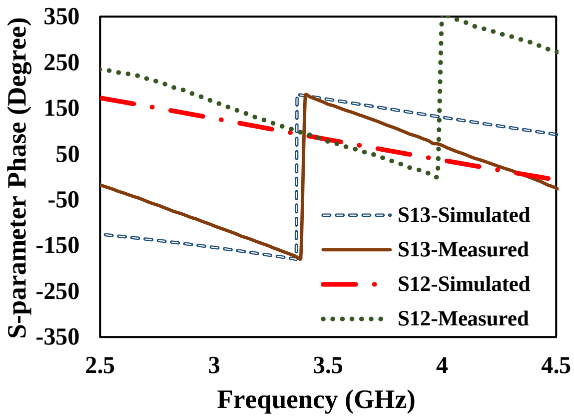

Fig. 6. Simulated and measured phase difference between port-2 and port-3.

Table 2: Results comparison of simulated conventional BLC design with proposed simulated and measured BLC Response at 3.5GHz

Parameter	Conventional BLC (Simulated)	Proposed BLC Design (Simulated)	Proposed BLC Design (Measured)
S_{11}	-24dB	-19dB	-12dB
S_{12}	-2.5dB	-3.04dB	-3.19dB
S_{13}	-3.6dB	-3.17dB	-2.8dB
S_{14}	-17dB	-19dB	-15.2dB
Phase Difference	89°	90.9°	88°
Bandwidth **@ S_{11} below -10dB**	3.1 GHz to 4.06 GHz	2.87 GHz to 4.17 GHz	2.74 GHz to 4.15 GHz
Size	30mm x 41.7mm	21.8mm x 26.65mm	23mm x 27mm
Percentage Reduction	54%		

A comparison between the simulated and measured results is shown in Fig. 5 (b) for the S_{11}, S_{12}, S_{13} and S_{14} magnitudes, and in Fig. 6 for the S_{12} and S_{13} phases, respectively. The proposed BLC shows good agreement between the simulated and measured results. The measured S_{11} is better than -10dB between 2.74 - 4.15 GHz frequency band, with a 40.2% relative bandwidth. The isolation loss (S_{14}) is also better than -10dB between 2.5 GHz to 4.1 GHz frequency band. Meanwhile, the performance of the insertion loss (S_{12}) and the coupling (S_{13}) are at -3.2dB and -2.8dB respectively, also lying in the same frequency range. So that the insertion and coupling LE is ±0.2dB with respect to the desired value. As depicted in Fig. 6, the measured phase of port-3 and port-2 at 3.5GHz is 166.4° (S_{13}) and 78.4° (S_{12}) respectively, when port-1 is excited. The BLC has a measured phase difference of 88° between Port-2 and Port-3 as per the Eq. (14). So, the phase error is 2° with respect to the desired value.

In the comparison between the simulated and measured results shown in Fig. 5 (b) and Fig. 6, there is a small shift in the centre frequency, but the range of frequency lies in the same frequency band between 2.74GHz to 4.15GHz, respectively. The dielectric loss tangent (tan δ) of the simulated FR-4 substrate is around 0.025, whereas for the fabricated FR-4 substrate based prototype is around 0.019. Because of this variation in the lossy FR4 substrate properties [30], there is a shift in the centre frequency, coupling and insertion LE of 0.2dB with respect to the standard value of 3dB, and the phase difference error (PDE) of 2^0. The dielectric constant of the FR-4 is also frequency-dependent and varies with the frequency. In the future, this frequency shift problem, LE, and the PDE can be improved by using a low-loss substrate.

A comparison of the proposed BLC with the previously published work related to BLC is summarized in Table 3. The researchers are attempting to either enhance the bandwidth or to minimize the size of the BLC in most of the design described in Table 3. The proposed work shows the bandwidth enhancement and minimize the size of the BLC together, which is considered as the main requirement for the design of 5G system. Moreover, the LE and PDE are also very small as compared to the previous designs.

Table. 3: Comparison of Proposed BLC design with the existing designs available in the literature

Operating Freq. (GHz)	Bandwidth (S_{11} = -10dB)	Size Reduction	Loss Error (dB)	PD Error (Deg)	Ref. / Year
3.22	5%	54.7%	± 1dB	-3°	[36] / 2013
3.5	6.57%	67 %	± 1.7dB	-4°	[33] / 2015
3.5	34%	63%	± 0.9dB	±5°	[34] / 2015
3.5	14.6%	61.76%	± 0.9dB	≈1°	[31] / 2016
3.5	≈17%	≈75%	± 0.5dB	-1.7°	[37] / 2016
3	13.3%	55%	± 0.3dB	1°	[32] / 2018
3.8	15.7%	40%	± 0.5dB	-2.5°	[35] / 2019
3.5	40.2%	54%	± 0.2dB	-2 °	[This work] / 2020

From Table 3, it is important to note that LE refers to the difference between the insertion loss/coupling loss with the desired value of -3dB. Also, the PDE refers to the phase difference between port-3 and port-2 of the BLC with the desired value of 90°.

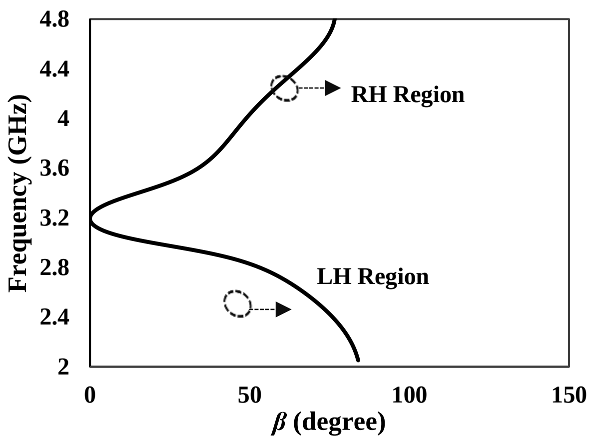

Fig. 7. Dispersion diagram of the proposed BLC.

Figure 7 shows the dispersion diagram of the proposed BLC. The dispersion diagram is plotted for the frequency and absolute value of β. The value of β is calculated using the S-parameter value, and it clearly shows that high frequency supports the forward wave and low-frequency support backward wave. Hence, the proposed BLC is designed to work in the right-hand (RH) region from above 3.2 GHz and left-hand (LH) region from below 3.2GHz. This indicates that the proposed BLC is a CRLH metamaterial TL [19],[38]. The main requirement for 5G technology is wide bandwidth and compact size of the components [39]. The CRLH-TL exhibit a bandpass behavior between the RH and LH regions, which shows improved bandwidth, as shown in Fig. 7 and the compact size of the proposed BLC.

V. CONCLUSION

A new BLC was proposed in this paper based on the interdigital capacitor unit-cell and open coupled lines technique that shows metamaterial TL properties. The simulated and measured results of the proposed BLC showed that the coupler has excellent S-parameter and phase difference performances at the desired operating frequency of 3.5GHz. The BLC is operating at the frequency band of 2.74 GHz - 4.15 GHz. The proposed BLC design is then fabricated, and it demonstrates a high fractional bandwidth of up to 40.2%. This article explained the compact and wide-band BLC has a good profile that is 54% less in size than conventional BLCs. The proposed BLC is potentially suitable to be used later in the butler-matrix based array antenna system for the 5G applications [40]. The structure can be integrated to form a compact and wideband butler-matrix for future array antenna beamforming systems.

ACKNOWLEDGMENT

The authors would like to thank the Ministry of Higher Education (MOHE), School of Postgraduate Studies (SPS), Research Management Centre, Advanced RF and Microwave Research Group, School of Electrical Engineering, and Universiti Teknologi Malaysia (UTM), Johor Bahru, for the support of the research under Grant 09G19 and 06G15.

REFERENCES

[1] W. Hong, et al., "Multibeam antenna technologies for 5g wireless communications," *IEEE Transactions on Antennas and Propagation*, vol. 65, no. 12, pp. 6231-6249, Dec. 2017.

[2] Y. Cao, K. S. Chin, W. Che, W. Yang, and E. S. Li, "A compact 38 ghz multibeam antenna array with multifolded butler matrix for 5g applications," *IEEE Antennas and Wireless Propagation Letters*, vol. 16, pp. 2996-2999, 2017.

[3] J. Zhang, X. Ge, Q. Li, M. Guizani, and Y. Zhang, "5g millimeter-wave antenna array: design and challenges," *IEEE Wireless Communications*, vol. 24, no. 2, pp. 106-112, Apr. 2017.

[4] T. A. Denidni and T. E. Libar, "Wide band four-port butler matrix for switched multibeam antenna arrays," *14th IEEE Proceedings on Personal, Indoor and Mobile Radio Communications, PIMRC 2003*, vol. 3, pp. 2461-2464 ,2003.

[5] C. Chen, H. Wu, and W. Wu, "Design and implementation of a compact planar 4 × 4 microstrip butler matrix for wideband application," *Progress In Electromagnetics Research C*, vol. 24, pp. 13, 2011.

[6] "Microwaves101 | Quadrature Couplers." [Online]. Available: https://www.microwaves101.com/encyclopedias/quadrature-couplers

[7] N. A. M. Shukor, N. Seman, and D. N. A. Zaidel, "Wideband six-port reflectometer design formed by enhanced branch-line couplers," *IEEE Asia-Pacific Conference on Applied Electromagnetics (Apace)*, pp. 63-66, 2014.

[8] S. I. Orakwue, R. Ngah, T. A. Rahman, and H. M. R. Al-Khafaji, "A 4 × 4 butler matrix for 28 ghz switched multi-beam antenna," *Int. J. Eng. Technol.*, vol. 7, no. 2, pp. 7, 2015.

[9] S. N. A. M. Ghazali, N. Seman, M. Rahim, S. Abdul Rahim, and R. Che Yob, "Design of complex ratio measuring unit (crmu) for 2 to 6 GHz WiMAX applications," *Asia-Pacific Microwave Conference Proceedings*, pp. 1271-1273, 2012.

[10] S. Gomha, E.-S. El-Rabaie, A.-A. Shalaby, and A. Elkorany, "Design of new compact branch-line coupler using coupled line dual composite right/left-handed unit cells," *J. Optoelectron. Adv. Mater.*, vol. 9, pp. 836-841, June 2015.

[11] Y. L. Li, Q. S. Liu, S. Sun, and S. S. Gao, "A miniaturised butler matrix based on patch hybrid couplers with cross slots," *IEEE Antennas and Propagation Society International Symposium*

(APSURSI), pp. 2145-2146, 2013.

[12] L. Geng, G.-M. Wang, P. Peng, and Y.-W. Wang, "Design of miniaturized branch-line coupler based on novel composite right/left-handed transmission line structure," *IEEE International Conference on Computational Electromagnetics (ICCEM)*, pp. 1-3, 2019.

[13] S. Gomha, E.-S. M. El-Rabaie, and A. A. T. Shalaby, "Miniaturization of branch-line couplers using open stubs and stepped impedance unit cells with meandering transmission lines," *Circuits Syst.*, vol. 1, pp. 14, 2014.

[14] Study on Implications of 5G Deployment on Future BusinessModels." [Online]. Available: https://berec.europa.eu/eng/document_register/subject_matter/berec/reports/8008-study-on-implications-of-5g-deployment-on-future-business-models

[15] "Press Release: Final Report on Allocation of Spectrum Bands for Mobile Broadband Service in Malaysia." [Online]. Available: https://www.mcmc.gov.my/en/media/press-releases/final-report-on-allocation-of-spectrum-bands-for-m

[16] A. Lai, T. Itoh, and C. Caloz, "Composite right/left-handed transmission line metamaterials," *IEEE Microw. Mag*., vol. 5, pp. 34-50, Sep. 2004.

[17] "F4B material datasheet." [Online]. Available: http://oneseine.com/edownload/12.html

[18] D. M. Pozar, *Microwave Engineering*. 3rd ed., John Wiley and Sons, 2005.

[19] G. D. Alley, "Interdigital capacitors and their application to lumped-element microwave integrated circuits," *IEEE Trans. Microw. Theory Tech.*, vol. 18, no. 12, pp. 1028-1033, Dec. 1970.

[20] D. Lacombe and J. Cohen, "Octave-band microstrip dc blocks (short papers)," *IEEE Trans. Microw. Theory Tech.*, vol. 20, no. 8, pp. 555-556, Aug. 1972.

[21] J. L. Hobdell, "Optimization of interdigital capacitors," *IEEE Trans. Microw. Theory Tech.*, vol. 27, no. 9, pp. 788-791, Sep. 1979.

[22] R. Esfandiari, D. W. Maki, and M. Siracusa, "Design of interdigitated capacitors and their application to gallium arsenide monolithic filters," *IEEE Trans. Microw. Theory Tech*., vol. 31, no. 1, pp. 57-64, Jan. 1983.

[23] X. Y. She and Y. L. Chow, "Interdigital microstrip capacitor as a four-port network," *Antennas Propag. IEEE Proc. H - Microw.*, vol. 133, no. 3, pp. 191-197, June 1986.

[24] I. J. Bahl and P. Bhartia, *Microwave Solid State Circuit Design*, Wiley, New York, 1988.

[25] R. Siragusa, H. V. Nguyen, P. Lemaître-Auger, S. Tedjini, and C. Caloz, "Modeling and synthesis of the interdigital/stub composite right/left-handed artificial transmission line," *Int. J. RF Microw. Comput.-Aided Eng.*, vol. 19, no. 5, pp. 549-560, Sep. 2009.

[26] C. Caloz and T. Itoh, *Electromagnetic Metamaterials: Transmission line Theory and Microwave Applications*, Wiley and IEEE Press, Hoboken, NJ, 2005.

[27] W. Arriola and I. S. Kim. "Wideband branch line coupler with arbitrary coupling ratio," *Asia-Pacific Microwave Conference*, Melbourne, VIC, USA, Dec. 2011.

[28] M. W. Sabri, N. A. Murad, and M. K. A. Rahim, "Wideband branch line coupler with open circuit coupled lines," *Int. J. Electr. Comput. Eng. IJECE*, vol. 7, no. 2, pp. 888-893, Apr. 2017.

[29] W. A. Arriola, J. Y. Lee, and I. S. Kim. "Wideband 3 db branch line coupler based on λ/4 open circuited coupled lines," *IEEE Microw. & Wireless Comp. Lett.*, vol. 21, no. 9, pp. 486-488, 2011.

[30] D. C. Nascimento and J. C. Da S. Lacava, "Design of low-cost probe-fed microstrip antennas," *Microstrip Antennas*, Apr. 2011.

[31] S. Azzeddine, et al., "A novel design of miniature coupler for wimax applications," *Int. J. Microw. and Opti. Tech.*, vol. 11, pp. 80-85, 2016.

[32] Z. Cai, et al., "Miniaturized branch-line coupler using delta stubs," *2018 Cross Strait Quad-Regional Radio Science and Wireless Technology Conference (CSQRWC)*, Xuzhou, China, July 2018.

[33] Y. Cao, J. Wen, H. Hong, and J. Liu, "Design of planar dual-band branch-line coupler with π-shaped coupled lines" *Progress In Electro-magnetics Research*, vol. 55, pp. 113-120, 2015.

[34] N. M. Jizat, N. M. Isa, J. S. Francisca, and S. K. A. Rahim, "3-dB branch-line coupler using coupled line radial stub with no restriction on coupling power," *2015 IEEE 12th Malaysia International Conference on Communications (MICC)*, Kuching, Malaysia, Nov. 2015.

[35] M. H. Seko and F. S. Correra, "Dual-band branch-line coupler with shorted stepped-impedance stubs arranged in a π-shaped topology," *Microw. and Opt. Tech. Lett*, vol. 61, no. 5, pp. 1154-1160, May 2019.

[36] X.-K. Zhang, et al., "Design of miniaturized branch-line coupler based on novel center-symmetrical spiral-interdigital resonators," *IEEE 2013 Cross Strait Quad-Regional Radio Science and Wireless Tech. Conference*, Chengdu, China, July 2013.

[37] H. Zhang, W. Kang, and W. Wu, "A novel compact dual-band branch-line coupler with cross-shaped stubs," *IEEE International Conference on Ubiquitous Wireless Broadband (ICUWB), Nanjing, China*, Oct. 2016.

[38] A. Rennings, T. Liebig, S. Otto, C. Caloz, and I. Wolff, "Highly directive resonator antennas based on composite right/left-handed (crlh) transmission

lines," *2nd International ITG Conference on Antennas*, pp. 190-194, 2007.

[39] H. Yu, H. Lee, and H. Jeon, "What is 5g? emerging 5g mobile services and network requirements," *Sustainability*, vol. 9, no. 10, pp. 1848, 2017.

[40] S. Trinh-Van, J. M. Lee, Y. Yang, K. Lee, and K. C. Hwang, "A sidelobe-reduced, four-beam array antenna fed by a modified 4× 4 butler matrix for 5g applications," *IEEE Trans. on Antennas and Prop.*, vol. 67, no. 7, pp. 4528-4536, July 2019.

Arshad Karimbu Vallappil received the B.Tech degree in Electronics & Communication Engineering from the University of Calicut, Kerala, India, in 2009 and M.Tech degree in Electronics Engineering from Pondicherry University, Puducherry, India in 2013. Currently, he is pursuing Ph.D. in Electrical Engineering from University Teknologi Malaysia, Malaysia.

Mohamad Kamal A. Rahim received the B.Eng. degree in Electrical and Electronic Engineering from the University of Strathclyde, U.K., in 1987, M.Sc. degree in Engineering from the University of New South Wales, Australia, in 1992, and the Ph.D. degree in the field of Wideband Active Antenna from the University of Birmingham, U.K., in 2003. From 1992 to 1999, he was a Lecturer with the Faculty of Electrical Engineering, Universiti Teknologi Malaysia (UTM), where he was a Senior Lecturer with the Department of Communication Engineering from 2005 to 2007. He is currently a Professor with UTM, Malaysia.

Bilal A. Khawaja received the B.S. degree in Computer Engineering from Sir Syed University of Engineering and Technology, Karachi, Pakistan, in 2002, the M.Sc. degree in Communication Engineering and Signal Processing from the University of Plymouth, Plymouth, U.K., in 2005, and the Ph.D. degree in Electrical Engineering from the University of Bristol, Bristol, U.K. in 2010. From 2010 to 2016, he was working as an Assistant Professor in Department of Electronics and Power Engineering, PN-Engineering College, National University of Science and Technology (NUST), Karachi, Pakistan. Currently, he is an Associate Professor with the Department of Electrical Engineering, Faculty of Engineering, Islamic University of Madina, Madina, Saudi Arabia. His current research interests include Antennas and Antenna Array design and characterization for the Wi-Fi, IoT, UAVs / FANETs and 5G Systems.

Murtala Aminu-baba obtained his first degree in 2010 from Abubakar Tafawa University Bauchi, Nigeria in Electrical/Electronic Engineering. He further received his MSc. degree in IT from the University of Wolverhampton, U.K, in 2013. He is currently pursuing his Ph.D. in the field of metamaterial antenna design for MIMO applications.

Ultra-Low Loss and Flat Dispersion Circular Porous Core Photonic Crystal Fiber for Terahertz Waveguiding

Aboulwafa M. Singer [1,2], Ahmed M. Heikal [1,3], Hamdi A. El-Mikati [1], Salah S. A. Obayya [3*], and Mohamed Farhat O. Hameed [1,2,3*]

[1] Faculty of Engineering
Mansoura University, Mansoura 35516, Egypt

[2] Nanotechnology and Nanoelectronics Engineering Program
Zewail City of Science and Technology, October Gardens, 6th of October City, Giza 12578, Egypt
mfarahat@zewailcity.edu.eg

[3] Centre for Photonics and Smart Materials
Zewail City of Science and Technology, October Gardens, 6th of October City, Giza 12578, Egypt
sobayya@zewailcity.edu.eg

Abstract **─** A novel design of circular porous core photonic crystal fiber (CCPCF) is proposed and studied for Terahertz propagation with an ultra-low-loss. The effective index, effective mode area, dispersion, material and bending losses of the suggested design are studied using full vectorial finite element method. The CCPCF with high cladding air filling factor and porous core exhibits ultra-low material absorption loss of 0.022 cm^{-1} at a frequency of 1.0 THz. Further, very low bending losses of 2.2×10^{-18} cm^{-1} can be achieved for 1.0 *cm* bending radius at 1.0 THz with low confinement loss of 1.37×10^{-5} cm^{-1}. Additionally, an ultra-flat low dispersion of 0.61 $\pm$ 0.035 ps/THz/*cm* can be obtained within the frequency range of 0.8-1.0 THz. Therefore, the reported CCPCF has a strong potential for transmission in the Terahertz regime.

Index Terms **─** Bending losses, dispersion, photonic crystal fiber, porous core, terahertz waveguiding.

I. INTRODUCTION

Recently, THz photonic crystal fibers (PCFs) have granted a great interest in the scientific community because of their promising applications in telecommunication, medical science, spectroscopy, security, imaging, and sensing [1]–[7]. Currently, the THz waveguide is still under extensive research due to the material absorption losses. Additionally, there are some problems associated with transmitter-receiver alignment and atmosphere-dependent losses [8]. Therefore, long-distance communication in the THz regime is a big challenge. The PCF is suggested to overcome such high absorption losses. However, the solid core of PCF still absorbs an intolerable amount of the transmitted signal energy. The porous core with air holes is then introduced to PCF to reduce the effective material loss (EML) [9]–[11]. In this context, Bao *et al.* [12] have proposed a honeycomb terahertz fiber with an absorption loss of 1.5 cm^{-1} at 1.0 THz. Additionally, a hexagonal porous core PCF with an absorption loss of 0.17 cm^{-1} has been presented with Teflon as a background material [13]. Further, a porous core photonic bandgap fiber was proposed with EML of 0.432 cm^{-1} and dispersion loss of 2.5 ps/THz/*cm* [14]. Kaijage *et al.* [15] have also suggested an octagonal PCF for terahertz wave guidance with an EML of 0.070 cm^{-1} at f= 1.0 THz. In 2015, Islam *et al.* [16] have proposed a rotated hexagonal porous core single-mode fiber with an EML of 0.066 cm^{-1} and a core power fraction of 40%. Additionally, a circular cladding with a circular porous core was introduced [17] with an absorption loss of 0.053 cm^{-1}. A kagome lattice and hexagonal core were also reported [18] with EML of 0.034 cm^{-1}, low confinement loss at 1.0 THz frequency, and near-zero flattened dispersion of 0.60 $\pm$ 0.14 ps/THz/*cm* within the frequency range of 0.75-1.15 THz. However, the fabrication of kagome-structured fiber is more challenging than regular fiber with circular-shaped air holes. Islam *et al.*[19] have also presented a circular cladding with hexagonal porous core with an absorption loss of 0.053 cm^{-1}. Furthermore, hexagonal cladding PCF with a circular porous core was proposed with an absorption loss of 0.057 cm^{-1} [20]. Using the same structure, Islam *et al*. [1] have reduced the absorption loss to 0.043 cm^{-1}. An ultra-low loss hybrid porous core fiber was introduced for broadband applications [21] with small EML of 0.043 cm^{-1} and near-zero flattened dispersion properties.

In this paper, a novel design of PCF is reported for

Submitted On: December 24, 2019
Accepted On: April 26, 2020

Terahertz waveguiding with circular lattice and circular porous core. The geometrical parameters are studied to minimize the material, confinement and bending losses with a nearly zero and flat dispersion over the studied frequency range. The simulation results are obtained using the full vectorial finite element method (FVFEM) via the Comsol Multiphysics software package [22]. The suggested design has a very low absorption loss of 0.022 cm^{-1} at f= 1.0 THz with low confinement loss of 1.37×10^{-5} cm^{-1}. Further, the proposed PCF exhibits low bending loss and small flat dispersion of 0.61 ± 0.035 ps/THz/*cm* within the frequency range 0.8-1.0 THz. The achieved EML and bending loss are smaller than those introduced in the literature [1], [15]–[17], [19], [20], [23]–[29]. Further, the guiding properties of the proposed PCF are better than the previously reported circular PCF with EML of 0.053 cm^{-1}, confinement loss of 1×10^{-2} cm^{-1}, and dispersion of 1.23 ± 0.09 ps/THz/*cm* [17].

The suggested PCF with low EML, confinement losses and bending losses can be used for telecommunication applications, medical spectroscopy and sensing purposes in the promising terahertz band. Additionally, the flat dispersion through the frequency range of 0.8-1.0 THz will offer an undegraded signal at the receiver terminal. This will in turn influence the speed and bandwidth of the transmitted signal.

II. DESIGN CONSIDERATIONS

The proposed CCPCF with the porous core is shown in Fig. 1. The cladding region consists of 8 successive rings of air holes. The first ring contains 10 holes with a diameter (d) of 90 μm. The total number of cladding air holes is 226. The spacing between two successive rings is called hole pitch (Λ) which depends directly on the cladding air filling factor (AFF). The AFF is the ratio between the hole diameter (d) and the hole pitch (Λ) which is kept constant at 0.96 to provide low effective material loss (EML). The second cladding ring holes' center is located at a distance of (d_{sc}) which depends on the hole pitch (Λ) and the core diameter (D_{core}). Therefore, (d_{sc}) could be changed automatically during the simulation with the core diameter and the hole pitch as well. In this study, $d_{sc}=(D_{core}/2)(1+\rho)+\Lambda$ where (ρ) is a constant factor. Therefore, we could obtain an explicit quasi TE mode and quasi TM mode as well [30]. The core has a diameter D_{core} of 460 μm and a total number of 37 holes whose diameter (d_{co}) depends directly on the porosity (P) of the core region. The porosity is the ratio between the total area of the air holes in the core region to the total core area [31]. In this study, 3 successive rings are used with 6, 12, and 18 air holes with hole pitch (Λ_{core}) of 66 μm. Additionally, a diameter d_{co}=75.6P μm is used for the reported design. The background material is TOPAS with refractive index n = 1.53 and bulk material absorption loss α_{mat} = 0.2 cm^{-1} at a frequency of 1.0 THz [15]. In this study, the effective index, EML, confinement losses, effective modal area, bending losses, fractional power, and dispersion of the quasi TE mode of the reported design are studied.

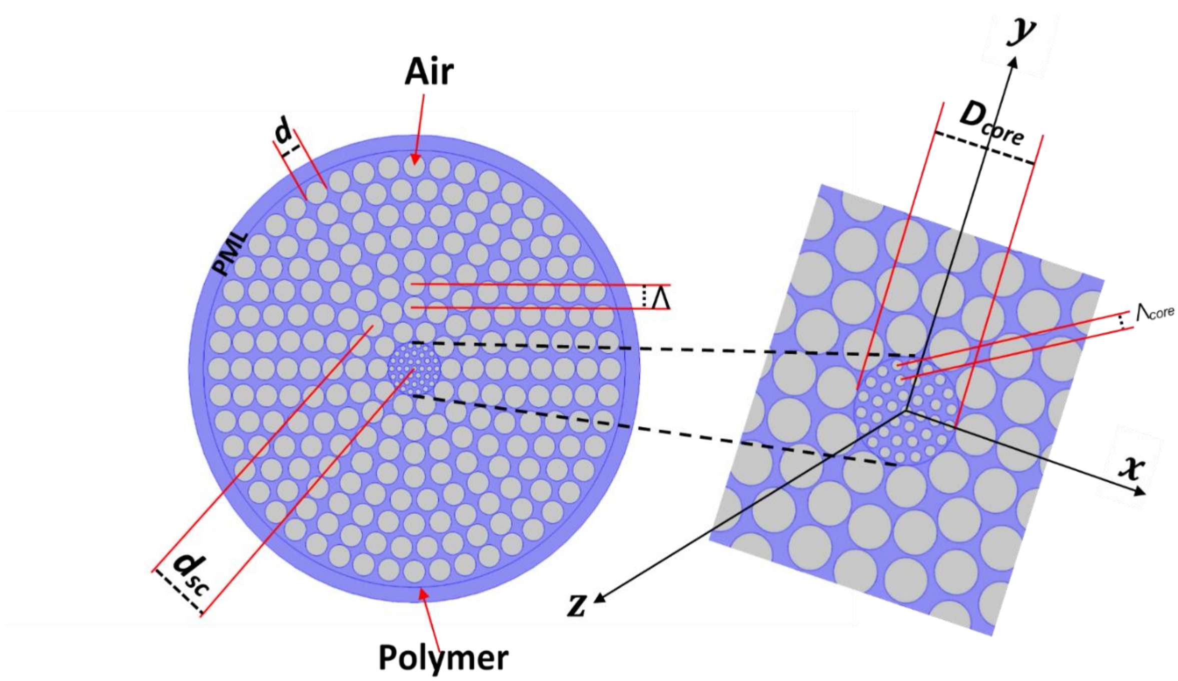

Fig. 1. Cross-section of the CCPCF with TOPAS as a background material.

III. NUMERICAL TECHNIQUE

The modal analysis of the suggested CCPCF is made by the full vectorial finite-element method (FVFEM) [32], [33] via the Comsol Multiphysics 5.2 commercial software package [22]. Starting from Maxwell's equations, the magnetic field-based vector wave equation can be obtained as:

$$\nabla \times (\varepsilon^{-1} \nabla\times\mathbf{H}) - \omega^2\mu_0\mathbf{H} = \mathbf{0}. \qquad (1)$$

where ω is the angular frequency, and μ_0 is the free space permeability. Further, $\varepsilon = \varepsilon_0\, \varepsilon_r$ is the permittivity of the waveguide material where ε_0 is the free space permittivity and ε_r is the relative permittivity of the waveguide material. The following eigenvalue equation can be obtained by applying the standard finite element method (FEM) procedure to equation (1):

$$[\mathbf{K}]\{\mathbf{H}\} - \beta^2[\mathbf{M}]\{\mathbf{H}\} = \{\mathbf{0}\}. \qquad (2)$$

where **[K]** and **[M]** are the global stiffness and mass matrices, [H] is the global magnetic field vector, **{0}** is the null vector and β is the propagation constant. The eigenvalue equation can be solved to obtain the eigenvector **H** and the corresponding eigenvalue β. Additionally, the effective index of the propagation mode is calculated from β since $N_{eff} = \beta/k$, where k is the free space wavenumber.

Through the modal analysis, a set of modes is calculated by the FVFEM and the dominant mode is defined as the mode with the highest real effective index value. Since $\nabla.\mathbf{H} = \mathbf{0}$ and interface boundary conditions are automatically satisfied in the formulation, then there is no chance for spurious (nonphysical) modes to appear in the spectrum of the solution. The cross-section of the waveguide structure is discretized using the VFEM. In this study, a minimum mesh element size of 1.19 μm is taken with a total number of degrees of freedom of 640381, with 65748 total number of elements. Additionally, A circular-shaped perfectly-matched layer is employed to calculate the leakage loss of the studied modes. An Intel Core i5 computer processor at 2.5 GHz with 8.0 GB RAM and 64-bit operating system was utilized to run the software with an average runtime of 89 seconds per run.

IV. RESULTS AND DISCUSSION

In order to calculate the confinement losses accurately, the PML thickness is studied. Figure 2 shows the confinement losses variation with the PML radius-to-cladding radius ratio. It may be seen from this figure that the confinement losses of the quasi TE and TM modes are nearly constant at 1.37×10^{-5} cm^{-1} and 3.65×10^{-6} cm^{-1} at a ratio of 1.03 and f = 1.0 THz. Therefore, the PML radius is kept at 1.07 of the cladding radius throughout the whole study.

Figure 3 shows the frequency-dependent effective index N_{eff} of the fundamental quasi TE and quasi TM modes of the CCPCF for three porosity cases 20%, 30%, and 40% in the Terahertz range of 0.8-1.3 THz. It may be seen that N_{eff} increases with increasing the frequency while it decreases with the porosity of the core region. As the frequency increases, the confinement of the light through the core region increases which increases the effective index of the supported modes. Further, the leakage of the mode toward the cladding region increases by increasing the porosity percentage as may be seen in the field plot in Fig. 3. Therefore, the maximum porosity of 40% has been used. If the porosity is further increased, the distance between the adjacent holes becomes small which will be a challenge for the fabrication process. Additionally, the mode will have high leakage to the cladding region which increases the confinement losses. As a result, the effective index of the quasi TE and TM modes decreases by increasing the porosity percentage as shown in Fig. 4. Further, the effective index of the quasi TE mode at a specific porosity percentage is very close to that of the quasi TM mode due to the symmetry of the proposed design.

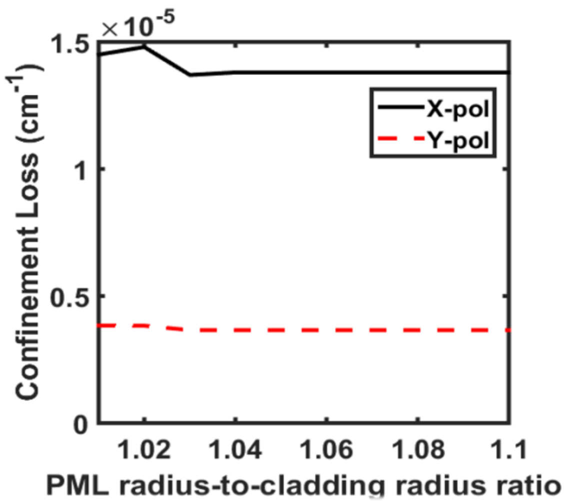

Fig. 2. Confinement loss of the quasi TE/TM mode versus the PML radius-to-cladding radius ratio.

The effective material loss (EML) α_{eff} could be considered as the main factor of the power dissipation in the THz band and can be calculated by the expression [34]:

$$\alpha_{eff} = \frac{\sqrt{\varepsilon_0/\mu_0}\ \int_{mat} n_{mat}|E|^2\alpha_{mat}dA}{|\int_{all} S_z\, dA|}. \qquad (3)$$

where n_{mat} is the material refractive index, α_{mat} is the bulk material absorption loss, ε_0 and μ_0 are the permittivity and permeability of the free space, respectively, and S_z is the z-component of the pointing vector defined as $S_z = ½(\mathbf{E} \times \mathbf{H}).\mathbf{z}$. The EML of the proposed fiber for different porosity values 20%, 30%, and 40% is shown in Fig. 5. It may be seen that the EML decreases by increasing the porosity percentage. The figure depicts that the EML values have a maximum of 0.031 cm^{-1} at a porosity of 20% at f = 1.3 THz and a minimum of 0.021 cm^{-1} at a porosity of 40% at f = 0.8

THz. At the operating frequency of 1.0 THz, the EML is equal to 0.022 cm^{-1} which is far better than those reported in Table 1. If a frequency of 0.8 THz is used, the EML will not exceed ≈ 0.021 cm^{-1}. Therefore, the proposed design is highly qualified for many Terahertz applications. The high density of the cladding air holes and the porosity of the core region are responsible for achieving low EML. This is due to the reduced amount of the bulk material in the whole design, especially through the core region.

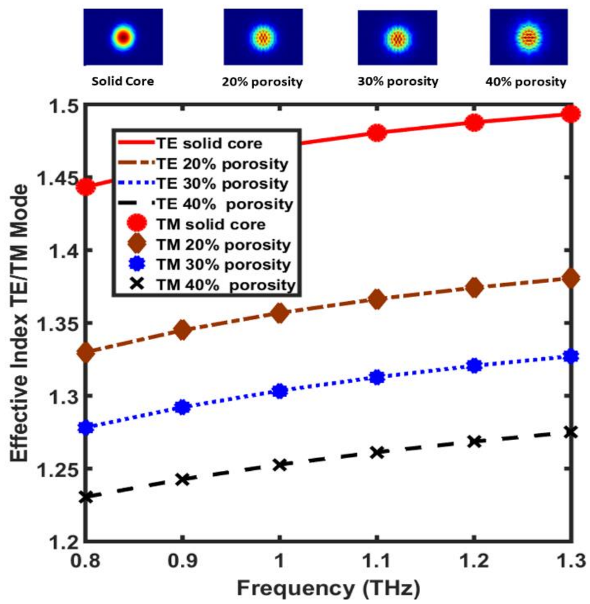

Fig. 3. The effective index of the fundamental quasi TE/TM mode versus the frequency at different porosity percentages. The inset shows the main electric field component of the quasi TM mode at different porosities.

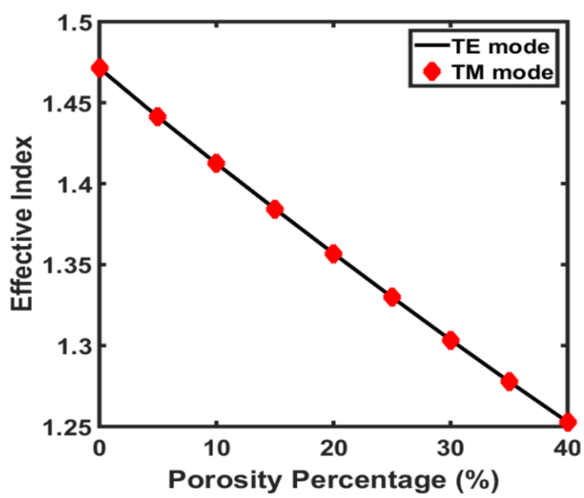

Fig. 4. The effective index of the fundamental quasi TE and quasi TM modes versus the porosity percentage (%).

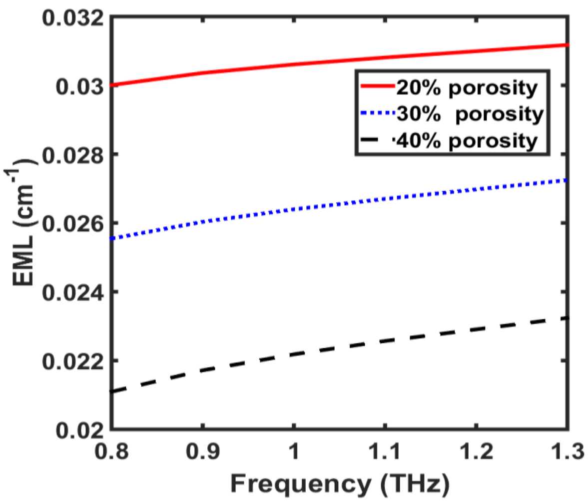

Fig. 5. EML versus the operating frequency at different porosity percentages.

The confinement loss of the supported modes is also implemented as given by [35]–[37]:

$$L_c = 8.686\, K_0\, Im\, (N_{eff}). \tag{4}$$

where K_0 is the propagation constant of free space and $Im(N_{eff})$ is the imaginary part of the effective index N_{eff} of the studied mode. Figure 6 shows the calculated confinement loss of the quasi TE mode supported by the proposed CCPCF versus the frequency at different porosity percentages. The mode field starts to leak out the core region by increasing the porosity percentage which increases the confinement losses. Additionally, as the frequency increases, the confinement of the mode through the core region increases. Further, the confinement losses are smaller than the material loss with a value of $1.37 \times 10^{-5}\ cm^{-1}$ at f= 1.0 THz and porosity of 40%. Therefore, the confinement losses can be neglected if compared to the material loss. It may be seen that the proposed structure enjoys a low confinement loss due to the high AFF value of the cladding. Therefore, a high index contrast is obtained between the cladding and the core regions with better field confinement in the core region.

The effective modal area (A_{eff}) of the quasi TE mode of the proposed CCPCF is also analyzed through the frequency band of 0.8-1.3 THz. The A_{eff} could show the mode confinement through the core region and is given by [1], [10],[37]:

$$A_{eff} = \frac{[\int I(r) r dr]^2}{\int I^2(r) r dr}. \tag{5}$$

where $I(r) = |E_t|^2$ is the transverse electric field intensity distribution in the fiber cross-section. Figure 7 shows the variation of the frequency-dependent effective mode area of the quasi TE mode. It is evident from this figure that the effective mode area is proportional to the porosity percentage and is inversely proportional to the operating frequency. This is due to the good confinement of the studied mode at high frequency and small porosity. The effective mode area at 1.0 THz and 40% porosity is equal to 1.22×10^5 μm^2, which is very comparable to most of the reported values in Table 1.

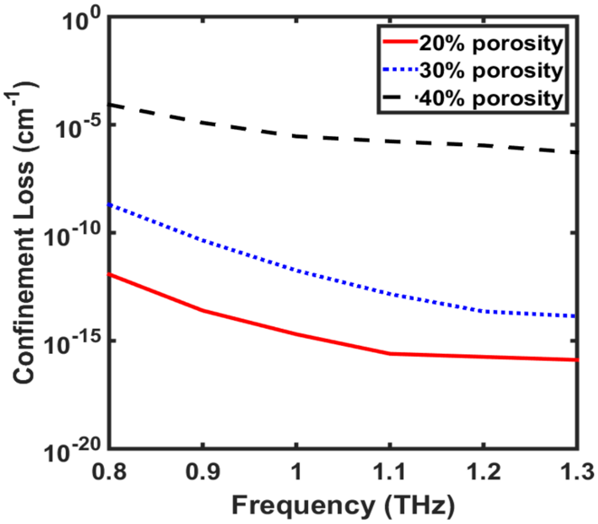

Fig. 6. Frequency-dependent confinement loss of the quasi TE mode at different porosity percentages.

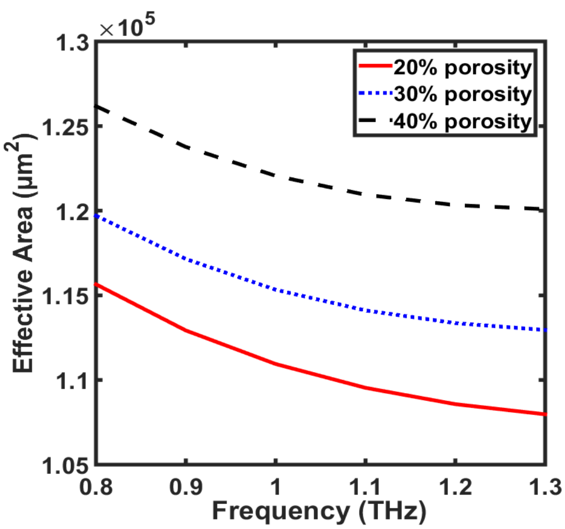

Fig. 7. Frequency-dependent effective mode area of the quasi TE mode at different porosity percentages.

The PCFs can also suffer from bending losses **(α_{BL})** which can lead to the distortion of the optical mode. The $\boldsymbol{\alpha_{BL}}$ can be expressed as [38]:

$$\alpha_{BL} \cong \left(\frac{\sqrt{\pi}}{8A_{\mathrm{eff}}}\right)\left(\frac{1}{\beta(\beta^2-\beta_{cl}^2)^{\frac{1}{4}}}\right)\left(\frac{exp\left(-\frac{2}{3}R_b(\beta^2-\beta_{cl}^2)^{\frac{3}{2}}\beta^{-2}\right)}{\sqrt{R_b(\beta^2-\beta_{cl}^2)\beta^{-2}+R_c}}\right). \quad (6)$$

where $\boldsymbol{\beta}$ is the propagation constant as $\boldsymbol{\beta = 2\pi N_{eff}/\lambda}$, $\boldsymbol{R_c}$ is the fiber core radius and $\boldsymbol{R_b}$ is the bending radius. In this study, it is assumed that the cladding refractive index is approximately unity due to the high filling factor of the cladding region. Further, $\boldsymbol{\beta_{cl}}$ is calculated for each frequency as $\boldsymbol{\beta_{cl} = 2\pi \times 1/\lambda}$. Figure 8 shows the frequency-dependent $\boldsymbol{\alpha_{BL}}$ at different porosity percentages. It may be seen that the bending losses increase with increasing the porosity while it decreases with increasing the frequency. This is due to the good confinement of the light through the core region at high frequency. Higher bending loss of $1.96\times10^{-13} cm^{-1}$ is achieved at f = 0.8 THz and porosity of 40%. However, a small value of $1.0\times10^{-37} cm^{-1}$ is obtained at a frequency of 1.3 THz and a porosity of 20%. The bending loss at f = 1.0 THz is equal to 2.2×10^{-18} cm^{-1} with a porosity of 40%.

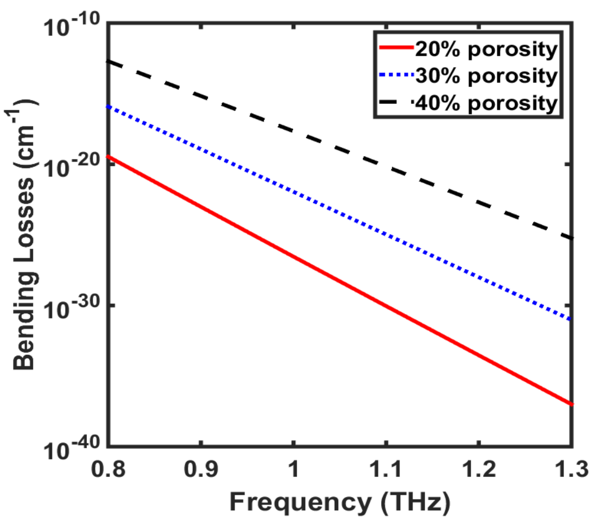

Fig. 8. Frequency-dependent bending loss of the quasi TE mode at different porosity percentages.

It is aimed to maximize the traveled power through the porous core region for efficient THz regime transmission. Therefore, we calculated the fractional propagated power through the proposed CCPCF using the expression [39], [40]:

$$\boldsymbol{\varphi = \frac{\int_{core} S_z\, dA}{\int_{all} S_z\, dA}}. \quad (7)$$

where the numerator represents the integration of the z-component of the pointing vector over the core holes only while the denominator shows the integration all over the whole design. Figure 9 shows the fractional power of the quasi TE mode through the proposed CCPCF versus the frequency at different porosity percentages. The figure shows that high fractional power of 41.7% is achieved at f =1.3 THz and porosity of 40%. Further, a fractional power of 41.16% is obtained at f=1.0 THz and porosity of 40%, which is a relatively high ratio. It should be also noted that the proposed CCPCF provides a nearly constant fractional power at low porosity value (20% and 30%) through the frequency range of 0.8-1.3 THz which increases accordingly with the porosity percentages.

Next, the dispersion characteristics of the proposed CCPCF are analyzed. It is worth noting that the refractive index of the TOPAS material is nearly constant in the frequency range of 0.1-1.5 THz where the material dispersion can be totally neglected [12]. Then, the waveguide dispersion is only analyzed. The dispersion coefficient ($\boldsymbol{\beta_2}$) can be calculated by [41]:

$$\boldsymbol{\beta_2} = \frac{1}{c}\left(2\frac{dN_{eff}}{d\omega} + \omega\frac{d^2N_{eff}}{d\omega^2}\right). \qquad (8)$$

where $\boldsymbol{\omega = 2\pi f}$ is the radial frequency.

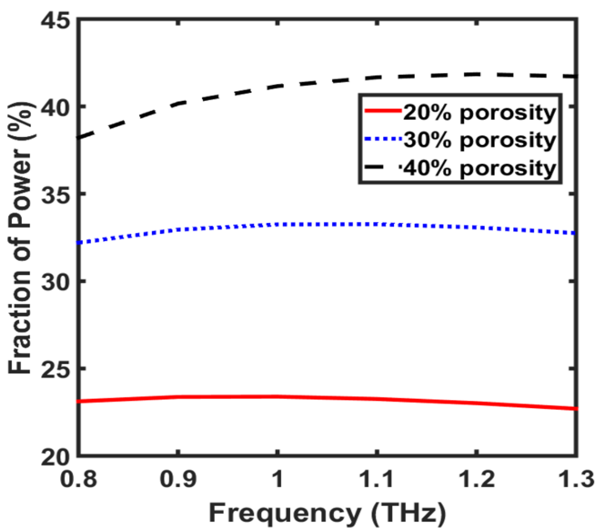

Fig. 9. The fraction of power percentage of the quasi TE mode through the core holes versus the frequency at different porosity percentages.

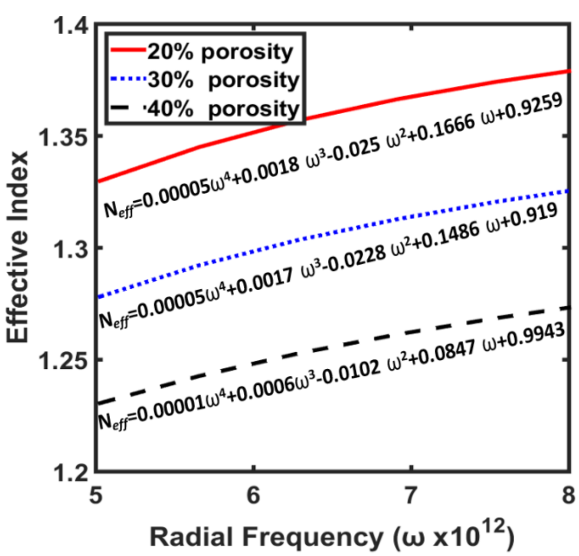

Fig. 10. The effective index N_{eff} of the quasi TE mode versus the radial frequency.

Figure 10 shows the relationship between $\boldsymbol{N_{eff}}$ and $\boldsymbol{\omega}$ for three different porosity percentages as derived using the least square method (LSM) with a polynomial of the fourth order. The three equations have been mathematically differentiated and applied to the formula in Eq. (8). Figure 11 shows the frequency-dependent dispersion of the quasi TE mode of the proposed CCPCF for the three porosity cases. The average dispersion in the range of 0.8-1.3 THz is 0.15±0.13 ps/THz/*cm* for 20% porosity, 0.12±0.05 ps/THz/*cm* for 30% porosity and 0.97 ± 0.39 ps/THz/*cm* for 40% porosity. It may be also seen from Fig. 11 that at 40% porosity, the maximum value of dispersion is 1.36 ps/THz/*cm* at 1.3 THz and the minimum value is 0.58 ps/THz/*cm* at 0.9 THz (both are very small). It should be also noted that the proposed CCPCF has a nearly zero flat dispersion in the frequency range of 0.8-1.0 THz with an average value of 0.61±0.035 ps/THz/*cm* at 40% porosity. Such a very small dispersion is obtained over a wide range of frequencies which is very comparable to those reported in Table. 1. The calculated dispersion is directly related to the effective index $\boldsymbol{N_{eff}}$ of the supported modes. Such modes are confined through the porous core and the innermost cladding air holes. Therefore, the $\boldsymbol{N_{eff}}$ and hence the dispersion can be controlled by the geometrical parameters of the PCF.

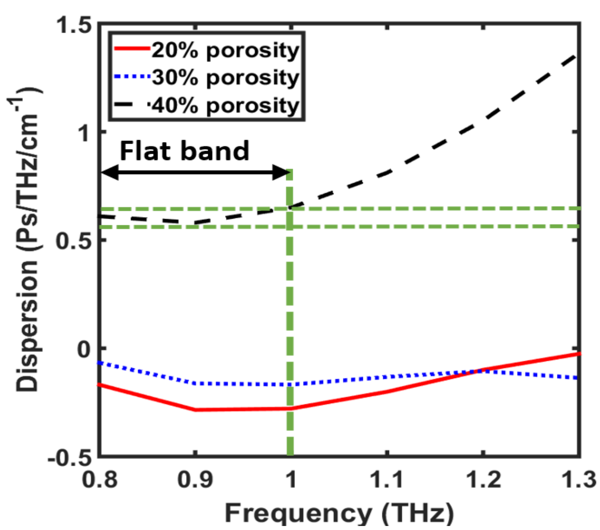

Fig. 11. The frequency dependent dispersion $\boldsymbol{\beta_2}$ at different porosity percentages.

The proposed design can be fabricated using the most common stack-and-draw method [42]. Our proposed CCPCF is assumed to be simple-to-stack as the whole structure enjoys a high degree of symmetry around the center of the core with relatively low core porosity percentages. Therefore, the stacking process will be easy and will provide a high degree of accuracy by the end of the drawing process.

A comparison between the proposed CCPCF and the previously-published PCF for THz guiding is shown in Table 1. It is revealed from this table that the proposed CCPCF has better comprehensive characteristics than those reported previously. The suggested design has EML of 0.022 cm^{-1} at f = 1.0 THz while the other PCFs have EML within the range from 0.034 to 0.070 cm^{-1}. Further, the confinement loss of the CCPCF of $1.37\times10^{-5} cm^{-1}$ which is very comparable to all of the mentioned papers including [23], [24], and [25]. It is also noticed that the obtained effective mode area has a value of 1.22×10^{5} μm^2 which is also very comparable to the previous results. The bending loss of the suggested design is only 0.2% of the minimum achieved result [20] as shown in Table 1. The fractional power is also comparable to the other values [27] with a nearly constant value over the studied frequency range of 0.8-1.3 THz at porosity percentages of 20% and 30%. Further, an ultra-flattened nearly zero dispersion of (0.61$\pm$ 0.035 Ps/THz/cm) is achieved over a frequency range from 0.8 to 1.0 THz which is very comparable to the minimum dispersion of (0.14$\pm$ 0.07Ps/THz/cm) reported in [23]. Therefore, the proposed design would be an efficient transmission structure for the THz regime. It may be noted that the suggested design has overall better guiding characteristics at the same time than those reported in the literature as shown in Table 1. However, short manufacture length and high price are the main disadvantages of using PCF as transmission media for telecommunications in THz regime. Additionally, the coupling of PCF with with other waveguides and devices is not straight forward.

V. CONCLUSION

In this paper, we proposed a CCPCF for the THz regime with an ultra-low EML of 0.022 cm^{-1}, low confinement losses of1.37×10^{-5} cm^{-1} and low bending losses of 2.2×10^{-18} cm^{-1} at 1.0 THz. Further, a wide-band flat low dispersion of 0.61 $\pm$ 0.035 ps/THz/cm is achieved within the frequency range of 0.8-1.0 THz. The structure has almost a constant fractional power for each porosity percentage through the frequency range of 0.8-1.3 THz with a comparable value of 41.16% at 1.0 THz. The reported CCPCF has a superior guiding mechanism than the previous circular PCF [17] with EML of 0.053 cm^{-1}, a confinement loss of 1×10^{-2} cm^{-1}, and dispersion of 1.23$\pm$0.09 ps/THz/cm. Therefore, the reported CCPCF has a strong potential for transmission in the Terahertz regime.

Table 1: A comparison between the CCPCF and the previously published papers

Structure	Year	EML (cm^{-1}) at f =1.0 THz	Confinement Losses (cm^{-1}) at f =1.0 THz	Effective Mode Area (μm^2) at f =1.0 THz	Bending Losses (cm^{-1}) at f =1.0 THz	Fraction of Power (%) at f =1.0 THz	Dispersion (Ps/THz/cm)	Flat Dispersion Bandwidth (THz)
CCPCF		0.022	1.37×10^{-5}	1.22×10^{5}	2.2×10^{-18}	41.16	0.61$\pm$0.035	0.8-1.0
[23]	2019	0.062	4.7×10^{-7}	-------------	-------------	-----------	0.14$\pm$0.07	0.6-0.85
[26]	2019	0.07	1.66×10^{-3}	9×10^{4}	2.61×10^{-14}	-----------	1.2$\pm$0.32	1.1-1.9
[27]	2019	0.04	1×10^{-4}	1.65×10^{5}	-------------	40	0.98$\pm$0.09	1.0-2.0
[24]	2018	0.065	3.8×10^{-9}	1.8×10^{5}	-------------	-----------	1.3$\pm$0.03	1.0-1.8
[25]	2018	0.05	1×10^{-9}	-------------	-------------	-----------	0.53$\pm$0.07	0.5-1.48
[1]	2017	0.043	$1\times10^{-2.5}$	2.1×10^{5}	------------	47	1.14$\pm$ 0.09	1.0-1.3
[20]	2017	0.057	6.9×10^{-3}	1.1×10^{5}	1.07×10^{-15}	42	1.3$\pm$0.55	0.7-1.2
[28]	2017	0.034	$1\times10^{-3.7}$	6×10^{5}	------------	44	0.94$\pm$0.09	0.7-1.3
[19]	2016	0.053	6.3×10^{-4}	-------------	-------------	47	1.2$\pm$0.25	1.0-1.55
[17]	2015	0.053	1×10^{-2}	-------------	-------------	46	1.23$\pm$0.09	0.9-1.3
[16]	2015	0.066	4.73×10^{-4}	-------------	$\approx 1.310^{-12}$	40	1.06$\pm$0.12	0.5-1.08
[15]	2013	0.070	1×10^{-1}	1.5×10^{5}	1.2×10^{-9}	-----------	---------------	-----------
[29]	2011	0.042	------------	1.04×10^{5}	-----------	50	≈3 with 0.0373 ps m^{-1} μm^{-1} SD	-----------

REFERENCES

[1] M. S. Islam, *et al.*, "Extremely low material loss and dispersion flattened TOPAS based circular porous fiber for long distance terahertz wave transmission," *Optical Fiber Technology*, vol. 34, pp. 6-11, 2017.

[2] Q. Chen, Z. Jiang, G. X. Xu, and X.-C. Zhang, "Near-field terahertz imaging with a dynamic aperture," *Optics Letters*, vol. 25, no. 15, pp. 1122-1124, 2000.

[3] H. Thenmozhi, M. M. Rajan, V. Devika, D. Vigneswaran, and N. Ayyanar, "D-glucose sensor using photonic crystal fiber," *Optik*, vol. 145, pp. 489-494, 2017.

[4] S. Chowdhury, S. Sen, K. Ahmed, and S. Asaduzzaman, "Design of highly sensible porous shaped photonic crystal fiber with strong confinement field for optical sensing," *Optik*, vol. 142, pp. 541-549, 2017.

[5] M. S. Islam, J. Sultana, A. Dinovitser, K. Ahmed,

B. W.-H. Ng, and D. Abbott, "Sensing of toxic chemicals using polarized photonic crystal fiber in the terahertz regime," *Optics Communications*, vol. 426, pp. 341-347, 2018.
[6] M. S. Islam, J. Sultana, A. A. Rifat, A. Dinovitser, B. W.-H. Ng, and D. Abbott, "Terahertz sensing in a hollow core photonic crystal fiber," *IEEE Sensors Journal*, vol. 18, no. 10, pp. 4073-4080, 2018.
[7] M. S. Islam, *et al.*, "A novel approach for spectroscopic chemical identification using photonic crystal fiber in the terahertz regime," *IEEE Sensors Journal*, vol. 18, no. 2, pp. 575-582, 2017.
[8] Z. Zhang, *et al.*, "Research on terahertz photonic crystal fiber characteristics with high birefringence," *Optik-International Journal for Light and Electron Optics*, vol. 125, no. 1, pp. 154-158, 2014.
[9] F. Poli, A. Cucinotta, and S. Selleri, *Photonic Crystal Fibers: Properties and Applications*. vol. 102. Springer Science & Business Media, 2007.
[10] Z. Frederic, R. Gilles, and N. Andre, *Foundations of Photonic Crystal Fibres*. World Scientific, 2005.
[11] M. Skorobogatiy and J. Yang, *Fundamentals of Photonic Crystal Guiding*. Cambridge University Press, 2009.
[12] H. Bao, K. Nielsen, H. K. Rasmussen, P. U. Jepsen, and O. Bang, "Fabrication and characterization of porous-core honeycomb bandgap THz fibers," *Optics Express*, vol. 20, no. 28, pp. 29507-29517, 2012.
[13] M. Uthman, B. M. A. Rahman, N. Kejalakshmy, A. Agrawal, and K. T. V. Grattan, "Design and characterization of low-loss porous-core photonic crystal fiber," *IEEE Photonics Journal*, vol. 4, no. 6, pp. 2315-2325, 2012.
[14] J. Liang, L. Ren, N. Chen, and C. Zhou, "Broadband, low-loss, dispersion flattened porous-core photonic bandgap fiber for terahertz (THz)-wave propagation," *Optics Commun-ications*, vol. 295, pp. 257-261, 2013.
[15] S. F. Kaijage, Z. Ouyang, and X. Jin, "Porous-core photonic crystal fiber for low loss terahertz wave guiding," *IEEE Photonics Technology Letters*, vol. 25, no. 15, pp. 1454-1457, Aug. 2013, doi: 10.1109/LPT.2013.2266412.
[16] R. Islam, G. K. M. Hasanuzzaman, M. S. Habib, S. Rana, and M. A. G. Khan, "Low-loss rotated porous core hexagonal single-mode fiber in THz regime," *Optical Fiber Technology*, vol. 24, pp. 38-43, 2015.
[17] R. Islam and S. Rana, "Dispersion flattened, low-loss porous fiber for single-mode terahertz wave guidance," *Optical Engineering*, vol. 54, no. 5, p. 055102, 2015.
[18] G. K. M. Hasanuzzaman, M. S. Habib, S. A. Razzak, M. A. Hossain, and Y. Namihira, "Low loss single-mode porous-core kagome photonic crystal fiber for THz wave guidance," *Journal of Lightwave Technology*, vol. 33, no. 19, pp. 4027-4031, 2015.
[19] M. S. Islam, S. Rana, M. R. Islam, M. Faisal, H. Rahman, and J. Sultana, "Porous core photonic crystal fibre for ultra-low material loss in THz regime," *IET Communications*, vol. 10, no. 16, pp. 2179-2183, 2016.
[20] M. A. Habib and M. S. Anower, "A novel low loss porous-core photonic crystal fiber for terahertz wave transmission," in *2017 Inter-national Conference on Electrical, Computer and Communication Engineering (ECCE)*, pp. 56-59, 2017.
[21] M. S. Islam, J. Sultana, J. Atai, D. Abbott, S. Rana, and M. R. Islam, "Ultra low-loss hybrid core porous fiber for broadband applications," *Applied Optics*, vol. 56, no. 4, pp. 1232-1237, 2017.
[22] COMSOL: Multiphysics Software for Optimizing Designs, *COMSOL Multiphysics®*. https://www.comsol.com/ (accessed Jan. 20, 2020).
[23] S. Mei, *et al.*, "Suspended graded-index porous core POF for ultra-flat near-zero dispersion terahertz transmission," *Optical Fiber Technology*, vol. 52, p. 101946, 2019.
[24] M. S. Islam, *et al.*, "A modified hexagonal photonic crystal fiber for terahertz applications," *Optical Materials*, vol. 79, pp. 336-339, 2018.
[25] J. Sultana, *et al.*, "Highly birefringent elliptical core photonic crystal fiber for terahertz application," *Optics Communications*, vol. 407, pp. 92-96, Jan. 2018, doi: 10.1016/j.optcom. 2017.09.020.
[26] M. A. Habib and M. S. Anower, "Design and numerical analysis of highly birefringent single mode fiber in THz regime," *Optical Fiber Technology*, vol. 47, pp. 197-203, 2019.
[27] J. Sultana, M. R. Islam, M. Faisal, K. M. A. Talha, and M. S. Islam, "Design and analysis of a Zeonex based diamond-shaped core kagome lattice photonic crystal fiber for T-ray wave transmission," *Optical Fiber Technology*, vol. 47, pp. 55-60, 2019.
[28] M. S. Islam, J. Sultana, J. Atai, M. R. Islam, and D. Abbott, "Design and characterization of a low-loss, dispersion-flattened photonic crystal fiber for terahertz wave propagation," *Optik*, vol. 145, pp. 398-406, 2017.
[29] J. J. Bai, J. N. Li, H. Zhang, H. Fang, and S. J. Chang, "A porous terahertz fiber with randomly distributed air holes," *Applied Physics B*, vol. 103, no. 2, pp. 381-386, 2011.
[30] S. Liang, *et al.*, "Influences of asymmetrical geometric structures on the birefringence of index-guiding photonic crystal fiber," *Optik*, vol. 180, pp. 973-983, 2019.
[31] M. H. Muhammad, M. F. O. Hameed, A. M.

Heikal, and S. S. Obayya, "Porous core photonic crystal fibre with metal-coated central hole for terahertz applications," *IET Optoelectronics*, vol. 9, no. 2, pp. 37-42, 2015.

[32] S. S. A. Obayya, B. M. A. Rahman, and H. A. El-Mikati, "New full-vectorial numerically efficient propagation algorithm based on the finite element method," *Journal of Lightwave Technology*, vol. 18, no. 3, p. 409, 2000.

[33] S. S. A. Obayya, B. M. A. Rahman, K. T. V. Grattan, and H. A. El-Mikati, "Full vectorial finite-element-based imaginary distance beam propagation solution of complex modes in optical waveguides," *J. Lightwave Technol., JLT*, vol. 20, no. 6, p. 1054, June 2002.

[34] A. W. Snyder and J. Love, *Optical Waveguide Theory*. Springer Science & Business Media, 2012.

[35] S. F. Kaijage, *et al.*, "Broadband dispersion compensating octagonal photonic crystal fiber for optical communication applications," *Jpn. J. Appl. Phys.*, vol. 48, no. 5R, p. 052401, May 2009, doi: 10.1143/JJAP.48.052401.

[36] Y. E. Monfared, A. R. Maleki Javan, and A. R. Monajati Kashani, "Confinement loss in hexagonal lattice photonic crystal fibers," *Optik*, vol. 124, no. 24, pp. 7049-7052, Dec. 2013, doi: 10.1016/j.ijleo. 2013.05.168.

[37] A. Medjouri, L. M. Simohamed, O. Ziane, and A. Boudrioua, "Analysis of a new circular photonic crystal fiber with large mode area," *Optik*, vol. 126, no. 24, pp. 5718-5724, Dec. 2015, doi: 10.1016/ j.ijleo.2015.09.035.

[38] M. D. Nielsen, N. A. Mortensen, M. Albertsen, J. R. Folkenberg, A. Bjarklev, and D. Bonacinni, "Predicting macrobending loss for large-mode area photonic crystal fibers," *Opt. Express, OE*, vol. 12, no. 8, pp. 1775-1779, Apr. 2004, doi: 10.1364/ OPEX.12.001775.

[39] N. Chen, J. Liang, and L. Ren, "High-birefringence, low-loss porous fiber for single-mode terahertz-wave guidance," *Applied Optics*, vol. 52, no. 21, pp. 5297-5302, 2013.

[40] Y. Hou, F. Fan, Z.-W. Jiang, X.-H. Wang, and S.-J. Chang, "Highly birefringent polymer terahertz fiber with honeycomb cladding," *Optik - International Journal for Light and Electron Optics*, vol. 124, no. 17, pp. 3095-3098, Sep. 2013, doi: 10.1016/j.ijleo.2012.09.040.

[41] X. Tang, *et al.*, "Elliptical hollow fiber with inner silver coating for linearly polarized terahertz transmission," *IEEE Photonics Technology Letters*, vol. 25, no. 4, pp. 331-334, 2013.

[42] D. M. Chow, S. R. Sandoghchi, and F. R. M. Adikan, "Fabrication of photonic crystal fibers," in *2012 IEEE 3rd International Conference on Photonics*, pp. 227-230, Oct. 2012, doi: 10.1109/ ICP.2012.6379830.

Fast Rise-Time Electromagnetic Pulse Protection Characteristics of ZnO Varistors

Wangwei Zhang [1], Yun Wang [2], and Junchao Shen [3]

[1] Academy of Software
Zhengzhou University of Light Industry, Zhengzhou, 450002, China
2018014@zzuli.edu.cn

[2] Department of science and technology of Henan Province
Zhengzhou, 450002, China
wangyunjunxie@163.com

[3] Henan University of Chinese Medicine, Zhengzhou, 450002, China
sjcwyyx2018@163.com

Abstract **─** In order to study the response of ZnO varistors under the radiation of fast rise-time electromagnetic pulse, an experiment system is built composed of square wave pulse source, coaxial cable, coaxial fixture, attenuator, oscilloscope and insulating gas vessel. Electromagnetic pulse protection characteristics of ZnO varistors are tested and analyzed. Results show that: appearance of negative pulse in the responsive waveform means the completion of field-induced insulator-conductor phase transition for ZnO varistors. Peak value of responsive positive pulse decreases after phase transition, and the residual voltage is generally constant for different pulse strength and widths. The phenomenon of overshoot voltage is observed. Negative pulse is caused by the reflection of electromagnetic wave after the phase transition. The resistance of ZnO after phase transition is less than 50 Ω and decreases linearly along with the increase of incident voltage or field, which leads to a highly nonlinear current-voltage characteristic of ZnO varistors in the radiating electromagnetic environment. Sum of energy of positive and negative pulse keeps constant, which indicates that the weakened positive pulse is converted into negative pulse. So impact of negative pulse needs to be taken into consideration when ZnO varistors are used to protection against strong electromagnetic pulse.

Index Terms **─** Coaxial fixture, fast rise-time electromagnetic pulse, grain boundary theory, insulator-conductor phase transition, nonlinear current-voltage characteristic, quantum tunnelling effect, ZnO varistor.

I. INTRODUCTION

Traditional materials of electromagnetic shielding, such as metal sheet or fiber [1], dope [2], fabric [3, 4], have constant electrical properties and shielding effectiveness. So they don't distinguish useful but weak signals from purposive strong electromagnetic disturbance, which are both shielded. Therefore they are failed to solve the contradiction between strong filed protection and normal operation of equipment. Alternatively, materials such as Zener diodes [5-7], junction field-effect transistors (FET) [8-10], heterogeneous composites filled with conductive particles [11, 12], ZnO-based [13, 14] or VO_2-based [15, 16] metal-oxides and so on, have changeable essential electromagnetic parameters and this change is adaptive and reversible. This type of materials will exhibit highly nonlinear current-voltage resistance switching characteristics or field-induced insulator-conductor phase transition, so they are expected to be used as repeatable transient suppression devices against the effect of strong electromagnetic pulse while some of them are already be used to absorb the voltage surges for circuit protection like metal ZnO arrester (MOA).

For the purpose of protection from fast rise-time electromagnetic pulses like nuclear electromagnetic pulse (NEMP), FET and diodes are unsuited because of their relatively slow response speed. According to IEC61000-2-9 [17], the rise time of NEMP lies in 1.8 ns~2.8 ns, so response time must be less than that values otherwise the peak of NEMP pulse is hard to be rejected. Meanwhile, the materials with the micro-structure of "conducting grains surrounded by thin insulating barriers" like heterogeneous composites filled with conductive particles and some kinds of metal-oxides, can satisfy the requirement of response time and endure the high incident energy, cause that their electrical properties are determined by the theory of grain boundary or quantum tunneling process [18], which is inherently fast as to the

Submitted On: November 12, 2019
Accepted On: February 21, 2020

scale of ~10^{-15} s. So these materials are widely applied in the field of integrated circuit, non-volatile resistive switching memories, sensors and so on [19]. One representative of these materials is ZnO-based metal-oxide varistors which are ceramic semiconductor devices and most used commercially for the protection of power or other low-frequency circuits against lightning or switching surges [20].

However, ZnO varistors are mostly analyzed and applied in the field of circuit protection. Research on the application of ZnO in electric field protection is inadequate, especially for fast rise-time electromagnetic pulse field. In some certain literatures about the response of ZnO against pulses [21-24], ZnO varistors are generally inserted in the circuits as circuit elements, based on the fact that ZnO can absorb the pulse voltage energy to make over-voltage dismiss or decrease rather than to shield pulse using the property of field-induced insulator-conductor phase transition. The former is injecting voltage or current pulses into ZnO varistors, and the latter means electromagnetic pulses are radiated onto ZnO varistors directly.

In this paper we build an experiment system to test the response of ZnO varistors for shielding fast rise-time electromagnetic pulses. A coaxial fixture with ZnO varistor fitted in is designed and manufactured to be an element of the system in order to make ZnO varistor exposed into the radiating fast rise-time electromagnetic pulses environment through coaxial lines. The results are compared with that of [21]. Some differences are found between responsive waveforms by conducting over-voltage pulses in [21] and waveforms by radiating electromagnetic pulses in our work.

II. EXPERIMENTAL PROCEDURES

A. Experiment system

The configuration of coaxial fixture is shown schematically in Fig. 1 and photographically in Fig. 2. The whole fixture is composed of outside conductor (marked by 1 in Fig. 1) and inside conductor (marked by 2 in Fig. 1). The outside and inside conductors both conclude four components connected with each other through thread. The insulating supports (marked by 3 in Fig. 1) are made by Teflon to isolate the conductors and have been grooved annularly to compensate discontinuous capacitance. Due to the reason that the coaxial fixture would be used to propagate very strong electromagnetic pulse and discharge must be refused, the air inlet and outlet (marked by 4 in Fig. 1) are designed to inject and outflow the insulating gas. And also the four zones marked by 5 in Fig. 1 are all chamfered to avoid discharge at sharp points. ZnO varistor with annular shape (diameter not bigger than 43 mm) and certain thickness (1 mm~5 mm) should be placed in the middle of fixture just like that in Fig. 2. According to (1) and (2) [25], the diameters of outside and inside conductors of coaxial fixture are set as 13 mm and 5.65 mm respectively, which makes the characteristic resistance as 50 Ω matched and the theoretical working frequency range from DC to 10.23 GHz:

$$f_c = \frac{2c_0}{\pi(R_1 + R_2)}, \tag{1}$$

$$Z_0 = \frac{60}{\sqrt{\varepsilon_r}} \ln\left(\frac{R_2}{R_1}\right), \tag{2}$$

where f_c is the cut-off frequency, c_0 is the velocity of light, R_1 and R_2 indicate respectively the diameters of inside and outside conductor, Z_0 means the characteristic resistance of coaxial line and ε_r is the relative dielectric constant of air as 1.

Based on the schematic diagram of Fig. 3, and using the coaxial fixture to clamp the ZnO varistor, the experiment system is built by more other elements like NOISEKEN INS-4040 noise generator, coaxial cables, attenuators, TEK TDS7404B oscilloscope and insulating gas (SF6) vessel as shown in Fig. 4. The NOISEKEN INS-4040 noise generator is used as square wave pulse source and can produce a variety of pulse width such as 50 ns up to 1 μs with the peak value of strength from 10 V up to 4 kV ideally and the rise time from 500 ps to 1 ns, which makes the max value of pulse field strength at the place of fitting materials in the coaxial fixture as almost 1.70 MV/m theoretically calculated by (3) [26]:

$$|\boldsymbol{E}|_{\max} = \frac{2U_0}{R_1 \ln\left(\frac{R_2}{R_1}\right)}, \tag{3}$$

where U_0 is the output peak value of square wave pulse source. Although this value is less than the air breakdown field strength 3 MV/m, we still have found the discharge phenomenon in the coaxial fixture sometimes in the experiment process. So insulating gas such as SF6 is adopted as the standby. The whole system has the matching resistance of 50 Ω for consistent.

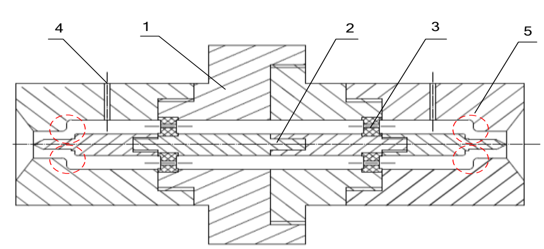

Fig. 1. Schematic diagram of the coaxial fixture.

Fig. 2. Photograph of the coaxial fixture.

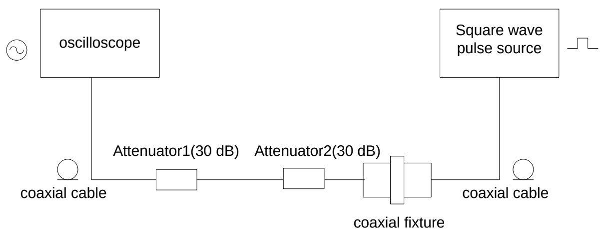

Fig. 3. Schematic diagram of experiment system.

Fig. 4. Photograph of experiment system.

B. Analyses of propagation performance of system

Good propagation performance should be satisfied for avoiding wave distortion, which can be reflected by S11 parameters of system. So S11 curves were obtained through vector network analyzer (VNA) in the frequency range of 300 kHz to 1.5 GHz and 10 MHz to 10.23 GHz respectively, as shown in Fig.5 and Fig. 6. We can see that S11 of this coaxial fixture is less than -10 dB and the standing-wave ratio (SWR) will be less than 2 in the frequency range of 300 kHz to 7.36 GHz, which is enough to ensure the well transmission performance of fast rise-time pulse in this paper. Propagation performance was proved from the output waveforms of system with no material tested shown in Fig. 7, which demonstrates good shape of 1 μs square waveforms. *U* represents the waveforms displayed by oscilloscope. The discrepancy in the frequency range of 7.36 GHz to theoretic 10.23 GHz maybe comes from the machining error, which can be ignored for that most of pulse energy are widely distributed throughout low frequencies.

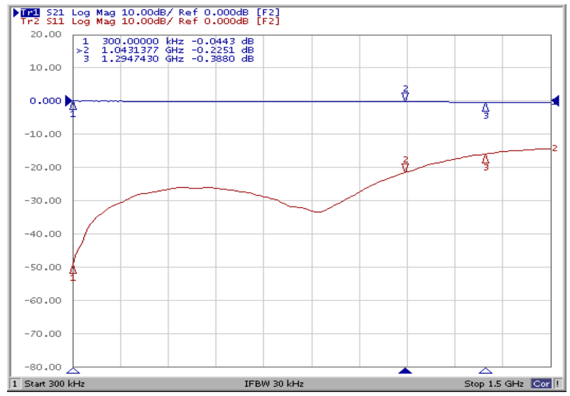

Fig. 5. S11 of coaxial fixture (partially shown in 300 KHz ~1.5 GHz).

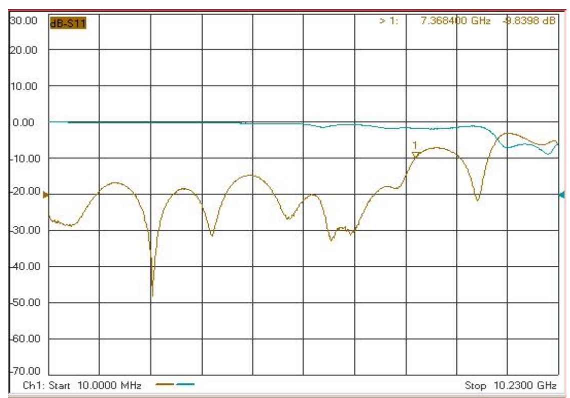

Fig. 6. S11 of coaxial fixture (partially shown in 10 MHz ~10.23 GHz).

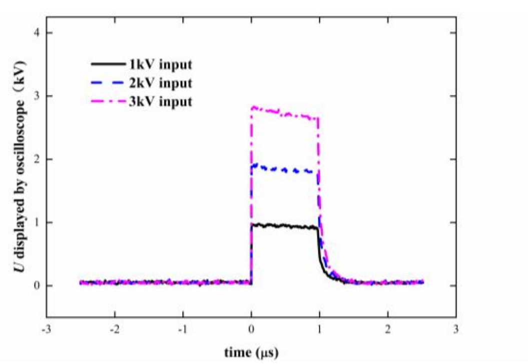

Fig. 7. Output waveforms of system without ZnO varistor fitted in.

C. Analyses of output error of system

Output error of system must be eliminated to assure the accuracy of experiment results. Fig. 8 shows the errors between input and output waveforms. U_i represents the ideal value of input voltage and U_o is the average peak value of output pulses of system in five times triggering. The black solid line with block symbols describes average output peak value of square wave pulse source. The blue dashed line with block symbols describes average error between practical values and ideal values. The black solid line with circular symbols describes the average output peak value of system under the situation that the coaxial fixture is connected with the pulse source and no ZnO varistor is fitted in. The blue dashed line describes average error between practical values and ideal values. It is obviously that errors introduced by the coaxial fixture are very little and can be dismissed. Good propagation performance has been satisfied, so errors introduced by coaxial cables and attenuators can be dismissed. Most of the errors come from the pulse source itself. As the practical output peak value of square wave pulse source is 3.621 kV, the max value of pulse field strength at the place of fitting materials in the coaxial fixture has to be modified from 1.70 MV/m to 1.54 MV/m.

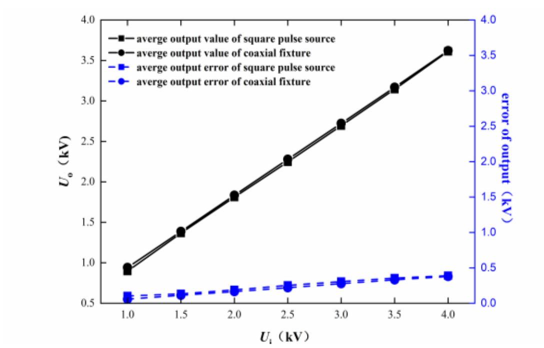

Fig. 8. Average output value and error of square pulse source and coaxial fixture respectively.

D. Analyses of experiment results

A type of ZnO varistors with the diameter as 34 mm and thickness as 3 mm, which are bought as commercial products with a standard sensitive voltage as 700V in circuits, were fitted in the coaxial fixture and tested by this experiment system. Before testing, the silver plated on both sides of ZnO have been erased, as the silver layer would cause the electromagnetic wave to be completely reflected. The responsive pulse waveforms and exciting pulse waveforms are both shown in Fig. 9 with pulse width as 1 μs and a series of input pulse voltages. As we can see from the figures, the output responsive pulse is same as the input exciting pulse when the input voltage is less than 2 kV mainly. This result means ZnO varistor is still a good insulator and doesn't affect the propagation of electromagnetic pulse before the input voltage comes bigger than 2 kV. When the input voltage increases over 2 kV mainly (the max electric field in the coaxial fixture is correspondingly almost 850 kV/m), the peak value of output responsive pulse becomes lower than input exciting pulse and negative pulse occurs. As the input voltage increases, the negative pulse increases too. This phenomenon suggests that ZnO varistor has change to be a conductor with certain resistance, which will be explained in detail by Section III of this paper. Under the condition that insulating gas has been injected to avoid discharging along the face of material, the responsive pulse can be observed repeatedly and similarly, which means ZnO varistor maintains the stable performance and is not broken down by strong electric field during the process of experiment. So conclusion can be gain as that appearance of negative pulse in the responsive waveforms indicates that field-induced insulator-conductor phase transition has happened simultaneously.

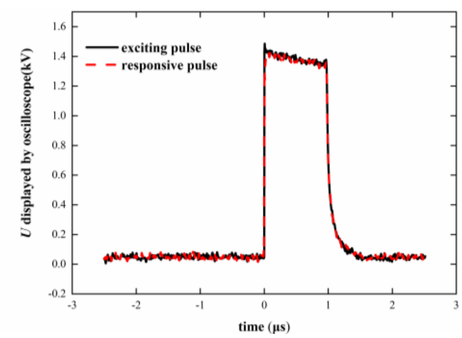

(a) $U_i = 1.5$ kV

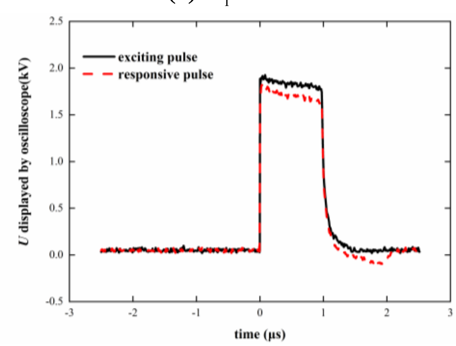

(b) $U_i = 2$ kV

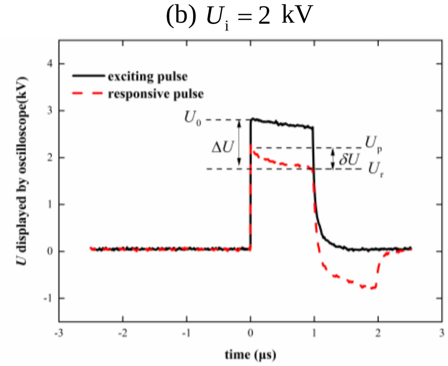

(c) $U_i = 3$ kV

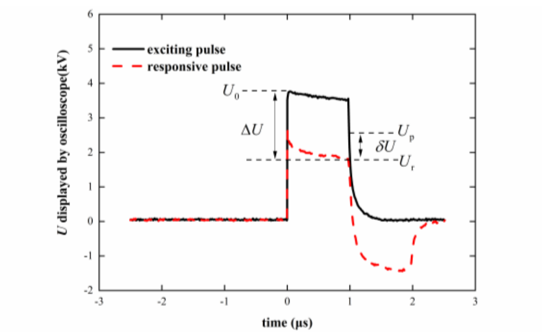

(d) $U_i = 4$ kV

Fig. 9. Comparison of exciting pulse waveforms and responsive pulse waveforms in a series of input voltages.

In contrast with the waveforms of input square pulses, there are three changes happened for the responsive waveforms: 1) the peak value of pulse decreases after phase transition; 2) the overshoot voltage exists with the phase transition; 3) the negative pulse emerges and increases as the input increases. Correspondingly, for the purpose of revealing the changing rules, we have observed three aspects of results which are 1) the voltage drops ΔU (shown in Fig. 9) from U_o to U_r, which is the residual voltage after phase transition; 2) the overshoot voltage δU (shown in Fig. 9) from the peak value of responsive pulse U_p to U_r; and 3) the radio distribution of positive pulse energy and negative pulse energy to the whole pulse energy respectively. Relevant values are listed by Table 1, from which we can find that: U_r is a basically constant value as almost 1.7 kV, ΔU and δU increases linearly as input voltage increases. Their respective radio distributions are shown in Fig. 10.

For the first aspect: ΔU, based on Table I and black solid line with block symbols in Fig. 10, we can know that the capability of ZnO to suppress the peak of radiated strong electromagnetic pulse is approximately enhanced linearly as the input voltage increases. The second one: overshoot voltage δU, whose change is shown as red dashed line with circular symbols in Fig. 10, has relationship with the mechanism of phase transition of ZnO and will be discussed in the next section. The last one is demonstrated by Fig. 11, in which energy is calculated with pulse amplitude multiplied by time. We can see that the positive pulse energy decreases and the negative pulse energy increases as the input pulse voltage increases. However, the sum of energy of positive and negative pulses is found to be a constant approximately. This fact means the suppression of input positive pulse is transferred to the increment of negative pulse by ZnO, which need to be taken sincerely into consideration when ZnO is used to protect against fast rise-time electromagnetic pulse.

Table 1: Changes of voltage in the field-induced insulator-conductor phase transition (all in kV)

U_i	U_o	U_p	U_r	ΔU	δU
2	1.835	1.843	1.655	0.21	0.188
2.5	2.28	2.138	1.753	0.527	0.385
3	2.723	2.304	1.761	0.962	0.543
3.5	3.169	2.59	1.763	1.406	0.827
4	3.621	2.635	1.772	1.849	0.863

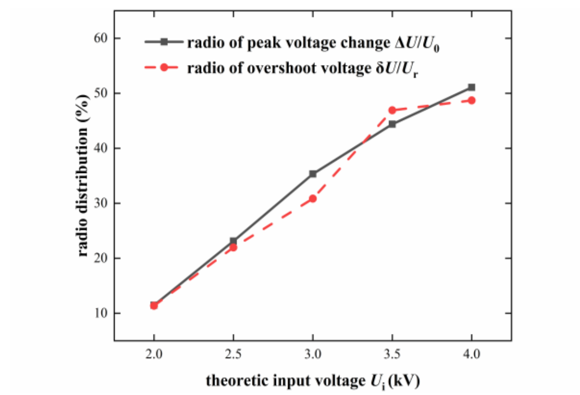

Fig. 10. The radio distribution of ΔU and δU.

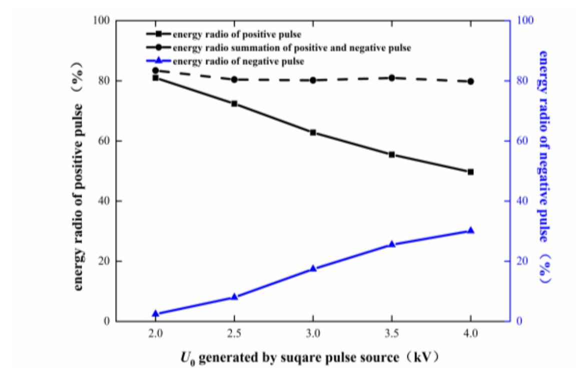

Fig. 11. The radio distribution of positive pulse energy and negative pulse energy to the whole pulse energy respectively.

III. DISCUSSION

For protection of fast rise-time electromagnetic pulse, the electric field threshold of phase transition and the responsive time are two most important indicators that we are concerned about. In the above experiments, the practical voltage threshold of phase transition is almost 1.835 kV (the ideal value is 2 kV), which means the electric field threshold is almost 780 kV/m calculated by (3), for the input pulses with 1 μs width. Father experiments indicate that the threshold of field strength is fixed to this value even though different pulse widths were injected. This is because in the electric field conduction region of ZnO nonlinear resistance (that is, the current-voltage characteristic region with high resistance to low resistance phase transition), the tunneling effect to generate tunnel current is related to the electric field or voltage applied on the grain boundary layer, and have nothing to do with pulse width [18]. Moreover, the quantum tunneling effect is basically in femtosecond, so under the action of electromagnetic pulse with fast rise-time in nanosecond, ZnO can respond in time when the electric field reaches the threshold. This has been proved by the fact that there is no delay between the response waveforms and the input excitation waveforms in all experimental results. The responsive speed is same as that in [21], which is less than or equal to 500 ps. From the above analyses, we can get a conclusion that even though this type of ZnO varistors can meet the requirement of response speed, they may be not suitable for NEMP protection due to their high threshold of electric field strength, which is much bigger than 50 kV/m. According to previous research, the threshold electric field of phase transition has a positive correlation to the thickness of ZnO. Obviously the ZnO varistors we test are too thick to be used as NEMP shielding materials.

Same as the responsive pulses in [21], there exists a constant residual voltage U_{r} with an overshoot voltage δU in our work. Figure 12 shows that the residual voltage U_{r} is generally constant even for different pulse widths. U_{r} represents the shielding capability of ZnO. In the process of experiments, the fact that U_{r} doesn't change with the increase of input electric field has proved that the shielding effectiveness of ZnO is enhanced and adaptable along with the change of incident field. Note that no unified standard about the shielding effectiveness for electromagnetic pulse in time domain has been defined [27, 28], so this paper would not give the exact value of it for ZnO varistors. In addition, the phenomenon of overshoot voltage in ZnO test can also be observed in the circuit experiments. There is no unified view on the cause of its formation in the academic world. An opinion generally accepted is that: when the applied voltage rises, the transition from capacitive current to resistive current passing through ZnO plate needs a certain time delay, which leads to an overshoot in the pulse waveform [18].

However, different from the responsive pulses obtained by injecting fast square wave voltage into ZnO in [21], in which only the peak of pulses decreases and the waveform does not change, for the response pulses of ZnO irradiated by fast square electromagnetic pulse, not only the peak deceases, but also the negative pulse emerges. In order to verify the reason of the negative pulse, a 20 m coaxial transmission line was adopted to substitute the original one (almost 0.2 m) to propagate the pulse. From the result shown by Fig. 13, we can see that the part of negative pulse has a time delay from the part of positive pulse, and the time delay is just the propagation time of electromagnetic pulse forward and backward along with the 20 m transmission line (time delay $\Delta t = 2\times 20\ \mathrm{m}/v$; v is the velocity of electromagnetic wave in the coaxial line and $v = c/\sqrt{\varepsilon_r}$ [29]; c is the velocity of light in the vacuum; ε_r is the permittivity of insulating medium in the coaxial line and $\varepsilon_r \approx 2.5$). So, the negative pulse indicates that ZnO varistors has occurred high-to-low resistance switching phase transition. It is considered to be a reflected signal generated by the mismatch between the low resistance of ZnO and the system impedance 50 Ω. According to the transmission line theory [26], the low resistance of ZnO after phase transition can be calculated by below equations:

$$\Gamma = \frac{Z_{\mathrm{L}} - Z_0}{Z_{\mathrm{L}} + Z_0} = \frac{U_{\mathrm{p}}^{'}}{U_{\mathrm{p}}}, \tag{4}$$

$$Z_{\mathrm{L}} = Z_0 \frac{1+\Gamma}{1-\Gamma}, \tag{5}$$

where U_{p} is the peak value of positive pulse and $U_{\mathrm{p}}^{'}$ is the peak value of negative pulse; Γ is the reflection coefficient in the end of transmission line; Z_0 is the equivalent impedance of coaxial line and $Z_0 = 50\ \Omega$; Z_{L} is the equivalent impedance of ZnO varistors. Note that for the purpose of simplifying calculation, here the dispersive capacitances of transmission line and ZnO varistors are dismissed and all the impedance is seemed as pure resistance. The calculated results are listed in Table 2, from which we can see that: the resistance of ZnO after phase transition is less than 50 Ω and decreases linearly along with the increase of incident voltage or field. Though the current of coaxial transmission line cannot be generally measured directly and is also not easily calculated by the equation in [21] due to the emergence of negative pulse, it is still clear to conclude that the current-voltage characteristic of ZnO varistors in the radiating electromagnetic environment is nonlinear based on the relationship of current, voltage and resistance, which agrees with the conductive mechanism of ZnO based on double Schottky barrier model [18].

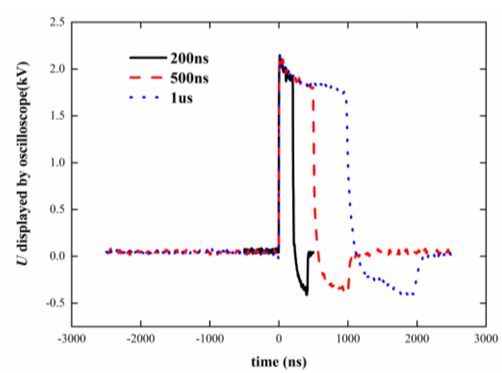

Fig. 12. The responsive waveforms of ZnO varistor with the 2.5 kV voltage but different pulse widths inputted.

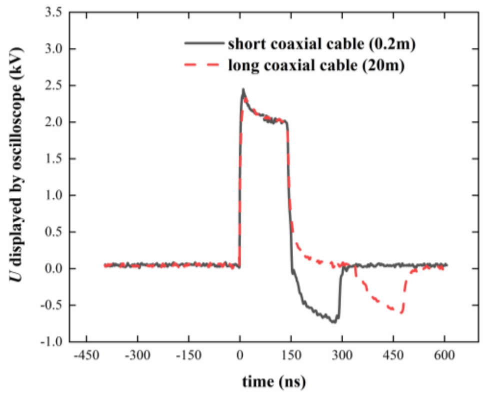

Fig. 13. The responsive waveforms of ZnO varistor with the 3 kV voltage and 150 ns pulse width inputted using the coaxial cable with different lengths.

Table 2: Impedance calculation of ZnO varistors (voltage in kV, impedance in Ω)

U_i	U_p	$U_p^{'}$	Γ	Z_L
2	1.843	-0.09	-0.049	45
2.5	2.138	-0.41	-0.192	34
3	2.304	-0.792	-0.344	24
3.5	2.59	-1.155	-0.446	19
4	2.635	-1.425	-0.541	15

IV. CONCLUSION

In this paper, an experimental system to test the response of ZnO for shielding fast rise-time electromagnetic pulses is built by using a coaxial fixture with gas insulation design. The electromagnetic pulse protection characteristics of ZnO varistors are measured and analyzed. The results show that:

1) The coaxial fixture has good transmission performance, and the actual S11 parameter is less than -10 dB in the range of 300 kHz to 7.36 GHz, introducing a very small test error to the experiment system. Analyses of output error shows that most of the errors come from the pulse source itself.

2) The insulator-conductor phase transition occurs when the 1.835 kV pulse is irradiated onto the surface of ZnO varistor, which means the threshold of electric field strength is 780 KV/m approximately. A negative pulse waveform appears after phase transition, which is different from that in the past studies when ZnO is injected with an overvoltage pulse.

3) There is no delay between the responsive waveforms and the input excitation waveforms, which indicates that the responsive speed of ZnO is less than or equal to 500 ps, so ZnO can respond in time when the electric field reaches the threshold.

4) The peak value of positive pulse decreases after phase transition, and the residual voltage is generally constant for different pulse strength and widths, which has proved that the shielding effectiveness of ZnO is enhanced and adaptable along with the increase of incident field. The phenomenon of overshoot voltage is observed, and overshoot voltage increases linearly as the input radiating pulse field strength increases.

5) The appearance of negative pulse in the waveform means the completion of field-induced insulator-conductor phase transition. Negative pulse is caused by the reflection of electromagnetic wave after the phase transition. The resistance of ZnO after phase transition is less than 50 Ω and decreases linearly along with the increase of incident voltage or field, which leads to the highly nonlinear current-voltage characteristic of ZnO varistors in the radiating electromagnetic environment.

6) Sum of energy of positive and negative pulses keeps constant, which means that the weakened positive pulses are converted into negative pulses. So impact of the negative pulse needs to be taken into consideration when ZnO varistors are used to protection against strong electromagnetic pulse.

In conclusion, there are some similarities and some differences between the results obtained by injecting fast square wave voltage into ZnO in previous works and that obtained by radiating square wave pulse onto ZnO surface in our work. This may possess certain reference value for solving the problem of electromagnetic pulse defense. What need to be added is that: due to the similarity in frequency distribution and fast rise time between square wave and NEMP, we use square waveform pulse source to substitute NEMP generator. Continuous wave usually lacks enough strength to induce phase transition of ZnO. The response for pulse with other waveforms can be observed by using corresponding pulse source to replace the pulse source in the existing system.

We wish to emphasize that the results presented here are preliminary. The varistors materials we used were not optimized for specific application of NEMP protection. The relationship between the thickness of ZnO varistors and the threshold field strength requires clarification. Meanwhile, the impact of negative pulse on protective effectiveness for electromagnetic pulse also needs further studies. These questions may be answered in following papers.

ACKNOWLEDGMENT

Thanks to Mr. Zhang Nanfa for his theoretical guidance.

Research of this paper has been funded by pre-research project of the 13th five-year plan in China.

REFERENCES

[1] W. Jianzhong, M. Jun, Z. Hao, and T. Huiping, "Preparation and electromagnetic shielding effectiveness of metal fibers/polymer composite,"

Rare Metal Materials & Engineering, vol. 46, pp. 73-77, 2017.

[2] Z. Shuang-Xi, H. Shui-Mei, D. Wen-Wu, X. Qing, and W. Wei-Dong, "Research progress of doped electromagnetic shielding conductive coatings," *Bulletin of the Chinese Ceramic Society*, vol. 31, pp. 604-608, 2012.

[3] J. P. Blanchard, F. M. Tesche, S. H. Sands, and R. H. Vandre, "Electromagnetic shielding by metallized fabric enclosure: theory and experiment," *Electromagnetic Compatibility IEEE Transactions on*, vol. 30, pp. 282-288, 1988.

[4] X. Zhu and X. Li, "Current status and research direction of electromagnetic shielding fabric," *Shanghai Textile Science & Technology*, vol. 1, pp. 104-107, 2010.

[5] T. Matsushima, M. Aoki, T. Hisakado, and O. Wada, "Equivalent circuit model with nonlinear characteristics of zener diode extracted from SPICE model for ESD simulation," in *Electromagnetic Compatibility of Integrated Circuits*, pp. 152-155, 2017.

[6] O. C. Spro, S. Basu, I. Abuishmais, O. M. Midtgard, and T. Undeland, "Driving of a GaN enhancement mode HEMT transistor with zener diode protection for high efficiency and low EMI," in *European Conference on Power Electronics and Applications*, pp. P.1-P.10, 2017.

[7] Y. Cheng, H. Xianjun, and L. Peiguo, "Protection and simulation of energy selective surface based on voltage conductive structure," *Chinese Journal of Ship Research*, vol. 7, pp. 98-103, 2012.

[8] X. Tang, H. Gao, S. Pan, J. Sun, X. Yao, and X. Zhang, "Electrical characteristics of individual In-dop ed ZnO nanob elt field effect transistor," *Acta Physica Sinica*, vol. 63, pp. 314-319, 2014.

[9] L. Yuan, H. Chen, Q. Zhou, C. Zhou, and K. J. Chen, "Gate-induced Schottky barrier lowering effect in AlGaN/GaN metal–2DEG tunnel junction field effect transistor," *IEEE Electron Device Letters*, vol. 32, pp. 1221-1223, 2011.

[10] W. Zhang, M. Li, Q. Wei, L. Cao, Z. Yang, and S. Qiao, "Fabrication and I-V characteristics of ZnO nanowire-based field effect transistors," *Acta Physica Sinica*, vol. 57, pp. 5887-5892, 2008.

[11] X. Wang, J. Guo, Y. Yao, Z. Jia, Q. Lv, and R. Huang, "Study of epoxy resin composites doped with nonlinear fillers and its electrical properties," in *IEEE Conference on Electrical Insulation and Dielectric Phenomenon*, pp. 54-57, 2017.

[12] X. Wang, S. Herth, T. Hugener, and R. W. Siegel, "Nonlinear Electrical Behavior of Treated ZnO-EPDM Nanocomposites," in *Electrical Insulation and Dielectric Phenomena, 2006 IEEE Conference on*, pp. 421-424, 2006.

[13] M. Y. Song, Y. Seo, S. Park, J. H. Lee, H. M. An, and T. G. Kim, "Observation of highly reproducible resistive-switching behavior from solution-based ZnO nanorods," *Journal of Nanoscience & Nanotechnology*, vol. 13, p. 6212, 2013.

[14] E. J. Yoo, J. H. Kim, J. H. Song, T. S. Yoon, Y. J. Choi, and C. J. Kang, "Resistive switching characteristics of the Cr/ZnO/Cr structure," *Journal of Nanoscience & Nanotechnology*, vol. 13, p. 6395, 2013.

[15] R. Hao, Y. Li, F. Liu, Y. Sun, J. Tang, P. Chen, *et al.*, "Electric field induced metal–insulator transition in VO 2 thin film based on FTO/VO 2/ FTO structure," *Infrared Physics & Technology*, vol. 75, pp. 82-86, 2016.

[16] J. Jeong, N. Aetukuri, T. Graf, T. D. Schladt, M. G. Samant, and S. S. Parkin, "Suppression of metal-insulator transition in VO2 by electric field-induced oxygen vacancy formation," *Science*, vol. 339, pp. 1402-5, 2013.

[17] Y. Z. Xie, Z. J. Wang, Q. S. Wang, and H. Zhou, "Comparison of several HEMP waveform standards," in *Radio Science Conference, 2004. Proceedings. 2004 Asia-Pacific*, pp. 516-518, 2005.

[18] W. WU, J. He, and Y. Gao, *Properties and Applications of Nonlinear Metal Oxide Varistors*. Beijing: Tsinghua University Press, 1998.

[19] Z. Yang, C. Ko, and S. Ramanathan, "Oxide electronics utilizing ultrafast metal-insulator transitions," *Annual Review of Materials Research*, vol. 41, pp. 337-367, 2011.

[20] J. He, J. Lin, J. HU, and W. Long, "Development of ZnO varistors in metal oxide arrestors utilized in ultra high voltage systems," *High Voltage Engineering*, vol. 37, pp. 634-643, 2011.

[21] H. R. Philipp and L. M. Levinson, "ZnO varistors for protection against nuclear electromagnetic pulses," *Journal of Applied Physics*, vol. 52, pp. 1083-1090, 1981.

[22] F. A. Modine and R. B. Wheeler, "Fast pulse response of zinc-oxide varistors," *Journal of Applied Physics*, vol. 61, pp. 3093-3098, 1987.

[23] F. A. Modine, R. B. Wheeler, Y. Shim, and J. F. Cordaro, "Origin of the pulse response characteristics of zinc oxide varistors," *Journal of Applied Physics*, vol. 66, pp. 5608-5612, 1989.

[24] F. A. Modine and R. B. Wheeler, "Pulse response characteristics of ZnO varistors," *Journal of Applied Physics*, vol. 67, pp. 6560-6566, 1990.

[25] X. Chen, "Testing and modeling for shielding effectiveness of planar materials against electromagnetic pulse" *Doctorate, Ordnance Engineering College*, Shijiazhuang, China, 2013.

[26] X. Zhou, *Microwave Technology and Antenna*. Nanjing: Southeast University Press, 2009.

[27] B. Zhou, G. Cheng, and H. Ren, "The definition

of EMP shielding effectiveness," in *Asia-Pacific Conference on Environmental Electromagnetics Ceem*, pp. 562-565, 2003.
[28] L. Klinkenbusch, "On the shielding effectiveness of enclosures," *IEEE Transactions on Electromagnetic Compatibility*, vol. 47, pp. 589-601, 2005.
[29] J. Gu, *Microwave Technology*. Beijing: Science Press, 2009.

Wangwei Zhang was born in China, 1983. He received doctor's degree in Theory and Technology of Weapon Launching from Ordnance Engineering College in Shijiazhuang. He is currently a University Teacher in Zhengzhou University of Light Industry in Zhengzhou. His research interests are Equipment Modeling and Simulation.

Yun Wang was born in China, 1985. He received Ph.D.'s degree in Information and Communication Engineering from the Academy of Equipment in Beijing, China, 2010. He is currently a Researcher in Department of Science and Technology of Henan Province, Zhengzhou, China. His research interests are electromagnetic pulse shielding and antennas.

Magneto-Mechanical Behavior Analysis using an Extended Jiles-Atherton Hysteresis Model for a Sheet Metal Blanking Application

Khaoula Hergli [1], Haykel Marouani [2], Mondher Zidi [1], and Yasser Fouad [2]

[1] Department of Mechanical Engineering
University of Monastir, LGM, Monastir, 5019, Tunisia
hergli.khaoula@gmail.com, mondher.zidi@enim.rnu.tn

[2] Department of Mechanical Engineering
King Saud University, P.O. Box 2454, Riyadh 11451, Saudi Arabia
hmarouani@ksu.edu.sa, yfouad@ksu.edu.sa

Abstract ─ Manufacturing processes affect the magnetic properties of the ferromagnetic components of electrical equipment. The optimization of the designed devices depends on two factors: the mechanical state of the material of a blanked part, especially near the cutting edge, and the magneto-mechanical behavior of the material used. In this paper we investigate the magnetic induction degradation of a blanked stator fabricated using fully processed, non-oriented Fe–(3 wt%)Si steel sheet. Owing to the geometric symmetry, we first simulated a half-stator teeth blanking using the Abaqus software. Subsequently, a magneto-mechanical extended Jiles–Atherton hysteresis model was used to determine the magnetic induction distribution on the blanked teeth stator. The numerical results show that the magnetic induction degradation can reach 25% upon applying moderate magnetic field, i.e., 1000 A/m, and 8% upon applying magnetic field close to the magnetic saturation, i.e., 3500 A/m. The depth of the affected region was approximately 1.25 mm before the material regained its initial magnetic state.

Index Terms ─ Blanking, finite element method, Jiles-Atherton hysteresis, magnetic properties, strain-magnetic coupling.

I. INTRODUCTION

Rotating electrical machines comprise ferromagnetic parts, which are manufactured using either conventional processes (blanking, drilling, shearing, etc.) or nonconventional ones (laser cutting or wire cutting). These processes, especially in ferromagnetic sheet metal forming, introduce local changes in the microstructure and generate internal stresses, thereby affecting the magnetic properties in the region of the cutting edge [1, 2] and increasing the magnetic losses near the cutting edge [3, 4]. Cao et al. [5] described the residual-stress distribution and magnetic domain structure on the cutting edge, demonstrating that the decrease in the width of the residual-stress-variation zone reduced the deterioration of magnetic properties. For punched ring structures, Lewis et al. [6] developed a simple model to represent the power loss as a function of the damaged-region width; The results showed that the power loss increased with decrease in the damaged width. Notably, elastic and plastic deformations significantly affect the magnetic properties of materials and alter the shape of the hysteresis curves. The elastic strain modifies the local internal nergy of the material, thereby affecting its magnetic behavior. However, compared with internal elastic stain, plastic deformations induce higher disorder in the magnetic behavior; therefore, the deterioration in magnetic properties is less noticeable over the elastic tensile stress range than that because of plastic deformation [7]. The adverse effects of plastic tension on magnetic properties are manifested in the range of the low plastic strain levels and in the low and medium magnetic field amplitudes [8–11]. The aforementioned phenomenon is more noticeable at high tensile stress, which results in increased losses [12]. Furthermore, the mechanical stresses affect magnetic anisotropy, decrease permeability, and increase power losses [10]. Blanking parameters (i.e., punch velocity and clearance) have also been investigated [13] to determine their contribution to the degradation of magnetic properties. Xiong et al. [14] demonstrated the mechanical-cutting-induced changes in the microstructure and texture of non-oriented Fe–Si, deterioration in its magnetic properties, and a significant change in the resulted hysteresis loop. They also reported that these variations were more apparent upon increasing the cutting length per mass. Wang et al. [15] and Kuo et al. [16] revealed the importance of punching clearance, which deteriorates the magnetic performance. In addition, Weiss et al. [17] demonstrated that smaller cutting clearances could result in higher residual stresses near the cutting surface. They further showed that both

Submitted On: February 3, 2020
Accepted On: April 19, 2020

1054-4887 © ACES

important cutting speed and wear of the tool increased the losses and deteriorated magnetization. Furthermore, material characteristics of electrical steels, such as thickness, grain size, and crystallographic texture strongly affect the magnetic properties of non-oriented electrical steel sheets [18]. Kuo et al. [16] indicated that a material with small grain size had low deformation during the punching process. Omura et al. [19] and Toda et al. [20] studied the effect of the hardness and thickness of non-oriented electrical steels on iron-loss deterioration by blanking process and, consequently, observed that material iron loss was low in thin or hard specimens.

Establishing a description for multiple physical coupling processes is essential. Several models have been developed and implemented into a numerical model to define the magneto-mechanical behavior of ferromagnetic materials in electrical devices. Coupling was employed to study the effect of blanking on the magnetic response [10] and the contribution of multiaxial stress on magnetization [10,11,13,21]. A certain amount of coupling was proposed as an extension of existing classical magnetic hysteresis models [13,22–24]. The numerical modeling of such problems requires sufficient computer capacity, powerful software for the simulations, and a well-defined and efficient approach. However, all of the cited studies have limitations. The coupled model of Ossart et al. [10] is based on the conversion of the local microhardness into an equivalent plastic strain, which cannot describe the complex state induced by blanking. Bernard and Daniel [13] extended the Jiles–Atherton (J–A) hysteresis model by introducing mechanical stress via anhysteretic magnetization and by modifying the pinning factor. This model was then implemented into a time-stepping finite element method. However, this approach suffers from critical convergence difficulties. The multiscale approach used by Aydin et al. [21] and based on the free energy in the domain scale is also insufficient, as it relies on only a few material parameters and provides a description of the coupled magneto-mechanical anhysteretic behavior only.

In this work, we present a coupled experimental and numerical analysis of magnetic behavior degradation for stator teeth blanking. Magnetic experiments on ferromagnetic sheet steel were carried out at different levels of plastic strain to develop an extended J–A hysteresis model considering the strain-magnetic field coupling. A sheet metal blanking model of a half-teeth stator was developed and validated using the Abaqus software. Then, a coupling analysis using Python and Abaqus was performed. The Python code obtained the plastic strain map from the finite element simulation and calculated the corresponding magnetic induction for a given magnetic field. These values were inserted in the teeth stator part to visualize the magnetic induction and distribution of degradation. An analysis performed close to the cutting edge revealed the "magnetic dead zone" depth.

II. THE JILES-ATHERTON HYSTERESIS MODEL

Jiles and Atherton [25] defined the total magnetization M as the sum of two components:

$$M = M_{rev} + M_{irr}, \tag{1}$$

where M_{rev} is the reversible component resulting from the deformation of the walls on the coupling sites under the action of an external field and M_{irr} represents the irreversible magnetization. They can be analyzed by the set of differential equations:

$$\begin{cases} \dfrac{dM_{rev}}{dH} = c\left(\dfrac{dM_{an}}{dH} - \dfrac{dM_{irr}}{dH}\right) \\ \dfrac{dM_{irr}}{dH} = \dfrac{M_{an} - M_{irr}}{\delta\, k - \alpha(M_{an} - M_{irr})} \end{cases}, \tag{2}$$

where c is the coefficient of reversibility in the range of 0–1, H is the applied magnetic field, δ is the directional parameter, taking the value of +1 or −1, α is the domain coupling parameter, and k is the pinning factor. The anhysteretic magnetization is denoted by M_{an} and it can be expressed by the modified Langevin function:

$$M_{an} = M_s\left(\coth\left(\frac{H_e}{a}\right) - \frac{a}{H_e}\right), \tag{3}$$

where a represents the domain density, M_s is the saturation magnetization and H_e is the Weiss effective field given by:

$$H_e = H + \alpha M. \tag{4}$$

Considering all these expressions, the J–A hysteresis model can be expressed by the differential equation:

$$\frac{dM}{dH} = (1-c)\frac{M_{an} - M_{irr}}{\delta k - \alpha\left(M_{an} - M_{irr}\right)} + c\frac{dM_{an}}{dH}, \tag{5}$$

which is a function of five parameters $\{M_s, a, \alpha, c, k\}$.

III. EXPERIMENTAL ASPECTS OF MAGNETO-MECHANICAL COUPLING

In this section, we present the experimental arrangement for the magnetic measurements, the obtained magnetic hysteresis at different levels of plastic strain, and the developed theoretical model based on the J–A hysteresis model, which considers the magneto-mechanical behavior coupling. It should be noted that a more detailed description of the magnetic measurement test apparatus is available in Refs. [22,26].

A. Arrangement for magnetic measurements

The samples were obtained from a fully processed, non-oriented Fe–(3 wt%)Si steel sheet with a thickness of 0.35 mm. The magnetic measurements were carried out in the "initial state" (i.e., without residual stress) and in the "loaded state" (i.e., different ranges of plastic strain applied up to 10% using a universal testing machine). The applied stress and the magnetic field were both in the rolling direction.

Figure 1 shows the obtained experimental hysteresis loop at different loaded states. The total strain is assumed to be plastic strain under a static regime (frequency of 1 Hz). As can be seen in Fig. 1, the magnetic properties are affected even at a low range of deformation. For example, it is noticeable that the magnetization at saturation and the remanence decrease with the increase in the deformation. Saturation is the state reached when an increase in the applied external magnetic field cannot increase the magnetization of the material and remanence is the magnetic flux density remaining in a material following the removal of the magnetizing field. However, the coercive field and hysteresis losses increase with the increase in the deformation. Magnetic coercivity is a measure of the ability of a ferromagnetic material to withstand an external magnetic field without becoming demagnetized and the hysteresis loss is proportional to the area of the hysteresis loop.

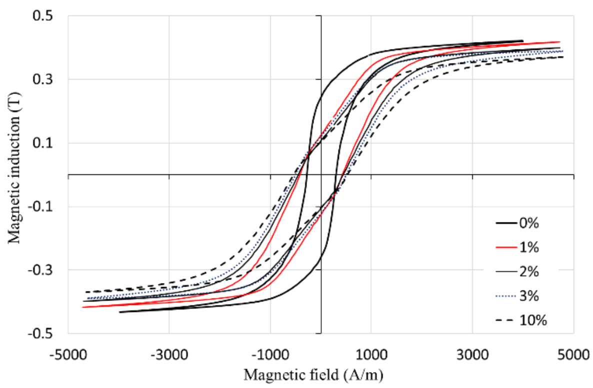

Fig. 1. Experimental hysteresis loops as functions of the applied elastoplastic deformation [23].

B. Hysteresis simulation

Several efforts have been made to develop hysteresis models suitable for different materials and frequencies. In our study, we employed the J–A model [22,25]. The implementation of such a model requires the identification of five parameters: the saturation magnetization, the domain-coupling parameter, the pinning factor, the coefficient of reversibility, and the domain density. The J–A parameters were successfully identified using a genetic algorithm procedure for each plastic strain range [22]. A parameter sensitivity investigation allowed us to assume that parameter a had the greatest effect on the shape of the hysteresis curve. The study of the evolution of the J–A model parameters for different elastoplatic deformations reveals that only the domain density a depends on the deformation. The results of the hysteresis curve simulation for non-deformation, low deformation, and even at high deformation, with α, c, and k constants, are in agreement with the measurements. Accordingly, we assume that they are independent of the elastoplastic deformation. Then, only parameter a is expected to be a function of εp and follows the law:

$$a = \frac{119 + 650.\varepsilon_p}{1 + \varepsilon_p}. \tag{6}$$

For the three other J–A parameters, we averaged the centered values of ten genetic algorithm simulations: $\alpha = 150 \times 10^{-6}$, $c = 31 \times 10^{-3}$, and $k = 498$ A/m. Figure 2 shows the experimental and simulated hysteresis for the initial state and 10% of mechanical deformation. Compared with the experimental results, all simulation results show a mean square error of less than 5%.

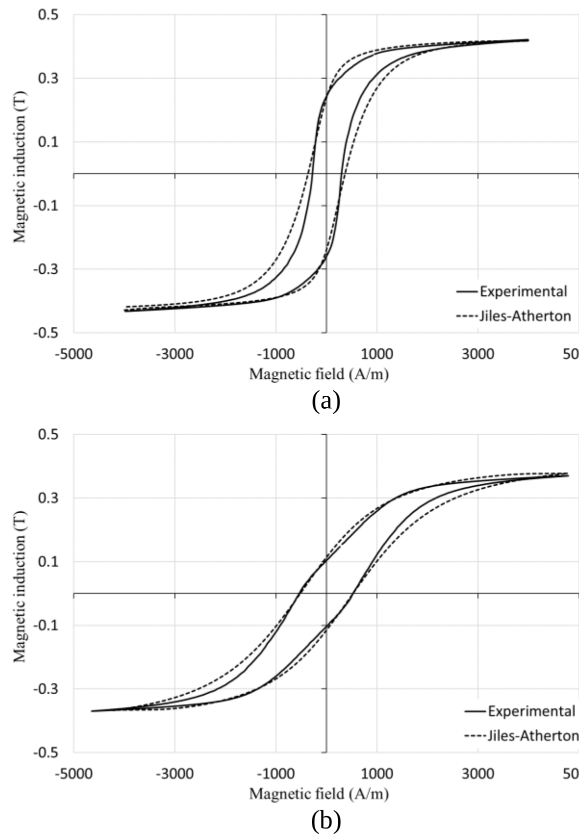

Fig. 2. Measured and simulated hysteresis loops for Fe–(3wt%)Si at different elastoplastic deformations (a) 0% and (b) = 10%) [22].

IV. NUMERICAL ASPECTS OF STATOR TEETH BLANKING

In this section, we present the finite element analysis of a half-teeth stator blanking by using the Abaqus software.

A. Finite element model

Figure 3 depicts the different tools employed for the simulation of the stator teeth blanking, where, owing to its geometric symmetry, only a half part is included. The half blank, which was rectangular, with dimensions 115 mm × 45 mm × 0.8 mm, was positioned between a die and blank holder. All the process tools had a fitting radius of 0.2 mm. The radial clearance between the punch and die, relative to the sheet thickness, was 10% (sheet thickness equal to 1.2 mm). The model of the tools was based on the application of rigid bodies. The die and blank holder were fixed, and the punch moved at 100 mm/s. The contact was described using a Coulomb friction model with a friction coefficient, μ, of 0.18.

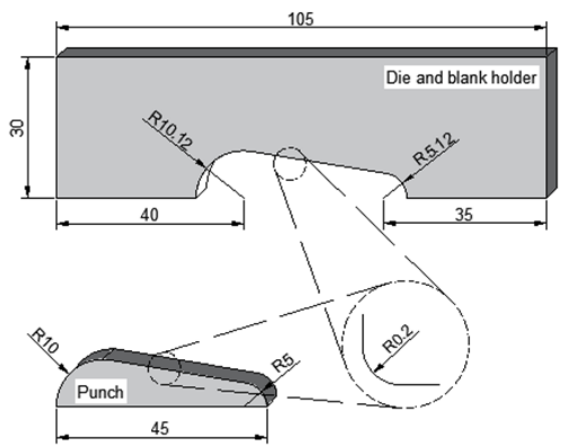

Fig. 3 Geometric description of the blanking tools.

The material investigated was a 1.2-mm-thick sheet of isotropic non-oriented full-process Fe–(3 wt%)Si steel. Various tensile tests were performed at the strain rate of 10^{-5} s^{-1}. This value of strain rate is, generally, used to describe the “quasi-static” behavior of the material. The material work hardening can be described using a conventional Ludwik’s law. The quasi-static yield stress is given as follows:

$$\bar{\sigma}_0(\bar{\varepsilon}_p) = 770(\bar{\varepsilon}_p)^{0.26} \ . \tag{7}$$

While assuming the quasi-static material behavior, we do not consider the high magnitude of the punch velocity. Therefore, it is better to improve the material-behavior description using a strain-rate-behavior law. In such a model, the rate of the effective plastic strain is related to the difference between the current stress and yielding stress, as proposed by Peirce et al. [27]. For one-dimensional rate-dependent plasticity and isotropic work hardening, the effective plastic strain rate is given as:

$$\dot{\bar{\varepsilon}}^p = \dot{\bar{\varepsilon}}_0^p \left(\frac{|\sigma|}{\bar{\sigma}(\bar{\varepsilon}^p)} \right)^m , \tag{8}$$

where $\bar{\varepsilon}^p$ is the equivalent plastic strain, $\dot{\bar{\varepsilon}}^p$ is the equivalent plastic strain rate, which is the reference strain rate used to measure the quasi-static yield stress, and m is the rate sensitivity parameter (m > 0).

As the blanking process is not time-dependent, the dependence on the strain rate is considered using the rate-dependent yield. When the dependences on the strain and strain rate are assumed to be separable and isotropic work hardening is considered, the strain rate dependent yield-stress $\bar{\sigma}$ is defined by:

$$\bar{\sigma}(\bar{\varepsilon}^p, \dot{\bar{\varepsilon}}^p) = \bar{\sigma}_0(\bar{\varepsilon}^p) \left(\frac{\dot{\bar{\varepsilon}}^p}{\dot{\bar{\varepsilon}}_0^p} \right)^m , \tag{9}$$

where $\bar{\sigma}_0(\bar{\varepsilon}^p)$ is the quasi-static yield stress at the quasi-static strain rate $\dot{\bar{\varepsilon}}_0^p$.

To study the strain rate sensitivity, the true stress–strain curves were measured using an Instron test machine equipped with a charge-coupled device (CCD) camera and a data acquisition system controlling the prescribed displacement to maintain a constant strain rate in the center of the specimen. The technique used for these video controlled tests is based on the procedure developed by G’sell and Jonas [28]. The experimental arrangement was used to perform tensile tests at different strain rates ranging from 10^{-5} to 5 $\times 10^{-3}$ s^{-1}, with a reference strain rate set as 10^{-5} s^{-1}. The result obtained for the investigated material shows a significant strain rate sensitivity value (m = 0.0085).

The numerical simulation of the sheet metal blanking process has been reported by several studies [2,29,30] Different approaches have been proposed to simulate the shearing process and to treat ductile fracture. In this work, we use the non-iterative explicit approach to model the high nonlinearity associated with the blanking process. An arbitrary Euler–Lagrange formulation was employed to treat the large mesh distortion occurring during the calculation and leading to strain localization and mesh degradation, resulting in significant errors. The blank is meshed using 22 610 hexahedral elements with reduced integration (type C3D8R), as shown in Fig. 4.

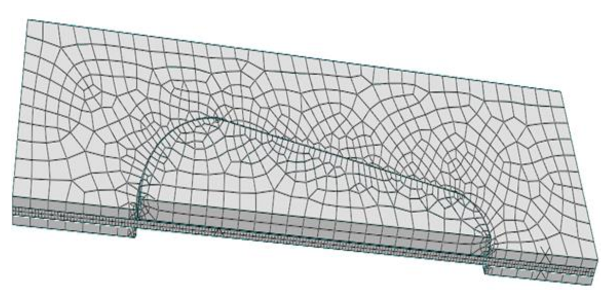

Fig. 4. Finite element model for the blanking test simulation.

Among the several existing sheet metal-forming processes, the blanking process is special in the respect that plastic straining is followed by ductile fracture and material separation. We used the well-known

Gurson–Tvergaard–Needleman model [31,32] to treat ductile fracture. The nine Gurson–Tvergaard–Needleman parameters are summarized in Table 1 [2,29], where term f_0 is the initial void fraction, $\{q_1, q_2, q_3\}$ are adjustable material parameters, f_N is the volume fraction of the nucleating void, ε_N is the mean strain for void nucleation, S is the standard deviation, f_c is the critical void volume fraction, and f_F is the void volume fraction at failure.

Table 1: Gurson–Tvergaard–Needleman parameters

f_0	q_1	q_2	q_3	ε_N	f_N	S	f_c	f_F
0.01	1.5	1	2.25	0.3	0.04	0.1	0.11	0.12

B. Finite element results

Because of the lack of experimental tests on stator teeth blanking, the validation of our numerical approach is based only on the numerical punch displacement as a function of the punch load. According to the literature, the maximum blanking load, F_{max}, is expressed by [33]:

$$F_{max} = k.P.e.\sigma_{max}, \qquad (10)$$

where k is a calibration factor ($0.8 < k < 0.95$), P is the perimeter of the punch, e is the thickness of the blank, and σ_{max} is the maximum tensile stress of the material.

According to equation (10), the maximum load needs to be in the range of 13.0–15.5 kN. In addition, for steel case blanking, fracture typically occurs between 85 and 95% of the thickness of the sheet [29]. These findings are confirmed by the curve of the simulated penetration as a function of load (Fig. 5). A reference point was assigned to the punch (rigid body) which enabled the acquisition of the tool displacement and total punch force required to penetrate the blank. The relative punch displacement is defined as the ratio of punch displacement and the blank thickness.

Figure 6 shows the von Mises stress distribution and the "equivalent plastic strain" (PEEQ) distribution.

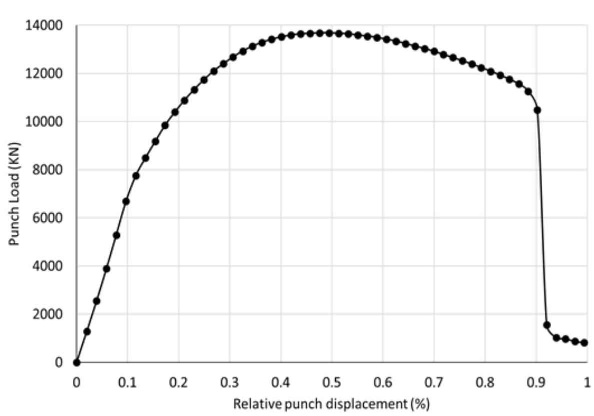

Fig. 5. Teeth stator load as a function of displacement (maximum load = 13 685 N; relative displacement at fracture = 0.88).

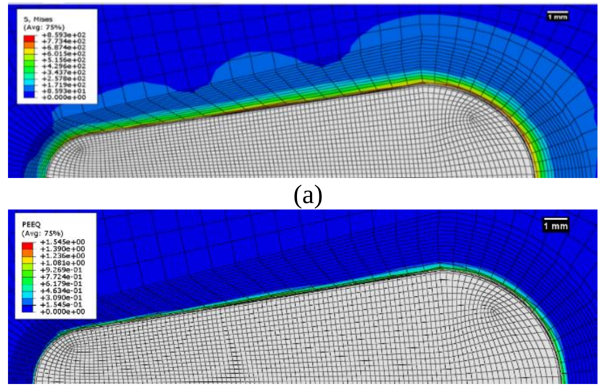

(a)

(b)

Fig. 6. (a) von Mises stress distribution, and (b) PEEQ distribution.

V. APPLICATION OF THE MAGNETO-MECHANICAL COUPLING

The magneto-mechanical coupling is realized following different steps and using the Abaqus software and a model in Python language. Figure 7 shows the applied numerical procedure. First, a blanking finite element simulation of the half-teeth stator is performed as described in the previous section. Then, the value of the equivalent plastic strain for each element of the specimen mesh is obtained. For a given value of magnetic field, H, we calculate the corresponding value of the magnetic induction using the extended J–A formulation (see section "Materials and Methods"). Two new variables are created and saved in the odb file used by Abaqus. The first variable is denoted as "magnetic induction," describing the magnetic distribution through the blanked part [Fig. 8 (a) and 9 (a)]. The second variable is denoted as "degradation," representing the relative degradation of the magnetic induction, and it corresponds to the percentage rate of corresponding magnetic induction and maximum magnetic induction [Fig. 8 (b) and Fig. 9 (b)].

Figure 8 and Fig. 9 show that far from the cutting edge, the material regains its original magnetic properties. For the better analysis of the magnetic efficiency and to provide guidance for electrical parts designers, it is important to characterize the magnetic properties near the cutting edge and to determine the width of the affected area. For this purpose, we defined two "paths," shown in Fig. 10, to analyze the evolution of the magnetic properties near the cutting edge. The results summarized in Fig. 11 show that the magnetic degradation is more substantial for the low and medium range magnetic fields: the magnetic induction degradation reached 23.8% for an applied magnetic field of 1000 A/m. Close to the magnetic saturation (H_s = 4500 A/m), the degradation is less severe: the magnetic induction degradation reached 7.4% for an applied magnetic field of 3500 A/m. The affected area is approximately 1.25 mm for all cases.

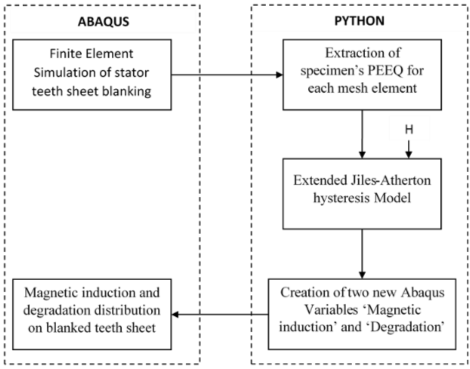

Fig. 7. Flowchart of the magneto-mechanical coupling process.

Figure 8 and Fig. 9 represent the magnetic flux distribution and the corresponding degradation for two magnetic field values, H = 1000 A/m and H = 3500 A/m, respectively.

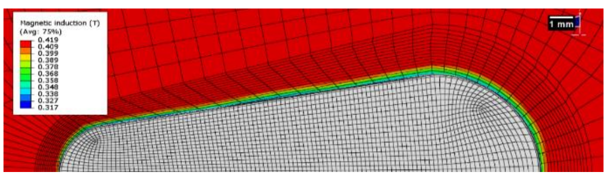

(a)

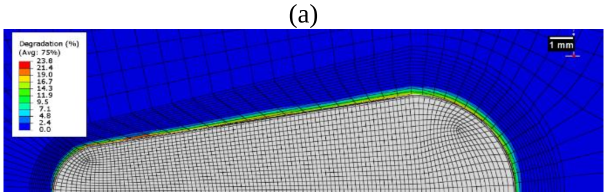

(b)

Fig. 8. Simulation at magnetic field of H = 1000 A/m: (a) Magnetic induction distribution and (b) degradation.

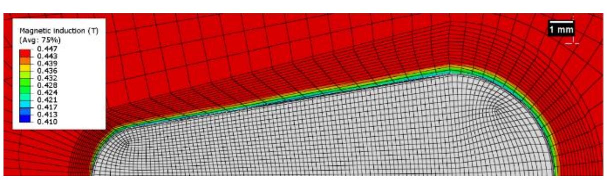

(a)

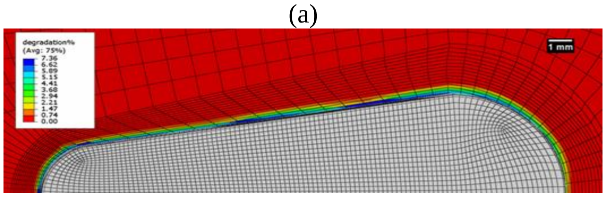

(b)

Fig. 9. Simulation at magnetic field of H = 3500 A/m: (a) Magnetic induction distribution and (b) degradation.

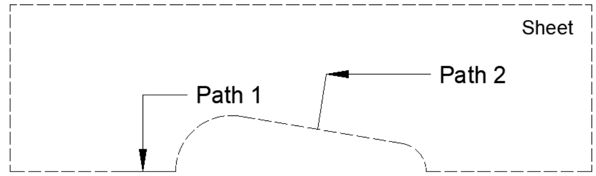

Fig. 10. Paths for monitoring the magnetic induction evolution.

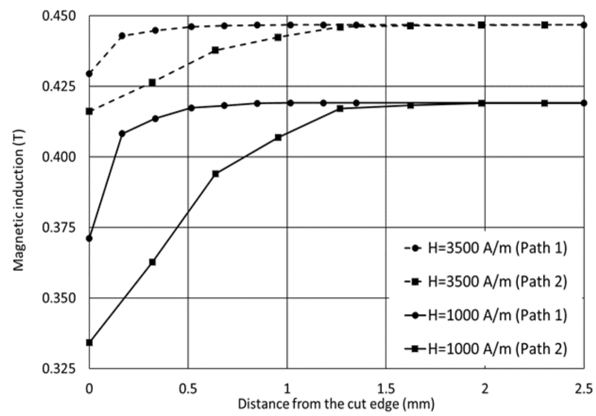

Fig. 11. Magnetic induction evolution along different paths.

VI. CONCLUSION

We performed both experimental and numerical studies on the magneto-mechanical coupling and applied them to stator blanking. The finite-element simulation of a teeth stator using the Gurson–Tvergaard–Needleman constitutive model and an arbitrary Euler–Lagrange mesh description were performed to obtain the accurate plastic strain distribution on the blanked part. A static model of a fully processed, non-oriented Fe–(3 wt%)Si steel sheet under plastic strain was developed on the basis of the classical J-A hysteresis model. In addition, genetic algorithms were used to identify the hysteresis model parameters and formulate an extended description of the J–A model. Using Python language, a simulation procedure was developed. First, the plastic strain state was obtained using the Abaqus process. Subsequently, we analyzed the magnetic induction corresponding to a given value of magnetic field. Finally, both the magnetic induction and magnetic degradation were described using the Abaqus software. From the results, it was evident that the magnetic degradation could reach 25% for a moderate value of the applied magnetic field, and that the width of the "magnetic dead zone" approached 1.25 mm near the cutting edge before the material regained its initial magnetic state. The developed procedure is a helpful tool for engineers and electrical equipment designers to optimize the performance of their electrical designs.

ACKNOWLEDGMENT

The authors would like to extend their sincere appreciation to the Deanship of Scientific Research at the King Saud University for its funding of this research through the Research Group [No. RG-1439/007].

REFERENCES

[1] H. M. S. Harstick, M. Ritter, and W. Riehemann, “Influence of punching and tool wear on the magnetic properties of monoriented electrical steel,” *IEEE Transactions on Magnetics*, vol. 50, no. 4, 2014.

[2] H. Marouani, A. Ben Ismail, E. Hug, and M. Rachik, “Rate-dependent constitutive model for sheet metal blanking investigation,” *Materials Science and Engineering A*, vol. 487, no. 1-2, pp. 162-170, 2008.

[3] H. Naumoski, B. Riedmüller, A. Minkow, and U. Herr, “Investigation of the influence of different cutting procedures on the global and local magnetic properties of non-oriented electrical Steel,” *Journal of Magnetism and Magnetic Materials*, vol. 392, pp. 126-133, 2015.

[4] H. Naumoski, A. Maucher, L. Vandenbossche, et al., “Magneto-optical and field-metric evaluation of the punching effect on magnetic properties of electrical steels with varying alloying content and grain size,” *in 2014 4th International Electric Drives Production Conference (EDPC)*, Nuremberg, pp. 1-9. 2014.

[5] H. Cao, L. Hao, J. Yi, et al., “The influence of punching process on residual stress and magnetic domain structure of non-oriented silicon steel,” *Journal of Magnetism and Magnetic Materials*, vol. 406, pp. 42-47, 2016.

[6] N. Lewis, P. Anderson, J. Hall, and Y. Gao, “Power loss models in punched non-oriented electrical steel rings,” *IEEE Transactions on Magnetics*, vol. 52, no 5, pp. 1-4, 2016.

[7] N. Leuning, S. Steentjes, M. Schulte, W. Bleck, and K. Hameyer, “Effect of elastic and plastic tensile mechanical loading on the magnetic properties of NGO electrical steel,” *Journal of Magnetism and Magnetic Materials*, vol. 417 pp. 42-48, 2016.

[8] V. E. Iordache and E. Hug, “Effect of mechanical strains on the magnetic properties of electrical steels,” *Journal of Optoelectronics and Advanced Materials*, vol. 6, no. 4, pp. 1297-1303, 2004.

[9] V. E. Iordache, F. Ossart, and Eric Hug, “Magnetic characterisation of elastically and plastically tensile strained non-oriented Fe-3.2%Si steel,” in *Journal of Magnetism and Magnetic Materials*, vol. 254-255, pp. 57-59, 2003.

[10] F. Ossart, E. Hug, O. Hubert, C. Buvat, and R. Billardon, “Effect of punching on electrical steels: Experimental and numerical coupled analysis,” in *IEEE Transactions on Magnetics*, vol. 36, no. 5, pp. 31370-3140, 2000.

[11] M. Rekik, O. Hubert, and L. Daniel, “Influence of a multiaxial stress on the reversible and irreversible magnetic behaviour of a 3%Si-Fe alloy,” in *International Journal of Applied Electromagnetics and Mechanics*, vol. 44, no. 3-4, pp. 301-315, 2014.

[12] H. Naumoski, A. Maucher, and U. Herr, “Investigation of the influence of global stresses and strains on the magnetic properties of electrical steels with varying alloying content and grain size,” *2015 5th International Conference on Electric Drives Production, EDPC 2015 – Proceedings*, pp. 1-8, 2015.

[13] L. Bernard and Laurent Daniel, “Effect of stress on magnetic hysteresis losses in a switched reluctance motor: Application to stator and rotor shrink fitting,” *IEEE Transactions on Magnetics*, vol. 51, no. 9, pp. 1-13, 2015.

[14] X. Xiong, S. Hu, K. Hu, and S. Zeng, “Texture and magnetic property evolution of non-oriented Fe-Si steel due to mechanical cutting,” *Journal of Magnetism and Magnetic Materials*, vol. 401, pp. 982-990, 2016.

[15] Z. Wang, S. Li, R. Cui, X. Wang, and B. Wang, “Influence of grain size and blanking clearance on magnetic properties deterioration of non-oriented electrical steel,” *IEEE Transactions on Magnetics*, vol. 54, no. 5, pp. 1-7, 2018.

[16] S. Kuo, W. Lee, S. Lin, and C. Lu, “The influence of cutting edge deformations on magnetic performance degradation of electrical steel,” *IEEE Transactions on Industry Applications*, vol. 51, no 6, pp. 4357-4363, 2015.

[17] H. A. Weiss, N. Leuning, S. Steentjes, et al., “Influence of shear cutting parameters on the electromagnetic properties of non-oriented electrical steel sheets,” *Journal of Magnetism and Magnetic Materials*, vol. 421, pp. 250-259, 2017.

[18] Y. Zaizen, T. Omura, M. Fukumura, K. Senda, and H. Toda, “Evaluation of stress distribution due to shearing in non-oriented electrical steel by using synchrotron radiation,” *AIP Advances*, vol. 6, no. 5, 055926, 2016.

[19] T. Omura, Y. Zaizen, M. Fukumura, K. Senda, and H. Toda, “Effect of hardness and thickness of nonoriented electrical steel sheets on iron loss deterioration by shearing process,” *IEEE Transactions on Magnetics*, vol. 51, no. 11, pp. 1-4, 2015.

[20] H. Toda, “Iron loss deterioration by shearing process in non-oriented electrical steel with different thicknesses and its influence on estimation of motor iron loss,” *IEEJ Journal of Industry Applications*, vol. 3, no. 1, pp. 55-61, 2013.

[21] U. Aydin, P. Rasilo, F. Martin, et al., “Magneto-mechanical modeling of electrical steel sheets,” *Journal of Magnetism and Magnetic Materials*, vol. 439, pp. 82-90, 2017.

[22] K. Hergli, H. Marouani, and M. Zidi, “Numerical determination of Jiles–Atherton hysteresis parameters: Magnetic behavior under mechanical deformation,” *Physica B: Condensed Matter*, vol. 549, pp. 74-81, 2018.

[23] F. Sixdenier, O. Messal, A. Hilal, et al., “Temperature-dependent extension of a static hysteresis model,” in *IEEE Transactions on Magnetics*, vol. 52, no. 3, pp. 1-4, 2016.

[24] R. Szewczyk and P. Frydrych, “Extension of the Jiles-Atherton model for modelling the frequency dependence of magnetic characteristics of amorphous alloy cores for inductive components of electronic devices,” in *Acta Physica Polonica A*, vol. 118, no. 5, pp. 782–784, 2010.

[25] D. C. Jiles and D. L. Atherton, “Theory of ferromagnetic hysteresis,” *Journal of Magnetism and Magnetic Materials*, vol. 61, no. 1-2, pp. 48-60, 1986.

[26] K. Hergli, H. Marouani, M. Zidi, Y. Fouad, and M. Elshazly, “Identification of Preisach hysteresis model parameters using genetic algorithms,” *Journal of King Saud University - Science*, 2018.

[27] D. Peirce, C. F. Shih, and A. Needleman, “A tangent modulus method for rate dependent solids,” *Computers and Structures*, vol. 18, no 5, pp. 875-887, 1984.

[28] C. G’sell and J. J. Jonas, “Determination of the plastic behaviour of solid polymers at constant true strain rate,” *Journal of Materials Science*, vol. 14, no. 3, pp. 583-591, 1979.

[29] H. Marouani, A. Ben Ismail, E. Hug, and M. Rachik, “Numerical investigations on sheet metal blanking with high speed deformation,” *Materials and Design*, vol. 30, no. 9, pp. 3566-3571, 2009.

[30] H. Marouani, M. Rachik, and E. Hug, “Experimental investigations and FEM simulations of parameters influencing the Fe-(Wt.3%)Si shearing process,” *Mechanics & Industry*, vol. 13, no. 4, pp. 271-278, 2012.

[31] A. L. Gurson, “Continuum theory of ductile rupture by void nucleation and growth: Part I—Yield criteria and flow rules for porous ductile media,” *Journal of Engineering Materials and Technology*, vol. 99, no. 1, pp. 2-15 1977.

[32] V. Tvergaard, “Influence of voids on shear band instabilities under plane strain conditions,” *International Journal of Fracture*, vol. 17, no. 4, pp. 389-407, 1981.

[33] H. Derterme and A. Maillard, *Données Métier En Découpage: Quantification de l’influence de La Vitesse de Découpage*. edited by R. D’étude, CETIM, 1997.

Khaoula Hergli was born in Tunisia on November 15, 1986. She received the engineering degree and the master diploma in Mechanical Engineering from the National college of Engineers of Monastir in Tunisia, in 2011 and 2013, respectively.

She is currently a Ph.D. student in the Laboratory of Mechanical Engineering at the National college of Engineers of Monastir since December 2015. She has focused her researches on magnetic hysteresis modeling of soft magnetic materials, sheet metal-forming processes and multiphysics coupling.

Haykel Marouani was born in Tunis, Tunisia, in 1978. He received the B.E. degree in Mechanical Engineering from the National Engineering College of Monastir (Tunisia) in 2001. He received the M.E. and Ph.D. degree from the University of Technology of Compiegne in 2002 and 2006, respectively. He has been the Head of the Mechanical Department of the National Enginering College of Monastir from 2011 to 2014. He is currently working at King Saud University (Saudi Arabia). His main research areas of interest are ferromagnetic sheet metal forming, especially by punching, piercing, and shearing.